Bacterial biofilms investigated by atomic force microscopy and electrochemistry

Hu, Yifan

Publication date:
2012

Document Version
Publisher's PDF, also known as Version of record

Bacterial biofilms investigated by atomic force microscopy and electrochemistry

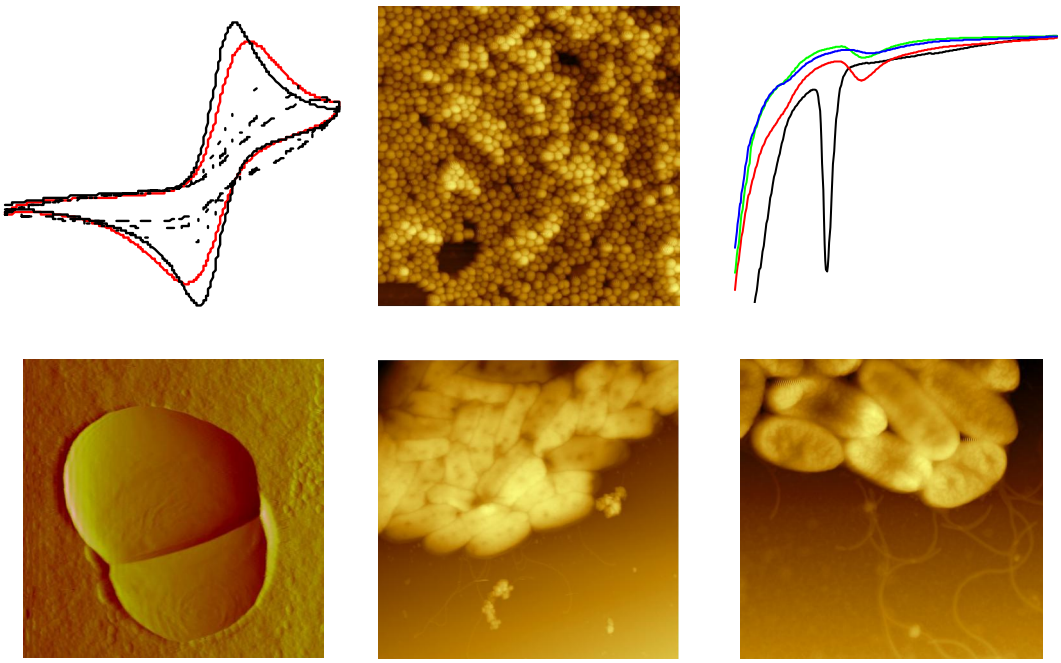

Ph.D thesis
Yifan Hu
Department of Chemistry
Technical University of Denmark
2012

To my great parents and my lovely daughter Sophie

Yifan

Preface and acknowledgement

This thesis is submitted to the Technical University of Denmark in partial fulfillment of the requirement for the Ph.D degree. The work was carried out in the NanoChemistry group, Department of Chemistry, Technical University of Denmark with Professor Jens Ulstrup as supervisor and Associate Professor Jingdong Zhang as co-supervisor. A three-month stay in the Nanobio group at the Institute of Condensed Matter and Nanosciences, Université catholique de Louvain, Belgium, in the spring of 2010 was also part of the work, supervised by Professor Yves F. Dufrêne and Postdoc Vincent Duprès. I belong to Copenhagen Graduate School of Nanoscience and Nanotechnology. Financial support from the Danish Strategic Research Council, the Danish research Council for Technology and Production Sciences, and the Lundbeck Foundation is acknowledged. P.A Fiskers Fond and Otto Mønsteds Fond (November 2009) are acknowledged for their external research Travel scholarship. Managing director Curt Sander at Danish Micro Engineering A/S (DME) and Professor Kjeld Schaumburg at Roskilde University Center are acknowledged for AFM discussions.

I wish to thank my two supervisors Professor Jens Ulstrup and Associate Professor Jingdong Zhang for discussions, theoretical insights, and understanding and helping my thesis in the right direction, and for a great help with the experimental work. I appreciate the freedom they have given me to explore new approaches and collaborations. I also appreciate the time Associate Professor Qijin Chi has spent discussing scientific issues with me. I wish to thank further our group members, Palle Skovhus Jensen, Princia Salvatore, previous member Anna Christina Welinder and Allan Glargaard Hansen, and other group members for sharing scientific discussions and daily life in the office and lab during these three years. I gratefully acknowledge Lise-Lotte Jespersen for giving me all necessary assistance in the lab.

I would like to thank Professor Yves F. Dufrêne and Postdoc Vincent Duprès during my three months in the Nanobio group at the Institute of Condensed Matter and Nanosciences, Université catholique de Louvain, Belgium. They helped me a lot in my

scientific career and personal life and we had a very good cooperation, which made me feel like part of a family. I would also like to thank Sylvie Derclaye for helping me in the lab and Ph.D student André Guillaume for sharing office with me and put up with my humming.

I would like to thank Professor Søren Molin and Dr. Liang Yang at DTU System Biology, Technical University of Denmark for great support in scientific discussions and for cooperation in areas of biofilm research and microbiology. I also thank the following people in their group: Ph.D student Yang Liu, Ph.D student Sara Bayard Dűhring, and Dr. Ninell Pollas Mortensen.

Finally, I would like to thank my husband Shuyuan Qin to share my happy life, love and support. I am so glad that my baby girl Sophie brings me so much surprise and happiness during my thesis writing. I owe gratitude to my mother and father to educate and support me for nearly 30 years, all my achievements belong to you. I greatly thank my parents-in-law for sharing our difficulties, happiness and love. My gratitude finally extends to all my dear friends in Denmark, in China and other countries for all the support you have given me.

Kgs. Lyngby April 1st, 2012

Yifan Hu

Abstract

Bacterial biofilms are aggregates of microorganisms in which cells adhere to each other and adhere to a solid surface or an animal host cavity. Bacterial biofilms play important roles in human life, and cause serious harm for human society and huge economic losses. The complex composition of bacterial biofilms with EPS (Extracellular polymeric substances) includes proteins, polysaccharides, extracellular DNA (e-DNA), peptidoglycans, lipids and phospholipids. These substances play an important role in the initial adhesion of bacteria to the surface and maintenance of the biofilm structure. In my thesis, Atomic Force Microscopy (AFM) and electrochemistry have been applied to investigate three pathogenic medically important bacterial biofilms, i.e. *Pseudomonas aeruginosa* (cystic fibrosis pneumonia), *Staphylococcus epidermidis* (contamination of surgical catheters and indwelling equipment) and *Streptococcus mutans* (dental caries).

AFM was used to investigate the adhesion force on single live cell surfaces. Four different strains of *Staphylococcus epidermidis* in liquid aqueous environments were adressed. These strains were selected because of their special surface proteins related with the initial attachment on the surface. High-resolution AFM imaging showed no detectable differences among the four strains. Adhesion maps using hydrophobically modified tips compared with bare hydrophilic silicon nitride tips also showed small differences only. This indicates that hydrophobic effects are not the primary driving forces towards adhesion. Two chemical inhibitor compounds were found to have strong effects on the adhesion between the bare tips and the bacteria.

Secondly, AFM and electrochemistry were combined to study bacterial biofilm formation on Au(111)-surfaces, to determine the surface charge and growth pattern of *Streptococcus mutans* biofilms. Five redox probes were chosen for cyclic voltammetry, i.e. positively, $[Ru(NH_3)_6]^{3+/2+}$, $[Co(phen)_3]^{3+/2+}$ and $[Co(terpy)_2]^{3+/2+}$ (phen = 1,10-phenanthroline; terpy = 2,2',2"-terpyridine) and negatively charged, $[Fe(CN)_6]^{3-/4-}$. $[IrCl_6]^{3-/4-}$. The inhibition and voltammetric patterns showed that *S. mutans* biofilm are negatively charged. Addition of DNAase suggests that the negative charges to a large extent originate from DNA excreted by the biofilm.

Thirdly, AFM and electrochemistry were combined to study *Streptococcus mutans* biofilm formation on bare Au(111) and Au(111) modified by self assembled molecular monolayers (SAMs) of thiol-based molecules. Four SAM molecules were chosen for reductive desorption (RD). Two are long straight-chain thiols with either a hydrophobic or a hydrophilic terminal group, i.e. hexadecanethiol, $HS(CH_2)_{15}CH_3$ and mercapto-hexadecanoic acid, $HS(CH_2)_{15}COOH$. Two others were the short rigid linker molecules L-cysteine and cysteamine. Strong RD peaks were obtained for all the four molecules both in PBS buffer at pH 7.4 and in 0.1M NaOH solution. Both AFM images and the electrochemical data show further, that the biofilms are bound more strongly to the hydrophobic surface than to the hydrophilic surfaces.

Finally, AFM was used to study two other kinds of bacteria, *Pseudomonas aeruginosa* and *Pseudomonas putida*, and their relationship with EPS. Different mutant strains were applied to investigate the roles of Pel and Psl polysaccharides and type IV pili during *P. aeruginosa* biofilm development. This study suggests that polysaccharides and e-DNA contribute to the *P. aeruginosa* biofilm development. Protein clusters were observed during *P. pudita* biofilm formation, but we need further investigation to identify or distinguish the surface protein Lap A and Lap F.

The combination of AFM and electrochemistry is a new approach to understand the bacterial biofilm/ medium / bare or modified Au(111) interface. Future efforts aim at observing the live bacterial biofilms with high resolution and controlling the biofilm formation on SAM-modified Au(111)-surfaces by the combination of AFM and electrochemical characterization.

Abstract (Danish)

Bakterielle biofilm er aggregater, hvor mikroorganismer danner sammenhængende kolonier fastgjort til faste overflader eller indesluttet i menneskelige og animalske værtsorganismer. Bakterielle biofilm er af stor betydning og kan være årsag til alvorlige patologiske og økonomiske skader. Bakterielle biofilms komplekse sammensætning indeholder protein, polysaccharid, ekstracellulært DNA (e-DNA), peptidoglycaner, lipider og phospholipider "Extra-cellular polymeric substances", EPS). Disse komponenter er vigtige både i biofilmenes indledende dannelsesfaser og i opretholdelse af selve biofilmstrukturerne. I mit ph.d.-projekt er atomar kraftspektroskopi, AFM og elektrokemi anvendt til at undersøge tre pathogene og medicinsk vigtige bakterielle biofilm, *Pseudomonas aeruginosa* (cystisk fibrose lungebetændelse), *Staphylococcus epidermidis* (kontaminering fra katedre og andet medicinsk udstyr) samt *Steroptococcus mutans* (dental caries).

AFM blev anvendt til en undersøgelse af levende individuelle cellers overefladeadhæsion repræsenteret ved fire forskellige *Staphylococcus epidermidis* stammer i vandigt medium. Stammerne var udvalgt ud fra deres specielle overfladeproteiner knyttet til indledende overfladebinding. Højopløst AFM viste ingen påviselige forskelle mellem de fire stammer. Adhæsionskortlægning baseret på hydrofobt modificerede AFM tippe sammenlignet med rene hydrofile siliciumnitrid tippe viste heller ikke nævneværdige forskelle. Dette indikerer, at hydrofobe kræfter ikke er afgørende i bakteriel adhæsion. To centrale inhibitorer fandtes at have stor effekt på adhæsionen mellem de rene tippe og bakterierne.

AFM og elektrokemi blev dernæst kombineret i en undersøgelse af biofilmdannelse på Au(111)-overflader for at bestemme elektrostatisk overfladeladning og vækstmønstre for *Streptococcus mutans* biofilm. Fem positivt $[Ru(NH_3)_6]^{3+/2+}$, $[Co(phen)_3]^{3+/2+}$ og $[Co(terpy)^2]^{3+/2+}$ (phen = 1,10-phenanthrolin, terpy, 2,2',2"-terpyridin) og negativt ladede, $[Fe(CN)_6]^{3-/4-}$ og $[IrCl_6]^{3-/4-}$ redoxprober blev udvalgt til cyklisk voltammetri. Inhibering og voltammetriske mønstre viste, at *S. mutans* biofilm er negativt ladede. Tilsætning af

DNAase peger på, at de negative ladninger i vid udstrækning kommer fra DNA udskilt af biofilmene (e-DNA).

AFM og elektrokemi blev kombineret i en videre undersøgelse af *Streptococcus mutans* biofilmdannelse på rene Au(111)-overflader og Au(111)-overflader modificeret af selvsamlende molekylære monolag (SAMs) af thiolbaserede molekyler. Fire SAM molekyler blev udvalgt som prober for reduktiv desorption (RD). To er lange ligekædede thioler med enten en hydrofob (hexadecanthiol) eller en hydrofil terminal gruppe (mercaptohexadecansyre) terminal funktionel gruppe. To andre var de korte, strukturelt stive linkermolekyler L-cystein og cysteamin. Alle fire molekyler udviste stærke RD signaler både i PBS buffer ved pH 7,4 og i 0,1 M NaOH opløsning. Både AFM og de elektrokemiske data viser videre, at biofilmene er bundet stærkere til de hydrofobe end til de hydrofile overflader.

AFM blev endelig anvendt på to andre bakterietyper, *Pseudomonas aeruginosa* og *Pseudomonas putida* og deres sammenhæng med EPS. Forskellige mutantstammer blev anvendt til at undersøge Pel og Psl polysaccharider og type IV pili under *P. aeruginosa* biofilm udvikling. Denne undersøgelse indikerer, at polysaccharider og e-DNA bidrager til *P. aeruginosa* biofilm udviklingen. Proteinklynger kunne ses under *P. putida* biofilmdannelse, men flere undersøgelser er påkrævet for at kunne identificere eller skelne overfladeproteinerne Lap A og Lap F.

Kombinationen af AFM og elektrokemi er en ny indgangsvinkel til at forstå interfaseområdet mellem bakterielle biofilm, det vandige reaktionsmedium og en ren eller modificeret metaloverflade. Kommende indsatser vil være rettet mod højopløst kortlægning af levende bakterier og kontrol af biofilmdannelsen på SAM-modificerede Au(111)-overflader ved kombination af AFM og elektrokemisk karakterisering.

Abbreviations

AFM	Atomic force microscopy
BHI	Brain heart infusion Broth
CFM	Chemical force microscopy
CV	Cyclic voltammetry / voltammogram
DNA	Deoxyribonucleic acid
E	Young's modulus
EM	Electron microscopy
EPS	Extracellular polymer substrates
erm	Erythromycin
ET	Electron transfer
LB	Luria-Bertani
LSV	Linear sweep voltammetry / voltammogram
MHD	1-hexadecanethiol
MHDA	ω-mercaptohexadecanoic acid
MQ	Millipore water
OCP	Open circuit potential
OD_{600}	Optical density at 600 nm
RHE	Reversible hydrogen electrode
SAM	Self-assembled monolayer
SCE	Saturated calomel electrode
SEM	Scanning electron microscopy
SFM	Scanning force microscopy
SQV	Square wave voltammetry / voltammogram
STM	Scanning tunneling microscopy
TEM	Transmission electron microscopy
tet	Tetracyklin
TSB	Trypic soy Broth
UHV	Ultra-high vacuum

Content

Chapter 1 Introduction

Bacterial biofilms are compositions of bacteria wrapped in secreted bacterial polysaccharide polymer membrane proteins (Extracellular Polymeric Substances, EPS) and e-DNA adhering on solid surfaces or in animal host cavities. Bacterial biofilms are widely found in nature, medical environments, food, industrial environments and many other areas. Bacterial biofilms play important roles in human life, and are causes of serious harm for human society and of huge economic losses.

The complex composition of bacterial biofilms includes proteins, polysaccharides, DNA, peptidoglycans, lipids and phospholipids. These substances play important roles in the initial adhesion of bacteria to the surfaces and in the maintenance of the biofilm structures. Studies of biofilms are in the forefront of life science, though identification of these macromolecules, and functional mechanisms of biofilm formation are still at the early stages of research. Bacterial biofilms develop in extremely complex and dynamic environments. Many details regarding structures of the surface of bacterial biofilms (such as flagella and cilia), secretion systems (secretion), ability to move (motility), quorum sensing system (quorum sensing), and chemoattractant systems (chemotaxis), have been proved to impact on the development and formation of bacterial biofilms[1].

With the understanding of bacterial pathogenesis, researchers have discovered that bacterial biofilms have strong resilience in the host immune system and resistance to antibiotics. This causes short-term or chronic medical problems in the clinical treatment, which are difficult to cure in a number of bacterial biofilm infections particularly inflammatory diseases. It is therefore, crucial to study bacterial biofilms in detail. Bacterial biofilms exist in human tissues such as teeth, gums, skin, lung, urinary tract and other organs. The biofilms forming on different kinds of the surfaces, can cause periodontal disease, dental caries, chronic bronchitis, septicemia, thrombophlebitis, intractable diseases such as lung infections, and endocarditis[1,2]. Biofilm formation can occur in blood, tissue fluid, and in lymph and other body fluids. These fluids contain the organic nutrients for bacterial biofilm formation. Once these fluids in the human body are

contaminated by bacteria, bacterial biofilms attach to artificial medical devices (such as contact lenses, artificial joints and artificial heart valves) and bring more serious diseases. In addition, bacterial biofilms can adhere on human-life-related facilities such as air-conditioning systems, water systems and food processing equipments, resulting in infectious diseases. It is estimated that approximately 65% of human bacterial infectious diseases are caused by bacterial biofilms[1].

Atomic force microscopy (AFM) is an advanced technology for observing the force interactions between the tip and the surface[3]. AFM has a nano-probe or tip, fixed on a sensitive cantilever which can handle the micrometer scale. When the probe is very close to the sample, the top surface of the probe on the cantilever will bend from the original location. A photo-detector receives the tiny signal from a laser beam deflected from the cantilever and transfers them into the images in a computer. AFM offers great advantages in many scientific areas, including mapping of biological samples such as bacterial biofilms.

The appearance of nanoscience and nanotechnology in the twenty-first century has impacted human life and offers a new insight at the nano-scale in a wealth of areas[4] (Fig 1.1). AFM has become a powerful tool for microbiology. High resolution AFM images of biological samples can be obtained in both liquid and air, Fig. 1.2[5-7]. Scientists can observe physical structures of live bacteria in greater depth than the human body[8-11]. AFM has been used to track and observe bacterial biofilm growth in their natural complex environment, as well as drug inhibition mechanisms and function in bacterial cells[12-15]. AFM can be used to study not only bacterial[16,17], but also cell walls, lipids, proteins, DNA, and some small molecular compounds[8-11]. Many AFM images of live cells have demonstrated details of the bacterial cell wall structure. Remarkably, real-time imaging enables monitoring microbial surfaces as they interact with enzymes[18,19], antibiotics[20,21] and to follow their growth[22,23]. Chemical force microscopy (CFM)[24-26], can also be used to detect the nanoscale physicochemical properties of cells. Chemical modification of the AFM tip using functional groups such as hydrophilic and

hydrophobic, alkyl and carboxyl groups can detect microbial surface functional groups, such as the microbial surface hydrophobicity[26,27] and surface charge [28].

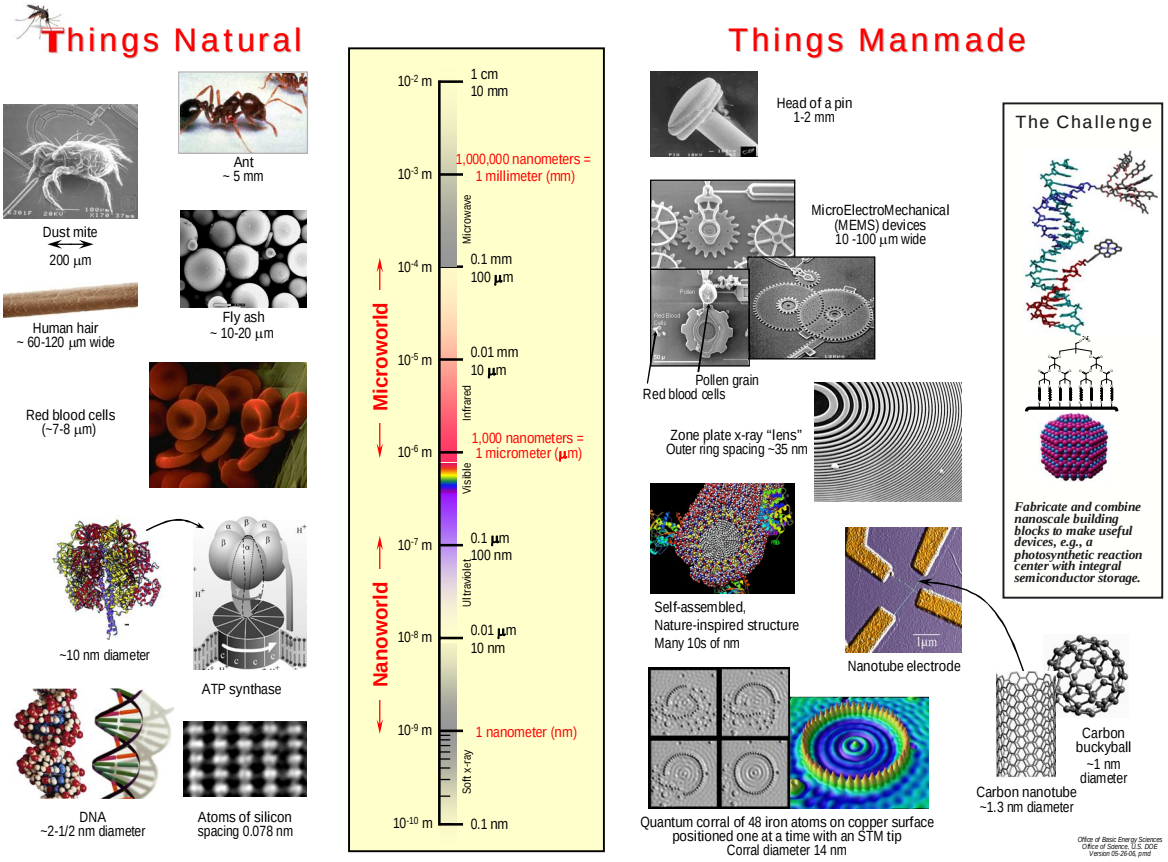

Fig 1.1. The scale of natural and man-made things in the Nanoworld and Microworld. [4]

Recently, electrochemical experimental techniques have been introduced to monitor the growth of bacteria in the process of biofilm growth (such as biofilm age, cell density, pH, etc.), as well as macromolecular compounds produced by the biofilms. Biofilms on the electrode surface have been studied using cyclic voltammetry (CV)[29-36], impedance spectroscopy[31], and infrared reflection spectroscopy[32]. Electrochemistry has been used to control biofilm growth, such as the stimulation on positively charged solid surfaces and inhibition on negatively charged surfaces[37]. Some studies have shown that the negatively charged bacterial biofilms are more likely to grow on positively charged electrode surfaces with faster growth, whereas negatively charged surface inhibit bacterial growth[38].

Other researches has shown that static electric fields play a major role in the in the adhesion of bacterial biofilms to the solid surfaces[33,35,36].

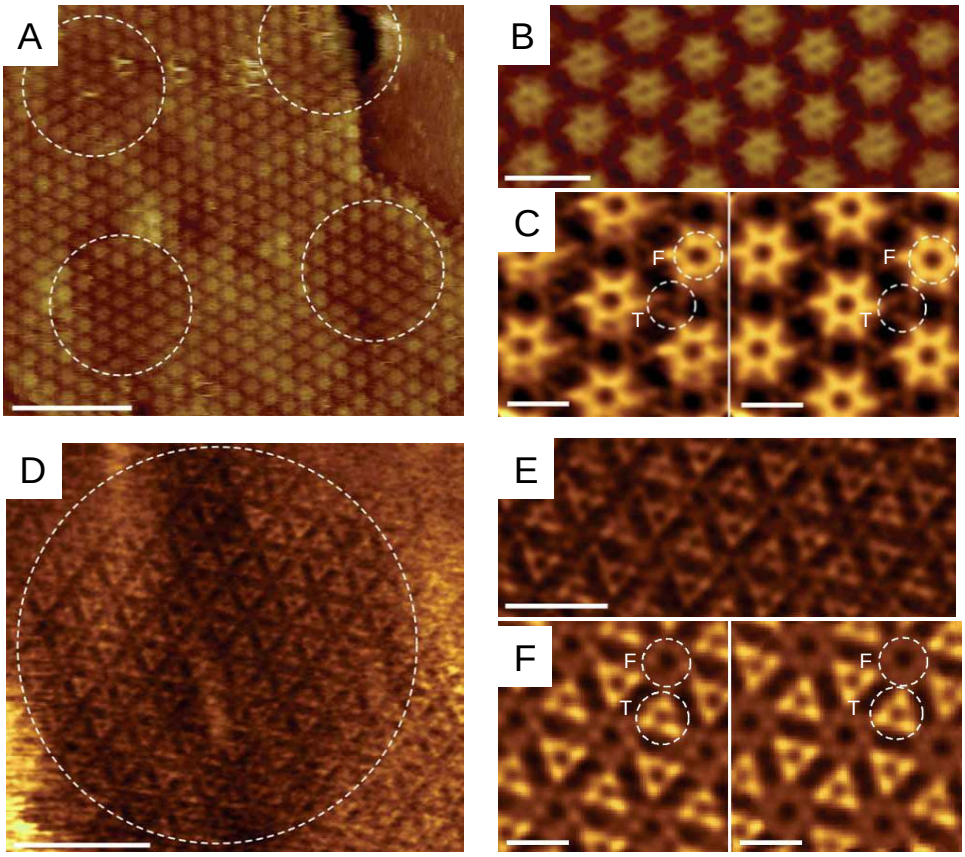

Fig.1.2 High-resolution imaging of membranes of *Corynebacterium glutamicum*. (A) High-resolution topography of the inner S-layer surface. (B) Fourier-filtered image of A. (C) Average topographies. (D) High-resolution topography of the outer S-layer surface. (E) Fourier filtered image of d. (F) Average topographies. Dashed lines in C and F highlight the structural pore in the center of the flower (F) and triangular (T) shaped surfaces of 15 Å. in diameter. Scale bars, 90 nm (A), 20 nm (B), 10 nm (C), 50 nm (D), 20 nm (E) and 10 nm (F), reprint from[5].

In my PhD project, I have used AFM and electrochemistry to investigate several pathogenic medical bacterial biofilms. They are *Pseudomonas aeruginosa* (cause of cystic fibrosis pneumonia), *Staphylococcus epidermidis* (causes of contamination of surgical catheters and indwelling equipment), and *Streptococcus mutans* (cause of dental

caries). The study has addressed the formation of bacterial biofilms, the interactions of bacterial biofilms on the modified Au(111) surface, the mechanisms of initial bacterial biofilm attachment, and the surface charge of bacterial biofilm. The purpose of the study is to characterize the biofilm structure with high resolution, the surface charge of bacterial biofilms, and adhesion properties, with a further view in finding new ways to struggle against human diseases.

The thesis is composed of two parts. The first part contains an introduction (Chapter 1), and description of some methodologies: Bacterial biofilm growth (Chapter 2), AFM (Chapter 3), Electrochemistry (Chapter 4), and Chemicals and experimental section (Chapter 5). The second part presents results and discussion, including the following:

1. Using AFM to investigate the adhesion forces on single live cell surfaces addressing four different strains of *Staphylococcus epidermidis* in liquid. These were selected for their particular surface proteins, which contributed for the bacterial biofilm initial attachments in the surface. These strains were applied in several advanced methods, such as polycarbonate membrane tracked single bacteria, adhesion mapping, force curve recording, functional probes and the interaction between the functional probe and single bacteria. The latter were further compared with the use of two selected drugs to understand the single-cell adhesion and the mechanism of the drug inhibition and function. (Chapter 6)

2. Using AFM and electrochemistry (cyclic voltammatry) to study the bacterial biofilm formation on the electrochemical Au(111)-surface. Use of small electrostatic probe molecules could determine among other things the sign of the surface charge or excreted polymer matrix (e-DNA) of *Streptococcus mutans* biofilms. Further experiments were carried out after removal of e-DNA with DNAase, which shows that to a large extent the negative charge affecting the voltammograms comes from DNA. (Chapter 7)

3. Using AFM and electrochemistry to study the bacterial biofilm formation on bare and modified Au (111)- electrode surfaces. The purpose of this study was to find relationships

between the surface of *Streptococcus mutans* biofilms and the modified Au (111)-surfaces. Four molecules that form thiol-based self-assembled molecular monolayers (SAMs) were used: two are long straight-chain thiols with either a hydrophobic or a hydrophilic terminal group, i.e. hexadecanethiol, $HS(CH_2)_{15}CH_3$ and mercapto-hexadecanoic acid, $HS(CH_2)_{15}COOH$, respectively. Two others are the short rigid linker molecules, L-cysteine and cysteamine. (Chapter 8)

4. Other AFM studies of bacterial biofilm formation of *Pseudomonas aeruginosa* and *Pseudomonas putida*, the relationships between EPS (extracellular polymeric substance) and bacterial biofilm formation. *Pseudomonas aeruginosa* focus was on the polysaccharides, DNA and pili while *Pseudomonas putida* focus was on two main surface proteins (Chapter 9).

Reference

1. Costerton, J.W.; Stewart, P.S. and Greenberg, E.P. Bacterial biofilms: a common cause of persistent infections. *Science*, **1999**, 284: 1318–1322.
2. Rodriguez-Martinez, J.M. and Pascual, A. Antimicrobial resistance in bacterial biofilms. *Reviews in Medical Microbiology*, **2006**, 17: 65-75.
3. Binnig, G.; Quate, C.F. and Gerber, C. Atomic force microscopy. *Physical Review Letters*, **1986**, 56: 930-933.
4. http://www.er.doe.gov/bes/scale_of_things.html
5. Goncalves, R.P.; Agnus, G.; Sens, P.; Houssin, C.; Bartenlian, B. and Scheuring, S. Two-chamber AFM: probing membrane proteins separating two aqueous compartments. *Nature Methods*, **2006**, 3 (12): 1007-1012.
6. Scheuring, S. and Sturgis, J.N. Chromatic adaptation of photosynthetic membranes. *Science*, **2006**, 309: 484-487.
7. Scheuring, S.; Stahlberg, H.; Chami, M.; Houssin, C.; Rigaud, J.L. and Engel, A. Charting and unzipping the surface layer of *Corynebacterium glutamicum* with the atomic force microscope. *Molecular Microbiology*, **2002**, 44 (3): 675-684.

8. Gaboriaud, F. and Dufrene, Y. F. Atomic force microscopy of microbial cells: application to nanomechnical properties, surface forces and molecular recognition forces. *Colloids and Surface B: Biointerfaces*, **2007**, 54: 10-19.
9. Dufrêne, Y. F. Using nanotechniques to explore microbial surfaces. *Nature Reviews Microbiology*, **2004**, 2: 451-460.
10. Muller, D. J. and Dufrene, Y. F. Atomic force microscopy as a multifunctional molecular toolbox in nanobiotechnology. *Nature Nanotechnology*, **2008**, 3: 261-269.
11. Dupres, V.; Alsteens, D.; Pauwels, K. and Dufrene, Y. F. In vivo imaging of S-layer nanoarrays on *Corynebacterium glutamicum*. *Langmuir*, **2009**, 25: 9653-9655.
12. Touhami, A.; Jericho, M. H. and Beveridge, T. J. Atomic force microscopy of cell growth and division in *Staphylococcus aureus*. *Journal of Bacteriology*, **2004**, 186: 3286-3295.
13. Andre, G.; Kulakauskas, S.; Chapot-Chartier, M.P.; Navet, B.; Deghorain, M.; Bernard, E.; Hols, P. and Dufrêne, Y.F. Imaging the nanoscale organization of peptidoglycan in living *Lactococcus lactis* cells. *Nature Communication*, **2010**, 1:27.
14. Schaer-Zammaretti, P. and Ubbink, J. Imaging of lactic acid bacteria with AFM—elasticity and adhesion maps and their relationship to biological and structural data. *Ultramicroscopy*, **2003**, 97: 199-208.
15. Qin, Z.; Zhang, J.; Hu, Y.; Chi, Q.; Mortensen, N. P.; Qu, D.; Molin, S. and Ulstrup, J. Organic compounds inhibiting *S. epidermidis* adhesion and biofilm formation. *Ultramicroscopy*, **2009**, 109: 881-888.
16. Hu, Y.; Zhang, J and Ulstrup. J. Interfacial Electrochemical Electron Transfer Processes in Bacterial Biofilm Environments on Au(111). *Langmuir*, **2010,** 26 (11): 9094-9103.
17. Doktycz, M. J.; Sullivan, C. J. ; Hoyt, P. R.; Pelletier, D. A.; Wu, S. and D. P. Allison, AFM imaging of bacteria in liquid media immobilized on gelatin coated mica surfaces. *Ultramicroscopy*, **2003**, 97: 209-216.

18. Ahimou, F. O.; Touhami, A. and Dufrêne, Y. F. Real-time imaging of the surface topography of living yeast cells by atomic force microscopy. *Yeast*, **2003**, 20: 25-30.
19. Francius, G. ; Domenech, O.; Mingeot-Leclercq, M. P. and Dufrene, Y. F. Direct observation of *Staphylococcus aureus* cell wall digestion by lysostaphin. *Journal of Bacteriology*, **2008**, 190: 7904-7909.
20. Verbelen, C.; Dupres, V.; Menozzi, F. D.; Raze, D.; Baulard, A. R.; Hols P. and Dufrêne, Y. F. Ethambutol-induced alterations in *Mycobacterium bovis* BCG imaged by atomic force microscopy. *FEMS Microbiology Letter*, **2006**, 264: 192-197.
21. Fantner, G. E.; Barbero, R. J.; Gray, D. S. and Belcher, A. M. Kinetics of antimicrobial peptide activity measured on individual bacterial cells using high-speed atomic force microscopy. *Nature Nanotechnology*, **2010**, 5: 280-285.
22. Dague, E.; Alsteens, D.; Latgé, J. P. and Dufrêne, Y. F. High-resolution cell surface dynamics of germinating *Aspergillus fumigatus* conidia. *Biophysical Journal*, **2008**, 94: 656-660.
23. Plomp, M.; Leighton, T. J. ; Wheeler, K. E.; Hill, H. D. and Malkin, A. J. In Vitro High-Resolution Structural Dynamics of Single Germinating Bacterial Spores. *Proceedings of the National Academy of Sciences* U. S. A., **2007**, 104: 9644-9649.
24. Frisbie, C. D.; Rozsnyai, L. F.; Noy, A.; Wrighton, M. S. and Lieber, C. M. Functional Group Imaging by Chemical Force Microscopy. *Science*, **1994**, 265: 2071-2074.
25. Noy, A. Chemical force microscopy of chemical and biological interactions. *Surface and Interface Analysis*, **2006**, 38: 1429-1441.
26. Dague,. E.; Alsteens, D.; Latge, J. P. ; Verbelen, C.; Raze, D.; Baulard, A. R. and Dufrêne, Y. F. Chemical force microscopy of single live cells, *Nano Letters*, **2007**, 7: 3026-3030.
27. Alsteens, D.; Dague, E.; Rouxhet, P. G.; Baulard A. R. and Dufrêne, Y. F. Direct measurement of hydrophobic forces on cell surfaces using AFM. *Langmuir*, **2007**, 23: 11977-11979.

28. Ahimou, F.; Denis, F. A.; Touhami A.; and Dufrene, Y. F. Probing microbial cell surface charges by atomic force microscopy. *Langmuir*, **2002**, 18: 9937-9941.
29. Giao, M.S. ; Montenegro, M.I. and Vieira, M.J. Monitoring Biofilm formation by using cyclic Voltammetry-effect of the experimental conditions on biofilm removal and activity. *Water science and technology*, **2003**, 47: 51-56.
30. Wang, Y.; Tsujimura, S. ; Cheng, S. and Kano, K. Self-excreted mediator from Escherichia coli K-12 for electron transfer to carbon electrodes. *Applied Microbiology and Biotechnology*, **2007**, 76: 1439-1446.
31. Busalmen, J. P.; Berna, A. and Feliu, J. M. Spectroelectrochemical examination of the interaction between bacterial cells and gold electrodes. *Langmuir*, **2007**, 23: 6459-6466.
32. Hu, Z.; Jin, J.; Abruna, H. D.; Houston, P. L.; Hey, A.G.; Ghiorse, W.C.; Shuler, M. L.; Hidalgo, G. and Lion, L. W. Spatial distributions of copper in microbial biofilms by scanning electrochemical microscopy. *Environmental Science and Technology*, **2007**, 41: 936-941.
33. Vostiar, I. ; Ferapontova, E. E. and Gorton, L. Electrical "wiring" of viable Gluconobacter oxydans cells with a flexible osmium-redox polyelectrolyte. *Electrochemistry Communications*, **2004**, 6: 621-626.
34. Timur, S. ; Haghigghi,B.; Tkac, J. ; Pazarhoĝlu, N. ; Telefoncu, A. and Gorton, L. Electrical wring of *Pseudomonas putida* and *Pseudomonas flluorescens* with osmium redox polymers. *Bioelectrochemistry*, **2007**, 71: 38-45.
35. Marsili, E.; Rollefson, J.B.; Baron, D.B.; Hozalski, R.M. and Bond, D. R. Microbial biofilm voltamemetry: direct electrochemical characterization of catalytic electrode-attached biofilms. *Applied and Environmental Microbiology*, **2008**, 74 (23): 7329-7337.
36. Kasemo, B. Biological surface science. *Surface Science*, **2002**, 500: 656-67**7.**
37. Van der Mei.; H.C. and Busscher, H.J. Electrophoretic mobility distributions of single-strain microbial populations. *Applied and Environmental Microbiology*, **2001**, 67 (2): 491-494.

38. Bos, R.; Van der Mei, H.C. and Busscher, H.J. Physico-chemistry of initial microbial adhesive interactions—its mechanisms and methods for study. *FEMS Microbiology Review*, **1999**, 23: 179-229.

Chapter 2 Biofilms

2.1 Biofilms

Bacteria that attach to surfaces aggregate in a hydrated polymeric matrix of their own synthesis to form biofilms[1]. During the biofilm development, extracellular polymeric substances (EPS), flagella, typeIV pili and bacterial cells are involved[1,2]. The EPS matrix is usually composed of polysaccharides, protein and DNA[3,4]. Generally biofilm formation has five stages, see Fig 2.1.

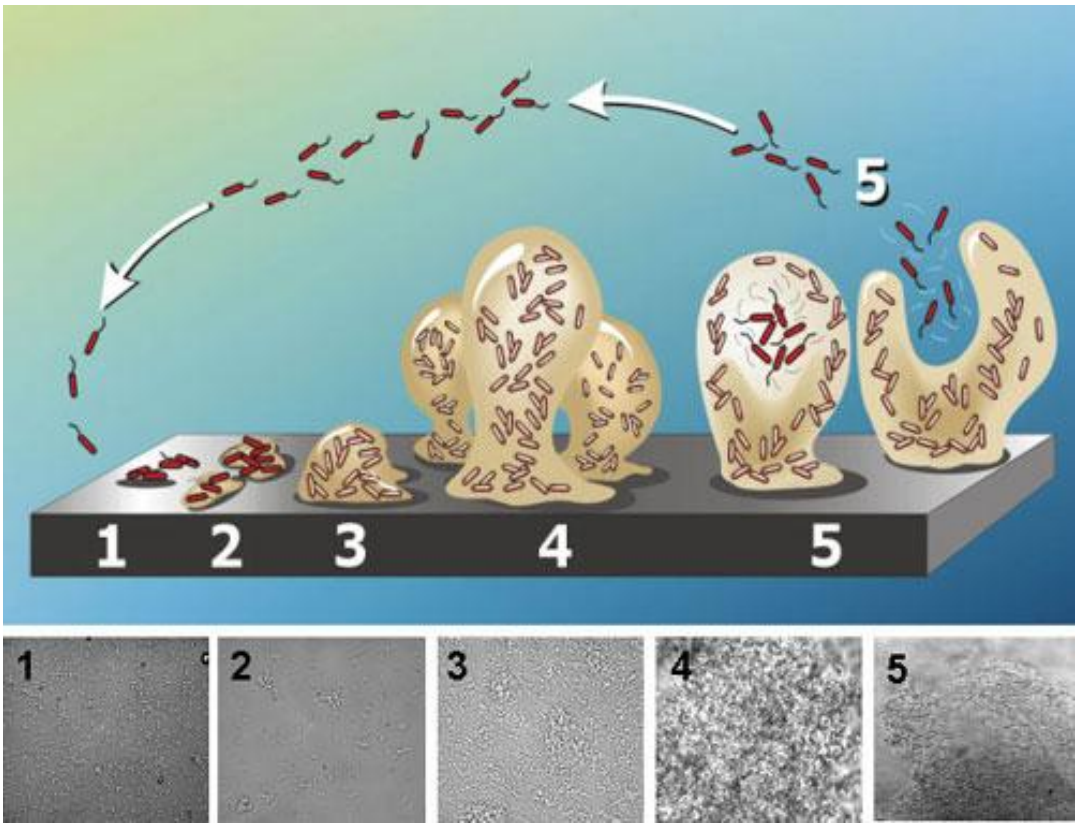

Fig. 2.1 Development of a biofilm as a five-stage process under continuous-flow conditions (e.g. flow cell system) from two dimensions to three dimensions. Stage 1: initial attachment of bacterial cells to the surface. Stage 2: production of EPS resulting in more firmly adhered cells. Stage 3: early development of biofilm architecture. Stage 4: maturation of biofilm architecture. Stage 5: dispersion of single cells from the biofilm. The bottom panels (1-5) show each stage represented by a photomicrograph of *P. aeruginosa* under continuous-flow conditions on a glass substratum[5].

Four plausible driving forces have been summarized in a review by K.K.Jefferson[6]: (1) protection from harmful conditions in the host (defense), (2) sequestration to a nutrient-rich area (colonization), (3) utilization of cooperative benefits (community), (4) bacteria normally grow as biofilms in nature or in these less-than-ideal environments and planktonic cultures are an *in vitro* artifact (biofilms as the default mode of growth*) (see Fig 2.2).

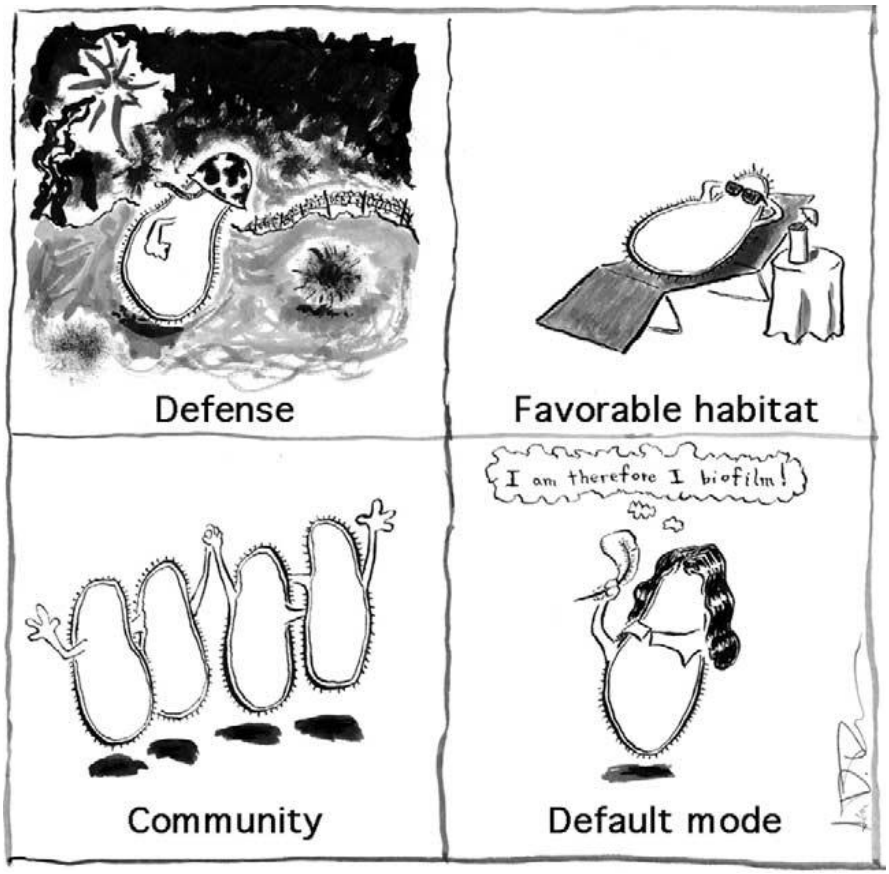

Fig 2.2 Four possible driving forces for bacterial biofilm formation[6].

*Explaination from ref 6: It almost seems counter-intuitive that the biofilm mode of growth could confer a reproductive fitness advantage when one considers that biofilm bacteria have a reduced rate of growth relative to bacteria growing planktonically in broth culture. Outside of the laboratory, however, bacteria rarely, if ever, find themselves in an environment as nutrient rich as culture media, and in conditions that there are a number of advantages imparted by the biofilm mode of growth.

Biofilm formation has brought a lot of problems to our life affecting for example: human teeth, cooling water, food processing, oil recovery, ship hulls, drinking water, paper manufacturing and medical implants. Microbial biofilms cost billions of dollars every year world-wide in equipment damage, product contamination, energy losses and medical infections. Many medical biofilms cause serious human infections, Table 2.1. Conventional methods for eradicating bacteria such as antibiotics and disinfection are less effective to biofilm populations due to their special physiology and physical matrix barrier[7]. Novel strategies based on detailed understanding of the biofilm formation mechanisms are therefore an important issue for many industries and hospitals.

Table 2.1. Main human infections involving biofilms [1,2]

Infection or disease	Common biofilm bacterial species
Cystic fibrosis pneumonia	*Pseudomonas aeruginosa* and *Burkholderia cepacia*
Dental caries	Acidogenic Gram-positive cocci (e.g., *Streptococcus*)
Periodontitis	Gram-negative anaerobic oral bacteria
Osteomyelitis	Various bacterial and fungal species, often mixed
Bacterial prostatitis	*Escherichia coli* and other Gram-negative bacteria
Otitis media	Non-typable strains of Haemophilus influenzae
Musculoskeletal infections	Gram-positive cocci (e.g., *staphylococci*)
Biliary tract infection	Enteric bacteria (e.g., *E. coli*)
Native valve endocarditis	Viridans group streptococci
Infections associated with foreign body material	
ICU pneumonia	Gram-negative rods
Urinary catheter cystitis	*E. coli* and other Gram-negative rods
Central venous catheters	*Staphylococcus epidermidis* and others
Mechanical heart valves	*Staphylococcus aureus* and *S. epidermidis*
Vascular grafts	Gram-positive cocci
Orthopedic devices	*S. aureus* and *S. epidermidis*
Arteriovenous shunts	*S. epidermidis* and *S. aureus*
Endotracheal tubes	A variety of bacteria and fungi
Sutures	*S. epidermidis* and *S. aureus*
Exit sites	*S. epidermidis* and *S. aureus*
Scleral buckles	Gram-positive cocci
Contact lens	*P. aeruginosa* and Gram-positive cocci
Peritoneal dialysis peritonitis	A variety of bacteria and fungi
Penile prostheses	*S. aureus* and *S. epidermidis*

In epidemiological studies, bacterial biofilms have long been recognized as primary causes of infections such as Cystic fibrosis pneumonia (*Pseudomonas aeruginosa*), infections from catheters and indwelling devices (*Staphylococcus aureus* and *Staphylococcus epidermidis*), biliary tract infection (*Escherichia coli*), and dental caries

(*Streptococcus mutans*).[1,2] Principles of biofilm formation and interaction between the surface and biofilms are intensely explored in combats against human diseases[1,2].

Focus in my Ph.D project has been on three medically important biofilms. These are *Pseudomonas aeruginosa*, *Staphylococcus epidermidis* and *Streptococcus mutans*, Table 2.2. Many advanced techniques such as AFM and electrochemical methods have been used to carry out investigations of the adhesion mechanisms of these biofilms on various substrates i.e. mica, glass, and pure and SAM-modified Au (111) surfaces. The present studies have included particularly approaches to *S. mutans* bacterial cell surface charge.

Table 2.2 Summary of some properties of the three bacteria.

Bacteria name	Gram test	Shape	Source in nature	Related disease
Streptococcus mutans	positive	spherical	Human oral cavity	dental caries
Staphylococcus epidermidis	positive	spherical	Human skin and medical devices	Infection on indwelling medical devices
Pseudomonas aeruginosa	negative	Rod-shaped	in soil, vegetation and water, and is capable of causing disease in many eukaryotic organism e.g. plants, insects, and humans	Cystic fibrosis pneumonia

Other methods reported and selected to study the adhesion of bacterial biofilms have included Quarts crystal microbalance (QCM), Surface Plasmon resonance (SPR), microcantilever /micromanipulation, AFM, and Optical tweezers (OP) [8,9]. We consider briefly some specific properties of the three bacterial species.

2.2 Streptococcus mutans.

Streptococcus mutans is a spherical Gram-positive bacterium, (Fig 2.3), belonging to the genus of streptococcus. *S. mutans* is classified as an alpha-hemolytic group. Alpha hemolysis is caused by bacterial oxidation of iron in hemoglobin, giving a greenish color on blood agar. *S.mutans* is an anaerobic bacterium commonly found in the human oral cavity and is a significant contributor to tooth decay. *S. mutans* is one of the early

colonizers on tooth surfaces to form plaque and finally dental caries. These species tolerate really extreme conditions, such as low pH, anaerobic conditions etc, and changes in local environmental conditions (e.g. pH, coaggregation, substrate availability), which assist other species to colonize and form dental plaques[10]. *S. mutans* can utilize sucrose to produce a sticky, extracellular, dextran-based polysaccharide which allows them to cohere and form plaques. *S. mutans* can also digest other sugars e.g. glucose, fructose, lactose and produce lactic acid as the final product.

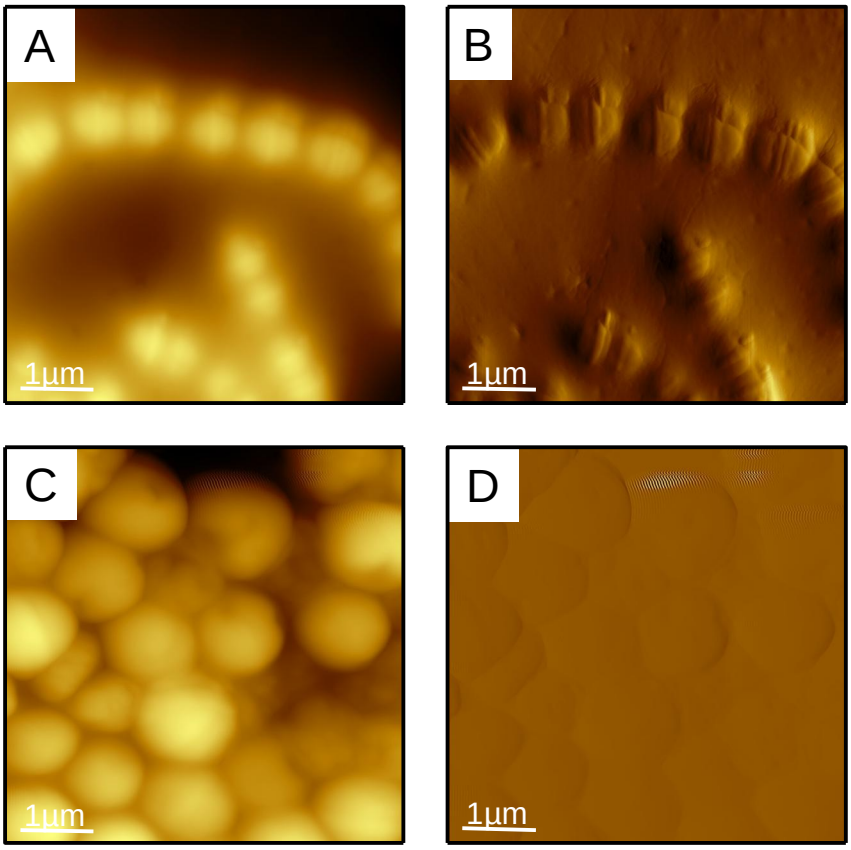

Fig 2.3 AFM images of *S. mutans* ATCC 25175 grown in BHI medium on Au (111)-surface in air. A and B: biofilms at initial stage attached on the surface for 6 hours. The colony is dividing in only in one direction. C and D Biofilms with many layers attached on Au for 24 hours. The cells are round and different from the cell shape of A and B. A and C topography; B and D deflection. Contact mode. 5×5 µm^2. From the present study.

In its growth pattern, *S. mutans* exhibits an initial sucrose independent attachment phase, cell-cell aggregation, biofilm stabilization stimulated by sucrose, and the ultimate biofilm

matrix of the mature biofilm. As the most cariogenic pathogen, *S. mutans* is highly acidogenic, producing short-chain carboxylic acids which dissolve even hard materials such as dental enamel and dentine[11]. *S. mutans* also ferments sucrose to produce glucans, i.e. insoluble extracellular polysaccharides (EPS) via three glucosyltransferase systems[12], which enhances bacterial adhesion to the tooth surface[13,14].

2.3 Staphylococcus epidermidis

Staphylococcus epidermidis is a spherical Gram-positive bacterium, Fig 2.4, belonging to the coagulase-negative Staphylococci (CONS, short name of coagulase-negative Staphylococci), which are different from coagulase-positive staphylococci, such as *S. aureus*, by their lack of the enzyme coagulase. Staphylococci are common bacterial colonizers of the skin and mucous membranes of humans and other mammals. *S. epidermidis* is the most frequently isolated bacterium from human epithelia, and predominantly colonizes the axillae (armpits), and nares (nostrils)[15,16]. *S. epidermidis* represents the most common main source of infections on indwelling medical devices. This is probably because *S. epidermidis* is a permanent and ubiquitous colonizer of human skin, resulting in high probability of device contamination during insertion, such as central venous catheters, mechanical heart valves, vascular grafts, orthopedic devices, arteriovenous shunts, sutures, exit sites, sclera buckles and contact lenses, Table 2.1. *S. epidermidis* infections rarely cause life-threatening diseases, but their frequent appearance and extremely difficult treatment are a big burden for hospitals. *S. epidermidis* is able to form biofilms on plastic devices as a major virulence factor, because its surface proteins bind blood and extracellular matrix proteins. The organism's capsule, know as polysaccharide intercellular adhesion (PIA) is made up of sulfonated polysaccharide. *S. epidermidis* infection treatments are complicated by its resistance to antibiotics and mechanisms of host defence[15].

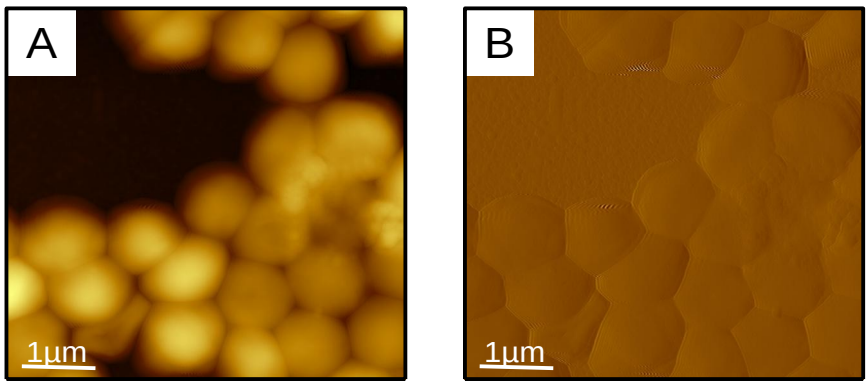

Fig 2.4 AFM images of *S. epidermidis* RP62A in TSB medium on mica surface for 6h in air. A topography; B deflection. Contact mode. 5×5 µm^2. From the present study.

2.4 Pseudomonas aeruginosa

P. aeruginosa is a Gram-negative rod shaped bacteria (Fig 2.5) belonging to the genus *Pseudonmonas*, which consists of several species of environmental bacteria. *P. aeruginosa* has a single polar flagellum and is non-sporulating and requires aerobic growth conditions. The bacterium is able to sustain nitrite/nitrate metabolism at low oxygen levels. *P. aeruginosa* can grow at a temperature as high as 42 ºC but optimally at 37 ºC, which is a feature enabling it to become one of the animal pathogens in the *Pseudomonas* genus. *P. aeruginosas* is ubiquitous in soil, vegetation and water, and is capable of causing disease in many eukaryotic organism e.g. plants, insects, and humans[17,18]. Flagella and type-IV pili were shown to play important roles in the early events in biofilm development by *P. aeruginosa*. *P. aeruginosas* rarely infects healthy tissue, but has emerged as a major opportunistic human pathogen accounting for a large number of hospital-acquired infections especially in intensive care units, Table 2.1. Acquired immune deficiency syndrome or acquired immunodeficiency syndrome (AIDS) and cancer patients undergoing chemotherapy often suffer further immune problems from *P. aearginosa*. It is the predominant cause of chronic lung infections in Cystic Fibrosis (CF) patients, which is the main cause of mortality of these patients[1]. *P. aeruginosa* has been ranked in the top three pathogens in human beings due to its wide existence in the

environment and extreme difficulties in medical treatment. It is therefore important to understand its pathogenicity and mechanisms of antimicrobial therapies.

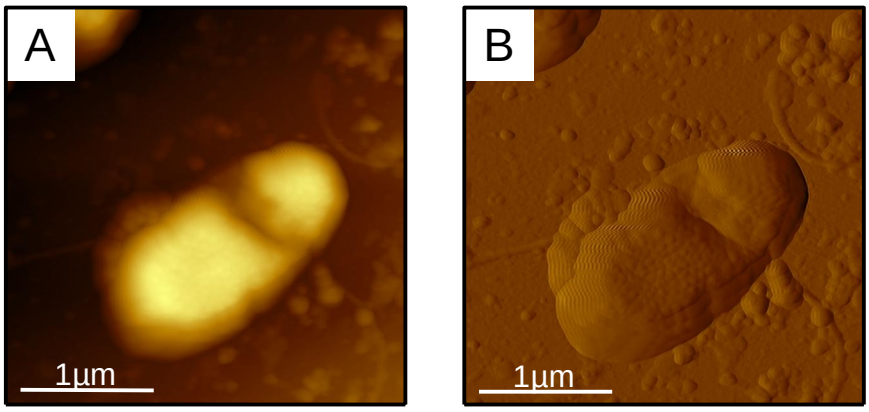

Fig 2.5 AFM images of *P.aeruginosa* PA01 in LB medium on mica surface for 6h in air. A topography; B deflection. Contact mode. $3 \times 3\mu m^2$. From the present study.

Reference

1. Costerton, J.W.; Stewart, P.S. and Greenberg, E.P. Bacterial biofilms: a common cause of persistent infections. *Science*, **1999**, 284: 1318–1322.
2. Rodriguez-Martinez, J.M. and Pascual, A. Antimicrobial resistance in bacterial biofilms. *Reviews in Medical Microbiology*, **2006**, 17: 65-75.
3. Flemming, H. C.; Neu, T. R. and Wozniak, D. J. The EPS matrix: the "house of biofilm cells". *Journal of Bacteriology*, **2007**, 189: 7945-7947.
4. O'Tool, G. Kaplan H.B. and Kolter, R. Biofilm formation as microbial development. *Annuual Review Microbiology*, **2000**, 54: 49-79.
5. Stoodley, P.; Sauer, K.; Davies, D. G. and Costerton, J. W. Biofilms as complex differentiated communities. *Annual Review of Microbiology*, **2002**, 56: 187-209.
6. Jefferson, K. K. What drives bacteria to produce a biofilm? *FEMS Microbiology Letters*, **2004**, 236: 163-173.
7. Stewart, P. S. Mechanisms of antibiotic resistance in bacterial biofilms. *International Journal of Medical Microbiology*, **2002**, 292: 107-113.

8. Otto, K. Biophysical approaches to study the dynamic process of bacterial adhesion. *Research in Microbiology*, **2008**, 159: 415-422.
9. Hall-Stoodley, L; Costerton, J.M. and Strodley, P. Bacterial biofilms: from the natural environmental to infectious diseases. *Nature Review Microbiology*, **2004**, 2: 95-108.
10. Vinogradov, A.M.; Winston, M.; Rupp, C.J. and Stoodley, P. Rheology of biofilms formed from the dental plaque pathogen *Streptococcus mutans*. *Biofilms,* **2004**, 1: 49–56.
11. Islam, B. ;Khan, S. N. and Khan, A. U. Dental caries: from infection to prevention. *Medical Science Monitor*, **2007**, 13: 196-203.
12. Cross, S. E. ; Kreth, J. ; Zhu, L. ; Sullivan, R.; Shi, W. ; Qi, F. and Gimzewski, J. K. Nanomechanical properties of glucans and associated cell-surface adhesion of *Streptococcus mutans* probed by atomic force microscopy under in situ conditions. *Microbiology*, **2007**, 153: 3124-3132.
13. Kuramitsu, H. K. *Streptococcus mutans*: molecular genetic analysis. In Gram-Positive Pathogens, Fischetti, V. A.; Novick, R. P. ; Ferretti, J. J.; Portnoy, D. A.; Rood, J. I. Eds. 2000, Washington, DC: *American Society for Microbiology*, pp. 280-286.
14. Busscher, H. J. ; Van De Belt-Gritter, B. ; Dijkstra, R. J. B. ; Norde, W. and Van der Mei, H. C. *Streptococcus mutans* and *Streptococcus intermedius* adhesion to fibronectin films are oppositely influenced by ionic strength. *Langmuir,* **2008**, 24: 10968-10973.
15. Otto, M. *Staphylococcus epidermidis*- the accidental pathogen. *Nature Review Microbiology*, **2009**, 7: 555 -567.
16. Otto, M. *Staphylococcal* Biofilms. *Current Topics in Microbiology and Immunology,* **2008**, 322: 207-228.
17. D'Argenio, D.A.; Gallagher, L.A.; Berg, C.A. and Manoil, C. *Drosophila* as a model host for *Pseudomonas aeruginosa* infection. *Journal of Bacteriology*, **200**1, 183: 1466-1471.

18. Plotnikova, J.M.; Rahme, L.G. and Ausubel, F.M. Pathogenesis of the human opportunistic pathogen *Pseudomonas aeruginosa* pa14 in arabidopsis. *Plant Physiology*, **2000**, 124: 1766-1744.

Chapter 3 Atomic force microscopy (AFM)

3.1 AFM

AFM belongs to the family of scanning probe microscopies (SPM) and was invented by Binnig, Quate and Gerber in 1986[1,2]. SPM was introduced in the early 1980s and has brought a revolution of microscopy. All the SPM instruments scan a surface, giving the morphology depending on the interaction between the surface and the probe. AFM became commercially available in 1989, and offers a new approach for biological applications using SPM[3,4]. Examples of the use of the different microscopies are shown in Fig 3.1. Table 3.1 shows a comparison of different microscopies.

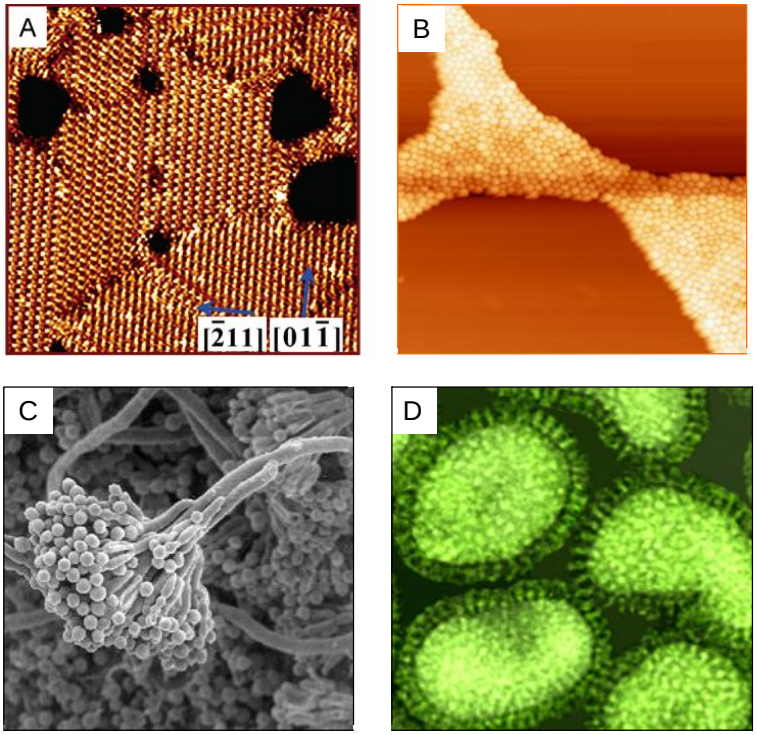

Fig 3.1 Images of four different microscopies. A: STM image of 1-propanethiol SAM on Au (111) in NH_4Ac buffer.[5]. B: AFM image of *S.mutans* in BHI medium on mica[6]. C: SEM image of *Penicillium chrysogenum* spores[7]; D: TEM image of Flu virus[7].

Compared with other microscopies, AFM has become a powerful tool in biological science and has been applied in many bio-related areas: biomolecules, such as DNA,

protein, and bacteria and other whole biological cells. In order to have a better understanding, the principle of AFM, cantilever, interaction forces between tip and sample, image modes, force curve, preparations of tip and sample, and AFM application in bacteriology are briefly described in the following.

Table 3.1 Comparison of different microscopies, adapted from 2,8,9.

Full name	Abbreviation	Advantage	Disadvantage
Optical microcopy	OM	Fast and easy preparation, μm	Cannot measure step heights and detailed information of the surface.
Scanning tunneling microscopy	STM	In principle in some cases, atomic resolution, Å	Can only be used for conductive or semi-conductive samples.
Scanning electron microscopy	SEM	High resolution of bulk specimens (no need to make the sample thin), atomic resolution; 3D appearance of the specimen image as a result of the large depth of field (depth of focus); capable of very high magnifications complementing the information available from optical images	Needs conductive coating, atomic resolution in ultra-high vacuum (UHV)
Transmission electron microscopy	TEM	High resolution of bulk specimens, 3D appearance of the specimen image, technique that provides crystallographic /structural information (lattice arrangement, orientation relationships, dislocations, 0.8 Å resolution.	Need conductive coating, expensive sample preparation
Atomic force microscopy	AFM	Can be operated in air, vacuum, and in liquids, for most solid samples adsorbed on a solid surface. Biological measurements, in particular, are often carried out *in vitro* in biological fluids. Extraordinary topographic contrast, direct height and force measurement, 3D surface features.	Low scanning speed, limited resolution

3.2 Principles of AFM

The AFM instrument consists mainly of a cantilever, a piezo scanner, a mirror, a photo-detector, a laser diode, and a feedback controller (Fig. 3.2). The laser beam is reflected from the back of the cantilever into the mirror and hit the photo-detector. The interactions between the tip and the sample cause deflection of the cantilever and change the position

of the laser on the photo-detector. Surface information is collected by the feedback controller and forms an image on a computer screen.

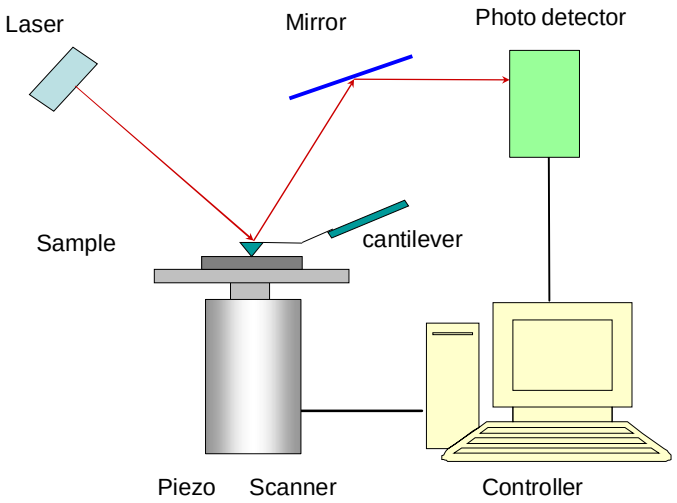

Fig 3.2 Schematic illustration of AFM., adapted from [10].

3.3 Cantilever and tip

The performance of the AFM instrument and the resolution of the images depend on the choice of cantilever and the geometry of the tip as well as the sample surface.

The cantilever is a long, flexible piece of metal or ceramic with a spring constant (k_C). For a rectangular cantilever and for normal bending, k_C is given by[11]

$$k_C = \frac{Ewt^3}{4l^4} \tag{3.1}$$

where w is the width, l the length, and t the thickness of the cantilever, and E is Young's modulus of the material. It is important to consider the value of the spring constant when we choose a cantilever for a given experiment. For soft biological samples, such as bacteria in liquid, a low spring constant means a flexible cantilever, and less deformation and damage of the sample.

Many commercially available AFM tips are pyramid shaped with a relatively low geometric aspect ratio. The aspect ratio is the height of the tip (H) to the width of the tip (W)[9]. However, a number of sharpened tips with a higher aspect ratio are also available and often costly. Fig 3.3 shows SEM pictures of these cantilevers applied in this thesis.

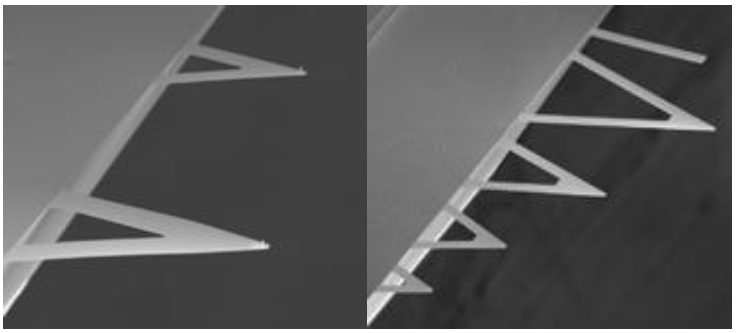

Fig 3.3 SEM pictures of AFM cantilevers made by Veeco. (detailed information in Appendix B). Left: Veeco NP-S; Right : Veeco MLCT.[12]

AFM tips are generally made of Si or Si_3N_4. Other materials have been used to construct the tip, such as carbon nanotubes for special applications. An ideal tip should have well-defined shape and sharp apex. In fact, the tip is often blunt after it has been used for longer times. All AFM images contain basically a convolution of the tip and the surface topography of the samples, Fig 3.4.

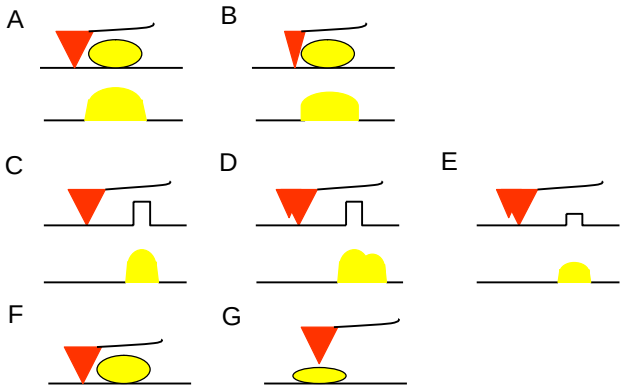

Fig 3.4 Schematic illustration of scans with different aspect ratios. A: low aspect ratio probe; B. a high aspect ratio probe; C. D and E: Tip geometry dependent artifacts; C: single tip ; D: double-tip on a high object; E: double tip on a low object; F and G: force induced artifacts; the tip presses the soft material such

as cells or bacteria, and makes the shape change. A, B, C, D and E: The top part of the figure shows the AFM tip scanning an immobilized bacterium or hard material. The bottom part of each figure, correspond to the profile, adapted from Eaton P. and West P. [8]

3.4 Interaction forces between tip and sample

When the tip is brought into proximity of a sample surface, forces between the tip and the sample lead to a deflection of the cantilever according to Hooke's law. Depending on the situation, forces measured by AFM include mechanical contact forces, Van der Waals forces, capillary forces, chemical bonding, electrostatic forces, and hydration forces.

3.4.1 Van der Waals force

Van der Waals force (vdW) is the sum of the attractive or repulsive forces between molecules (or between parts of the same molecule) other than those due to covalent-bonds or to the electrostatic interaction of ions with one another or with neutral molecules. They include dipole-dipole forces between non-permanent dipoles (dispersion forces), forces between a permanent dipole and a corresponding induced dipole (Debye force), and forces between two instantaneously induced dipoles (London dispersion force).

It is well known that the vdW potential between two atoms has a distance dependence of ~z^{-6}. In the case of AFM measurements, however, there are several hundred atoms at the tip and sample, and the resultant force should be calculated from a vector sum of vdW forces between them. The vdW interaction between macroscopic samples was calculated by Hamaker. This approach is applicable for a sample and tip of ~10 nm scale. For a spherical tip with radius R and a flat sample, the vdW potential V_{vdW} and force F_{vdW} are given by [11].

$$V_{vdW} = -\frac{A_H R}{6z} \tag{3.2}$$

$$F_{vdW} = -\frac{A_H R}{6z^2} \tag{3.3}$$

where z is the closest distance between the tip and the sample and A_H the Hamaker constant. The Hamaker constant is determined by the physical properties of materials such as atomic polarizability and the density of the tip and the sample.

Typically, A_H is in the order of 1 eV for solids. Depending on the shape of the tip and the sample, vdW can have different power laws. In order to reduce the vdW interaction, we can perform the AFM measurement by immersing the tip and sample in water[13]. The van der Waals forces are exerted by the water molecules instead of the force directly between the tip and sample.

3.4.2 Capillary forces

These are essentially also vdW forces. They are very important for dry samples, since a point contact with a small radius of curvature, such as the tip resting on a surface, acts as an ideal nucleation site for the condensation of water vapor present in air. This liquid meniscus attracts the tip and glues it to the sample surface because of capillary forces. The influence of capillary forces can be reduced by controlling the humidity of the atmosphere around the sample by an environmental chamber. By immersing the sample in liquid, i.e. performing the scan in an aqueous environment, capillary interaction can be avoided.

3.4.3 Chemical forces

When two or more atoms come together to form a molecule, the force that tightly binds the atoms is called a chemical force. When the AFM tip is close to the sample, surface-attraction leading to covalent bonding between a single pair of atoms can occur. One atom is the outermost atom on the tip, and the others are from the sample surface.
The chemical boding energy is described by the Morse potential V_{Morse}.[11]

$$V_{Morse} = -E_{bond}\left(2e^{-k(z-\sigma)} - e^{-2k(z-\sigma)}\right) \qquad (3.4)$$

Where E_{bond} is bonding energy, σ equilibrium distance and $1/k$ a 'decay' length. The Morse potential is an approximation of the covalent boding interaction.

3.4.4 Electrostatic forces

The force exerted by stationary objects bearing electric charge on other stationary objects bearing electric charge. If the charges are of the same sign, the force is repulsive; if they are of opposite signs, the force is attractive. The strength of the force is described by Coulomb's law.

The Coulomb force (F) acting between the point charges (q_1) and (q_2) is given by

$$F = k_e \frac{q_1 q_2}{r^2} \tag{3.5}$$

Where r is the separation distance and k_e is a proportionality constant, k_e also called Coulomb constant. A positive force implies that it is repulsive, while a negative force implies that it is attractive. This long range force is nearly always present but not always immediately notable due to dominating short-range repulsive forces.

In an electrolyte solution both the solvent and counter-ions close to the charges, screen Coulomb field strongly. Over a large distance the decay is exponential with distance. Coulomb interactions between the charged surface and particles are significant at short distances. The electrostatic force is more important for sample-to-substrate interaction than for tip-sample interaction, since silicon or silicon nitride is unlikely to bind electrostatically to the biological sample.

3.4.5 Hydration forces

Hydration forces are due to hydrophobic-hydrophilic interactions in fluids. Repulsive hydration forces arise when water molecules bind to a surface containing hydrophilic groups and thereby hydrate the hydrophilic surface groups[11,14].

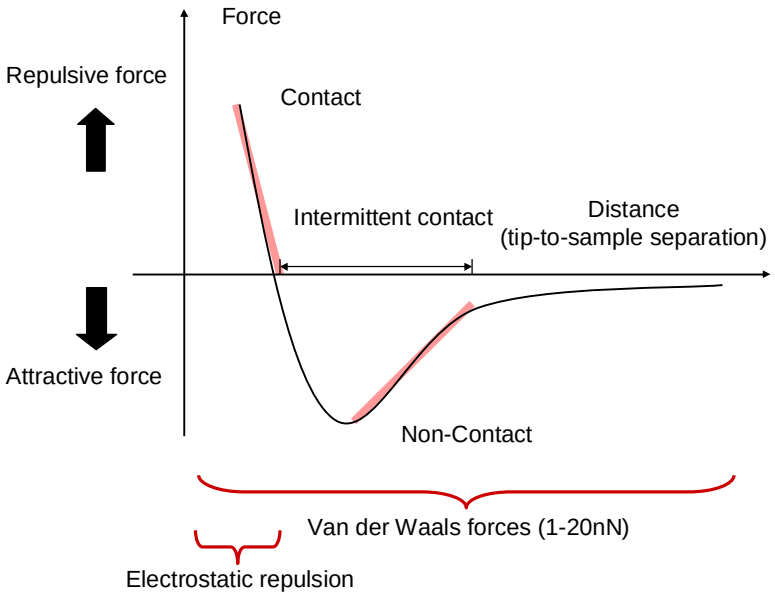

Fig 3.5 Contact mode AFM exploits the repulsive forces at close distance. Non-contact mode AFM is operated in the regime of attractive force, adapted from User's guide, Agilent technologies[10].

In AFM, the force between the samples and the tip is used to sense the proximity of the tip to the sample. There are both long and short-range contributions to the tip sample force. The forces are repulsive at close range and attractive at long-range[10], Fig 3.5. Overall, choosing a suitable mode and force is essential to avoid artifact imaging.

3.5 Image modes

AFM can be operated in several different modes. In general the image modes are divided into the static mode and the dynamic mode. Static AFM modes include contact mode and friction force microscopy (FFM, or lateral force microscopy, LEM). Dynamic AFM modes include 1. tapping mode, Non-contact mode; 2 force modulation mode (FMM), atomic force acoustic microscopy (AFAM) mode; 3. torsional resonance (TR) mode; 4. Lateral excitation (LE) mode[15]. In my thesis, I will focus on contact mode, tapping mode and non-contact mode. The relationship between tip and sample surface of these three modes are summarized in Fig 3.6.

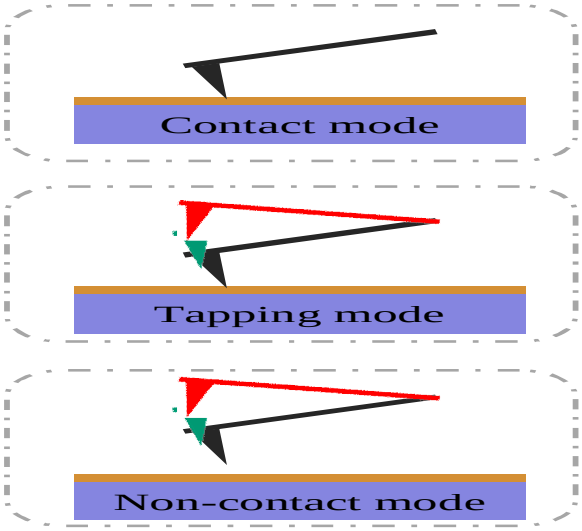

Fig 3.6 the relationship between tip and sample surface by contact mode, tapping mode and Non-contact mode.

3.5.1 Contact mode

The contact mode can be run in two different modes which are the constant height or the constant force. In my study, I used the constant force mode. The laser beam measures the deflection of the cantilever, and imaging is collected on the basis of feedback to a piezoelectric scanner that keeps the force constant. Low spring constant AFM probes are used for contact mode imaging. The force applied between the tip and a surface in contact is given by Hooke's law.

$$F = -k_c d \tag{3.6}$$

Where F is the force, k_c is the force constant of the cantilever and d the deflection distance. Forces between the tip and samples can be studied by using different tip materials and surfaces. The hardness / elasticity of the surface can be analyzed by varying the force at each point, which is commonly measured for biological samples in air or in liquid. Contact mode is used for high resolution imaging. However, this mode has some limitations: 1.Tip contamination caused by attachment of particles on a surface; 2 it is easy to damage the surface when a strong force is applied to scanning of soft samples.

3.5.2 Tapping mode

Tapping mode is dynamic and intermittent contact imaging in which the tip senses the surface with only minimal contact to the surface at a given amplitude. The tip oscillates with an amplitude of several nm. The typical frequency of the tip is 50-400 kHz.

A resonant oscillation frequency is given by the equation:

$$\omega = \sqrt{\frac{k_{eff}}{m}} \tag{3.7}$$

Where k_{eff} is the effective force constant and m the effective cantilever mass.

3.5.3 Non-contact mode

Similar to the tapping mode, the non-contact mode brings the cantilever into oscillation slightly higher than the resonance frequency but the tip does not actually touch the sample surface, remaining 5-10 nm from the surface. The tip oscillates with the amplitude of several nm. The typical frequency of the tip is 50-400 kHz. This operation mode is suitable for ‘soft’ materials like bacteria and proteins.

3.5.4 Comparisons of three modes

In my thesis, I also used the DMI instrument. The detailed information regarding this instrument is govem in Appendix A.

Table 3.2 comparison of these three common modes, adapted from [15].

Operation mode	Contact Mode	Non-contact Mode	Tapping Mode
tip loading force	low → high	Low	Low
contact with sample surface	Yes	No	Periodical
manipulation of sample	Yes	No	Yes
contamination of AFM tip	Yes	No	Yes
In site	Good	Not good	Fine
Advantages	High scan speeds. "Atomic resolution" is possible. Easier scanning of rough samples with extreme changes in vertical topography.	Low force is exerted on the sample surface and no damage is caused to soft samples	Higher lateral resolution (1 nm to 5 nm). Lower forces and less damage to soft samples in air. Almost no lateral forces.
Disadvantages	Lateral forces can distort the image.Capillary forces from a fluid layer can cause large forces normal to the tip-sample interaction. Combination of these forces reduces spatial resolution and can cause damage to soft samples.	Lower lateral resolution, limited by tip-sample separation. Slower scan speed to avoid contact with fluid layer. Usually only applicable to extremely hydrophobic samples with a minimal fluid layer.	Slower scan speed than in contact mode.

3.5.5 Image signals

Topography image (Height image) is the image information of the vertical movement of the piezoelectric tube and is the main signal to the entire image modes. It can be used in contact mode, tapping mode and non-contact mode.

Deflection image (error signal) is the signal from the feedback loops compared to the set-point values and used in contact mode.

Friction force (lateral force image) is the horizontal movement of the laser spot measured in the photodiode and used in contact mode.

Phase signal (phase lag) is the phase shift between excitation and oscillation of the cantilever and used in tapping mode and non-contact mode.

3.5.6 AFM scanner calibration

When we start to use AFM, it is important to first to calibrate the AFM. AFM scanner includes several piezoelectric elements for moving the probe along the X, Y and Z axes. The scanner can manipulate samples and probes with extreme precision in three dimensions. Sensitivity of the scanner does not have a linear relationship with respect to scan size. Piezo scanners exhibit more sensitivity (i.e., more movement per volt) at the end of a scan line than at the beginning. The relationship between movement and applied voltage is nonlinear. The reason is that the forward and reverse scan directions behave differently and display hysteresis between the two scan directions. Nonlinearity and hysteresis can cause feature distortion in AFM images if not properly corrected.

Fig 3.7 shows a typical way to calibrate the scanner in X, Y and Z axes. The scanning data X =10.1 µm is bigger than the actual data 10 µm, and Y = 9.3 µm is smaller than the actual data 10 µm, Z = 295 nm is also bigger than 200 nm. According to these data, we could follow the Calibration Manual from Agilent Technologies and do the calculations[10].

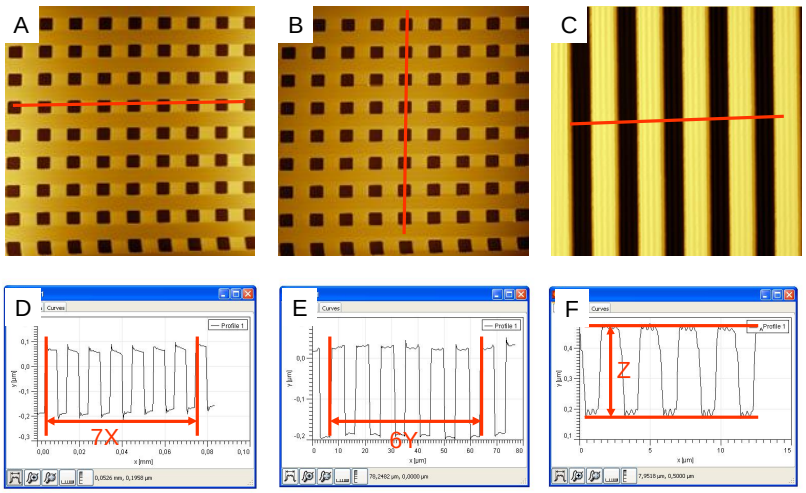

Fig 3.7 AFM calibration. AFM calibration grid from Aurora NanoDevices inc. The standard parameter for A,B: 10 µm pitch pits and 200 nm deep; C: 2 µm pitch line and 200 nm deep; A: trace images (from left to right) 90×90 μm^2 and B: retrace images (from right to left) 90×90 μm^2; C topography images 15×15 μm^2 . D, E, F display the cross section of the red line of A, B, C separately. Actual data of D: 7X = 70.5 µm; E: 6Y=56.9 µm; F: Z= 295 nm. From this work.

3.6 Force distance curves

A typical force curve is illustrated in Fig.3.8. Force curves offer a wealth of information on the mechanical properties, surface forces, adhesion energies and viscoelasticity resulting from the interactions between the tip and the sample surface. When the tip is approached towards the surface, a negative deformation of the cantilever i.e. cantilever bending downwards is formed due to attractive Van der Waals interactions (B). Once the tip contacts the sample, a deformation of the cantilever is observed (C), providing direct information on the mechanical properties of the sample. When the tip is withdrawn from the sample (D), the curve shows hysteresis referred to as the adhesion 'pull-off' force, (E). Force curves can be recorded either at a single, well-defined location in the (x, y) plane or at multiple locations to yield a so-called 'force–volume image' (for more details see Heinz and Hoh[16]). Spatially resolved maps of sample properties and molecular interaction forces can be produced.

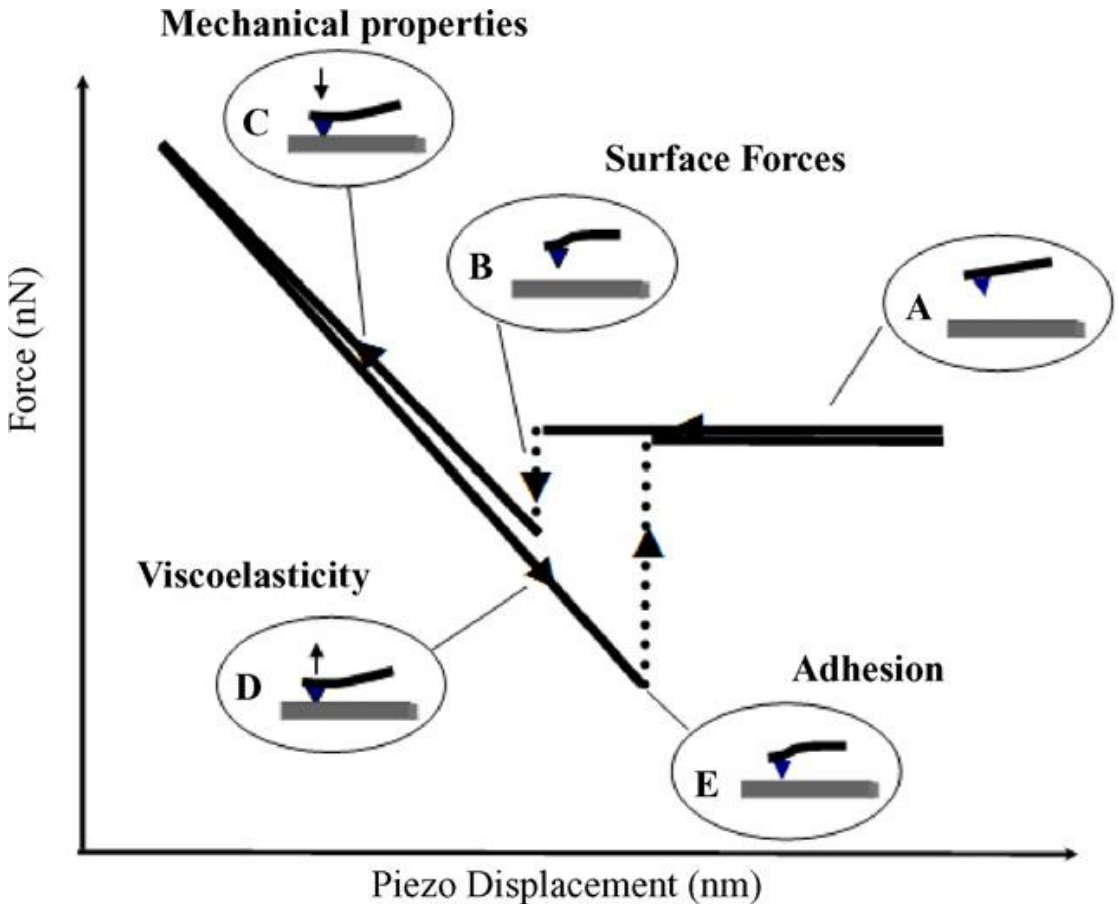

Fig 3.8 Schematic diagram of a typical force curve for a non-deformable surface with attractive forces between the AFM tip and the sample. A. tip approaching the surface; B tip attracted to the surface; C. Tip driven into the surface (region where compliance information can be extracted); D. Tip withdrawn from a sample. E. adhesion. The figure is reprinted from the review of Gaboriaud and Dufrene[3].

3.7 Preparation of sample and tip

3.7.1 Immobilization of cells

AFM requires the sample attached on a solid substrate. The solid substrates can be glass slides, mica, metal surfaces, etc. Glass is made of SiO_2 and is not atomically flat, whereas mica can provide atomically flat surfaces ideal as a supporting substrate for AFM studies. Biosamples can be immobilized on a solid surface by physical adsorption or chemical adsorption. For physical adsorption, a drop of sample solution is put on a surface and dries in air. For chemical adsorption, a functional chemical is used to immobilize the target sample on a surface through formation of chemical bonds. L-lysine, fibonectin, glutin are example of linkers for chemical adsorption or electrostatic adsorption. Along this line, a surface modified by a chemical can change its original physical or chemical properties and increase the adhesion of cells. Denaturation of biological samples is an essential problem for any immobilization method. Many efforts have been put into seeking an approach with high AFM resolution and little denaturation. Mechanic fixation of individual cells in a polymer membrane is among the most successful developments[3].

Some approaches with modified surfaces, like self-assembling monolayers (SAMs) on Au (111) or the changes of molecular charges on a surface, offer a promise to improve the bacterial adhesion[6]. Some attachment on the solid surface uses extracellular polymeric substrates, or agar gel or a porous membrane to immobilize the cells mechanically[3]. In the latter, the spherical cells are trapped in a polycarbonate membrane with similar size of pore for high-resolution images without cell detachment or cell damage[3]. This approach has two advantages: 1. it is simple and it does not involve drying, coating or chemical fixation. 2. it can be used for AFM oberservations in situ, which is close to the natural environment during bacterial growth. In general, mechanical

trapping of the bacterial cell is the most reliable method for immobilization[3]. The limitation is that it only works for spherical cells (e.g. some bacteria: *Streptococcus mutans*, *Staphylococcus aureus* and *Staphylococcus epidermidis*, functional spores, yeasts), but not for rod-shaped cells (*Escherichia coli* and *Pseudomonas aeruginosa*). In addition, it works for single cells but is hard to use for biofilms.

3.7.2 Chemically modified tips

Chemically modified tips is a prerequisite for reliable, quantitative surface force measurement. The surfaces of commercial tips have defined surfaces, such as silicon nitride (Si_3N_4), or gold coated films, which are easily contaminated. Functional tips with SAMs of alkanethiols give high-resolution images due to their chemical sensitivity. The procedure is described in the experimental section. These thiols with different terminal functional groups: -OH, -CH_3, -COOH, -NH_2, can be used to detect the physical and chemical properties (hydrophobicity, charge) of biological surfaces.

3.7.3 Biologically modified tips

Some biomolecules are used to modify tips with the purpose of measuring intermolecular forces between individual ligand-receptor contacts, the adhesion of the biofilms or the protein location on single cell surfaces. The binding of the biomolecules to the tips should here be much stronger than the intermolecules force, see Fig 3.9.

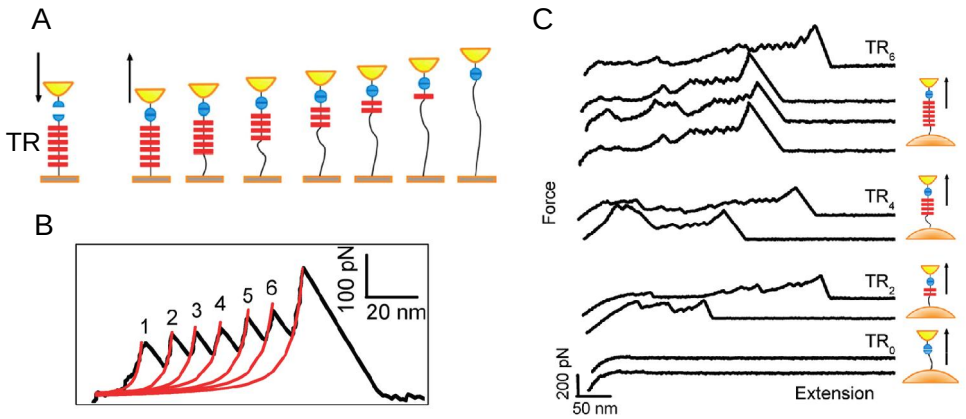

Fig 3.9 Unfolding Als5p proteins on live cells by AFM. Als proteins possess four functional regions that is, an N-terminal immunoglobulin (Ig)-like region, which initiates cell adhesion, followed by a threonine-rich region (T), a tandem repeat (TR) region that participates in cell-cell aggregation, and a stalk region projecting the molecule away from the cell surface. A: The schematic of experiment, showing the 6 fold protein unfolding. Representation of an Als molecule projecting outward from the *C. albicans* cell wall by the stalk region. The tandem repeat (TR) region comprises multiple glycosylated 36 amino acid repeats that are arranged in antiparallel-sheets.. B: Force-extension curves obtained by stretching single Ig-T-TR_6 showing periodic features reflecting the sequential unfolding of the TR domains (black line: experiments). Force peaks were well-described by the worm-like-chain model (inset, red line: simulation), C: Force-extension curves recorded between an Ig-T-tip and the surface of *S. cerevisiae* cells expressing Als5p with six, four, two, and no TR repeats. The figure is reprinted from Alsteens et al.[17].

3.7.4 Cell modified probes

A method has been developed to attach cells directly onto an AFM cantilever. This approach can probe cell–solid and cell–cell interactions. The method preserves the native ultrastructure of the cells during measuring. Firstly, cells were immobilized by using glutaraldehyde treatment to create covalent cross-linking between the bacterial layer and the polyethylene glycol (PEI)-coated tip[18-20] or by attaching single yeast cell with a small amount of glue (Loctite Glass Bond-LoctiteLtd.)[21,22]. Lower and co-workers brought bacteria to adsorb physically onto poly-l-lysine-coated glass beads and subsequently attached a cell-coated bead to a cantilever by using a small amount of epoxy resin[23,24]. Another elegant approach is to attach individual cells to an AFM cantilever via lectins such as wheatgerm agglutinin[25]. However, these treatments most likely affect the structure and properties of the cell surface[26].

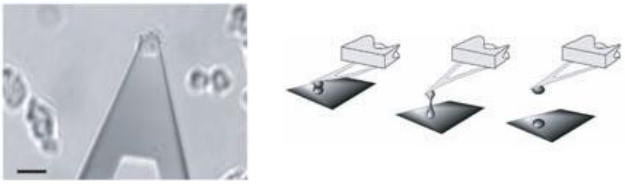

Fig 3.10 Attachment of living cells. Light-microscopy image of *Dictyostelium discoideum* cell mounted on an AFM cantilever (left). By applying a repulsive contact force between the cantilever-mounted cell and a target cell at the bottom of a special Petri dish, and then retracting the cantilever from the target cell (right), specific cell-cell adhesion forces can be measured. Scale bar, 20 μm. Reprinted from Benoit etc[27].

3.8 AFM applications in bacteriology

3.8.1 Imaging of bacterial morphology and morphology changes

Bacteria can be imaged either under dry conditions or in aqueous solution. The advantage of imaging dry samples is a better resolution than for bacteria examined in aqueous media. As a drawback, the dehydration of the sample will unavoidably affect the bacteria to a larger extent rather than just the immolbilization step for liquid state examination. The dehydration treatment may also give secondary effects e.g. antimicrobial peptide treatment that may be difficult to distinguish from the primary effects of the treatment.

AFM can be used to examine single bacterial morphology[28] or bacterial communities such as biofilms[6,29-34]. Biofilm formation plays an important role in clinical microbiology, and the biofilm leads to increased tolerance to antibiotics and antimicrobial peptides, and more persistent infections. The effect of biofilm matrix components curli, cellulose and the cell surface protein BapA, in *S. typhimurium* biofilm and colony morphology[32] has been reported. These investigations suggest that curli and cellulose, rather than BapA, have an impact on the formation and morphology of a biofilm, where the curli seem to be more important for the formation of cell aggregates than cellulose[32]. Another study of *Streptococcus mutans* biofilm shows that increased strain carcinogenicity is inversely proportional to the cell surface roughness, and the correlation between genetically modified *S. mutants* and morphology[33]. The death and survival of *E. coli* biofilm after exposure to the predator *Bdellovibrio bacteriovorus*, a Gram-negative bacteria preying on other Gram-negative bacteria, have also been studied[34]. AFM visualized that the nutrition level of the culture media played a role for the *E. coli* survival. In dilute media, *Bdellovibrio* kills the entire biofilm, whereas in rich media some *E. coli* survive[34]. In the present thesis, the biofilm formation of *S. mutants* on the mica, Au(111) and modified Au (111)[6,29], the different strain biofilm morphology of *Pseudomonas aeruginosa*[30], and organic compounds inhibiting *S. epidermidis* adhesion and biofilm formation have been studied[31].

3.8.2 Functionalized AFM tips for studying intact bacteria

A unique potential of the AFM is the possibility to measure forces at the single-molecule level. The AFM tip approaches the surface, interaction forces deflect to the cantilever when the tip is retracted from the surface. This technique can measure molecular scale forces as small as a single hydrogen bond or as weak as Van der Waals interaction. This extreme sensitivity of the cantilever can be exploited to measure forces both within and between biomolecules. A schematic view of AFM tip functionalization and precautions of single molecule recognition is shown in Fig 3.11.

Fig 3.11 shows three techniques for functionalizing the AFM tip from the review of single molecular recognition using AFM by Hinterdorfer and Dufrene[35]. Functionalization of AFM tips is a challenging process and several important factors must be considered: 1. the force for immobilization of the molecules to the tip must be stronger than the interactions between the tip and the sample. 2. The attached molecule must be flexible enough to interact with complementary molecules. 3. Binding must be selective. 4. Well controlled orientation, like site-directed coupling is favorable to make the interacting molecules face the same way.

A force-distance curve can be recorded when the tip approaches the surface until it touches the surface, followed by retraction. If a biomolecule is attached to both the tip and the surface, the distance traveled to retract the tip and the forces required to extend the biomolecule can be determined. Fig 3.11 D shows a typical force-distance curve obtained upon retraction. To obtain the force-distance curve, the loading rate and interaction time are two important parameters that depend on unbinding forces between receptors and ligands. The loading rate is the force which increases with time during pulling on the receptor-ligand complex and can be approximated by the effective spring constant of the whole system (cantilever and bound molecules) multiplied by the pulling velocity. To preserve the binding sites for both the receptor and the ligand, it is important to keep the biological sample being hydrated during the experiment[35].

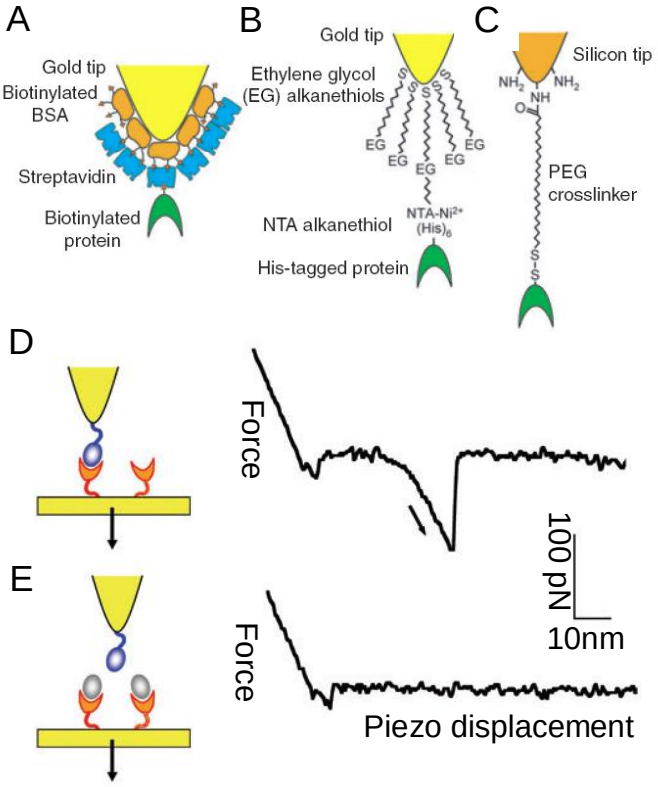

Fig 3.11 Schematic presentation of three different techniques for AFM tip chemical modification . A: Physisorption of protein, in this case biotinylated bovine serum albumin (BBSA), which afterwards has reacted with streptavidin and further modified with biotinylated proteins. B: Chemisorption of nitrilotriacetate (NTA) terminated alkanethiols on a gold tip, to which histidin containing proteins are attached. C. covalent coupling of a heterobifunctional polyethylene glycol (PEG) crosslinker on silicon oxide tip. D-E: are measurements of molecular recognition interaction forces. D: an AFM tip functionalized with oligoglucose carbohydrates (blue part) on a surface, modified with the lectin concanavalin A (orange part). Force-displacement curves shows an unbinding force of about 100 pN, attributed to the rupture of a single carbohydrate-lectin pair. The unbinding event is accompanied by a nonlinear elongation force (arrow on the right) reflecting essentially the stretching of the flexible spacer. E: Blocking experiment demonstrating that the 100 pN unbinding force is not observed when the measurements are performed in the presence of blocking agents like glucose or mannose (grey part). This figure is taken from a review of Hinterdorfer and Dufrene[35].

By chemically functionalizing the AFM tip, the hydrophobic forces on the bacterial surface can be studied i.e. by Chemical Force Microscopy (CFM). Dague et al. chemically modified a gold tip with CH_3-termined alkanethiols and mapped the surface

of *Aspergillus Fumigatus* and *M.bovis* [36]. In the present thesis, chemically modified gold tips with CH_3-termined alkanethiols were used to map the surface of *S. epidermidis*, to investigate the drug effects on *S. epidermidis*[28].

Reference

1. Binnig, G.; Quate , C.F. and Gerber C. Atomic force microscopy. *Physical Review Letters*, **1986**, 56: 930-933.
2. Binnig, G. and Rohrer, H. Scanning tunneling microscopy. *IBM Journal of Research and Development*, **1986**, 30: 355-369.
3. Gaboriaud, F. and Dufrene, Y. F. Atomic force microscopy of microbial cells: application to nanomechnical properties, surface forces and molecular recognition forces. *Colloids and surface B: Biointerfaces*, **2007**, 54: 10-19.
4. Heinz, W. F. and Hoh, J. H. Spatially resolved force spectroscopy of biological surfaces using the atomic force microscope. *Trends in Biotechnology*, **1999**, 17:143-150.
5. Zhang, J.; Chi, Q. and Ulstrup, J. Assembly dynamics and detailed structure of 1-propanethiol monolayers on Au (111) surfaces observed real time by in situ STM. *Langmuir*, **2006**, 22 (14): 6203-6013.
6. Hu, Y.; Zhang, J. and Ulstrup. J. Interfacial Electrochemical Electron Transfer Processes in Bacterial Biofilm Environments on Au(111). *Langmuir*, **2010,** 26 (11): 9094-9103.
7. www.etseq.urv.es,Topic_in_NANOBT_Lecture_15.ppt, **2011.01.11**
8. Eaton, P. and West, P. Atomic force microscopy, Oxford University Press. **2010.**
9. Braga, P.C. and Ricci, D. Atomic force microscopy in biomedical research methods and protocols. *Methods in Molecular Biology*, **2011**, 736: 1-29.
10. Agilent Technologies 5500 scanning probe microscopy, User's guide, *Agilent technologies.* **2008.**
11. Israelachivili, J. Intermolecular and surface forces-with application to Colloidal and biological systems. Academic press, London, 2nd edition, **1991.**

12. a.http://www.brukerafmprobes.com/Product.aspx?ProductID=3444
b.http://www.brukerafmprobes.com/Product.aspx?ProductID=3373
13. Seo, Y. and Jhe, W. Atomic force microscopy and spectroscopy. *Reports on Progress in Physics*, **2008**, 71: 1-23.
14. Leikin, S.; Parsegian, V.A.; Rau, D.C. and Rand, R.P. Hydration forces. *Annual Review of Physical Chemistry*, **1993**, 44:369-359.
15. Song, Y and Bhushan, B. Atomic force microscopy dynamic modes: modelling and applications. *Journal of Physics: Condensed Matter*, **2008**, 20: 1-29
16. Heinz, W.F.; and Hoh, J.H. Spatially resolved force spectroscopy of biological surfaces using the atomic force microscope. *Trends in Biotechnology*, **1999**, 17: 143.
17. Alsteens, D. ; Dupres, V.; Klotz, S .A. ; Gaur, N. K. ; Lipke, P. N. ; and Dufrene, Y. F. Unfolding individual Als5p adhesion proteins on live cells. *ACS Nano*, **2009**, 3 (7): 1677-1682.
18. Ong, Y.L.; Razatos, A.; Georgiou, G. and Sharma, M.M. Adhesion forces between *E. coli* bacteria and biomaterial surfaces. *Langmuir*, **1999**, 15: 2719-2725.
19. Razatos, A.; Ong, Y.L.; Sharma, M.M. and Georgiou, G. Molecular determinants of bacterial adhesion monitored by atomic force microscopy. *Applied Biological Sciences*, **1998**, 95 (19): 11059–11064.
20. Razatos, A.; Ong, Y.L.; Boulay, F.; Elbert, D.; Hubbell, J.A.; Sharma, M.M. and Georgiou, G. Force measurements between bacteria and poly(ethylene glycol)-coated surfaces. *Langmuir*, **2000**, 16: 9155-9158.
21. Bowen, W.R.; Hilal, N.; Lovitt, R.W. and Wright, C.J. Direct measurement of the force of adhesion of a single biological cell using an atomic force microscope. *Colloids and Surfaces A: Physicochemical and Engineering Aspects*, **1998**, 136: 231-234.
22. Bowen, W. R.; Lovitt, R. W. and Wright, C. J. Atomic force microscopy study of the adhesion of *Saccharomyces cerevisiae*. *Journal of Colloid and Interface Science*, **2001**, 237: 54-61.

23. Lower, S. K.,; Tadanier, C. J. and Hochella, M. F. Measuring interfacial and adhesion forces between bacteria and mineral surfaces with biological force microscopy. *Geochimica* et Cosmochimica *Acta* , **2000**, 64: 3133-3139.

24. Lower, S.K.; Hochella, M.F. and Beveridge, T.J. Bacterial Recognition of Mineral Surfaces: Nanoscale Interactions Between *Shewanella* and α-FeOOH. *Science*, **2001**, 292: 1360-1363.

25. Benoit, M. Cell adhesion measured by force spectroscopy on living cells. *Methods* in *Cell Biology*, **2002**, 68: 91-114.

26. Velegol, S. B. and B. E. Logan. Contributions of bacterial surface polymers, electrostatics, and cell elasticity to the shape of AFM force curves. *Langmuir*, **2002**, 18:5256-5262.

27. Benoit, M.; Gabriel, D.; Gerisch, G. and Gaub, H.E. Discrete interactions in cell adhesion measured by single-molecule force spectroscopy. *Nature Cell Biology*, **2000**, 2, 313–317.

28. Hu, Y.; Ulstrup, J.; Zhang, J.; Molin, S. and Dupres, V. Drug effect on *S. epidermidis* adhesion investigated by AFM. *Physical Chemistry Chemical Physics* **2011**,13 (21): 9995-10003.

29. Hu, Y.; Zhang, J. and Ulstrup, J. Investigation of *Streptococcus mutans* biofilm growth on modified Au (111)-surfaces using AFM and electrochemistry. *Journal of Electroanalytical Chemistry*, **2011**, 656 (1-2): 41-49.

30. Yang, L.; Hu, Y.; Liu, Y. Zhang, J.; Ulstrup, J. and Molin. S. Distinct roles of extracellular polymeric substances during *Pseudomonas aeruginosa* biofilm development**.** *Environmental Microbiology*, **2011**,13 (7): 1705-1717.

31. Qin, Z.; Zhang, J.; Hu, Y.; Chi, Q.; Mortensen, N. P.; Qu, D.; Molin, S. and Ulstrup, J.. Organic compounds inhibiting *S. epidermidis* adhesion and biofilm formation. *Ultramicroscopy*, **2009**, 109: 881-888.

32. Jonas, K.; Tomenius, H.; Kader, A.; Normark, S.; Romling, U.; Belova, L.M. and Melefors, O. Roles of curli, cellulose and bapa in *Salmonella* biofilm morphology studied by atomic force microscopy. *BMC Microbiology*, **2007**, 7 (70): 1-9.

33. Cross, S. E. ; Kreth, J. ; Zhu, L. ; Qi, F. ; Pelling, A. E. ; Shi, W. and Gimzewski, J. K. Atomic force microscopy study of the structure-function relationships of the biofilm-forming bacterium *Streptococcus mutans*. Nanotechnology, **2006**, 17: 1-7.

34. Nunez, M.E.; Martin, M.O.; Chan, P.H. and Spain, E.M.. Predation, death and survival in a biofilm: *Bdellovibrio* investigated by atomic force microscopy. *Colloids Surf B Biointerfaces*, **2005**, 42: 263-271.

35. Hinterdorfer, P. and Dufrene, Y.F. Detection and localization of single molecular recognition events using atomic force microscopy. *Nature Methods*, **2006**, 3: 347-355.

36. Dague, E.; Alsteens, D.; Latge, J.P.; Verbelen, C.; Raze, D.; Baulard, A.R. and Dufrene, Y.F.. Chemical force microscopy of single live cells. *Nano Letters*, **2007**, 7: 3026-3030.

Chapter 4 Electrochemistry

4.1 Introduction

Electrochemistry is an important branch of chemistry broadly used to interconnect chemical and electrical energy. Chemical oxidation / reduction processes produce electrical energy and conversely, electrical energy can carry out chemical reactions. These transformations take place through flow of electrons. Many physical techniques have been developed to exploit and characterize electrochemical reactions, and are called electrochemical methods. The great achievements in electrochemistry are widely applied in all many scientific areas and bring about tremendous advances in science and technology. Electrochemistry appears widely in our life, such as, cars batteries, watches and mobile phones, corrosion, electroplating, and electro-refining of metals, electro-polymerizations and electrochemical synthesis.[1]

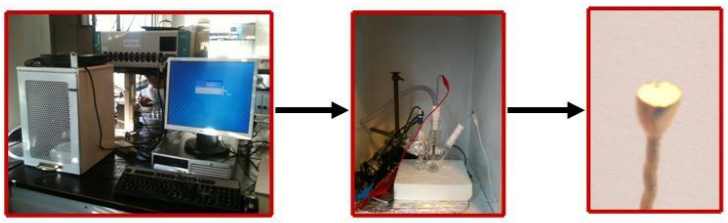

Fig 4.1 single crystal electrochemistry from left to right: whole instrument of electrochemistry, electrochemical cell, and single-crystal Au (111)-electrode.

Single–crystal surfaces, have been used in the present project. These are crucial for imaging individual molecules by AFM and maintaining a low background current in electrochemical measurement.(Fig 4.1)

Bacterial biofilms grown on pure and modified Au (111) electrode surfaces have been extensively explored in this project. We shall overview here briefly elements of interfacial electrochemistry, voltammetric methods, cyclic voltammetry and electrochemistry on biofilm coated electrodes .

4.2. Interfacial electrochemistry

4.2.1 Faraday's Laws

Michael Faraday introduced a number of new concepts, such as electrolysis, electrolyte, electrode, anode, cathode, etc. Relations between charge and time, current, and mass, are expressed in Faraday's laws:

$$Q = I \times t \tag{4.1}$$

$$Q = (m / M_w) nF \tag{4.2}$$

Where Q is the charge (C), I the current (A), and t the time (s), M_w the molecular mass (g/mol), m the mass (g), n the number of electrons transferred, and F the Faraday constant, 96485.3 C mol^{-1}.

4.2.2 The Nernst equation

The Nernst equation shows the relation between the equilibrium electrode potential (E) and both the standard electrode potential (E^0) and the concentration (C) of the oxidized and reduced component of the redox couple:

$$O + ne \Leftrightarrow R \tag{4.3}$$

$$E = E^0 + \frac{RT}{nF} In \frac{C_o}{C_R} \tag{4.4}$$

T is the temperature (K), and R the gas constant, 8.31 (J $K^{-1}mol^{-1}$). At 25 ºC.

$$E = E^0 - 0.059 \log(C_R / C_O) \tag{4.5}$$

According to the Nernst equation, the potential of the hydrogen electrode depends on pH as

$$E = - 0.059pH \text{ (V)} \tag{4.6}$$

4.3 Electrochemical processes at an electrode surface

Two electrode systems, metal deposition, anion adsorption, corrosion, polycrystalline materials and the liquid Hg electrode are major tools for electrochemistry from the 19th to the mid 20th century. New electrochemical techniques are based on three-electrode

systems developed in 1960s-1980s. Single-crystalline metallic substrates, microelectrodes and nanoelectrodes, and a wealth of surface spectroscopic and other surface techniques were introduced in electrochemistry from the 1980's. The introduction of surface sensitive methods and spectroscopies into electrochemistry offers a unique opportunity to study interfacial electrochemical phenomena in situ and dynamically. Prompted by this development, electrochemistry has become an essential technique to study biological molecules, nano-materials, single molecules and to construct highly sensitive biosensors and other ultra-sensitive devices.[2]

4.3.1 Three-electrode systems and the general electrochemical process

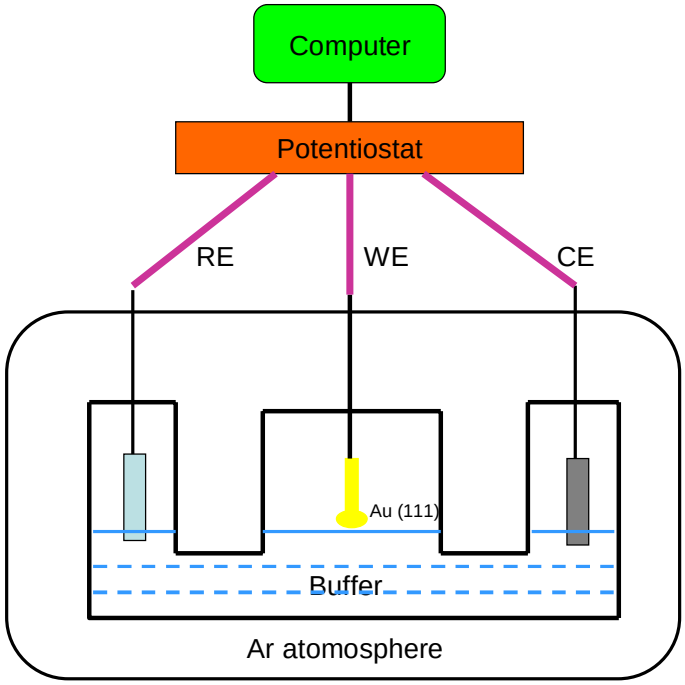

Fig 4.2. A schematic illustration of a three-electrode system, with focus on the electochemical reaction at the working electrode (WE), with potentiostatic control of the WE relative to a reference electrode (RE). An Ar atomosphere was maintained. The electrochemical current flows between the working electrode and the counter electrode (CE) and is also measured precisely. The reference electrode (RE) has a fixed potential independent of the current flow between working and counter electrodes. The RE is a reversible Hydrogen-Pt. The CE is Pt.

Three-electrode systems are now common electrochemistry tools. A three-electrode system contains a working electrode (WE), a reference electrode (RE) and a counter electrode (CE), Fig 4.2. We focus on the electrochemical reaction at the working electrodes. Current flows between the working and counter electrodes and is the primary quantity measured. The potential of the working electrode is controlled and measured as the difference between working electrode and reference electrode potential independent of the current flow between working electrode and counter electrode. The advantage of three-electrode systems is perfect potential control of WE and RE, as well as precise current measurement between the WE and CE.

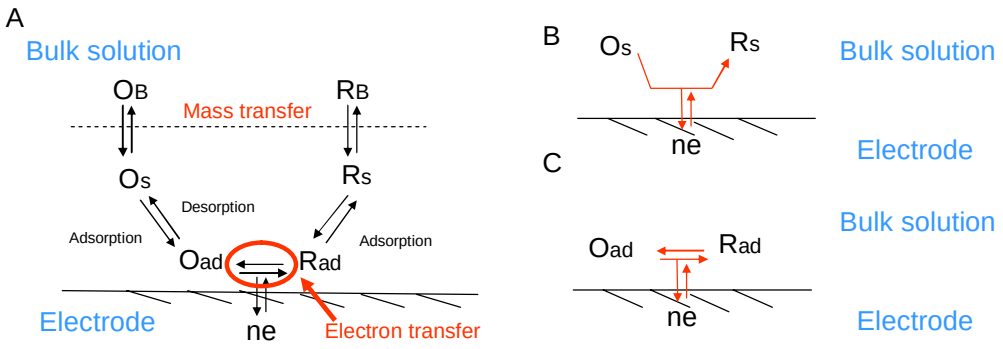

Fig 4.3. Schematic overall view of an interfacial electrochemical process[3,4]. A: The overall reaction $O + ne \Leftrightarrow R$ consist of mass transfer or diffusion of O or R toward and from the electrode surface, chemical reactions, adsorption, and interfacial electron transfer. B: In the diffusion mode and fast interfacial electron transfer, redox species are not adsorbed on the electrode surface. C: In the adsorption mode, redox species are immobilized on the electrode surface and dominate electron transfer; Adsorption and diffusion modes follow different equations in voltammetry. Adapted from [4].

A general electrochemical interfacial process includes mass transport (migration, diffusion or convection) from the bulk solution and transient adsorption onto the electrode surface. This is followed by electron transfer (ET) between the electrode and the active species (O and R), desorption from the electrode surface, and mass transport away from the electrode surface back into the solution, Fig 4.3. These steps can be followed by a range of electrochemical techniques among which voltammetric methods are used in the present work.

4.3.2 Voltammetric methods

Voltammetry includes a multitude of electrochemical methods. Properties of the target molecule are derived from measurements of current as a function of applied potentials between a working electrode and a reference electrode. Voltammetry has been extensively used in inorganic, physical and biological chemistry for studies of redox processes in various media, adsorption processes on surfaces, and electron transfer mechanisms at pure and chemically modified electrodes. [4]

The four most widely used methods of voltammetry are potential step, linear scan, differential pulse, square wave and cyclic voltammetry. The potential changes in these methods are schematically illustrated in Fig 4.4, where the potential (*E*) is plotted as a function of time (t). The two main electrochemical methods used in the present work are cyclic voltammetry (CV) and linear sweep voltammetry (LSV). This chapter is focused on linear scan and cyclic voltammetry in both diffusion controlled and diffusion-less systems, as theses modes have been the ones of primary use in the project.

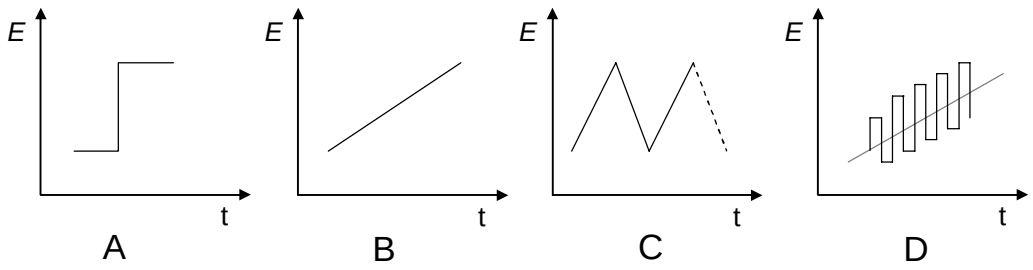

Fig 4.4. Potential (*E*) vs. time (t) waveforms used in voltammetry: A. potential step; B. Linear sweep voltammetry; C. cyclic voltammetry; D. Square wave voltammetry.

4.3.3 Cyclic voltammetry

Cyclic voltammetry is a potential sweep technique used for rapidly obtaining an electrochemical 'spectrum' indicating the potentials at which the processes occur. The current dependence on the sweep rate dE/dt can be used to identify the type of

electrochemical reaction and recognition of other secondary effects such as adsorption. Kinetic data such as rate constants for the electrochemical electron transfer reaction can also be estimated with sweep techniques. Potential sweep methods, including CV, are extremely useful for mechanistic investigations.

Fig 4.5 shows three (theoretical) examples of cyclic voltammograms (I vs E plots) representative of different electrochemical systems, i.e. Capacitive currents only (A), a diffusion controlled redox reaction (B), and a process of an adsorbed species (C). For each type of voltammogram, the effect of increasing scan rate is shown. The general characteristics of Faradaic voltammograms are current peaks at potentials where a Faradaic reaction occurs. (adsorption and surface reorganization processes can also produce peaks) The peak positions E_p and peak currents I_p and their dependence on scan rate are the keys to determining the underlying mechanism of the electrode reactions.
In the Fig 4.5A and B, the scan is started at a value negative of E^0 (the standard potential), where the electroactive molecule is in its reduced form. As the electrode potential approaches E^0, oxidation begins and current starts to flow. The concentration of the electro-active molecules at the electrode surface drops to zero at the potential E_P^A. At potentials higher than E_P^A, the current decreases as depletion of electroactive molecules close to the electrode surface sets in. This appears as a peak in the voltammogram. When the sweep is reversed, a significant concentration of the oxidized species is at first present near the electrode surface. Some oxidation continues until the potential has approached E^0, where the oxidized species will be reduced and a reverse current flow. The current depends on two steps in the process. The diffusion of electro-active material to the electrode surface and the electron transfer reaction.

The following equations apply

$$E^0 = (E_p^A + E_p^C)/2 \tag{4.7}$$

$$d = \frac{4.4RT}{nF} = \frac{113}{n} mV \quad (25\ ^oC) \tag{4.8}$$

d is the peak half-width and n the number of electrons transferred. Equation 4.7 states that the equilibrium redox potential is the midpoint potential between the peak potentials

of the oxidation and reduction process. Equation 4.8 correlates the peak half-width with the number of electrons transferred in the process. We can thus measure the standard redox potential of a redox system and the number of electrons involved in the electron transfer process from equations 4.7 and 4.8.

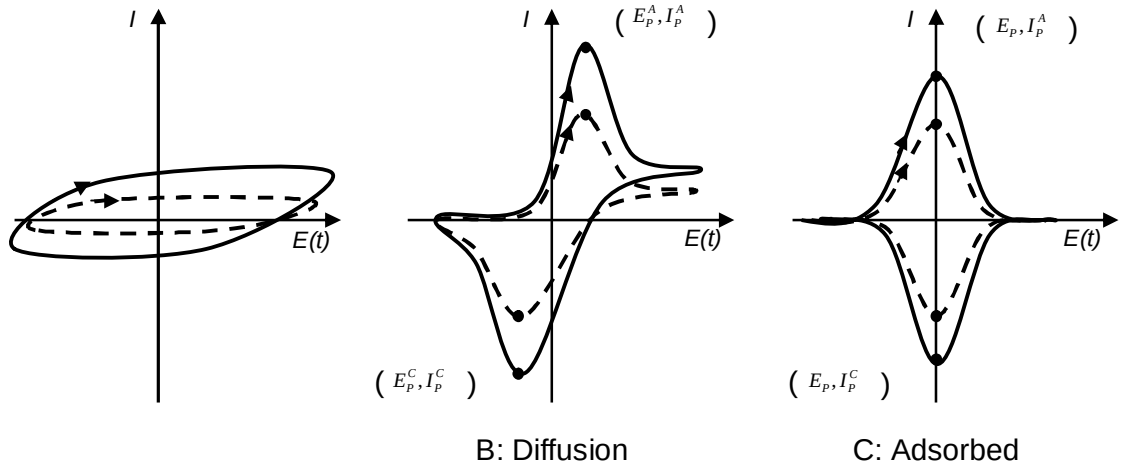

Fig 4.5. Theoretical cyclic voltammograms (CV) representative of different electrochemical systems. Each plot includes a single cycle modeled with different scan rates: fast (_) and slow (---). A: No Faradic reaction, the capacitive current from the charging of the double layer is the primary contribution to the CV. The magnitude of the current depends on the capacitance of the electrode and is generally independent of potential. In aqueous solution there is always such a flat baseline-like current contribution from the double layers. B: A CV for a Faradaic reaction with both product and reactant in solution, and where the electron transfer rate is fast compared to that of diffusion. The main characteristics are an anodic I_P^A (positive) and a cathodic I_P^C (negative) current peak. The peak height increases with increasing scan rate while the peak positions E_P^A and E_P^C remain constant. C: An electrode reaction involving only adsorbed species produces a CV with symmetric peaks with little or no peak separation, adapted from[5].

Analysis and interpretation of CVs has traditionally evolved around shape characteristics such as the peak height and peak potentials as mentioned above. The peak area, however, is a more accurate measure of the amount of current passed. CVs can be rather complex, and mathematical description is either limited to well-defined cases or very advanced. Many of the most common electrochemical techniques, including CV, were invented before digital computers of modern capacity were available for acquisition and processing of data. (The potential waveforms used in CV, as well as more complex waveforms, can be generated with relatively simple analogue devices)[4]. Quantitative

analysis of CV has therefore focused on characteristics that are easy to identify, in particular the peak height and peak potential. We have used both peak height and peak area for the analysis of electrochemical results in the present work.

4.3.4 Linear sweep voltammetry and thiol-compounds

Cyclic and linear sweep voltammetry can also be used to detect adsorption and desorption processes. Molecules with a thiol-compound (HS-R) can be covalently bound to a gold-surface forming a self-assembled monolayer. At negative potentials the sulfur-gold bond breaks and the RS^- anion will desorb from the surface. The desorption is a one-electron process[6]:

$$RS - Au + e^- \rightarrow RS^- + Au \qquad (4.9)$$

Where R represents the organic part of the molecule.

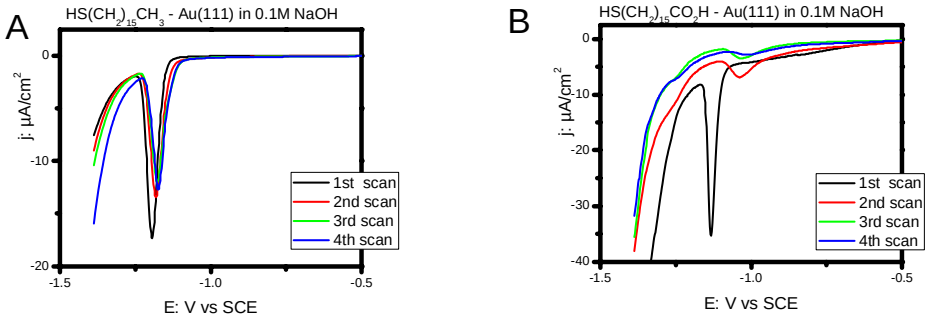

Fig 4.6 LSV for reductive desorption of $HS(CH_2)_{15}CH_3$ and $HS(CH_2)_{15}CO_2^-$ SAMs on Au(111)-surfaces. 0.1 M NaOH solution, pH 13. Scan rate 10 mV s^{-1}. A: $HS(CH_2)_{15}CH_3$; B: $HS(CH_2)_{15}CO_2^-$. The surface coverage and RD peak potentials are: Black line: 1st scan (A: 7.13×10^{-10} mol cm^{-2}, -1.19 V and B: 8.88×10^{-10} mol cm^{-2}, -1.13 V); Red line: 2nd scan (A: 5.93×10^{-10} mol cm^{-2}, -1.18V and B: 2.62×10^{-10} mol cm^{-2}, -1.04V); Green line: 3rd scan (A: 5.71×10^{-10} mol cm^{-2}, -1.18 V and B: 1.93×10^{-10} mol cm^{-2}, -1.03V); Blue line: 4th scan (A: 5.45×10^{-10} mol cm^{-2}, -1.17 V and B: 6.01×10^{-11} mol cm^{-2}, -0.99 V). From the present work. See Chapter 8.

The desorption is often irreversible, but re-adsorption can also be observed in a cyclic voltammogram appearing mostly as a small peak. The voltammogram can also give an

indication of the homogeneity of the adsorbed layer by the peak shape and the peak width. If the monolayer is highly homogenous, the peak will be quite sharp, because most of the molecules have the same properties, while the peak will be broadened for a highly disordered monolayer.

The cleavage of the Au-S bond is a one-electron cathodic process. An example is shown in Fig. 4.6. The linear scan voltammetry thus provides a convenient and accurate way to determine the surface coverage of the adsorbate, particularly suitable for thiol-based SAMs on Au (111) electrode surfaces,

$$\Gamma = \frac{Q}{FA} \tag{4.10}$$

where Γ is the surface coverage. The Faradaic charge Q can be obtained by integrating the area of the reductive desorption peak. There is in principle also a capacitive contribution to the reductive desorption peak.

4.4 The Au (111) surface

4.4.1 Gold surfaces

Gold is a very useful metal for the study of bioinorganic processes at surfaces. Firstly, gold is a biocompatible material, and there are no undesirable local or systematic effects of the interaction with biological systems in host tissue and the material itself [7-9]. Gold can be easily purified and is resistant to corrosion in air and aqueous solutions [10-11]. Gold surfaces of uniform and well defined atomic structure is a requirement for visualization of nanoscale samples e.g. by AFM[12,13]. The strong chemical bond between gold and sulfur is extremely useful, both for direct adsorption of sulfur-containing molecules and in the modification of gold surfaces with self-assembled monolayers. The electrochemical properties of gold make it an excellent electrode material in aqueous electrolytic solutions, and atomically flat gold electrodes are responsive to electrochemical signals down to 1 nA or less. Finally, electrochemistry and well defined electrochemical surfaces provide exceptional perspectives not only for accommodating, but also for controlling, molecular and biomolecular adsorption, electron transfer and

electrocatalytic processes via the electrochemical potential. It is the combination of these properties, the broad electrochemical potential window of gold, its remarkable stability and biocompatibility that altogether makes gold an excellent choice for electrochemically controlled biological surface processes.

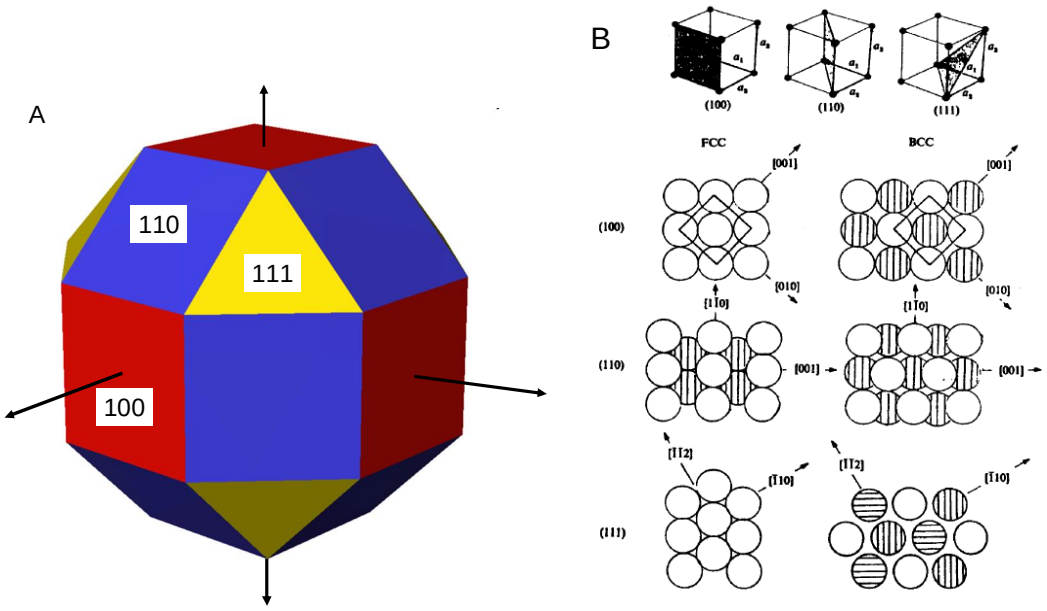

Fig 4.7 A: Rhombicuboctahedron of Au crystal with yellow (111), red (100) and blue (110) surface planes; B: The schematics of a gold single-crystal showing the crystallographic planes, reprint from [14].

The surface structure of a given crystallographic plane depends strongly on the alignment between the plane and the arrangement of atoms in the crystal. Since the crystallographic planes are purely mathematical planes, and since one cannot actually cut through atoms, only certain planes are in perfect alignment with the atomic ordering. By definition of the unit cell for fcc crystals, these are the three low-index planes (111), (100) and (110). The orientation and relative positions of the (111), (100) and (110) surface planes of a simple cubic crystal are shown in Fig 4.7 A and the atomic surface structures in Fig 4.7B.

4.4.2 Au (111)

Au(111)-surfaces have a well defined structure, where the atoms are organized in a hexagonal pattern. This pattern gives the highest packing density and Au(111) is the most stable of the three crystal faces. The Au atoms on a Au(111)-surface are

coordinatively unsaturated compared to the bulk metal. The surface structure is therefore intrinsically unstable compared to other, more densely packed surface structures such as the (1×23) structure described below. Conversion to such structures can be achieved by a rearrangement of the surface atoms. This process is called reconstruction. The Au (111) surfaces reconstruct spontaneously from a (1×1) to a (1×23) structure. This means that every 23rd atom along a given row is in register with the (1×1) structure[3,15]. It is now well known that Au (111) –surfaces can reconstruct either by electrochemical or flame annealing. When single-crystal electrodes were first introduced, they were only investigated by methods based on UHV, but it was recognized later that the same reconstruction could be achieved by flame annealing in air[3,16]. An interesting and important feature for reconstructed Au(111)-surfaces is that the structure is stable in aqueous solution, if certain precautions are taken.

The reconstruction can be lifted in various ways, particularly by adsorption of anions or at high positive potentials. Moreover the higher the adsorbed anion coverage, the faster the lifting of the reconstruction[11]. Au (111) gives characteristic voltammograms in H_2SO_4, where sharp peaks represent the reconstruction of the sulfate ion lattice on Au(111) –surfaces, Fig 4.8. As the (1×23) structure is 4% more densely packed than the de-reconstructed (1×1) Au (111) –surfaces' excess' atoms are left over. The left-over atoms form islands of monoatomic height on the surface. Island formation is a useful fingerprint that reconstruction has been lifted[3].

Another way of lifting the reconstruction is by shifting the potential to high positive values, where the surface changes to the ureconstructed structure. After lifting the reconstruction the surface can again be reconstructed by electrochemical annealing, where the potential is kept at a negative value, which depends on the metal and the crystal plane. The reconstruction lines are more disordered by this reconstruction which therefore differs from the reconstruction induced by flame annealing[3,16].

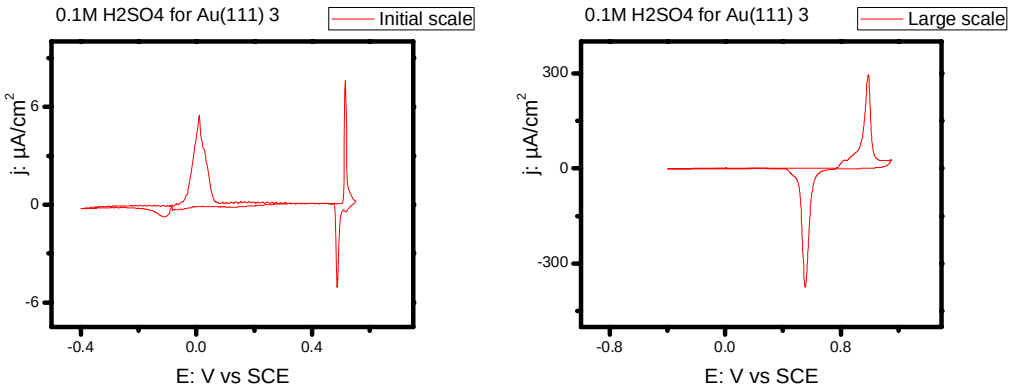

Fig 4.8 Cyclic voltammogram of a Au (111) –electrode in 0.1M H_2SO_4, scan rate 10 mv/S. Left: initial scan, two sign peaks of Au (111) –electrode from Au reconstruction at potential around 0 V, the 0.5V peak is from reconstruction of the SO_4^{2-}surface layer; Right : Large scan the upper peak has a right shoulder, which is a mark of Au (111) –electrode. From the present work, it is used for Au (111) –electrode identification.

Gold has long been used as electrode material because of the stability and easy purification of the metal. Gold surfaces are easy to modify with thiols or other molecules that form the strong chemical Au-S bond in SAMs.

4.5 Electrochemistry and Biological samples

Electrochemical methods have recently been designed to monitor bacterial biofilm growth (such as biofilm age, density of cells, pH etc.) as well as production of macromolecular compounds in the biofilm during the growth. Whole biological cells of several unicellular organisms immobilized on electrode surfaces have been addressed using cyclic voltammetry (CV) [17-24], impedance spectroscopy [19], and infrared reflectance spectroscopy [20]. Redox proteins in the bacterial outer membrane are apparently close enough to the bacterial surface that good electronic contact with the electrode surface is established. In addition, electrochemical methods have been used to control the bacterial biofilms. Such studies offer new insight, for example into the operation of bacterial membrane respiratory redox metalloproteins, the bacterial surface binding modes, bacterial coverage, and perhaps growth dependence on the electric field in the composite electrode/ bacterial/aqueous interfacial region. In addition, well known fingerprint features such as the hydrogen adsorption signal on platinum electrodes[17] have been

suggested as molecular monitors of bacterial cell coverage of metallic electrode surfaces. Positively charged surfaces have thus been found to stimulate and negatively charged surfaces to inhibit biofilm growth [25]. Based on 250 references, Bos et al. concluded that negatively charged bacteria adhere more rapidly and more strongly to positively than to negatively charged surfaces [26]. Electrostatic forces have thus a key role in the overall bacterial surface adhesion.

Reference

1. Holze, R. Experimental electrochemistry: a laboratory textbook, **2009**, Wiley-VCH Verlag GmbH& Co.KGaA, Wenheim
2. http://en.wikipedia.org/wiki/Electrochemistry
3. Zhang, J.; Chi, Q. and Ulstrup, J. Chemistry at the nanoscale, Department of Chemistry, Technical University of Denmark. **2010.**
4. Fish, A.C. Electrode Dynamics, Oxdord University press, Oxford, 1996.
5. Welinder, A.C. Insulin adsorption and surface behavior on monocrystalline Au (111), Au (100) and Au (110) surfaces studied with STM, AFM and electrochemistry. DTU kemi, **2010,** Ph.D thesis.
6. Hu, Y.; Zhang, J. and Ulstrup, J. Investigation of *Streptococcus mutans* biofilm growth on modified Au (111)-surfaces using AFM and electrochemistry. *Journal of Electroanalytical Chemistry*, **2011**, 656 (1-2): 41-49.
7. Mitragotri, S. Lahann Physical approaches to biomaterial design. *Nature Materials*, **2009**, 8: 15-23.
8. Wilson, R. The use of gold nanoparticles in diagnostics and detection. *Chemical Society Reviews*, **2008**, 37: 2028-2045.
9. Sperling, R.A.; Rivera, Gil P. ; Zhang, F.; Zanella, M. and Parak, W.J. Biological applications of gold nanoparticles. *Chemical Society Reviews*, **2008**, 37: 1896-1908.
10. Nicol, M.J. The Anodic Behavior of Gold—Oxidation in acidic solution. *Gold Bulletin*, **1980**, 13: 46-55.

11. Nicol, M.J. The Anodic Behavior of Gold—Oxidation in alkaline solution. *Gold Bulletin*, **1980**, 13: 105-111.
12. Hamelin A. cyclic voltammetry at gold single –crystal surface. Part 1. Behaviors at low index faces. *Journal of Electroanalytical Chemistry*, **1996**, 407: 1-11.
13. Hamelin A. Martins A. cyclic voltammetry at gold single –crystal surface. Part 2. Behaviors at high index faces. *Journal of Electroanalytical Chemistry*, **1996**, 407, 13-21.
14. Hansen, A.G. In situ scanning tunneling microscopy and mictrocantilever investigations of yeast cytochrome c on gold. DTU kemi, **2002**, Ph.D thesis.
15. Dakkouri, A.S. Kolb D.M. Reconstruction of gold surfaces. *Interfacial Electrochemistry*, Wieckowski, A, Ed.; Marcel Dekker, USA, **1999**.
16. Kolb, D.M. Surface reconstruction at metal-electrolyte interfaces. *In Nanoscale probes of the solid/liquid interface*. Gewirth, A. A.; Siegenthaler, H., Eds. Nato-ASI Series C, Vol 288: **1995**.
17. Giao, M.S. ; Montenegro, M.I. and Vieira, M.J. Monitoring Biofilm formation by using cyclic Voltammetry-effect of the experimental conditions on biofilm removal and activity. *Water Science and Technology*, **2003**, 47: 51-56.
18. Wang, Y.; Tsujimura, S. ; Cheng, S.; and Kano, K. Self-excreted mediator from Escherichia coli K-12 for electron transfer to carbon electrodes. *Applied Microbiology and Biotechnology*, **2007**, 76: 1439-1446.
19. Busalmen, J. P.; Berna, A. and Feliu, J. M. Spectroelectrochemical examination of the interaction between bacterial cells and gold electrodes, *Langmuir*, **2007**, 23: 6459-6466.
20. Hu, Z.; Jin, J.; Abruna, H. D.; Houston, P. L.; Hey, A.G.; Ghiorse, W.C.; Shuler, M. L.; Hidalgo, G. and Lion, L. W. Spatial distributions of copper in microbial biofilms by scanning electrochemical microscopy. *Environmental Science and Technology*, **2007**, 41: 936-941.
21. Vostiar, I. ; Ferapontova, E. E. and Gorton, L. Electrical "wiring" of viable Gluconobacter oxydans cells with a flexible osmium-redox polyelectrolyte *Electrochemistry Communications*, **2004**, 6: 621-626.

22. Timur, S. ; Haghigghi, B.; Tkac, J. ; Pazarhoĝlu, N. ; Telefoncu, A. and Gorton, L. Electrical wring of *Pseudomonas putida* and *Pseudomonas flluorescens* with osmium redox polymers. *Bioelectrochemistry,* **2007**, 71: 38-45.
23. Marsili, E.; Rollefson, J.B.; Baron, D.B.; Hozalski, R.M. and Bond, D. R. Microbial biofilm voltamemetry: direct electrochemical characterization of catalytic electrode-attached biofilms. *Applied and Environmental Microbiology*, **2008**, 74 (23): 7329-7337.
24. Kasemo, B. Biological surface science. *Surface Science*, **2002**, 500: 656-67**7.**
25. Van der Mei., H.C. and Busscher, H.J. Electrophoretic mobility distributions of single-strain microbial populations. *Applied and Environmental Microbiology*, **2001**, 67 (2): 491-494.
26. Bos, R., Van der Mei, H.C. and Busscher, H.J. Physico-chemistry of initial microbial adhesive interactions—its mechanisms and methods for study. *FEMS Microbiology Review*, **1999**, 23: 179-229.

Chapter 5 Experimental section

5.1 Chemicals

5.1.1 Buffers and media

Phosphate buffered saline (PBS) buffer tablets (Medicago, Sweden): 0.010 M phosphate, 0.14 M NaCl, 0.027 M KCl, pH=7.4)

Brain heart infusion broth (BHI) medium (Sigma- Aldrich)

Trypic soy Broth (TSB) medium (Sigma- Aldrich)

Luria-Bertani (LB) medium (Sigma- Aldrich)

Agrobacterium induction (AB) minimum medium (Sigma- Aldrich)

Millipore water (Millipore housing, 18.2 MΩ cm)

5.1.2 Other reagents

$K_4[Fe(CN)_6] \cdot 3H_2O$ (Merck, > 99 %).

$K_3[IrCl_6]$ (Sigma-Aldrich, > 99 %)

$[Ru(NH_3)_6]Cl_3$ (Sigma-Aldrich, > 99 %)

$[Co(phen)_3](ClO_4)_3 \cdot 2H_2O$ was prepared as described[1-3]. Available in DTU NanoChemistry.

$[Co(terpy)_2](ClO_4)_3 \cdot 2H_2O$ was prepared as described[1-3] Available in DTU NanoChemistry.

$[Co(NH_3)_6]Cl_3$ was prepared as described[1-3]. Available in DTU NanoChemistry.

Deoxyribonuclease I (DNase I) (Sigma, >99%)

Sucrose (Sigma-Aldrich, > 99 %)

Ethanol (Merck, 99.99 %)

NaOH ultrapure solution (Merck, 30 %)

Acetone (Riedel-de Haen, > 99.5 %)

Chloroform (VWR, > 99 %)

H_2SO_4 (Suprapur, 99.5 %)

5.1.3 Reagents for preparation of self-assembled monolayers

$HS(CH_2)_{15}CH_3$ (1-hexadecanethiol, MHD, Merck, > 90 %).

$HS(CH_2)_{15}CO_2H$ (ω-mercaptohexadecanoic acid, MHDA, Sigma-Aldrich, 98 %)

$HS(CH_2)_{17}CH_3$ (1-Octadecanethiol, Sigma-Aldrich, 98 %).

L-Cysteine (Sigma-Aldrich, > 98 %).

Cysteamine (Fluka, 98 %).

5.1.4 Polymer materials for Au (111) bead preparation

DER resin grade 736 (polysciences, INC, Cat# 02923) 1.2 g

Nonenylsuccinic anhydride (polysciences, INC Cat #01542) 5.28 g

Electron microscopy grade epoxy hardener MW 224

4-vinycyclohexene dioxide mw 140.2 (polysciences, INC Cat# 1912) 2 g

2-dimethyl aminoethanol (polysciences, INC Cat 1458) 0.08 g

5.1.5 Gases

Argon (Strandmøllen, Denmark, 99.999 %)

Dioxygen (Strandmøllen, Denmark, 99.999 %)

Dihydrogen (Strandmøllen, Denmark, 99.999 %)

Dinitrogen (Strandmøllen, Denmark, 99.999 %)

5.1.6 Metals and surfaces

Gold Ø1mm (Dansk Hollandsk Ædelmetal, 99.999 %)

Platinum wire Ø 1mm (Dansk Hollandsk Ædelmental, 99.999 %)

Platinum / iridium (80:20) wire Ø 0.25 mm (Goodfellow. 99.999 %)

Gold (111) disk Ø14mm or Ø12 mm d 2.5mm (Surface Preparation Laboratory, 99.999 %)

Mica (Doll Artist's Workshop, Gardnerville, USA)

Substances Gold (111) coated substrates (12 x 12 mm borosilicate glass, 2 nm chromium, 300 nm gold, Arrandee, Inc. Lienen, Germany)

5.2 Bacterial strains

Streptococcus mutans (ATCC 25175) was a gift from Laboratory of Microbiology, Department of Odontology, Faculty of Health Sciences, University of Copenhagen (Associate Professor Tove Larsen and Laboratory Technician Natalia Christiansen). *S. mutans* was stored in Brain Heart Infusion broth (BHI) medium at -80 ^{o}C and incubated in BHI broth shaken at 37 ^{o}C overnight.

Staphyloccus epidermidis (RP62a, ATCC12228, 1457 and 1457atlE) were provided by Department of Systems Biology, Technical University of Denmark. RP62a and 1457 are biofilm positive wild type strains, ATCC 12228, 1457atlE biofilm negative strains. RP62a, 1457 and ATCC 12228 are wild type while 1457atlE is a mutant type with the deficiency atlE gene (autolysin adhesion). Bacteria were cultured overnight with tryptone soya broth (TSB) medium.

Pseudomonas aeruginosa (PA01, *pelA, pelBCD and pelApslBCD*) were provided by Department of Systems Biology, Technical University of Denmark. PA01 is a biofilm positive wild type strain, the other three are mutant strains. *P. aeruginosa* overnight cultures were diluted 100 times in AB minimal medium supplemented with 30 mg/l glucose with or without 10 μg/ml DNaseI (Sigma Aldrich) and incubated in Eppendorf tubes with mica sheet at 37 ºC for 24 hours without shaking.

5.3 Electrochemical setup

Electrochemical measurements were carried out using an autolab PGSTAT 12 system (Eco Chemie, Netherlands) controlled by the general-purpose electrochemical system (GPES) software at room temperature (23 ± 2ºC). A three –electrode system consisting of a working electrode (WE), a counter electrode (CE) and a reference electrode (RE), Fig 4.2 was used. The electrochemical cell and electrodes were confined in a Faraday cage, see Fig 4.1. (Detailed information in Chapter 4). Purified argon (Chrompack, 5N) was used to purge dioxygen from the solution before the measurement, and a gas stream was maintained over the solution during the measurements.

5.3.1 The reference electrode

Reversible hydrogen electrodes (RHE) were freshly made before measurements. A Pt-wire, was cleaned by burning to red heat in a hydrogen flame and quenched by Millipore water. The Pt-wire was inserted into a cleaned glass tube (Pasteur pipette) and the end of the glass melted tightly around the Pt-wire over a hydrogen flame. Hydrogen saturated buffer solution (as used in the electrochemical cell during the electrochemical measurements) was transferred into the newly prepared electrode after a short cooling period and hydrogen gas bubbled into the upper 1.5 cm of the electrode. The RHE was checked versus a saturated calomel electrode (SCE) (Radiometer, Denmark) after each measurement. All potentials are reported versus this electrode.

5.3.2 The Counter electrode

A homemade coiled Pt-wire was used as a counter electrode in all electrochemical measurements. The coiled Pt-wire was cleaned by heating to red heat in a hydrogen flame and quenched in Millipore water before transfer to the electrochemical cell. A counter electrode is essential in electrochemical measurements in order to minimize current flow through the reference electrode, which destabilizes the reference electrode.

5.3.3 The working electrode

The working electrode was always a Au(111)-electrode prepared as described in Appendix E. The electrode preparation differs from experiment to experiment. Electrode preparation procedures will therefore be described in the individual experimental sections. However, prior to use all electrodes were annealed at 860 ºC for at least six hours and heated to red heat in a hydrogen flame before quenching in H_2 saturated Millipore Water.

5.3.4 The electrochemical cell

A homemade two-compartment electrochemical class cell designed to contain a three – electrode system as described above was used throughout the measurements. A Luggin

capillary tube was placed with one end directly under the WE-surface in one compartment, while the other end was close to the RE in the other compartment. The CE was placed in the other compartment. A two-way inlet valve with one capillary tube placed at the bottom of the cell and another one above the electrolyte solution allows for degassing the solution and maintaining a gas stream over the electrolyte surface during the measurements.

5.4 AFM

The basic elements of Atomic force microscopy (AFM) were described in Chapter 3, Fig 3.1. Three different types of AFM instruments AFM PicoScan 5500 from Agilent instrument AFM DualScopeTM microscope from DME, Nanoscope IIIa AFM from Veeco were applied in this study, see Fig. 5.1. The further detailed information of the AFM is described in Chapter 6, 7, 8 and 9.

5.5 Data analysis

Electrochemistry data from Autolab and AFM force curve measurements were analyzed by Origin Pro version 8. AFM images from AFM Picoscan 5500 were analyzed with Gwyddion SPM data analysis software version 2.18. AFM images from Nanoscope IIIa AFM were analyzed by Nanoscope 7.30.

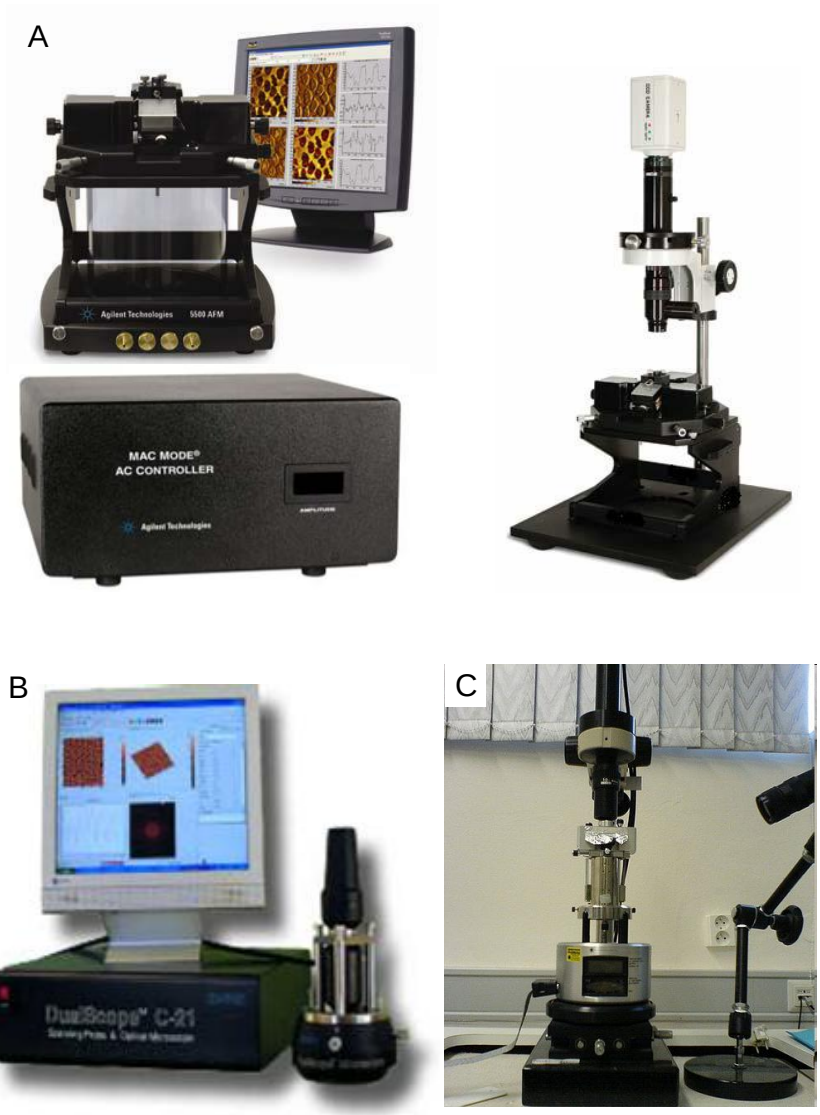

Fig 5.1 The three different types of AFM instruments used. A: AFM PicoScan 5500 from Agilent instrument (Agilent technologies, Chandler, AZ, USA)[4]; B: AFM DualScope™ microscope equipped with a C-21 controller (DME A/S, Copenhagen, Denmark)[5]; C: Nanoscope IIIa AFM (Digital Instruments, Veeco Metrology Group, Santa Barbara, CA, USA)[6]

5.6 General procedure

5.6.1 Cleaning

All glassware and the cells for both electrochemistry and AFM were boiled in 15% HNO_3 and washed thoroughly with Millipore water. The glassware and cells were then placed in an ultrasound bath for at least 20 minutes and washed again to ensure that all impurities had been removed. Both the electrochemical cell and the AFM cell were kept in a beaker filled with Millipore water and sealed with parafilm after cleaning.

5.6.2 Procedure for cleaning gold surfaces

All gold electrodes were annealed in an oven at 860 ºC overnight. Prior to use, the surfaces were flame-annealed in a hydrogen flame and quenched in Millipore water saturated with hydrogen gas. Gold surfaces that had been in contact with metal ions were electropolished in sulfuric acid before the annealing procedures. The electro-oxidation produces a thin crust of gold oxide containing possible surface impurities, which are subsequently removed by dissolution in hydrochloric acid.

5.6.3 Self-assembled monolayers

Self-assembled monolayers on Au (111) surfaces were prepared by immersion of the freshly annealed metal surface in 1-2 mM solutions of the monolayer-forming compound for 24 hours. The solvent was either Millipore water or ethanol as required. The surfaces were thoroughly rinsed both in solvent and Millipore water before further use.

References:

1. Kjær, A.M. and Ulstrup, J. Effects of reactant ionic charges and nonlocal dielectric screening on electron transfer between bis(terpyridine)cobalt(II) and tris(phenanthroline) tris(bipyridine) and analogous, electrically neutral sulfonated cobalt(III) complexes. *Inorganic Chemistry*, **1986**, 25: 644-651.

2. Bjerrum, J.; McReynolds, J. P. In: Inorganic Synthesis; Fernelius, W. C. , Ed.; McGraw-hill, New York, **1946**, Vol.II, pp. 217-218.
3. a. Baker, B. R. ; Basolo, F. ; Neumann, H. J. Chem. Soc. **1959**, 371-375. b. Hogg, R. ; Wilkins, R. G. Exchange studies of certain chelate compounds of the transition metals. Part VIII. 2,2′,2″-terpyridine complexes *Journal of Chemical Society*, **1962**: 341-350. c. Conrad, L. S. ; Christensen, H. E. C. and Ulstrup, J. Electron transfer and spectral α-band properties of the di-heme protein cytochrome c_4 from *Pseudomonas stutzeri*. *European Journal of Biochemistry*, **1995**, 231: 133-141.
4. Agilent Technologies 5500 scanning probe microscopy, user's guide, Agilent technologies. **2008**.
5. http://www.dme-spm.dk/products.html 2011.02.10
6. http://commons.wikimedia.org/wiki/File:AFM_Nanoscope_IIIa.jpg 2011.02.10

Chapter 6 Adhesive properties of *Straphyloccus epidermidis* probed by AFM

6.1 Introduction

Coagulase-negative *Straphyloccus epidermidis* is an opportunistic human pathogen and normally colonizes the skin and mucous membranes of the human body[1]. However, *S. epidermidis* forms biofilms on indwelling medical devices, which causes many problems and is hard to remove due to its antibiotic multi-resistance, including methicillin, rifamycin, fluoroquinolones, gentamycin, tetracycline, chloramphenicol, erythromycin, clindamycin and sulphonamides, but 80% of catheters infected with *S. epidermidis* can still be treated with vancomycin without catheter removal[2]. Previous studies have established and screened a library of the 76 organic molecules and proved that organic compounds 47 and 73 had strong efficient effect of the *S. epidermidis* biofilm formation and growth inhibition, see section 6.2.4[3,4]. These two compounds have carbonyl and carboxamide fuctional groups, and a linear array of condensed homocyclic and heterocyclic aromatic ring systems. The structures of these two compounds are shown in Fig 6.1. AFM is an advanced technology to explore microorganisms at the nanoscale, and can image microbial systems in aqueous solutions and with nanometer resolution. In addition to recording images, AFM can be used to measure cell wall properties including adhesion properties, such as force curves and adhesion maps. Since the primary adhesion between bacterial cells and a surface is the first step in the biofilm formation, it is important to investigate the cell surface adhesion properties. Chemically modified AFM tips are useful approaches to study hydrophobicity of live cells. In this chapter, AFM was used to study the growth of *S. epidermidis* biofilm on mica, adhesion properties of the bacterial biofilm at the initial step, surface hydrophobicity of the bacteria, and the effect of chemical inhibition on nanoadhesion.

This part of the work was done in Yves Dufrene's group. In this chapter, AFM has been used to investigate the adhesive properties of different *S. epidermidis* strains: two biofilm positive, RP62a (Bhp positive[5]) and 1457 (atlE positive[6]), but also two biofilm negative,

12228 (Bhp negative) and 1457atlE (atlE negative). AltE and Bhp are two kinds of specific surface proteins of *S. epidermidis*: the protein atlE[7] controls a bifunctional adherent and autolysin, while the Bap protein[8] (also known as Bhp) is an intercellular protein adherent. Focus was first on the interaction between bare silicon nitride tips and the four *S. epidermidis* strains. Then, using hydrophobically modified tips, Chemical force Microscopy (CFM)was used to map the hydrophobicity of these different strains with nanoscale resolution. Finally, the effect of two chemical inhibitor compounds 47 and 73 on the adhesive properties was investigated using force spectroscopy with silicon nitride tips.

6.2 Experiments

6.2.1 Bacterial cultures

Staphylococcus epidermidis strain RP62a, ATCC 12228, 1457 and 1457atlE were provided by Department of System Biology, Technical University of Denmark. RP62a and 1457 are biofilm positive wild type strains, ATCC 12228, and 1457atlE biofilm negative strains. RP62a, 1457 and ATCC 12228 are wild type while 1457atlE is a mutant type with the deficiency atlE gene (autolysin adhesion).

These four strains were selected to apply due to their specific surface proteins. These specific proteins that affect surface adhesion seem likely to contribute to the hydrophobic or hydrophilic character of the cell surface. Some specific surface proteins are of particular interest such as the protein atlE[7], a bifunctional adherent and autolysin, and the Bap protein[8] (also known as Bhp), an intercellular protein adherent. It is of importance to use AFM to study the hydrophobic character of the cell surface.

Bacteria were cultured in TSB medium overnight with specific antibiotic resistant (the bacteria themselves can survive in the this resistant and other bacteria will be killed) 10μg /ml (RP62a (erm), 12228 (tet), 1457 atlE (erm)) and refreshed with new tryptone soya broth (TSB) medium keeping the OD_{600} at 0.3. The cells were harvested by centrifugation for 10 min at 7500 x g (Sorvall RC-5B; Du Pont Instruments), washed

twice with deionized water (Millipore) and resuspended in the same liquid. The properties of the strains are summarized in Table 6.1.

Table 6.1. Summary of *Straphyloccocus epidermidis* strain. RP62A: characterized by accumulation-associated protein (aap), which plays an important role in the accumulation of multilayer clusters during biofilm formation; 1457: produces the polysaccharide intercellular adhesion (PIA) during the accumulation phase of biofilm formation; *Ica ADBC*: the intercellular adhesion locus, which encodes the polysaccharide intercellular adhesion protein with a key role in biofilm formation and bacterial accumulation on host surfaces. Bap: the cell wall associated biofilm protein; Bhp: Bap homologous protein; altE: Autolysin adhesion; erm: erythromycin; tet: tetracycline; amp: ampicillin; strep: streptomycin. [9]

Strain nr.	Biofilm	Resistant	Gene	Genome
RP62A	+	erm, amp, kan, strep	*icaADBC*(+)Bap(+) Bhp(+)	Online
12228	-	tet	*icaADBC*(-)Bap(-) Bhp(-)	Online
1457	+	--	*icaADBC*(+), atlE (+)[2]	unknown
1457 atlE	-	erm	*icaADBC*(+), atlE (-)[2]	unknown

6.2.2 Biofilm growth

Mica was used for growing biofilms. 2.0 ×1.0 cm^2 Mica (Doll Artist's Workshop, Gardnerville, USA) sheets were cut and freshly cleaved by tape on both sides. Prior to use, they were sterilized by immersion into sodium hypochlorite solution (0.5 %) for 2 h. The mica slices were then washed three times with sterilized Millipore water, autoclaved at 121 ^oC and 15 psi for at least 30 min and immersed into a Petri dish (Plastiques-Gosselin, France) containing 10 ml tryptone soya broth (TSB) medium. *S. epidermidis* was cultivated on mica in TSB medium for 4 hours and 24 hours. Overnight cultures of *S. epidermidis* strains grown in TSB medium with designed antibiotics were diluted to OD_{600} = 0.05 into fresh TSB medium, added over the mica sealed by Parafilm, and incubated for given lengths of time at 37 ºC. The mica was then washed three times with Millipore water, and put into a new Petri dish to dehydrate naturally for one day.

The images were collected by AFM PicoScan 5500 from Agilent instrument (Agilent Technologies, Chandler, AZ, USA) with a 100 μm scanner and cantilevers (NP-S) from Veeco (Camarillo, CA, USA). The instrument was used in the contact mode. The images were analyzed with Gwyddion SPM data analysis software version 2.18.

6.2.3 Preparation of hydrophobic tips and surfaces

Gold coated surfaces were obtained as follows: silicon wafers (Siltronix, France) were coated by electron beam thermal evaporation with a 5 nm thick Cr layer followed by a 30 nm thick Au layer. The gold coated surfaces and gold coated AFM tips (OTR_4, Olympus Ltd., Tokyo, Japan; MLCT, Veeco, USA) were cleaned for 15 min by UV and ozone treatment (Jelight Co.) rinsed with ethanol, dried with a gentle nitrogen flow and immersed overnight in 1 mM solutions of $HS(CH_2)_{17}CH_3$ (Sigma) in ethanol and then rinsed with ethanol. (For detailed information, see Appendix C).

6.2.4 Compound inhibitors

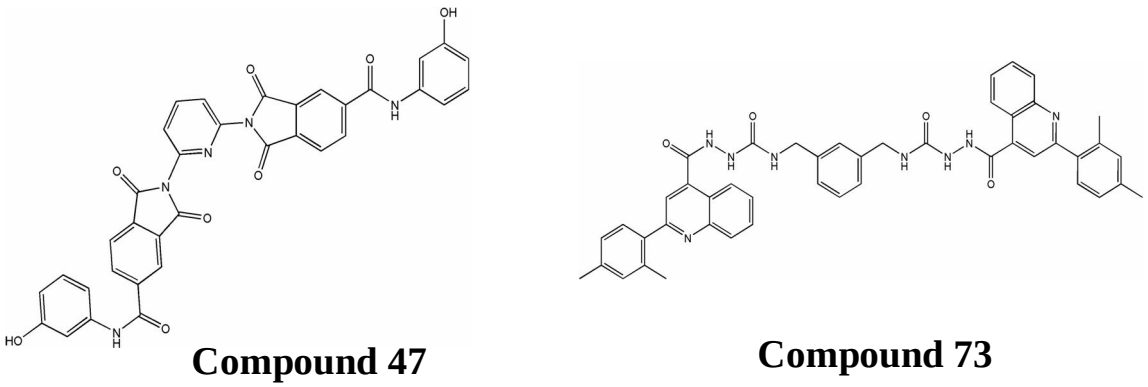

Fig 6.1 Chemical structures of the two selected organic compounds inhibiting *S. epidermidis* biofilm formation: compounds 47 and compound 73, reprinted from[4].

From the library of 76 compounds, compounds 47 and 73 (SPECS Company, Amsterdam, Netherlands) were chosen and used in the study [3,4] , Fig 6.1. The high inhibitory effects of these two compounds are due to their chemical structure. The core structure of the

compounds are: (a) carbonyl and carboxamide functional groups, and (b) a linear array of condensed homocyclic and heterocyclic aromatic ring systems. So compounds 47 and 73 were selected to observe efficient *S. epidermidis* biofilm growth inhibition, and investigate interplay between the hydrophobic, hydrophilic, hydrogen bonding, and perhaps even covalent (the carboxamide group) interactions between the compound molecules and either the substrate surface, the bacterial cell surface, or even the AFM tip surface. Mechanistic details of the interaction are not known, but they have great inhibition effects on biofilm formation.

The purities of the compounds were > 97% according to liquid chromatography mass spectrometry (LC–MS) from the manufacture. All compounds were dissolved in 1% dimethyl sulfoxide (DMSO, Sigma, Germany) due to their limited solubility in water. DMSO itself at this concentration did not affect bacterial biofilm growth[3].

6.2.5 AFM measurements

AFM measurements in Millepore water were performed using a Nanoscope IIIa AFM (Veeco Metrology Group) and oxide-sharpened microfabricated Si_3N_4 cantilevers (Olympus Ltd., Tokyo, Japan). To probe *S. epidermidis* in their native state by AFM, bacteria were immobilized by mechanical trapping into porous polycarbonate membranes (Millipore), with a pore size similar to the bacterial cell size (about 0.8 µm diameter)[8,11]. Filtration was carried out by placing a filter on a vacuum filtration flask; a concentrated cell suspension was then filtered through the polycarbonate membrane by applying a vacuum. After filtration, the polycarbonate membrane was gently rinsed with Millepore water, carefully cut (1 cm × 1 cm) and attached to a round steel sample supporter (Veeco Metrology Group) using a small piece of double-face adhesive tape. We applied MQ water not PBS buffer, because PBS buffer will influence cell surface adhesion and make the force curve indistinguishable. The mounted sample was transferred into the AFM liquid cell while avoiding dewetting. The imaging force was kept as low as possible (~250 pN) to minimize sample damage. (For detailed descriptions see Appendix D)

Both topography and deflection images were recorded as they yield complementary information. Topography images provide quantitative information on sample surface topography (surface roughness and height measurements). Deflection images often exhibit higher contrast of the morphological details and are especially useful for rough surfaces. Real time images were collected with time intervals, for example, every 15 minutes.

6.2.6 Roughness analysis

Surface roughness values of the extracellular ultra structure of cells were taken from high-resolution AFM topography images and calculated by using Gwyddion (free download software). In general, roughness analysis is a relative height analysis. The arithmetic roughness average R_a values and the root mean square roughness R_q were applied to calculate the roughness analysis. R_a and R_q were collected for three 400 nm^2 area on single cells.

The equation[10]: $R_a = \frac{1}{n}\sum_{i=1}^{n}\left|h_i - \langle h \rangle\right|$ (6.1)

$$R_q = \sqrt{\frac{1}{n}\sum_{i=1}^{n}\left(h_i - \langle h \rangle\right)^2} \quad (6.2)$$

was used. n is the number of the data points, R_a is the average distance between the i th height (h_i) to the mean height (h) of all the n data points. R_q is the standard deviation, i.e. the root mean square distance between the i th height (h_i) to the mean height (h) of all n data points.

6.2.7 Adhesion maps and force curves

Adhesion maps were obtained by recording arrays of 16-by-16 force-distance curves over a 400 x 400 nm^2 area, using either bare tips or hydrophobic tips, calculating the adhesion force for each force curve and displaying the value as a gray pixel.

In order to study the elasticity of the stretched molecules, elongation forces were fitted using the wormlike chain (WLC) model[12]. The WLC model is useful to apply in biological polymers, including double-stranded DNA and RNA, unstructured RNA, and unstructured polypeptide (Proteins)[13]. In AFM studies, proteins that behave like continuous deformable rods are generally well described by the WLC model[14,15]. This model describes the polymer as an irregular curved filament, which is linear on the scale of the persistence length l_p, a parameter which represents the stiffness of the molecule. The extension of the molecule is limited by the contour length L_c, i.e., the length of the linearly extended molecule without stretching the molecular backbone. In this model, the force F versus extension x is given by

$$F(x) = k_B T/l_p [0.25(1 - x)/L_c)^{-2} + x/L_c - 0.25] \quad (6.3)$$

Where, k_B is the Boltzmann constant and T the absolute temperature.

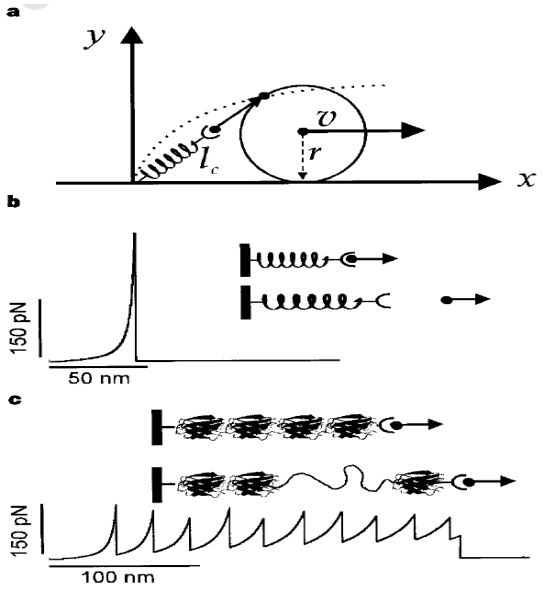

Fig 6.2 A simulation of the protein –ligand bond and force curve. a, During cell rolling, we assume a protein bound to a cell ligand is stretched along a cycloidal path (dotted line) and the cell will move left. The protein is represented by a coil and the ligand which is a black circle near the coil. b, Simulation of a bound 50-nm long protein, without extensible modules, stretched at a speed of 0.2 nm ms^{-1}, predicts a force–extension curve where the protein module is unfolded after a 45-nm extension and at a force of 330 pN. c, At the same pulling speed, the simulated force–extension curve of a cell-bound protein in the

unfolding domains (inset; only four are shown) shows bond breakage Unfolding after modular stretching to 268 nm and at 69 pN. Reprinted from[15].

The WLC model was used to fit the force curves between the hydrophobically modified tips and the unfolding of domains in the cell surface protein construct. The characteristic sawtooth pattern of unfolding can be explained as stepwise increases in the contour length of a polymer whose elastic properties are described by the wormlike chain model (WLC).

6.3 Biofilm growth of the four strains of Staphyloccus epidermidis

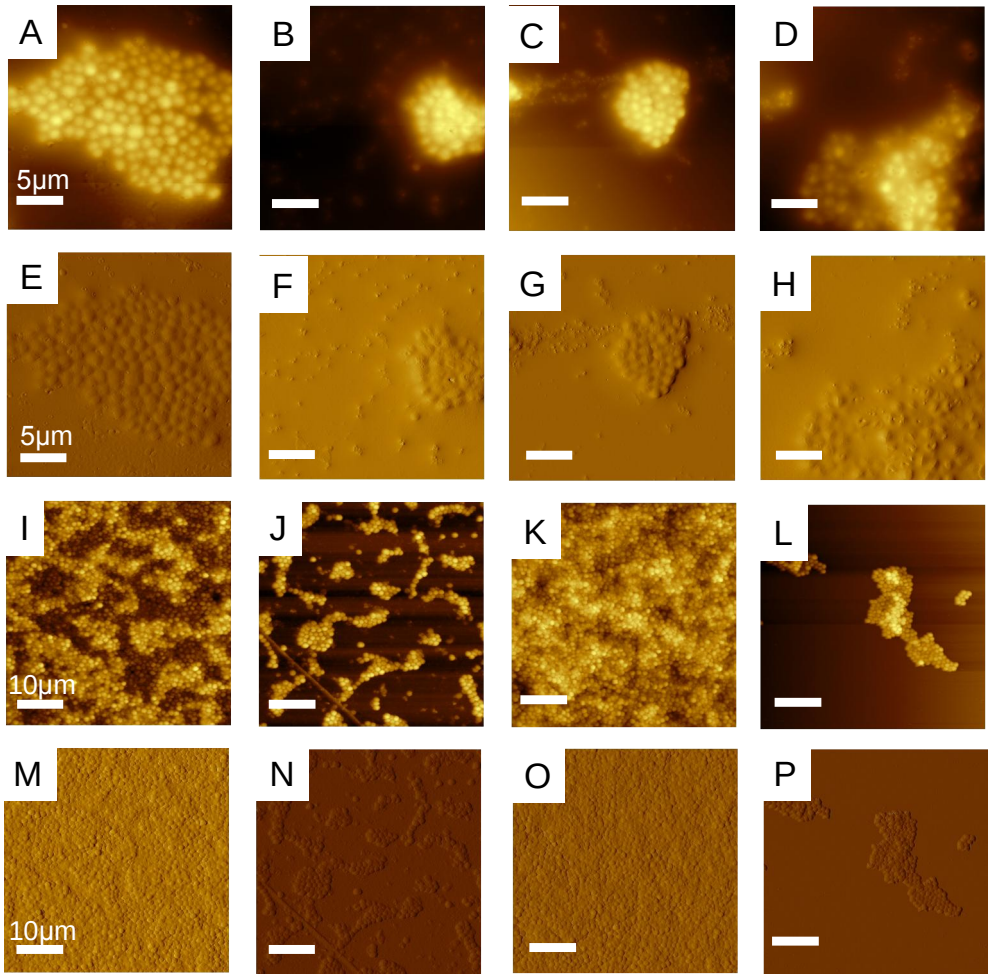

Fig 6.3 Biofilm growth of the four strains of *Staphyloccus epidermidis* on mica for 4 hours and 24 hours imaged in air. A, E, I and M: strain RP62a; B, F, J and N: strain ATCC 12228; C, G, K and O: strain 1457; D, H, L and P: strain 1457 atlE. A, B, C, D, I, J, K and L: topography images; E, F, G, H, M, N, O and P: deflection images. A, B, C, D, E, F, G and H: biofilm grown for 4 hours, scale bar 20 μm ; I, J, K, L, M, N, O and P: biofilm growth for 24 hours, scale bar 40 μm.

Fig 6.3 shows the general biofilm formation of the four *S. epidermidis* strains on mica. RP62a and 1457 are biofilm positive strains and formed biofilms and fully covered the mica surfaces after 24 hours; ATCC 12228 and 1457 atlE are biofilm negative strains and did not form biofilm after 24 hours growth, only a few cells assembled together. The growth differences indicated that the single cell of these four strains may have different surface proteins or surface hydrophobicity.

6.4 Real time imaging of RP62a strains and force measurements

Prior to imaging in aqueous biological media, bacterial cells have to be anchored to the surface in order to withstand the lateral forces from the tip during scanning. Different approaches have been described in the literature to immobilize bacteria. These include treatment of the support with polycations (poly-L-lysine, polyethyleneimine, …) or covalent attachment[16]. To avoid air drying or pretreatment by chemical fixation that could denature the bacteria and contaminate the AFM tips, bacteria were mechanically immobilized onto porous polycarbonate membranes[8]. This method allows live cell imaging in buffer and appears to a very suitable approach[16,17].

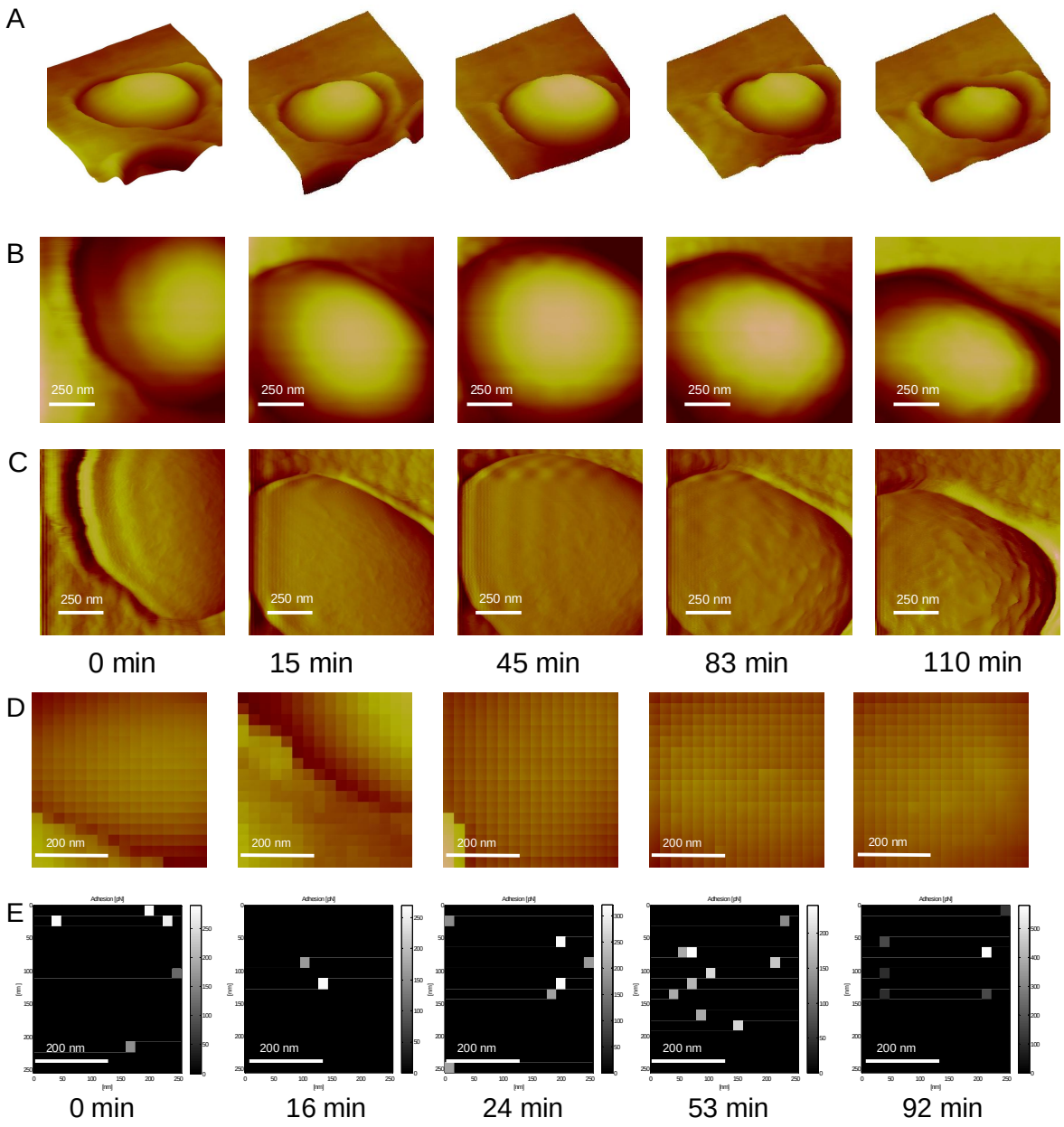

Fig 6.4 A-C Real time imaging of a single *S. epidermidis* RP62a cell in TSB medium at 37°C. Series of five topography images (A,B) and deflection images (C) in TSB media at 37°C showing a single cell trapped into a pore with time 0 min, 15 min, 45 min, 83 min and 110 min. (D,E) Series of low resolution topography images (D) and adhesion force maps (E) using a bare tip with time 0 min, 16 min, 24 min, 53 min and 92 min. Scale bar: A: 2 µm; B and C: 1 µm; D and E: 400 nm.

Strain RP62a is biofilm positive and a model strain of *S. epidermidis*. Single cells were trapped into a polycarbonate membrane (0.8 µm pore size) and imaged in culture media (TSB media at 37°C). The topography and deflection images revealed a homogeneous and smooth surface, Fig 6.4 (A-C). With time, the roughness slightly increases, but there were no big differences in the adhesion properties and few adhesion events using bare MLCT tip (Fig 6.4 D, E). The size of the single cell also seemed to grow and the cell seemed to take off from the polycarbonate membrane (Fig 6.5) or one single cell split into two cells (Fig 6.6). Similar experiments were performed in the same conditions using bare tips and hydrophobically modified tips without showing real differences in adhesion properties and no differences with time.

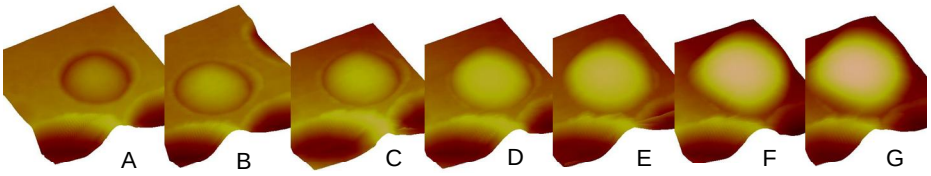

Fig 6.5 Real time topography imaging of a single *S. epidermidis* RP62a cell in TSB media at 37°C. A: 0 min: B: 53 min; C: 63 min; D: 93 min; E: 106 min; F: 123 min; G:143 min. Scale bar: 2µm

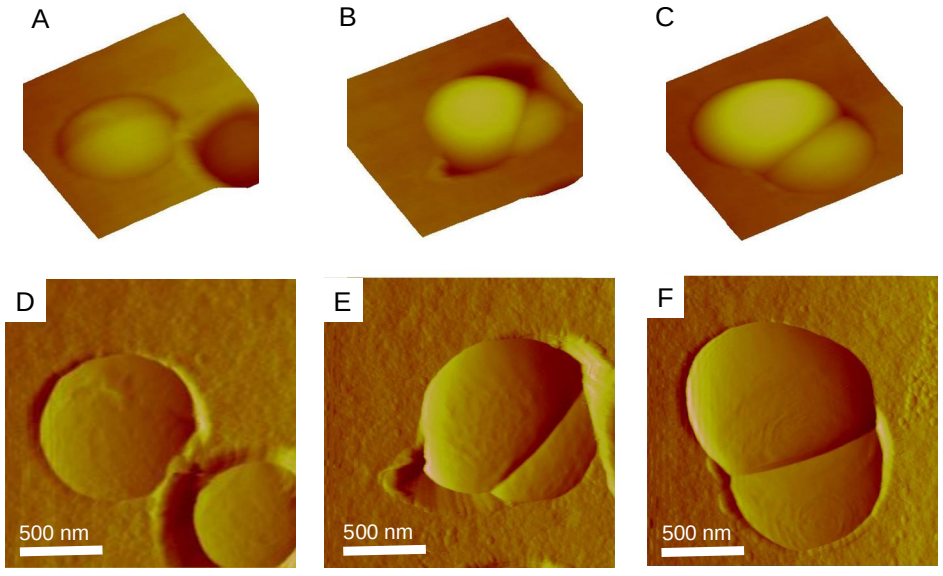

Fig 6.6 Imaging of a single *S. epidermidis* RP62a cell split into two cells in TSB media at 37°C. A, B, C: topography; D,E,F: deflection images. Scale bar: 2µm A and D: cell wall of the single bacteria start to divide into two cells. B, C, E and F: clear cell wells between the two bacteria.

6.5 Ultrastructure of single cells of Straphyloccus epidermidis

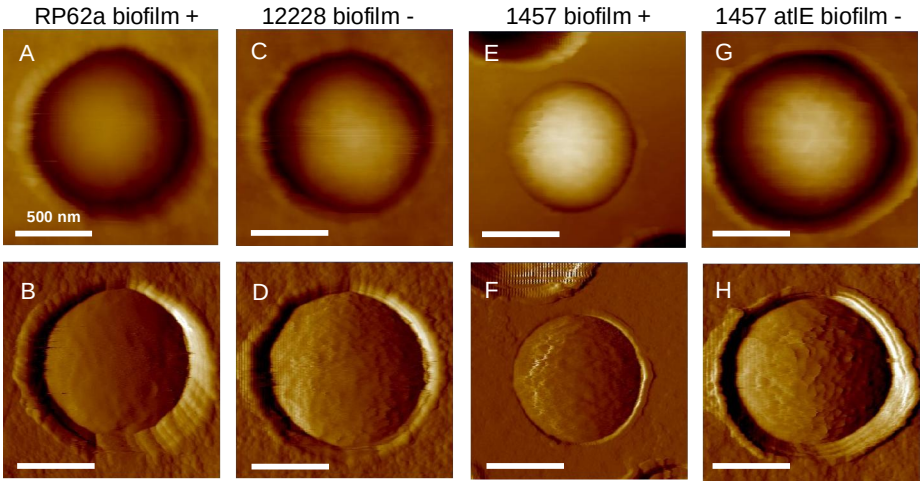

Fig 6.7. Imaging of a single bacterium in its native state. AFM topography (A,C,E,G) and deflection (B,D,F,H) images recorded in Millipore water for RP62a (A,B), 12228 (C,D), 1457 (E,F) and 1457atlE (F,G). Cells were trapped into a porous polycarbonate membrane for noninvasive, *in situ* imaging. Scale bar: 2μm.

The surface topography of the four strains was investigated using high-resolution imaging. Representative images of native bacteria at the exponential (OD_{600} = 0.3, not biofilm forming) growth stage are shown in Fig. 6.7. These images were obtained using small imaging forces (~250 pN) since surface topography is very sensitive to the applied force. Moreover, thermal drift during imaging required that the applied force was adjusted between each recording. Otherwise, the bacteria were removed from the pores by the scanning probe. Due to the large curvature of the cells, the image resolution in the topography mode (Fig. 6.7 A, C, E, G) is fairly poor, while the image obtained in the deflection mode (Fig. 6.7.B, D, F, H) is much more sensitive to fine surface details.

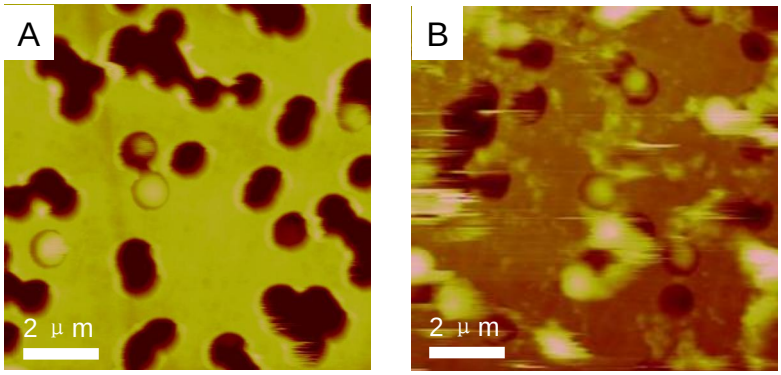

Fig 6.8. Topography images of *S. epidermidis* strain RP62a (suspended solution) A: clear image, it is easy to have high resolution on the cell; B: worse images, including EPS layer, such as protein, DNA or dead cells. Scale bar: 10 μm.

As shown in Fig. 6.7, the topography and deflection images revealed a homogeneous and smooth surface. No differences in the surface texture were noted among the four strains. More specifically, no difference in surface morphology between the biofilm positive and negative strand was found. Instead a sponge-like structure that could be attributed to the surrounding layer of extracellular polymers substance (EPS) including some dead cells, protein and DNA was observed in both cases. In order to obtain high resolution images and force curves, we have to remove the EPS layer using centrifugation and filtration, Fig 6.8. Fig 6.8 A is a clear image and easy to have high resolution on the cell; B is a worse image, including EPS layer, such as protein, DNA or dead cells. If we don't remove the EPS layer properly, AFM tips and modified tips will be easily demaged.

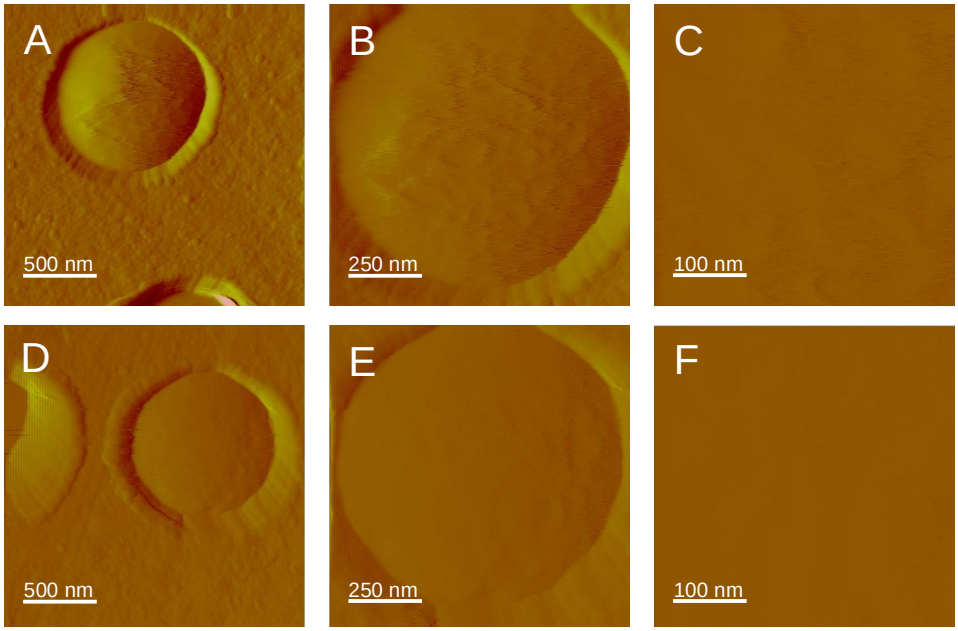

Fig 6.9. High resolution deflection images of *S. epidermidis* strain RP62a biofilm at 16 h (A, B, and C), RP62a suspended solution (D, E and F) Scale bar: A and D: 2 μm, B and E: 1 μm, C and F: 400nm.

The differences between the suspended cells and cells from biofilm formation were also addressed the following experiments. Glass surfaces were used for strain RP62a biofilms growth. After 16 hours of incubation, fully developed biofilms covered the glass surfaces. The biofilm cells on the glass surface were gently washed by Millipore water and collected into a tube, harvested by centrifugation and washed three times with Millipore water. The cells were then immobilized into the porous membrane using the same protocol as above. If we compared the biofilm of 16 hours and single suspended bacteria at the exponential growth stage (OD_{600}=0.3), no differences were apparent. According to the roughness analysis of the two images in Fig 6.9 C and F, the roughness of the former (R_q = 16.4 nm, R_a = 13.6 nm) is just slightly higher than that of the latter one (R_q = 14.2 nm, R_a = 11.7 nm). The roughness of the single cell may therefore not be the driving-force factor of the biofilm formation.

6.6 Adhesive properties

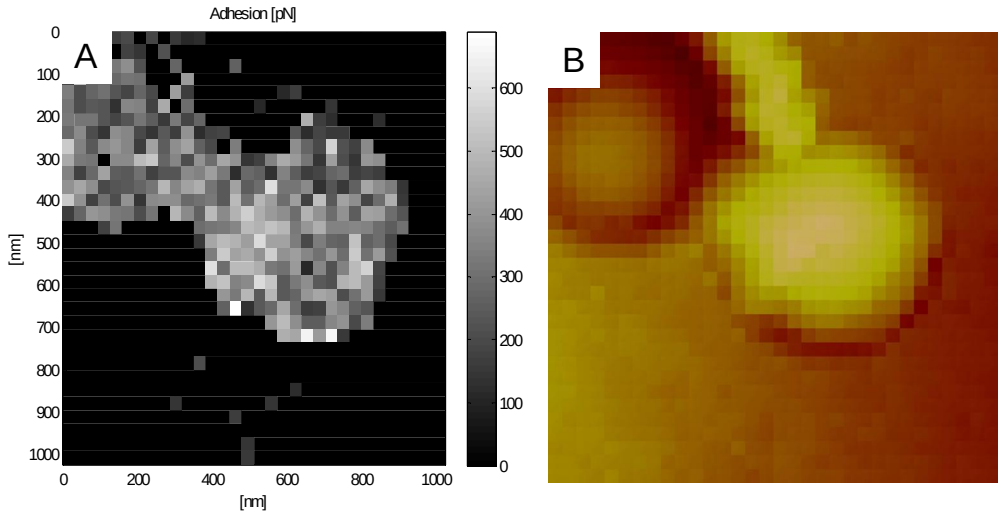

Fig 6.10. An example of adhesion map recorded with silicon tip on *Staphylococcus epidermidis* strain 1457 atlE in Millipore water. Using a maximum applied force of 250 pN. A: adhesion map of two cells on polycarbonate membrane was obtained by arrays of 32-by-32 force –distance curves and defined on an area of 2 μm by 2 μm. B: Low-resolution topography scanning images; Scale bar, A, B: 2 μm.

In addition to recorded images, AFM can provide much more information. AFM can record the force through force curve measurement. This technique can be used to measure the long-range attractive or repulsive forces between the probe tip and the sample surface, such as adhesion and elasticity, and even thickness of adsorbed molecular layers or bond rupture lengths. Force curves (force-versus-distance curve) typically show the deflection of the free end of the AFM cantilever as the fixed end of the cantilever is brought vertically towards and then away from the sample surface. In this study, adhesion forces between the bare or hyhrophobically modified tips and the bacterial cell surfaces were measured. When the adhesion forces are measured continually from left to right, from up to down , line by line, we could obtain the adhesion map that characterizes the adhesion force between the tips and the target surfaces.

Fig 6.10 shows an adhesion force map and a low-resolution topography image. Fig 6.10A shows that most of the adhesion between the bare tip and surface came from the cell surface according to the left force scale bar from 0 pN (black) to around 700 pN (white).

There was almost no adhesion between the bare tips and the polycarbonate membrane. The polycarbonate membrane had totally different characters from the cell surface. It was therefore easy to identify the cell surface and polycarbonate membrane. The adhesion map was a very good way to understand the adhesion conditions of the single cell surface. In the following experiments, we will use adhesion force maps and adhesion histograms to investigate the different character of the surfaces of the four strains.

Adhesive properties were first investigated by force measurements on the four different strains (RP62a, 12228, 1457 and 1457atlE) using bare silicon nitride tips (Fig. 6.11). To probe different locations, adhesion maps were recorded on the top of cells trapped in the porous membrane[8,11]. Imaging was first performed to localize individual cells. A matrix of 16-by-16 force-distance curves was then defined on an area of 400 nm by 400 nm. In general, there are 256 force–distance curves from one image. The adhesion force was then calculated for each force curve and force values displayed as a gray pixel on an adhesion map. The more tendency to white color, the higher is the force value, (Fig. 6.11 A, C, E, G). Adhesion events were frequently detected and adhesion maps reveal homogeneous distribution of adhesion events on the whole cell. In Fig 6.11 B,D, F and H , the first column from left side means the percentage of the non-adhesion events. The adhesion frequencies were significantly higher for biofilm positive strains than for biofilm negative strains. (RP62a: 92.5%, 12228: 74%, 1457: 99.5% and 1457atlE: 45%). This matches that RP62a and 1457 form biofilms with higher adhesion event. Typical force-distance curves are shown on Fig. 6.11 B, D, F and H. In general, the curves showed essentially single adhesion events, along with elongation forces and rupture lengths below 50 nm. These peaks are attributed to non-specific, physical adsorption of the cell surface molecules to the AFM tip and given the observed short rupture lengths, corresponding to short proteins and polysaccharides rather than to long stretchable polysaccharides. In some cases the curves obtained showed multiple adhesion peaks with much longer rupture distances, typically in the 100-300 nm range, revealing macromolecular stretching, Fig 6.11 F force curve with red star.

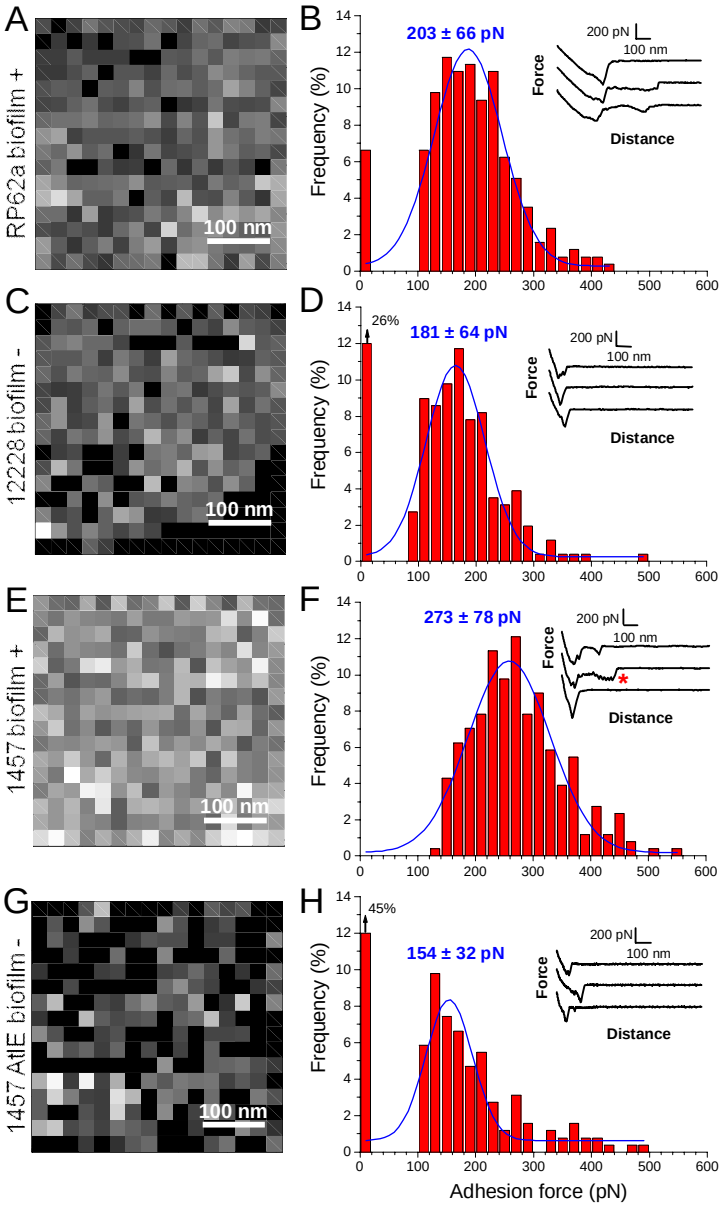

Fig 6.11. Adhesion force maps (400 nm x 400 nm) recorded with silicon tips on *Staphylococcus epidermidis* strain RP62a (A) , ATCC 12228 (C), 1457 (E) and 1457atlE (G) using a maximum applied force of 250 pN. (B, D, F, G) Adhesion histograms and representative force curves (inset top right) obtained for the four strains. The first red column of (B, D, F, G) shows the percentage of the adhesion frequency (force less than 90 pN) is 7.5%, 26%, 0.5% and 45% ; F red star: multiple adhesion peaks with much longer rupture distances.

Fig 6.11 shows the typical adhesion map for each strain. The average adhesion force is obtained from adhesion maps of ten different cells for each strain. The force histograms show that the mean adhesion forces are slightly higher for biofilm positive than for biofilm negative strains: 200 ± 70 pN and 270 ± 80 pN for biofilm positive strains (RP62a and 1457), and 180 ± 60 pN and 150 ± 30 pN for non-biofilm-forming strains (12228 and 1457atlE). Such small differences can hardly explain biofilm formation properties of these different strains. Moreover, the mean adhesion forces are weak compared to values obtained under similar conditions for other microorganisms[18]. It also notice that the unfolding events were much more frequently observed for biofilm positive strains (~ 15% among adhesive force curves) than for biofilm negative ones (less than 1%), see Fig 6.11 F.

6.7 Hydrophobic properties

Hydrophobically modified tips were then used to probe the hydrophobic character of the four strains. Fig 6.12 A-H show typical adhesion maps, adhesion histograms, and representative force curves obtained for RP62a (Fig. 6.12 A, B), 12228 (Fig. 6.12 C, D), 1457 (Fig. 6.12 E, F) and 1457atlE (Fig. 6.12 G, H) strains. The frequency of the adhesion events for the three strains is around 50%; only 12228 is higher, i.e. around 90%. We also calculated the mean adhesion force for every strain using 10 cells. The adhesion maps and adhesion forces were rather homogeneously distributed across the cell surfaces but the mean adhesion forces were lower on biofilm positive strains than on biofilm negative strains (typically 150 pN (RP62a and 1457) versus 200 pN (12228 and 1457atlE)). It was a surprise that there is no increase of the mean adhesion forces with hydrophobic tips compared to the values obtained on the same strains with bare tips (Fig. 6.12). If the strains have a hydrophobic character, large adhesion forces are generally measured between hydrophobic tips and hydrophobic cells[19]. For example, mean adhesion forces of about 3 nN between hydrophobic tips and the surface of *Mycobacterium bovis*[19], which is covered with hydrophobic mycolic acids were reported. These results indicate that the four *Staphylococcus* strains are not hydrophobic, and thus that hydrophobic forces are not the driving forces for adhesion as could be observed for other microorganisms[19,20]. Another possibility is that there might be a potential

contamination of the hydrophobic tips during the experiments – e.g. by loosely bound polymers - that could lead to smaller detected forces.

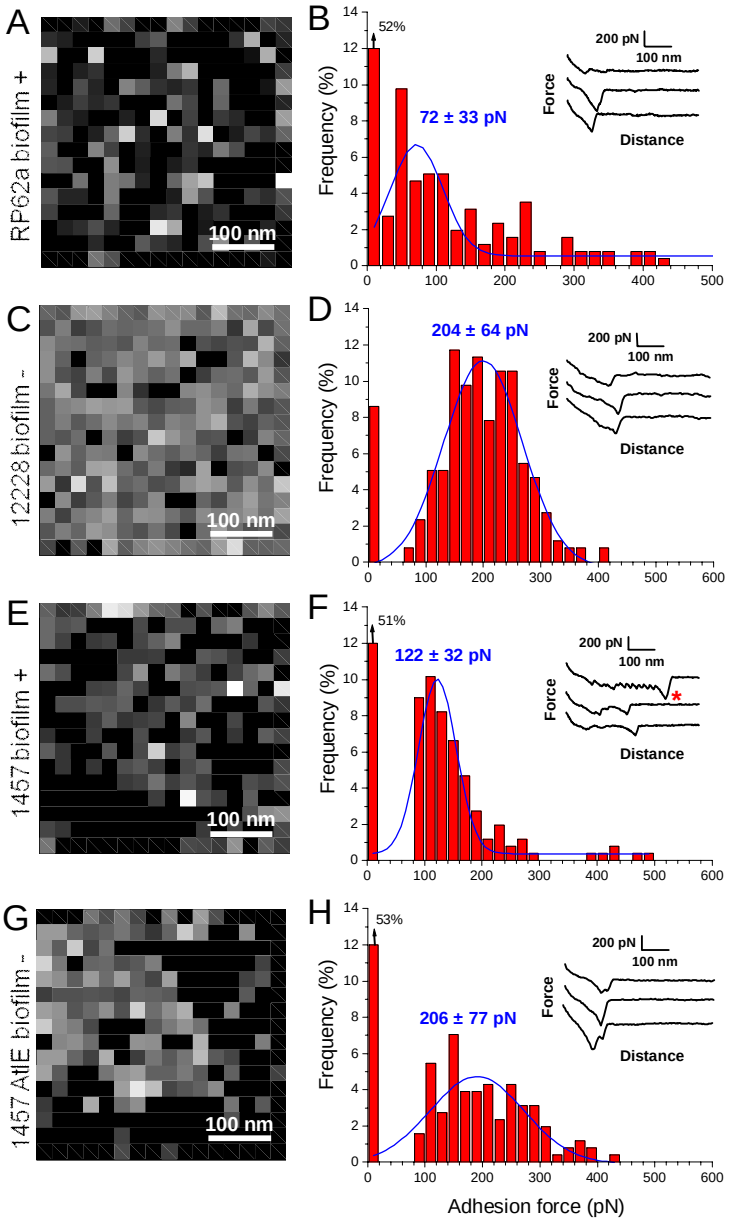

Fig 6.12. Adhesion force maps (400 nm x 400 nm) recorded with hydrophobically modified tips on *Staphylococcus epidermidis* strain RP62a (A) , ATCC 12228 (B), 1457 (C) and 1457atlE (D) using a maximum applied force of 250 pN. (B, D, F, G) Adhesion histograms and representative force curves (inset) obtained for the four strains. The first red column of (B, D, F, G) shows the percentage of the adhesion frequency (force less than 90pN) is 52 %, 8 %, 51 % and 53 % ; F red star: multiple adhesion peaks with much longer rupture distances.

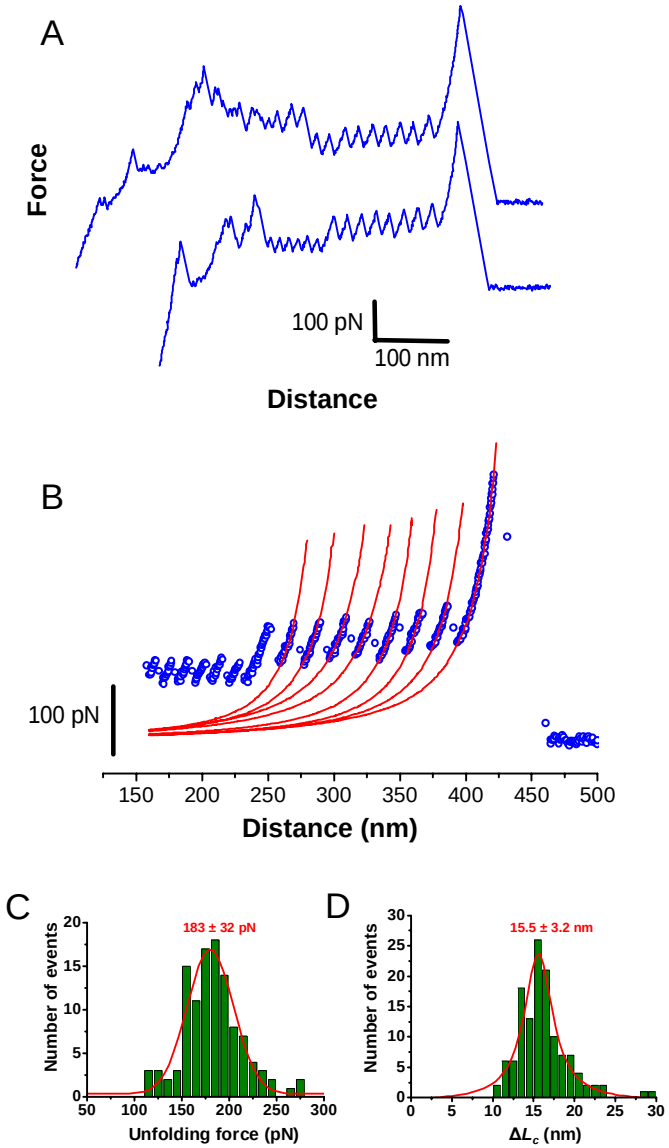

Fig 6.13. A: Representative force-distance curves obtained with hydrophobically modified tips on *Staphylococcus epidermidis* strain RP62a. Typical force-distance curve (open circles) show several peaks corresponding to the unfolding of domains in the cell surface protein construct. The last peak corresponds to the detachment of the protein from the cantilever. B: Force peaks were well described by the worm-like chain model (solid lines), using a persistence length of 0.4 nm. C: Histogram of peak unfolding forces (n = 115 force curves) and D: distribution of the change in contour length between consecutive force peaks ΔL_c (n = 129 force curves).

We observed the sawtooth-like pattern in force curves with either bare silicon nitride tips or hydrophobic tips (see red stars in Fig. 6.11 and 6.12, Fig 6.13A). Such patterns have been widely observed when pulling on several isolated proteins including titin[14], tenascin[15], spectrin[21] or Als adhesion protein on live cells[22]. This sawtooth-like pattern is due to force-induced conformational changes: when the tip contacts the polypeptide chain, every tiny step changes successively from a folded to an unfolded, extended state. *S. epidermidis* has some cell-surface proteins containing sequence repeats, and the sequence domain repeats of these proteins (Aap and SasG) are known as G5 domains[23]. We are not sure that the observed sawtooth-like force curves are from either Aap or SasG, or from both of them. We can take an example of G5 domains from Aap proteins, which are composed of 5 distinct regions, including the B-repeat region with a variable number (5 to 17) of nearly identical 128-aa repeats. According to the number of successive small peaks detected in the sawtooth pattern, the number of repeats ranges from 3 to 15. That variability depends on the tip picking on any domain of the protein chain. Sometimes, lots of small peaks were observed but probably because more than one protein molecule was stretched by the tip. The force peaks are well matched by the worm-like chain model, (Equation 6.3), e.g. using a persistence length of 0.4 nm, which is typical for proteins[14] (Fig. 6.13 B). The sawtooth-like force curves thus show that there were unfolding proteins on the cell surface.

115 sawtooth-like force curves were chosen to characterize and analyze the unfolding peaks by histograms, (Fig. 6.13 C). The mean adhesion force is around 180 pN, which could specifically correspond to unfolding of β-sheets that compose domains of *S. epidermidis* cell-surface proteins[23]. Previous experiments showed that binding forces below 100 pN are observed during unfolding of α-helices[21,24,25], while much larger forces (150 to 300 pN) are required to unfold domains with β-sheets, like immunoglobulin or fibronectin domains in titin and tenascin[14,15]. In addition, the last peak often shows larger unbinding force compared to the previous small peaks due to the detachment of the protein from the tip. In analyzing 129 similar sawtooth-like pattern peaks and using by equation 6.3, the change in contour length between consecutive peaks was found to be constant, $\Delta L_c = 15.5 \pm 3.2$ nm (Fig. 6.13 D).

In summary, the unfolding events were much more frequently observed for biofilm positive strains (~ 15% among adhesive force curves) than for biofilm negative ones (less than 1%). That is because Aap proteins or related repeat proteins were either lacking or less exposed on biofilm negative strains. Therefore, the remarkable mechanical properties of these proteins are necessary be investigated.

6.8 The effects of chemical inhibitors on nanoadhesion

Force spectroscopy with bare tips was finally used to investigate the inhibitor effects of the two chemical compounds (47 and 73) on the two biofilm positive strains (Fig. 6.14). In a first approach, cells were cultured until exponential growth conditions were reached (OD_{600} = 0.3). Cells were then collected, washed three times with water and filtered to trap the cells into the porous polycarbonate membrane. The two compounds were added into the liquid cell during the AFM scanning experiments (compounds were dissolved in DMSO and diluted to a concentration of 200 µM, DMSO with compounds was diluted 100 times in Millipore water before use). No difference compared to similar experiments in pure Millipore water (data not shown) could be detected. One reason might be that the effects of the compounds are bound to the surface of the bacteria, and thus not detected by AFM.

The chemical compounds (the same concentration before) were next added during the growth of the strains. Compounds were added to the TSB medium and cells cultured until exponential growth conditions were achieved (OD_{600} = 0.3). Cells were then collected, washed three times and filtered to trap the cells into the porous membrane. As seen on Fig 6.14, similar major effects were clearly observed for the two compounds on the two strains: in each case, the number of adhesion events clearly decreased (see adhesion maps and adhesion frequency on the adhesion force histograms) compared with results obtained for pure water (Fig. 6.11). These results show that compounds 47 and 73 modify the nanoscale adhesion properties of biofilm-forming strains.

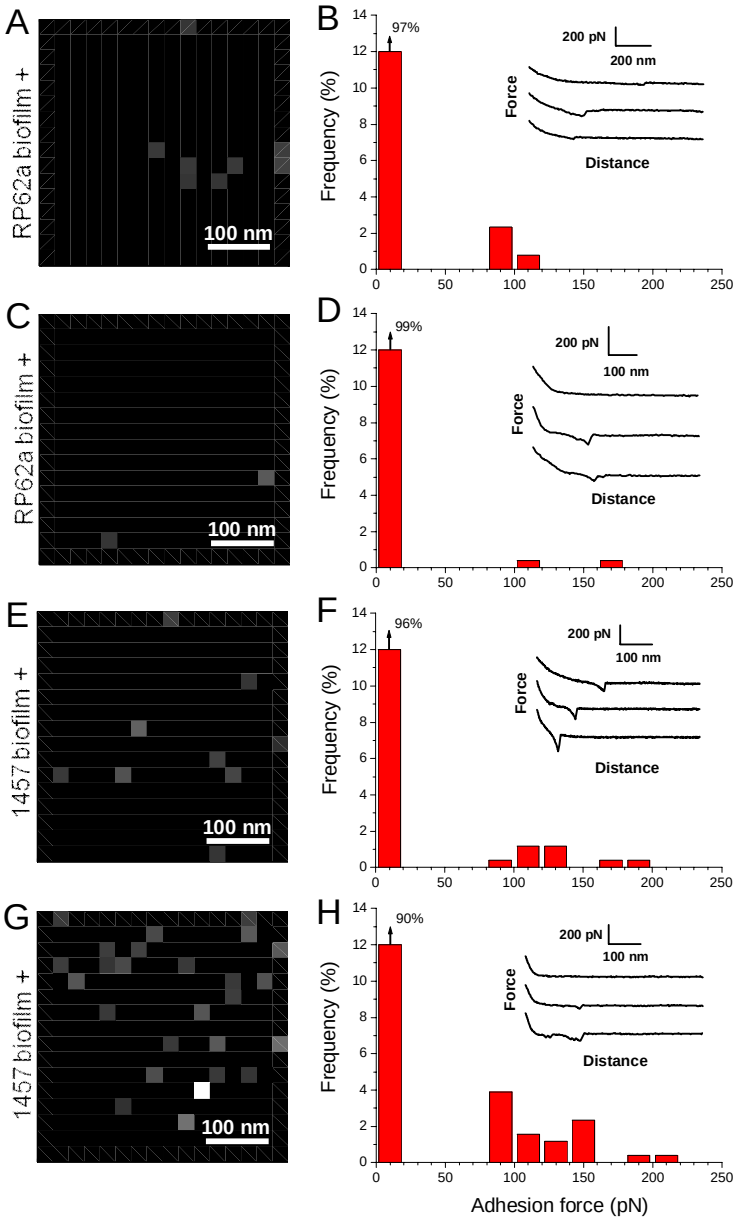

Fig 6.14 Adhesion force maps (400 nm x 400 nm) recorded with silicon tips on *Staphylococcus epidermidis* strain RP62a (A, B), and 1457 (C, D) using a maximum applied force of 250 pN after treatment with compounds 47 (A, C) and 73 (B, D). (B, D, F, G) Adhesion histograms and representative force curves (inset) obtained for the two strains.

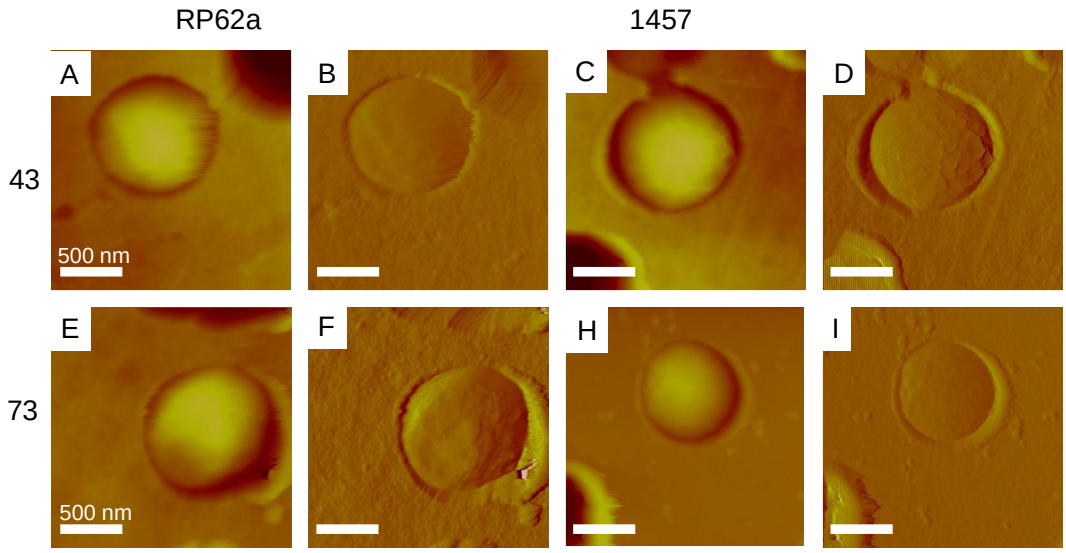

Fig 6.15. High-resolution images of *S. epidermidis* with compounds 47 and 73 in TSB medium. Strain RP62a (A, B, E and F), 1457 (C, D, H and I); cell treated with compounds 47 (A, B, C and D), cell treated with compounds 73 (E, F, H and I); topography images (A, E, C and H) and deflection images (B, F, D and I), Scale bar: 2μm.

Subtle modifications were observed on high-resolution images, Fig 6.15. It seemed that the cells were not intact round. It is common for bacterial cells to lose shape of the cell on cell lysis. In the polycarbonate membrane, there were many more dead cells fragments observed in Fig 6.8B. The result showed that the two compounds had inhibition effects during the biofilm growth and bacterial growth.

6.9 Conclusion

We have studied two biofilm positive and two biofilm negative strains of *S. epidermidis* in the pore-confined state directly in aqueous media. There are no big differences among the physical properties of the four strains. Two molecular inhibitor compounds (compounds 47 and 73) contacted with the *S. epidermidis* were chosen to investigate the efficient of inhibitors in *S. epidermidis* biofilm formation and growth.

AFM imaging showed no detectable differences among the four strains. Very similar adhesion properties of the four strains were also found when bare hydrophilic silicon nitride tips were used. Adhesion forces were weak compared with some other organisms. Adhesion maps and force curves of the four strains showed lower adhesion forces when hydrophobically modified tips were used and no increase in the mean adhesion forces was observed. These results suggest that hydrophobic effects are not the primary driving force towards adhesion.

Sawtooth patterns, although only with a few "teeth" were observed for all the four strains on pulling by either bare silicon nitride tips or hydrophobically modified tips. Sawtooth patterns appear on unfolding of the proteins on the cell surfaces. These dynamic effects were displayed much more frequently for biofilm positive than for biofilm negative strains .

When either of the two molecular inhibitors was added directly to the pore-confined target samples, no immediate effects on the adhesion were observed. Drastic decreases of the numbers of adhesion events were, however, observed for both biofilm positive strains when the inhibitor molecules had been added *during* the bacterial growth phase. This observation is also notable as it suggests that the inhibitory effect is rooted as much in molecular interactions on the bacterial cell surface as in interactions on the solid substrate surface.

This study provides a new way to study differential adhesion patterns of bacterial cells and mechanistic elements of molecular compound inhibition of bacterial biofilm growth by AFM.

Reference

1. Otto, M. *Staphylococcus epidermidis* the accidental pathogen. *Nature Review Microbiology*, **2009**, 7: 555 -567.
2. Gill, S. R.; Fouts, D. E.; Archer, G. L.; Mongodin, E. F.; DeBoy, R. T. ; Ravel, J.; Paulsen, I. T.; Kolonay, J. F.; Brinkac, L.; Beanan, M.; Dodson, R. J.; Daugherty,

S. C.; Madupu, R.; Angiuoli, S. V.; Durkin, A. S.; Haft, D. H.; Vamathevan, J.; Khouri, H.; Utterback, T. ; Lee, C.; Dimitrov, G.; Jiang, L. X.; Qin, H. Y.; Weidman, J.; Tran, K.; Kang, K.; Hance, I. R.; Nelson, K. E. and Fraser, C. M. Insights on Evolution of Virulence and Resistance from the Complete Genome Analysis of an Early Methicillin-Resistant *Staphylococcus aureus* Strain and a Biofilm-Producing Methicillin-Resistant *Staphylococcus epidermidis* Strain. *Journal of Bacteriology*, **2005**, 187: 2426-2438.

3. Qin, Z. Q.; Zhang, J.; Xu, B.; Chen, L. L.; Wu, Y. ; Yang, X. M. ; Shen, X.; Molin, S.; Danchin, A.; Jiang, H. L. and Qu, D. Structure-based discovery of inhibitors of the YycG histidine kinase: New chemical leads to combat *Staphylococcus epidermidis* infections. *BMC Microbiology*, **2006**, 6: 1-18.
4. Qin, Z.; Zhang, J.; Hu, Y.; Chi, Q.; Mortensen, N. P.; Qu, D.; Molin, S. and Ulstrup, J. Organic compounds inhibiting *S. epidermidis* adhesion and biofilm formation. *Ultramicroscopy*, **2009**, 109: 881-888.
5. Qin, Z.; Yang, X. ; Yang, L.; Jiang, J. ; Ou, Y.; Molin, S. and Qu, D. Formation and properties of *in vitro* biofilms of ica-negative *Staphylococcus epidermidis* clinical isolates. *Journal of Medical Microbiology*, **2007**, 56: 83-93.
6. Qin, Z.; Ou, Y.Z.; Yang, L.; Zhu, Y.L.; Tolker-Nielsen, T.; Molin, S. and Qu, D. 2007. Role of autolysin-mediated DNA-release in biofilm formation of *Staphylococcus epidermidis*. *Microbiology*, **2007**, 153: 2083-2092.
7. Heilmann, C.; Hussain, M.; Peters, G. and Gotz, F. Evidence for autolysin-mediated primary attachment of *Staphylococcus epidermidis* to a polystyrene surface. *Molecular Microbiology*, **1997**, 24: 1013-1024.
8. Kasas, S. and Ikai, A. A Method for Anchoring Round Shaped Cells for Atomic-Force Microscope Imaging. *Biophysical Journal*, **1995**, 68: 1678-1680.
9. Hu, Y.; Ulstrup, J.; Zhang, J.; Molin, S. and Dupres, V. Drug effect on *S. epidermidis* adhesion investigated by AFM. *Physical Chemistry Chemical Physics*, **2011**, 13 (21): 9995-10003.
10. Cross, S. E. ; Kreth, J. ; Zhu, L. ; Qi, F. ; Pelling, A. E. ; Shi, W. and Gimzewski, J. K. Atomic force microscopy study of the structure-function relationships of the biofilm-forming bacterium *Streptococcus mutans*. *Nanotechnology*, **2006**, 17: 1-7.

11. Dufrêne,Y.F.; Boonaert, C.J.P. ; Gerin, P.A. ; Asther, M.; Rouxhet, P.G. Direct probing of the surface ultrastructure and molecular interactions of dormant and germinating spores of *Phanerochaete chrysosporium*. *Journal of Bacteriology*, **1999**, 181:5350-5354.
12. Janshoff, A.; Neitzert, M.; Oberdorfer, Y. and Fuchs, H. Single molecule spectroscopy of polymers and biomolecules. *Angewandte Chemie-International Edition*, **2000**, 39: 3213-3237.
13. Bustamante, C.; Marko,J. F.; Siggia, E. D. and Smith, S. Entropic elasticity of lambda-phage DNA. *Science*, **1994**, 265: 1599-1600.
14. Rief, M.; Gautel, M.; Oesterhelt, F. ; Fernandez, J. M. and Gaub, H. E. Reversible Unfolding of Individual Titin Immunoglobulin Domains by AFM. *Science*, **1997**, 276: 1109-1112.
15. Oberhauser, A. F.; Marszalek, P. E.; Erickson, H. P. and Fernandez, J. M. The molecular elasticity of the extracellular matrix protein tenascin. *Nature*, **1998**, 393: 181-185.
16. El Kirat, K.; Burton,I.; Dupres, V. and Dufrêne, Y. F. Sample preparation procedures for biological atomic force microscopy. *Journal of Microscopy*, Oxford, **2005**, 218: 199-207.
17. Vadillo-Rodriguez,V.; Busscher, H. J. ; Norde, W.; De Vries, J. ; Dijkstra, R. J. B.; Stokroos, I. and Van der Mei, H. C. Comparison of Atomic Force Microscopy Interaction Forces between Bacteria and Silicon Nitride Substrata for Three Commonly Used Immobilization Methods, *Applied and Environmental Microbiology*, **2004**, 70: 5441-5446.
18. Abu-Lail, N. I. and Camesano, T. A. Specific and Non-specific Interaction Forces between Escherichia coli and Silicon Nitride, Determined by Poisson Statistical Analysis. *Langmuir*, **2006**, 22: 7296-7301.
19. Alsteens, D.; Dague, E.; Rouxhet, P. G.; Baulard A. R. and Dufrêne, Y. F. Direct measurement of hydrophobic forces on cell surfaces using AFM. *Langmuir*, **2007**, 23: 11977-11979.

20. Dague, E.; Alsteens, D.; Latge, J. P. ; Verbelen, C.; Raze, D.; Baulard, A. R. and Dufrêne, Y. F. Chemical force microscopy of single live cells, *Nano Letters*, **2007**, 7: 3026-3030.
21. Rief, M. Pascual, J.; Saraste, M. and Gaub, H. E. Single molecule force spectroscopy of spectrin repeats: low unfolding forces in helix bundles. *Journal of Molecular Biology*, **1999**, 286: 553-561.
22. Alsteens, D.; Dupres, V.; Klotz, S. A. ; Gaur, N. K.; Lipke, P. N. and Dufrene, Y. F. Unfolding individual Als5p adhesion proteins on live cells. *ACS Nano*, **2009**, 3: 1677-1682.
23. Conrady, D.G., Brescia, C.C., Horii, K., Weiss, A.A., Hassett, D.J., and Herr, A.B. A zinc-dependent adhesion module is responsible for intercellular adhesion in staphylococcal biofilms. *Proceedings of the National Academy of Sciences of the United States of America*, **2008**, 105: 19456-19461.
24. Janovjak, H.; Struckmeier, J.; Hubain, M.; Kedrov, A.; Kessler, M. and Muller, D. J. *Structure*, **2004**, 12: 871-879.
25. Lee, G.; Abdi, K.; Jiang, Y.; Michaely, P.; Bennett, V. and Marszalek, P. E. Nanospring Behavior of Ankyrin repeats. *Nature*, **2006**, 440: 246-249.

Chapter 7 Interfacial Electrochemical Electron Transfer Processes In Bacterial Biofilm Environments on Au (111)

7.1 Introduction

In chapter 6, atomic force microscopy (AFM) was used to investigate the adhesion properties of bacterial biofilm at the single cell level in liquid. In this chapter, we address the bacterial biofilms in a different way. AFM combined with electrochemistry was used to study biofilms of the bacterial *Streptococcus mutans* (*S. mutans*). This is a new way of addressing biofilm structure and dynamics in the natural aqueous media, and adds other aspects to the chemical as well as cell surface properties important in biofilm formation and growth, particularly in the early stages of biofilm formation and adhesion[1-9].

S. mutans is a class of Gram-positive cocci strongly implicated as the principal etiological agent in human dental caries formation. In its growth pattern *S. mutans* exhibits an initial sucrose independent attachment phase, followed first by cell-cell aggregation, then by sucrose stimulated biofilm stabilization, and finally by the mature biofilm stage in the ultimate biofilm matrix.[10] As the most cariogenic pathogens, *S. mutans* is highly acidogenic, producing short-chain carboxylic acids which dissolve even hard tissues such as dental enamel and dentine[2]. *S. mutans* also ferment sucrose to produce glucans, which are insoluble extracellular polysaccharides (EPS) via three glucosyltransferase systems[11], which enhances bacterial adhesion to the tooth surface[4,12]. The natural *S.mutans* growth habitat is non-conducting calcium phosphate base dental surface, while the substitutional dental material can be gold or the ceramics. *S. mutans* is a safe bacterial strain and previous studies showed *S.mutans* with high-resolution imaging, and force spectroscopy on different kinds of surfaces [5,11,13,14]. *S.mutans* was therfore chosen for its potential connection with gold surfaces is covered with biofilms.

High-resolution imaging, force measurements, and force spectroscopy specifically of *S. mutans* on different kinds of surfaces have been reported [5,11,13,14]. These studies have included the relationship between tips and bacterial cells, at the level of the single

bacterium and bacterial sub-structural surface units, and the forces between the bacteria and the solid surface, mediated by the extracellular polysaccharide or DNA-based matrix[15,16]. These non-covalent forces take a variety of different "specific" and "non-specific" forms (hydrophilic/hydrophobic, gene/antigene, van der Waals, hydrogen bonding, electrostatic). The highly specific spatial distribution of electrostatically charged or hydrogen bonding bacterial, protein, DNA, and polysaccharide surface groups involved in the bacterial biofilm adhesion makes electrostatic forces particularly important.

Electrochemical studies of whole biological cells immobilized on electrode surfaces using cyclic voltammetry (CV)[17-24], impedance spectroscopy[19], and infrared reflectance spectroscopy[20] have been reported. Redox proteins in the bacterial outer membrane are apparently close enough to the bacterial surface that they can establish good electronic contact with the electrode surface. These studies bring insight, for example, of the operation of bacterial membrane respiratory redox metalloproteins, the bacterial surface binding, bacterial coverage, and perhaps growth dependence on the electric field in the electrode/ bacterial/aqueous interfacial region. The hydrogen adsorption signal on platinum electrodes has also been used as molecular monitors of bacterial cell coverage of metallic electrode surfaces[17].

The present AFM-electrochemical approach is to study electrostatic interactions between the bacteria and both the electrode surface and electroactive probe molecules. It differs from previous approaches in the following ways:

1. Single-crystal, atomically planar Au(111)-electrode surfaces were used both for bacterial growth and for the AFM and electrochemical studies[25,26]. These surfaces are structurally well-defined and the surface structure can be controlled at the atomic level using different low-index electrode surfaces ((111), (110), (100)). The *S. mutans* biofilms actually grow on non-conducting calcium phosphate-based dental surfaces[5]. We choose the (atomically planar) metal surfaces due to the electrochemical view, which can provide a variety of different pure and modified, electrically charged and neutral, hydrophobic

and hydrophilic surfaces. AFM has been used to observe *S. mutans* growth, without electrochemical potential control on mica and Au(111). The growth followed different patterns at the initial growth stages while the final biofilm on the two surfaces after 24 h appeared quite similar.

2. Six transition metal complexes were used as simple redox probes. These were chosen to compare positively ($[Ru(NH_3)_6]^{3+/2+}$, $[Co(phen)_3]^{3+/2+}$ and $[Co(terpy)_2]^{3+/2+}$. (phen = 1,10-phenanthroline; terpy = 2,2',2"-terpyridine) and negatively charged ($[Fe(CN)_6]^{3-/4-}$. $[IrCl_6]^{3-/4-}$), purely inorganic ($[Ru(NH_3)_6]^{3+/2+}$ and $[Co(NH_3)_6]^{3+/2+}$) and aromatic ligand-based ($[Co(phen)_3]^{3+/2+}$and $[Co(terpy)_2]^{3+/2+}$), and differently metal-based ($[Ru(NH_3)_6]^{3+/2+}$ and $[Co(NH_3)_6]^{3+/2+}$) molecules. All the six probes have equilibrium redox potentials suitable for cyclic voltammetry (CV) without Au-oxidation and –reduction and dihydrogen evolution and dioxygen reduction. This kind of electrochemical probes have shown to be suitable monitors of electrostatic field effects in the interfacial electrode / bacterial / aqueous region, of probe binding to the bacterial surface, and of bacterial growth inhibition.

3. There are two other perspectives. One is that the CV behaviour of these probe molecules are sensitive to the presence of bacteria on the Au(111)-electrode surface. The redox probes are therefore monitors of bacterial presence on the surface. The other perspective is that although the natural *S. mutans* growth environment is non-conducting dental surfaces, the conducting surfaces of Au- and Ag/Hg-fillings are electrochemical surfaces and therefore in a certain sense represented by the model systems introduced. Even the dental material itself is electroactive by being piezoelectric.

7.2 Experimental section

7.2.1 Bacterial strains and growth medium

A *S. mutans* strain (ATCC 25175) was a gift from Laboratory of Microbiology, Department of Odontology, Faculty of Health Sciences, University of Copenhagen

(laboratory technician Natalia Christiansen). *S. mutans* was stored in Brain Heart Infusion broth (BHI) medium at -80 ^{o}C and incubated in BHI broth shaken at 37 ^{o}C overnight.

7.2.2 Cultivation of biofilms on solid surfaces

Two solid surfaces, mica and single-crystalline Au(111) were used for growing biofilms. 2.0 ×1.0 cm^2 Mica (Doll Artist's Workshop, Gardnerville, USA) sheets were cut and freshly cleaved by tape on both sides. Prior to use, they were sterilized by immersion into sodium hypochlorite solution (0.5 %) for 2 h. The mica slices were then washed three times with sterilized Millipore water, autoclaved at 121 ^{o}C and 15 psi for at least 30 min and immersed into a Petri dish (Plastiques-Gosselin, France) containing 10 ml BHI medium. Au(111)-electrode surfaces were used either in the form of bead electrodes prepared by the method of Hamelin[25,26], or as 12 or 14 mm diameter Au(111)-discs (Surface Preparation Lab, Netherlands). The Au(111)-surface quality was checked by voltammetry according to the method of Hamelin[26]. Before use, Au (111) was annealed in a hydrogen flame, quenched in Millipore water saturated with hydrogen gas and transferred to freshly prepared BHI medium in a Petri dish. *S. mutans* was cultivated on Au (111) and on mica in BHI media for 5 days and sampled by AFM after suitable time periods (1 h, 2 h, 4 h, 6 h, 8 h, 24 h, 72 h and 120 h). Overnight cultures of *S.mutans* strains grown in BHI medium were diluted to OD_{600} = 0.05 into fresh BHI medium, added over the mica or gold sample, sealed by Parafilm, and incubated for various times at 37 ºC. The mica or Au(111) sample was then washed three times with Millipore water, and put into a new Petri dish to dehydrate naturally for one day. Bare Au(111) and bare mica kept in BHI medium without *S. mutans* inoculated were used as reference experiments.

7.2.3 Reagents

$K_4[Fe(CN)_6]\cdot 3H_2O$ (> 99%) was from Merck, $K_3[IrCl_6]$ (> 99%), $[Ru(NH_3)_6]Cl_3$ (> 99%) and sucrose (> 99%) from Sigma-Aldrich. $[Co(phen)_3](ClO_4)_3\cdot 2H_2O$, $[Co(terpy)_2](ClO_4)_3\cdot 2H_2O$ and $[Co(NH_3)_6]Cl_3$ were prepared as descibed[27-29], available in the DTU Nanochemistry group. Deoxyribonuclease I (DNase I) was purchased from

Sigma. The PBS buffer (0.010 M phosphate, 0.14 M NaCl and 0.027 M KCl, pH = 7.4) was prepared from PBS tablets (Medicago, Sweden). Millipore water (18.2 MΩ cm) was used throughout.

7.2.4 Structures of the six probe compounds

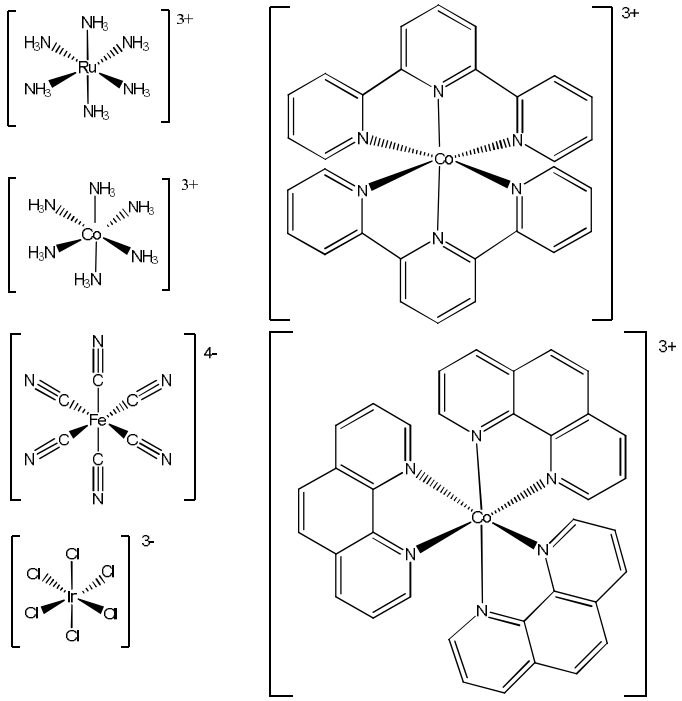

Fig.7.1 Schematic molecular structures of the six probe coordination chemical compounds: $[Ru(NH_3)_6]Cl_3$, $[Co(NH_3)_6]Cl_3$, $[Co(phen)_3](ClO_4)_3$, $[Co(terpy)_2](ClO_4)_3$, $K_4[Fe(CN)_6]$ and $K_3[IrCl_6]$.

Six inorganic probes: $[Ru(NH_3)_6]Cl_3$, $[Co(NH_3)_6]Cl_3$, $[Co(phen)_3](ClO_4)_3$, $[Co(terpy)_2](ClO_4)_3$, $K_4[Fe(CN)_6]$ and $K_3[IrCl_6]$ were used. Fig. 7.1 shows the molecular structures and electrostatic charges of the compounds. As noted, these were selected for their electrostatic charge (positive or negative), inorganic or organic aromatic ligands, different metal centres (Co vs. Ru, Fe vs. Ir), their small ligand group character (toxic CN^- vs. non-toxic Cl^-), and for their suitable equilibrium redox potentials.

7.2.5 Mica pre-treated with charged inorganic compounds and DNAase I

To investigate the charge effect on the growth and inhibition of the differently charged inorganic molecules on the biofilms growth, mica surfaces were treated with the inorganic compounds. Two groups of experiments were carried out. In one group, prior to *S.mutans* incubation in 10 ml BHI medium with 0.1 M sucrose for 24 h, 1 ml 10 mM of each of the compounds $K_4[Fe(CN)_6]$, $[Ru(NH_3)_6]Cl_3$, $K_3[IrCl_6]$, $[Co(phen)_3](ClO_4)_3$, $[Co(terpy)_2](ClO_4)_3$ and $[Co(NH_3)_6]Cl_3$ was mixed into the growth media followed by biofilm growth. In a second series of experiments a *S. mutans* biofilm was first grown for 24 h. The growth medium was then exchanged with Millipore water holding the same concentration of compound as in the first series, and left for one hour. The biofilm sample was finally rinsed with pure Millipore water, dried naturally and imaged. Sucrose enhances the rate of the biofilm growth, but has no influence on the final developed stage of the biofilms.

To study the effects of DNA, mica surfaces were treated with DNase I. In one series of experiments, prior to *S. mutans* incubation in 5 ml BHI medium for 1 h, 2 h, 4 h, 6 h and 24 h, 0.1 ml 1 mg/ml DNase I was added to the media. In a second series the biofilm was incubated in 5 ml BHI medium for the same length of time, and 0.1 ml 1 mg/ml DNase I then added to the media. All biofilm samples were rinsed with pure Millipore water, and left to dry for subsequent imaging.

To investigate the effect of mica surface pre-treatment with the four compounds, we tested two kinds of samples. In one case, after the mica slices were placed in 10 ml Millipore water, 1 ml 10 mM $K_4[Fe(CN)_6]$, $[Ru(NH_3)_6]Cl_3$, K_3IrCl_6 or $[Co(NH_3)_6]Cl_3$ was added separately and kept for 18 h. The mica slices were then washed three times with Millipore water and incubated in 10 ml BHI medium with 0.1 M sucrose for 24 h. In a second series 1 ml 10 mM $K_4[Fe(CN)_6]$, $[Ru(NH_3)_6]Cl_3$, $K_3[IrCl_6]$ or $[Co(NH_3)_6]Cl_3$, i.e. the same amount of compound but in ten times higher concentration, was dropped to adsorb separately onto a biofilm sample, dehydrated naturally for 18 h, then washed three

times by Millipore water followed by incubation in 10 ml BHI medium with 0.1 M sucrose for 24 h.

All reported experiments were repeated at least three times. In all cases *S. mutans* was incubated in 10 ml BHI medium solely with 0.1 M sucrose for 24 h as a reference. All the mica slices were dehydrated naturally for one day after incubation.

7.2.6 Atomic force microscopy (AFM), sample preparation and image acquisition

Two AFM instruments were used. One was a DualScopeTM microscope equipped with a C-21 controller (DME A/S, Copenhagen, Denmark). Tapping mode was used to record all images. Tips (Arrow-NCR-50) were from Nano World (Neuchatel, Switzerland). All AFM images shown are representative of a large number of images. The second instrument was a PicoScan 5500 from Agilent instrument (Agilent Technologies, Chandler, AZ, USA) with a 100 μm scanner and cantilevers (NP-S) from Veeco (Camarillo, CA, USA). This instrument was used in the contact mode.

7.2.7 Electrochemistry

Cyclic voltammetry was carried out using an Autolab-system (Eco Chemie, The Netherlands). The electrochemical cell was kept in a Faraday cage. The hanging meniscus method was used. A freshly prepared reversible hydrogen electrode (RHE) was used as a reference electrode and checked against a saturated calomel electrode (SCE) after each measurement. A clean coiled Pt wire served as counter electrode. All potentials are reported vs. SCE. Purified Ar (5 N, Chrompack) was used to deoxygenate all solutions and an argon stream kept over the solution. The PBS buffer (0.010 M phosphate, 0.14 M NaCl, 0.0027 M KCl, pH = 7.4) was the supporting electrolyte solution. 1 ml 10 mM $K_4[Fe(CN)_6]$, and $K_3[IrCl_6]$ (negatively charged molecular probes), $[Ru(NH_3)_6]Cl_3$ and $[Co(terpy)_2](ClO_4)_3$ (positively charged molecular probes) were added independently

to the PBS buffer. 0.1ml 1 mg/ml DNase was added before or after cyclic voltammetry, cf. below.

7.3 AFM results for S.mutans biofilm

7.3.1 Sucrose effects of *S.mutans* on mica in air

S. mutans exposed to a sucrose-rich diet, is able to utilize the sucrose to form glucans, which are extracellular polysaccharides. The adhesive nature of the glucans enables the bacteria to adhere, for example to tooth surfaces. In my thesis, variable sucrose concentrations in BHI medium were used to find the most suitable medium, which can help *S.mutans* biofilms to adhere to the surface. Mica was used in this part of the study. This part of the experiments was a collaboration with diploma student Juliet Wairimu Frederiksen, who had studied the sucrose effects for *S.mutans* at the initial stages.

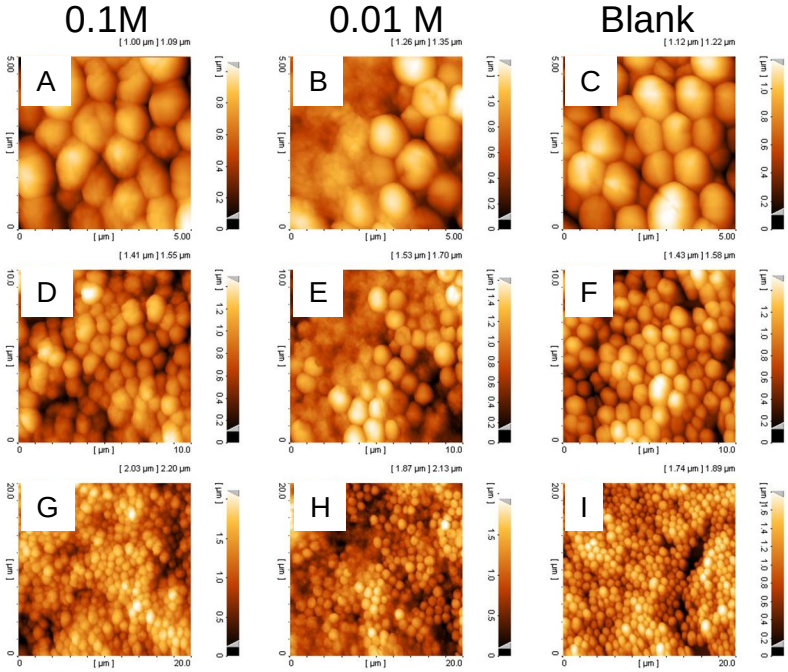

Fig 7.2 Sucrose effects on *S.mutans* for 24 hour on mica surface. A, D and G: BHI medium with 0.1 M sucrose; B, E and H : BHI media with 0.01 M sucrose; C, F and I : pure BHI medium. Scan size: A, B, C: 5 µm; D, E, F : 10 µm; G, H, I : 20 µm. Tapping Mode, DME. Sucrose had no big effects at the final stage of the biofilm formation.

Mica gives ultraflat surfaces. Although the deposited film surface is still rough, the reverse side of the film at the mica-film interface provides ultraflatness, when the film is removed from the substrate. Such ultraflat substrates are common substrates for sample preparation for atomic force microscopy. Freshly cleaved mica surfaces have been broadly used as clean imaging substrates in atomic force microscopy, enabling for example the imaging of bacterial biofilms, plasma glycoproteins, membrane bilayers, and DNA molecules. In my thesis, Mica was used as solid surface to observe biofilm formation by AFM.

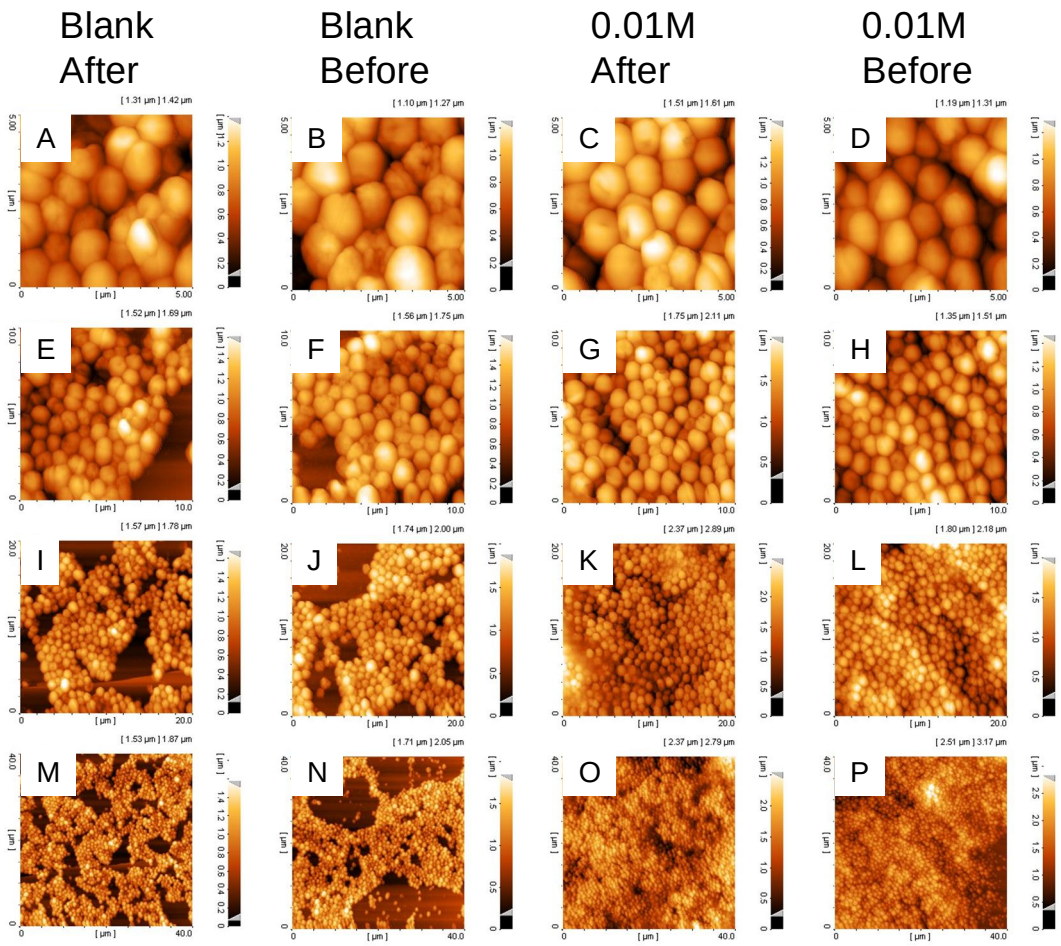

Fig 7.3 Sucrose effects of biofilm growth on DNAase treated in BHI media on mica surface. A, E, I, M: *S. mutans* with BHI media after 24h biofilm formation and then treated with 10 µg/ml DNAase in MQ for 1 hour; B, F, J, N: *S. mutans* with BHI media at 0 hour treated with 10 µg/ml DNAase and then grown for 24h; C, G, K, O: *S. mutans* with 0.01M sucrose BHI media after 24h biofilm formation and then treated

with 10 µg/ml DNAase in MQ for 1 hour ; D, H, L, P: *S. mutans* with 0.01M sucrose BHI media at 0 hour treated with 10 µg/ml DNAase and then grown for 24h. Scan size: A, B, C, D: 5 × 5 μm^2; E, F, G, H: 10 × 10 μm^2; I, J, K, L: 20 × 20 μm^2; M, N, O, P: 40 × 40 μm^2. Tapping mode, DME instrument.

Fig 7.2 shows that sucrose enhances the biofilm growth rate, but does not have any influence on the biofilm structure or formation. Fig 7.3 shows results similar to those in Fig 7.2 with DNAase added. DNAase can remove eDNA from the biofilm surface Fig 7.2 C and Fig 7.3 B or Fig 7.2B and 7.3D. *S.mutans* utilizes sucrose to excrete more EPS and enable the bacteria to adhere strongly on the surface. Sucrose enhances the rate of the biofilm growth, but has no influence on the final developed stage of the biofilms.

7.3.2 *S. mutans* growth on Au (111) –surfaces and mica

Au (111) and Mica-surfaces are two kinds of different solid surfaces. Mica is commonly used for AFM due to its native ultraflat layer surface and stability. The Au(111)-surface is a low-index electrode surface at the atomic level and extensively used in electrochemistry. Au(111)-surfaces can be viewed as a bridge to combine electrochemistry and AFM, with Mica as a normal control surface. Mica is more hydrophilic than the Au(111) surface.

Bacterial growth on both mica and Au (111)-surfaces was followed by AFM after natural drying of the emersed biofilms at given times. Fig. 7.4 shows a sequence of AFM images of the bacterial growth on mica and Au (111)-surfaces after natural drying under the standard conditions in the absence of compounds. When the AFM images on the different surfaces are compared significant differences between mica and Au (111)-surfaces in the initial stage of the biofilm development are noted. On Au (111)-surfaces, The bacteria are distributed independently on the Au (111)-surface with small groups of 4-7 cells after 1 or 2 h, Fig 7.4 A and B. The bacteria multiply on the surface and have connected together after 4-8 h, Fig 7.4 C and D. In comparison the bacteria group into small islands on mica surfaces. These islands become significantly larger already after 1 or 2 h, Fig7.4 A’ and B’. After a few hours 4-8 h the bacterial biofilm islands multiply to form bridges and connect to other islands, Fig 7.4 C’ and D’. These observations must be viewed with

the reservation of drying artifacts on the different surfaces. After 24 h the biofilm covers fully both mica and Au(111)-surfaces with no significant difference between the two surfaces, Fig 7.4 H and H'.

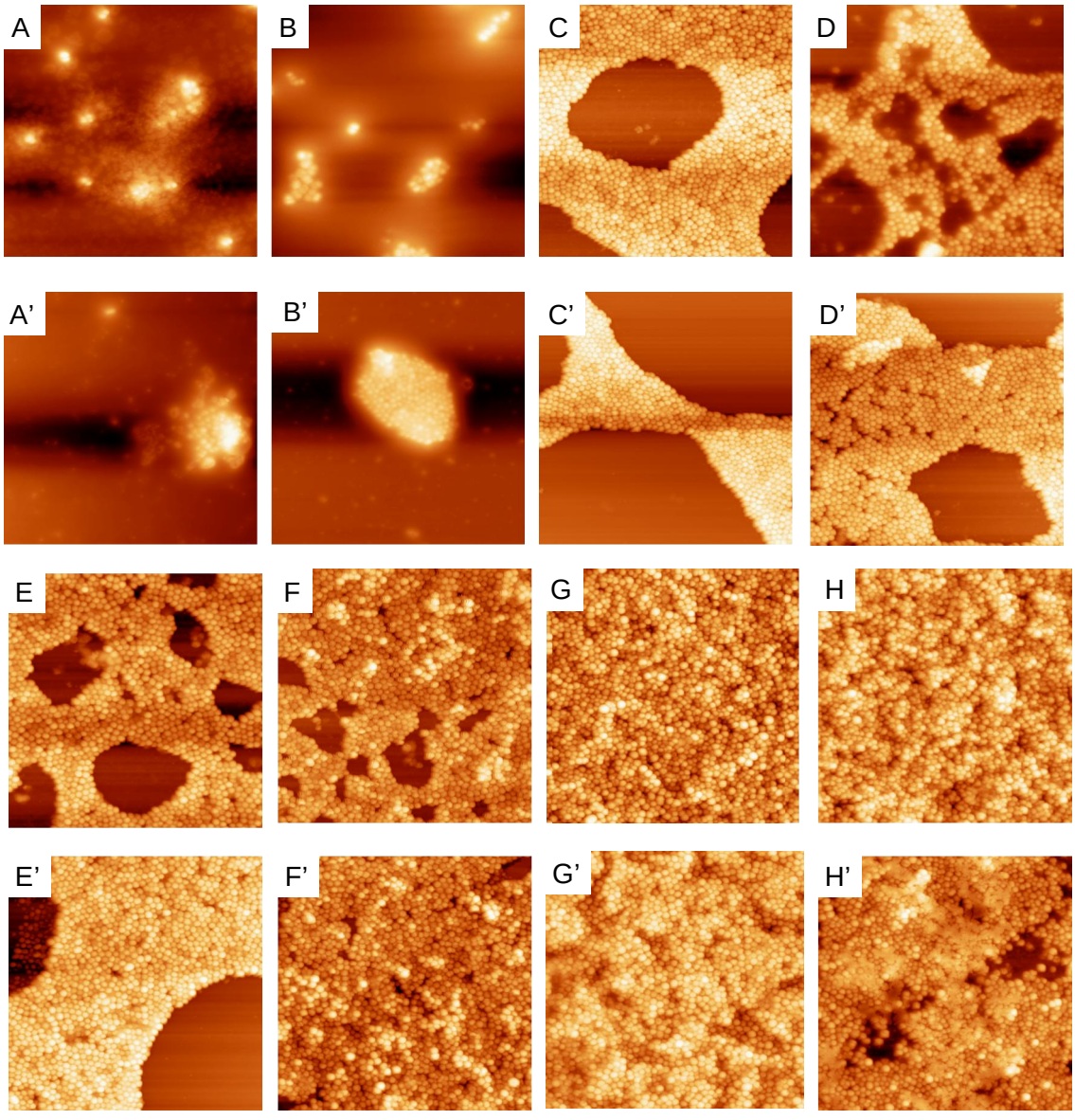

Fig. 7.4 AFM images of the bacterial growth in BHI medium on Au(111)-surfaces (top, A-H) and on mica (bottom, A'-H') after natural drying under the standard conditions in the absence of compounds. Growth times from 1 h (A and A'), 2 h (B and B'), 4 h (C and C'), 6 h (D and D'), 8 h (E and E'), 24 h (F and F'), 72 h (G and G'), 120 h (H and H'). 40 × 40 μm^2. contact mode.

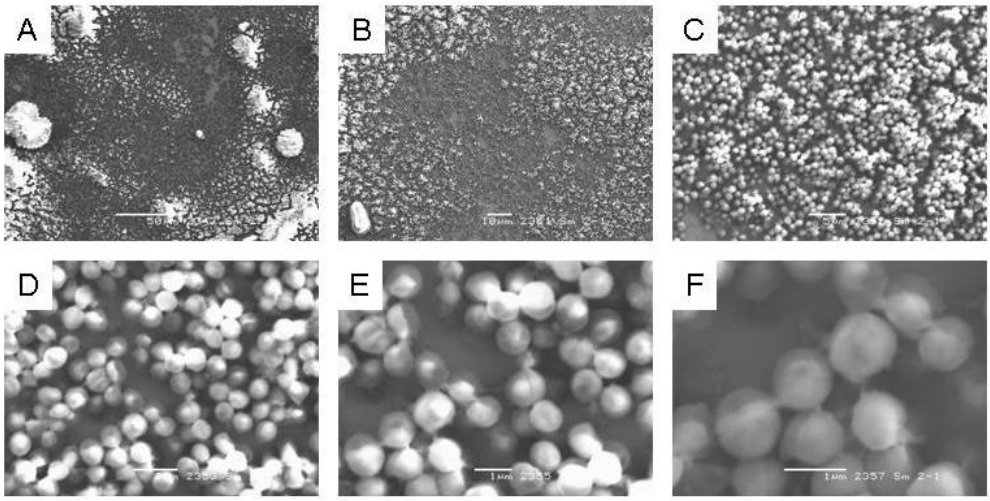

Fig 7.5 SEM images of *S.mutans* biofilms on Au (111)-surfaces after 13 days in 0.01 M sucrose BHI medium with 0,4 mmol/L $AuCl_3$ solution. Image ratio: width to height: 4:3. Scale bar: A: 50 µm ; B: 10 µm; C: 5 µm; D: 2 µm; E: 1 µm; F: 1 µm. This work was done in DTU building 204, in the 06.12.2009. Jingdong Zhang helped me.

Fig 7.5 shows details of a mature *S.mutans* biofilm pattern in 3D- dimensional topography obtained by scanning electron microscopy. As described in Fig 2.1, biofilm development has five stages. Stage 1: initial attachment of cells to the surface. Stage 2: production of EPS resulting in more firmly adhered cells. Stage 3: early development of biofilm architecture. Stage 4: maturation of biofilm architecture to form mushroom-shaped biofilms. Stage 5: dispersion of single cells from the biofilm. Fig 7.5 follows stage 4 and 5. The bright big spots in Fig 7.5 A are independent mushroom-shaped biofilm. Fig 7.5 A, B and C show that the biofilm cells are distributed non-uniformly. Some parts of the surfaces have dense multilayer biofilms and some parts of the surfaces only have thin layer biofilms. In Fig 7.5 E and F, the biofilm cells have some bridges between the cells, which make the cells connect to each other. Fig 7.5 E shows some single cells dividing into two cells. It is concluded that mature *S.mutans* biofilms in the final stage have similar growth patterns on mica and Au (111)-surfaces.

The growth patterns on the two surfaces were thus different in the initial growth phases, 1-2 h. The bacteria at the Au (111)-surface at first seem to be distributed randomly in

small clusters from where they grow and get connected to other clusters, eventually forming the whole biofilm. Larger islands form initially on mica surfaces, followed by growth and bridging to other islands and full biofilm coverage. The different initial growth patterns may be associated with the different nature of Au(111) and mica surfaces. The former is hydrophobic and may bind to hydrophobic patches on the bacterial surface. Mica is more hydrophilic with the bacteria more inclined to island formation via mutual lateral hydrophobic interactions at the early growth stages.

7.3.3. Inhibitory effects of probe molecules on *S. mutans* growth

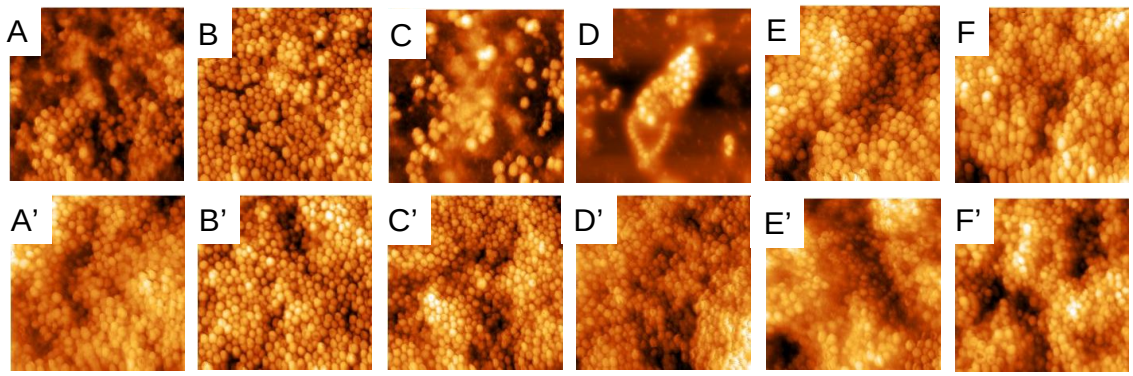

Fig. 7.6 AFM imaging of the effects of the six compounds in the *S. mutans* biofilm formation. From left to right: $[Co(phen)_3]^{3+/2+}$ (A and A'), $[Co(terpy)_2]^{3+/2+}$ (B and B'), $[Co(NH_3)_6]^{3+/2+}$ (C and C'), $[Ru(NH_3)_6]^{3+/2+}$ (D and D'), $[Fe(CN)_6]^{3-/4-}$ (E and E'), $[IrCl_6]^{3-/4-}$ (F and F') Top row: 1 mM compound added to the 0.1 M sucrose BHI media for 24 h (A-F). Bottom row: 1 mM compound added after *S. mutans* biofilm growth in the 0.1 M sucrose BHI media for 24 h (A'-F').

In the electrochemical method, six probe molecules were added to the solution. It is important to know if those six probe molecules will affect the *S.mutans* biofilm formation. Three different inhibition modes were therefore applied. First mode: initial compound addition to the growth medium; second mode: compound addition after *S .mutans* growth for 24 h; Third mode: surface pre-treatment prior to bacterial growth. Fig. 7.6 shows the effects of the six compounds on the bacterial growth in the first two inhibitory modes. Sample preparation for these two modes, i.e. washing and natural drying followed the same procedure as in the absence of added compounds. The third mode showed no effect

(data not shown) and lots of crystallization, due to poor compound adsorption on the surfaces. The observations are summarized in Table7. 1.

Table 7.1 Summary of the growth inhibition effects and the voltammetric effects of the six probe complexes.

Compound	Charge	Voltammetric effect	Compound treatment on the surface before growth	Compound treatment in the solution before growth	Compound treatment after growth
$[Co(phen)_3]^{3+/2+}$	+	Potential too high		No effect	No effect
$[Co(terpy)_2]^{3+/2+}$	+	No effects		No effect	No effect
$[Co(NH_3)_6]^{3+/2+}$	+		No effect	Inhibition	No effect
$[Ru(NH_3)_6]^{3+/2+}$	+	No effects	No effect	Inhibition	No effect
$[Fe(CN)_6]^{3-/4-}$	-	Shows effects	No effect	No effect	No effect
$[IrCl_6]^{3-/4-}$	-	Shows effects	No effect	No effect	No effect

From Fig 7.6 and Table 7.1, the following is notable: 1. The negatively charged compounds $[Fe(CN)_6]^{3-/4-}$ and $[IrCl_6]^{3-/4-}$ showed no inhibition in either mode. This points to little importance of CN^- that could be released during the growth process. 2. The positively charged aromatic compounds $[Co(phen)_3]^{3+2+}$ and $[Co(terpy)_2]^{3+/2+}$ also showed no inhibition in either mode. 3. $[Ru(NH_3)_6]^{3+/2+}$ and $[Co(NH_3)_6]^{3+/2+}$ show strong inhibition, different from those of the other probe molecules. As for all the compounds, no inhibition was apparent when the compounds were added after bacterial biofilm maturation but strong inhibitory effects were observed when either of the compounds were added initially to the growth medium. As an easily accessible and inexpensive compound, $[Co(NH_3)_6]^{3+/2+}$ may thus hold a prospect for bacterial biofilm growth inhibition.

In conclusion, AFM disclosed significant bacterial growth inhibition of $[Ru(NH_3)_6]^{3+}$ and $[Co(NH_3)_6]^{3+}$ whereas no growth inhibition of negatively charged molecules were observed.

7.4 CV of S.mutans

7.4.1 CV of probe complexes at bare Au(111)-electrodes

Fig. 7.7 shows CVs of all the compounds except $[Co(NH_3)_6]^{3+/2+}$ in PBS buffer at bare Au (111)-electrodes. $[Ru(NH_3)_6]^{3+/2+}$, $[Fe(CN)_6]^{3-/4-}$ and $[Co(terpy)_2]^{3+/2+}$ display fully reversible diffusion controlled voltammograms undisturbed by Au (111)-surface related electrochemical processes. The voltammetric midpoint potentials accord with reported values, Table 7.2.

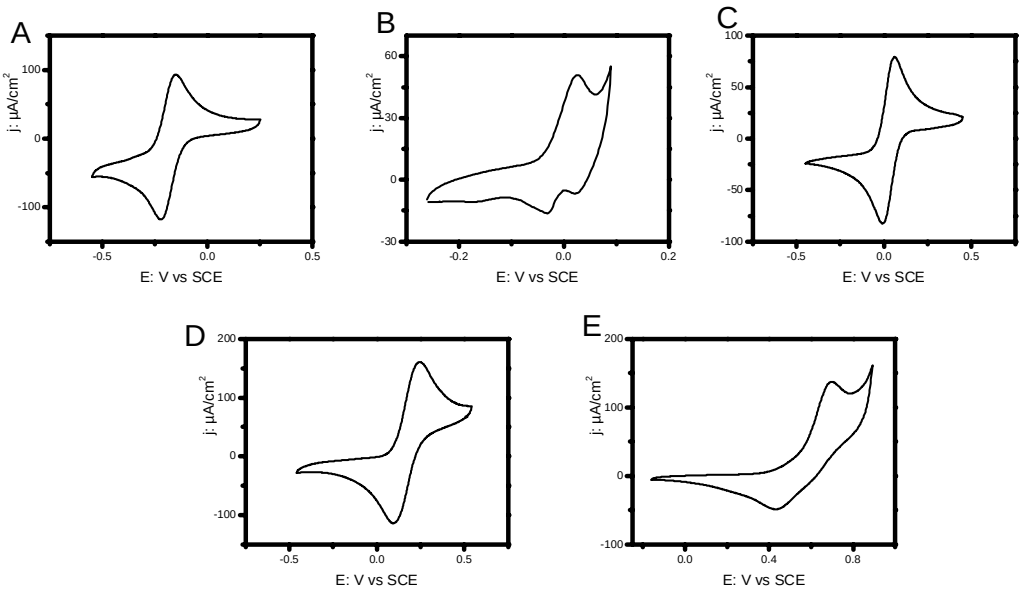

Fig.7.7 CVs of the five molecular probe compounds on bare Au(111)-electrode surfaces. 10 mM PBS buffer, pH 7.4. Scan rate 50 mV s^{-1}. A: $[Ru(NH_3)_6]^{3+/2+}$, B: $[Co(phen)_3]^{3+/2+}$, C: $[Co(terpy)_2]^{3+/2+}$, D: $[Fe(CN)_6]^{3-/4-}$, E: $[IrCl_6]^{3-/4-}$.

The voltammograms give rise to the following observations: 1. $[Ru(NH_3)_6]^{3+/2+}$, $[Co(terpy)_2]^{3+/2+}$, $[Fe(CN)_6]^{3-/4-}$ and $[IrCl_6]^{3-/4-}$ display voltammetric features for probing the Au(111)/bacterial/aqueous interface. The $[Fe(CN)_6]^{3-/4-}$/$[IrCl_6]^{3-/4-}$ comparison is also important for the assessment of possible effects on the bacterial growth from CN^- released from $[Fe(CN)_6]^{3-/4-}$. [30] 2. The midpoint potentials of $[Co(phen)_3]^{3+/2+}$ and $[IrCl_6]^{3-/4-}$ are borderline cases for bacterial electrochemistry probing but $[IrCl_6]^{3-/4-}$ could still be used as a comparison with $[Fe(CN)_6]^{3-/4-}$. In the absence of a large excess of free NH_3-

ligand $[Co(NH_3)_6]^{3+/2+}$ has no reversible voltammetry but is included in the growth inhibition study as a reference for $[Ru(NH_3)_6]^{3+/2+}$. 3. The midpoint potentials in the PBS buffer differ somewhat from reported value. That is because we might have different solution system and different pH, Table 7.2.

Table 7.2 Summary of measured equilibrium redox potentials of the six probe complexes. The superscript numbers refer to the reference list. [a]The redox potential of the $[Fe(CN)_6]^{3-/4-}$ couple refers to zero ionic strength but this value increases significantly with increasing ionic strength.

Compound	$[Ru(NH_3)_6]^{3+/2+}$	$[Co(phen)_3]^{3+/2+}$	$[Co(terpy)_2]^{3+/2+}$	$[Fe(CN)_6]^{3-/4-}$	$[IrCl_6]^{3-/4-}$
Midpoint Potential (mV Vs SCE)	-180	1	33	177	573
Literature Value (mV Vs SCE)	-184[31]	165[32], 135[33]	105[32],35[33]	199[34]	657[35]

7.4.2 CV of *S. mutans* biofilms

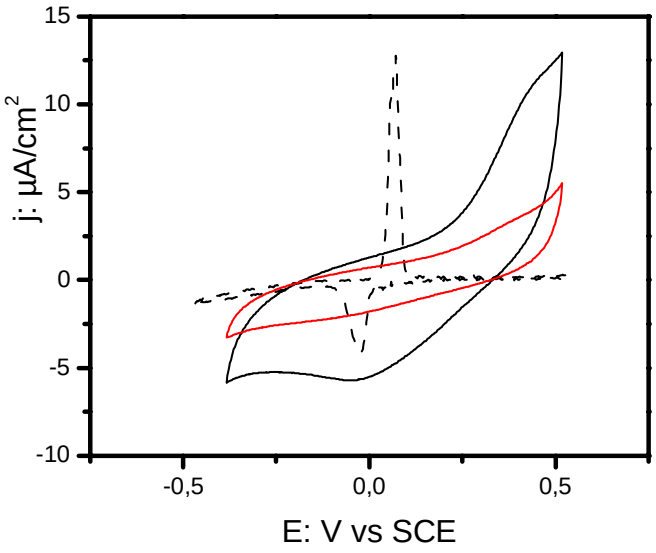

Fig 7.8 CVs of *S. mutans* biofilm (black solid line) on Au (111)-electrode surface in 10 mM PBS buffer, pH 7.4. Scan rate 50 mV s^{-1}. The biofilm was grown for five days on the Au (111)-surface, dried naturally, and the biofilm covered electrode then inserted in the buffer solution. A CV of BHI in solution (red line) on a bare Au(111)-electrode surface is shown for comparison. The dashed line shows the reconstruction peak in the voltammetric response of the bare Au(111)-electrode surface.

Fig 7.8 shows CVs of bare *S. mutans* biofilms in the BHI growth medium and of the growth medium itself. Both *S. mutans* biofilms grown for five days and dried, and the BHI medium itself prepared in the same way give a featureless voltammetric background. With the concentrations of probe molecules used, cf. below, this background is insignificant. This part of experiments was done as a control experiment.

7.4.3 CV of probe molecules in mature biofilm environment

CVs of the redox probe complexes at Au(111)-electrode surfaces with five days mature *S. mutans* biofilms was recorded. CVs of the probe complexes on bare Au(111)-surface, Fig.7.7 and of the biofilm alone, Fig.7.8 can be regarded as references. Fig.7.9 shows CVs of all the compounds except $[Co(NH_3)_6]^{3+/2+}$ and $[Co(phen)_3]^{3+/2+}$, in the presence of *S.mutans* biofilm. Voltammetry of $[Ru(NH_3)_6]^{3+/2+}$ was notably largely unaffected by a fully covered bacterial biofilm even though $[Ru(NH_3)_6]^{3+/2+}$ is a growth inhibitor. Compared with the $[Ru(NH_3)_6]^{3+/2+}$ voltammograms at bare Au(111), the voltammetry of $[Ru(NH_3)_6]^{3+/2+}$ with biofilm has a slight tendency of peak sharpening, Fig. 7.7. This cannot be detected for $[Co(terpy)_2]^{3+/2+}$ (with aromatic ligands), for which no growth inhibition was observed.

The CVs of both positively charged molecular probe pairs i.e. $[Ru(NH_3)_6]^{3+/2+}$ and $[Co(terpy)_2]^{3+/2+}$ were largely unaffected by the *S. mutans* biofilm on the Au(111)-electrode surface, although they have inhibition effects on biofilm formation, Fig.7. 9 A and C. The voltammograms were stable for twenty or more scans. The peak Current followed a linear correlation with the square root of the scan rate up to 1 V s^{-1} with a weaker dependence at higher scan rates (Fig. 7.10). $[Ru(NH_3)_6]^{3+/2+}$ and $[Co(terpy)_2]^{3+/2+}$ behave similarly. These results support that the bacteria are negatively charged[36] and that the positively charged probe couples are attracted to the surface.

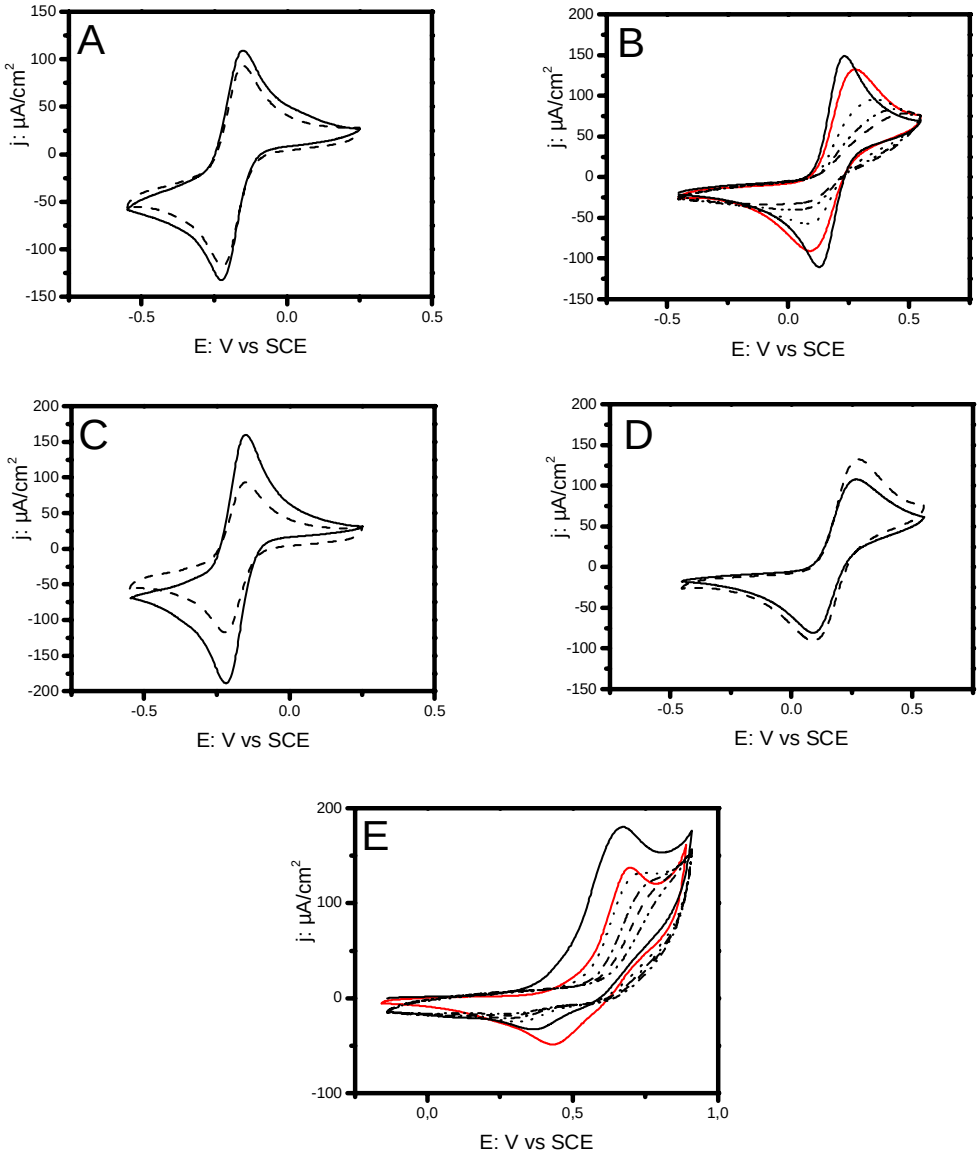

Fig.7.9 Cyclic voltammograms on *S. mutans* biofilms grown in BHI medium for 5 days or BHI media for 5 days on Au(111) in PBS buffer, pH 7,4. Scan rate 50 mV s^{-1}. A and C: 1 mM $[Ru(NH_3)_6]Cl_3$ in PBS buffer as a positively charged molecular probe. B and D: 1 mM $K_4[Fe(CN)_6]$ in PBS buffer as a negatively charge molecular probe. E: 1 mM $K_3[IrCl_6]$ in PBS buffer as a negatively charge molecular probe. A: Solid line: *S. mutans* on Au (111), dashed line: Bare Au(111). B: Black solid line: *S. mutans* on Au (111), 2nd cycle; black dotted line: 20th cycle; black dotted-dashed line: 40th cycle; black dashed line: 60th cycle; red solid line: bare Au (111). C: Solid line: BHI medium on Au (111), dashed line: bare Au (111). D: Solid line: BHI medium on Au (111), dashed line: Bare Au (111). E: Black solid line: *S. mutans* on Au (111), 1st cycle; black dotted line: 3rd cycle; black dotted-dashed line: 5th cycle; black dashed line: 7th cycle; black short dotted line: 10th cycle; red solid line: bare Au (111).

The negatively charged probe molecules, $[Fe(CN)_6]^{3-/4-}$ and $[IrCl_6]^{3-/4-}$ behave differently. $[Fe(CN)_6]^{3-/4-}$ shows largely unaffected voltammetry over the first few scans but the voltammograms broaden and show increasingly non-ideal planar diffusion behaviour as the number of cycles increases. After 40-60 cycles a sigmoidal shape stabilizes, Fig.7.9B. Similar effects are noted for $[IrCl_6]^{3-/4-}$ although the equilibrium potential of this redox couple is slightly too high for a clear view, Fig 7.9 E. This pattern also confirms a negatively charged bacterial surface that kinetically hinders probe molecule access to the Au(111)-electrode surface. Chemical reactivity of CN^- released from $[Fe(CN)_6]^{3-/4-}$ might inhibit the biofilm formation, but no inhibition of the biofilm formation was observed for $[Fe(CN)_6]^{3-/4-}$, Fig 7.6 E and E', and the voltammetric shape variation as similar effects of $[Fe(CN)_6]^{3-/4-}$, are observed for $[IrCl_6]^{3-/4-}$, Fig 7.9 D and E.

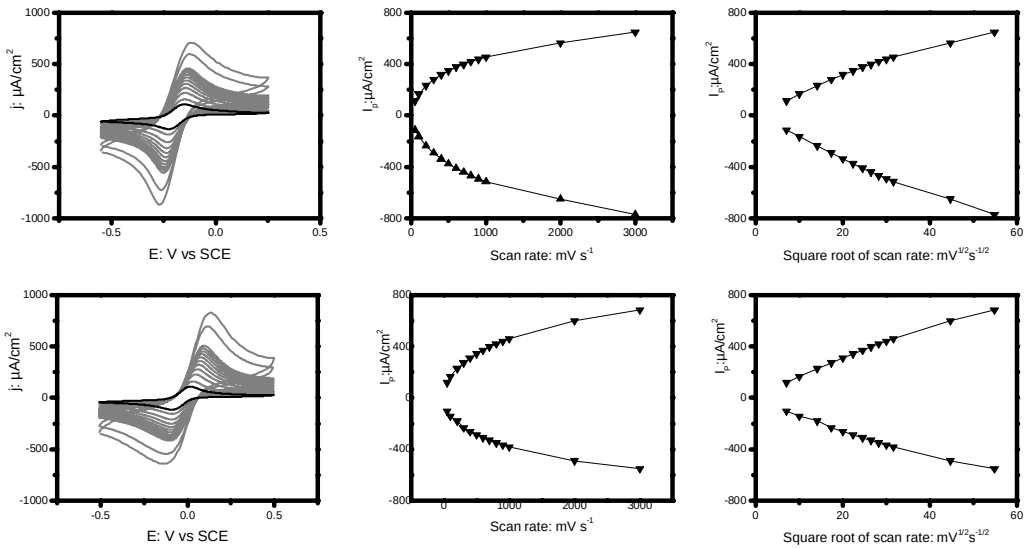

Fig.7.10 Cyclic voltammograms of *S.mutans* in BHI medium for 5 days on Au (111) in PBS buffer, pH 7.4, scan rate from 50 mV s^{-1} to 3 V s^{-1}. Top row: CVs in 1 mM $[Ru(NH_3)_6]Cl_3$. Bottom row: 1 mM $[Co(terpy)_2](ClO_4)_3$. Left: CV with different scan rate. Middle: the correlation between peak current and scan rate. Right: the correlation between peak current and square root of scan rate.

7.4.4 Summary

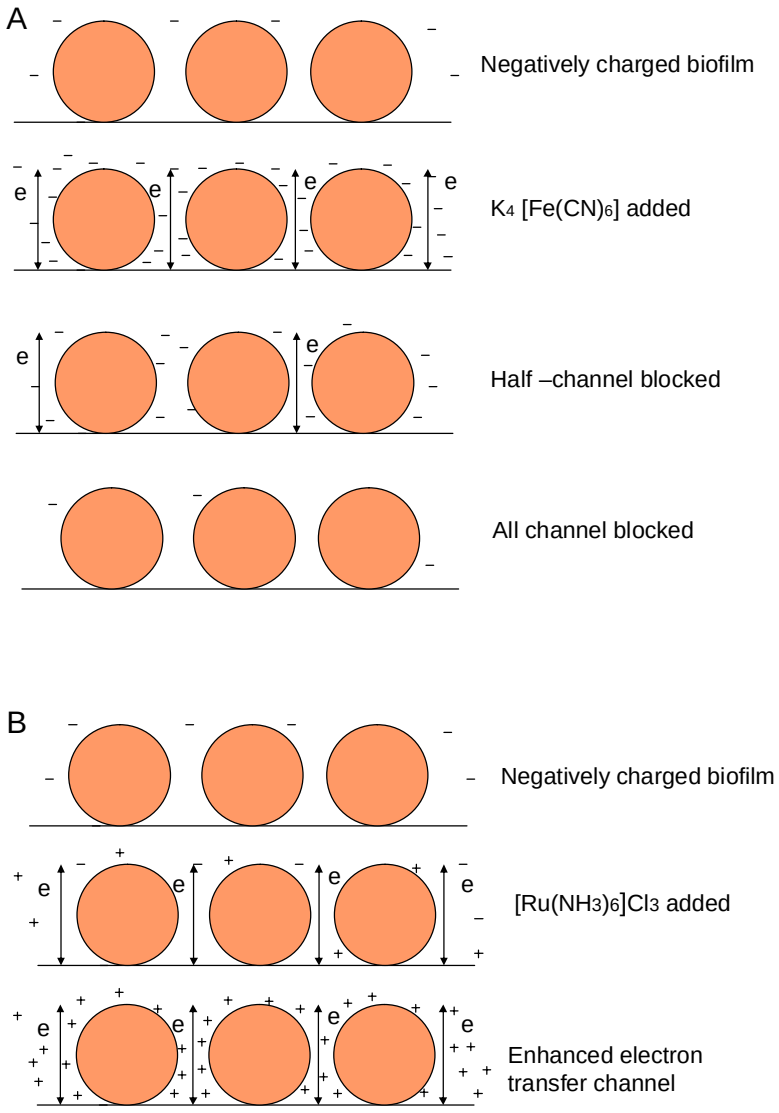

Fig 7.11 Scheme for possible mechanisms of electron transfer in A: K_4 [$Fe(CN)_6$].B: [$Ru(NH_3)_6$]Cl3;

Negatively and positively charged probe molecules were investigated by AFM and cyclic voltammetry. Control experiments were also applied. It is known that the cell surface is negatively charged[36]. According to the behavior of the positively and negatively probe compounds, a model was designed in Fig 7.11 A and B. It is supposed that the Au(111)-surface is fully covered with bacterial biofilm. From a biological view, the biofilm surfaces have pore channels and the biofilm shows apparently negative charge. When the

negatively charged probe is added into the solution, the pore channels in the biofilm are open at the beginning. The electron transfer events are however, increasingly impeded with time and the channels increasingly blocked (Fig 7.11B). When the positively charged probe molecules are added into the solution, the electron transfer is simulated and the electro-pore channel openings strengthened at the same time (Fig 7.11 A).

The negatively charged redox molecules $[Fe(CN)_6]^{3-/4-}$ and $[IrCl_6]^{3-/4-}$ thus behave differently from the positively charged probe molecules. The voltammetric signals are unchanged from the signals at *S.mutans* Au(111)-electrode surfaces in the first few scans but the peaks separate and flatten as the number of scans is increased. A sigmoidal signal stabilizes after about 40 scans with the midpoint potential remaining the same as on bare Au(111). This pattern is seen for both $[Fe(CN)_6]^{3-/4-}$ and $[IrCl_6]^{3-/4-}$ but most clearly for the former as the redox potential of the Ir-complex overlaps with the potential for beginning oxidation of the Au-surface.

The voltammograms of the positively charged probe molecules $[Ru(NH_3)_6]^{3+/2+}$ and $[Co(terpy)_2]^{3+/2+}$ at high bacterial biofilm coverage Fig.7.9, remained virtually unchanged on the biofilm surface compared with the bare Au(111)-surface. As noted, in spite of the dense coverage and bacterial excretions in the matrix between the individual bacteria, this points to extensive pore channel formation in the biofilm matrix and almost free passage of the probe molecules from the solution to the Au(111)-surface.

The sigmoidal voltammetric shape of the negatively charged probe molecules could been explained by spherical diffusion followed by molecular transport through pore channels in the biofilm. Both the diffusion pattern of the positively charged probe complexes and the time evolution towards sigmoidal voltammetry of the negatively charged probe complexes, need a further experiments to explain. The time evolution could be caused by structural changes in the biofilm on successive scanning. If we could observe the bacterial biofilm *in situ* by AFM, we could compare AFM images before and after electrochemical scanning. A changed pore structure in the biofilm may not significantly affect the transport of positively charged probe molecules which would be strongly

attracted to the negatively charged interphase. The biofilm/pore channel structure is thus more selective to negatively charged probe molecule, i.e. spherical diffusion to particular channels is more significant for negatively than for positively charged probe molecules.

The voltammetric patterns seem to be dominated by electrostatic field effects in the Au(111)/ bacterial/aqueous interphase. $[Ru(NH_3)_6]^{3+}$ (and $[Co(NH_3)_6]^{3+}$) are strong growth inhibitors but show reversible voltammetry through the biofilm. Reversible voltammetry of $[Co(terpy)_2]^{3+}$ also remains but this compound has no effect on the bacterial growth. Neither does growth inhibition seem to be specific to the metal. $[Ru(NH_3)_6]^{3+}$ and $[Co(NH_3)_6]^{3+}$ are both inhibitors whereas the biofilm growth is unaffected by $[Co(phen)_3]^{3+}$ and $[Co(terpy)_2]^{3+}$. Growth inhibition could perhaps be associated with the nature of the ligand. Metabolic reduction of the amine complexes would lead to more substitution labile and therefore potentially bacteriotoxic, Co(II)-complexes whereas reduction of $[Co(phen)_3]^{3+}$ and $[Co(terpy)_2]^{3+}$ with aromatic ligands give Co(II)-complexes that remain substitution inert.

Neither $[Fe(CN)_6]^{3-}$ nor $[IrCl_6]^{3-}$ affect the biofilm growth. $[Fe(CN)_6]^{3-}$ and $[Fe(CN)_6]^{4-}$ might undergo light-induced dissociation of CN^- but this does not seem to inhibit bacterial growth either.[37] The fact that the CVs of these complexes are the ones most affected by the bacterial biofilm therefore supports that electrostatic field effects is a dominating controlling factor in the voltammetric behaviour of the probe molecules at the biofilm covered surfaces.

7.5 DNAase-treated biofilms

7.5.1 AFM of probe complexes on DNAase-treated biofilms

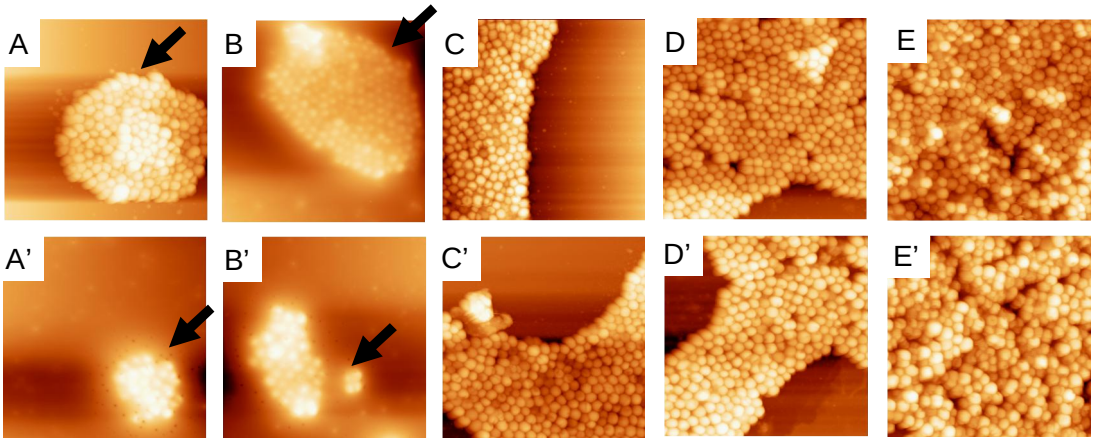

Fig.7.12 AFM images to show the effect of DNAase addition. Top row (A-D): No 10 μg/ml DNAase treatment. BHI medium for 24 h. Bottom row (A'-D'): 10 μg / ml DNAase added initially. From left to right: 1 h (A and A'), 2 h (B and B'), 4 h (C and C'), 6 h (D and D') and 24h (E and E'). 20 × 20 μm^2. Contact mode. Arrow: the boundary of the biofilm. A' and B' has some small holes around the biofilm boundary

Fig. 7.12 shows the effect of DNAase treatment on the biofilm at the initial growth stages imaged by AFM. In addition to slower growth, lots of small dots have appeared, particularly at the edges of the clusters of the DNAase treated biofilm 1, 2, 4, and 6 h after DNAase addition, see arrow on Fig 7.12 A and A', B and B'. These holes, possibly associated with DNA fragments do not appear on DNAase free samples. The biofilms have developed to full coverage after 24h, with no visible hole structures any more. This might be due to DNAase functioning only a short time, and because DNAase may be used up or inhibited after a few hours.

7.5.2 CVs of probe complexes on DNAase-treated biofilms

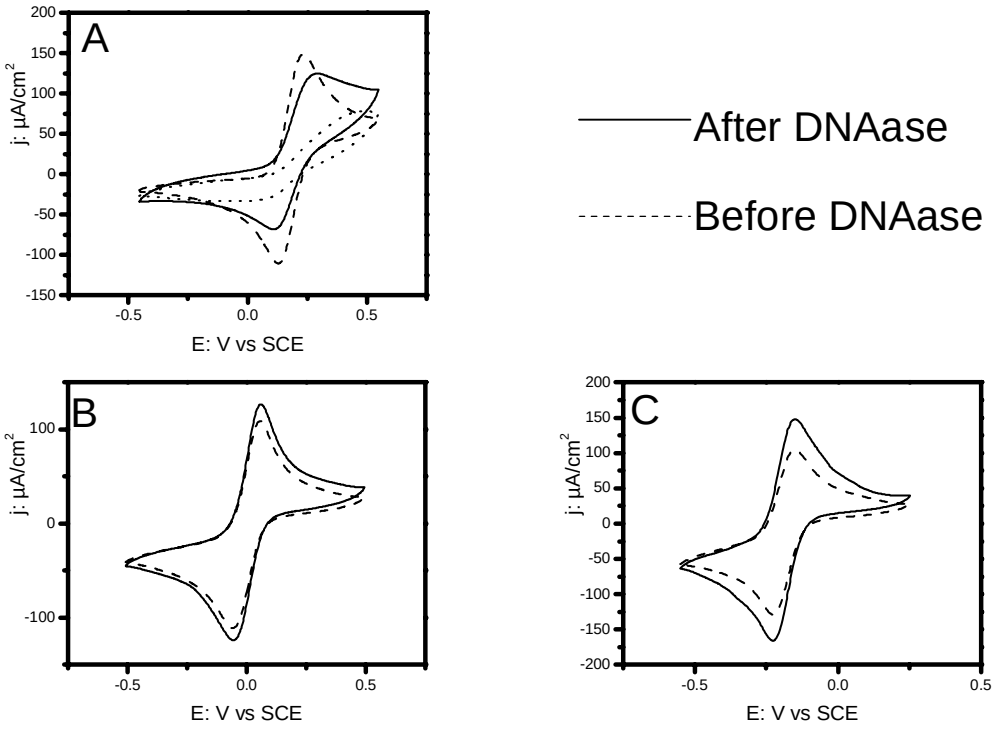

Fig.7.13 CVs of $[Fe(CN)_6]^{3-/4-}$ (A), $[Co(terpy)_2]^{3+/2+}$ (B) $[Ru(NH_3)_6]^{3+/2+}$ (C) in the absence and presence of DNAase. Au(111)-electrode in PBS buffer, pH 7,4, scan rate 50mV s^{-1}. Black lines are CVs recorded for 5 days old *S. mutans* biofilm on Au(111) after addition of 10mg/ml DNAase to the PBS buffer. Dashed lines are CVs after 5 days of biofilm growth but before 10 µg/ml DNAase addition. Top, left shows the time evolution of the $[Fe(CN)_6]^{3-/4-}$ voltammogram. Dashed line: *S. mutans* grown for 5 days on Au (111), 2nd cycle. No DNAase added. Dotted line: same conditions, 60th cycle (stable). Solid line: 40th cycle (stable) on *S. mutans* grown for 5 days on Au (111) after 10 µg/ml DNAase.

The biofilms excrete polysaccharides and DNA to form a polymeric matrix and strengthen the bacterial adherence to the surface[36]. Extracellular DNA (e-DNA) which is part of the extracellular polymeric substances (EPS) would be degraded by added DNAase, and also be detected via the voltammetric patterns of the probe molecules. DNAase has significant effects on the biofilm development in the initial growth stages, but smaller effects in the final growth stages Fig 7.12, but the effects of e-DNA decomposition on the probe molecule voltammetry is more sensitive to show that e-DNA would be degraded at these later stages. A five day old fully matured multi-layer film has more EPS, in which DNAase-based degradation of e-DNA in the EPS would be most

clear and was therefore chosen for voltammetry. The electrostatic charges of the probe molecules, $[Ru(NH_3)_6]^{3+/2+}$, $[Co(terpy)_2]^{3+/2+}$ and $[Fe(CN)_6]^{3-/4-}$ would be selective to these events.

Fig.7.13 shows the effect of DNAase on the CVs of $[Ru(NH_3)_6]^{3+/2+}$, $[Co(terpy)_2]^{3+/2+}$ and $[Fe(CN)_6]^{3-/4-}$. The *S. mutans* biofilms were grown for five days and dried naturally. This was followed by insertion of the biofilm-covered electrode into the electrochemical cell containing PBS buffer, to which 10 μg/mL DNAase had been added. The data support the expectations and the positively and negatively charged probe molecules in fact respond differently to DNAse addition to the biofilm covered Au (111)-electrode. The voltammetric peak height of the positively charged probe molecules increases only slightly and the sharp peak shape is unchanged, Fig.7.13B and 7.13C. In contrast, the negatively charged probe signal shows stronger effects on both voltammetric peak height and shape, Fig.7.13A. DNAase leads the peak both to increase and sharpen. The time evolution is shown in Fig.7.13A. The voltammetric peak of $[Fe(CN)_6]^{3-/4-}$ on the biofilm without DNAase added first decreases and flattens with increasing number of scans, as noted above. After DNAase addition the signal again rises and sharpens notably. DNAase thus seems to open channels initially blocked by negatively charged DNA. This effect is stronger for negatively than for positively charged probe molecules as the diffusion of the latter to the electrode surface is not hindered electrostatically such as for the former. We used the same PBS buffer to repeat the experiments and found that only the fresh DNAase can remove the DNA. It might be that DNAase can only function for a short time and that the enzyme functional group become occupied by the surrounding DNA and cut DNA fragments. If a new biofilm covered Au (111)-electrode is put into the same PBS buffer, enough DNAase is needed to remove the eDNA from this new biofilm covering Au (111)-electrode.

7.5.3 Summary

AFM of samples with DNAase added initially displayed both slower initial growth and excreted small structures around the edges of the bacterial colonies, possibly DNA or

DNA fragments. However, bacterial growth was not prevented and a fully covered-biofilm appeared after 24 h for both DNAase and DNAase free samples.

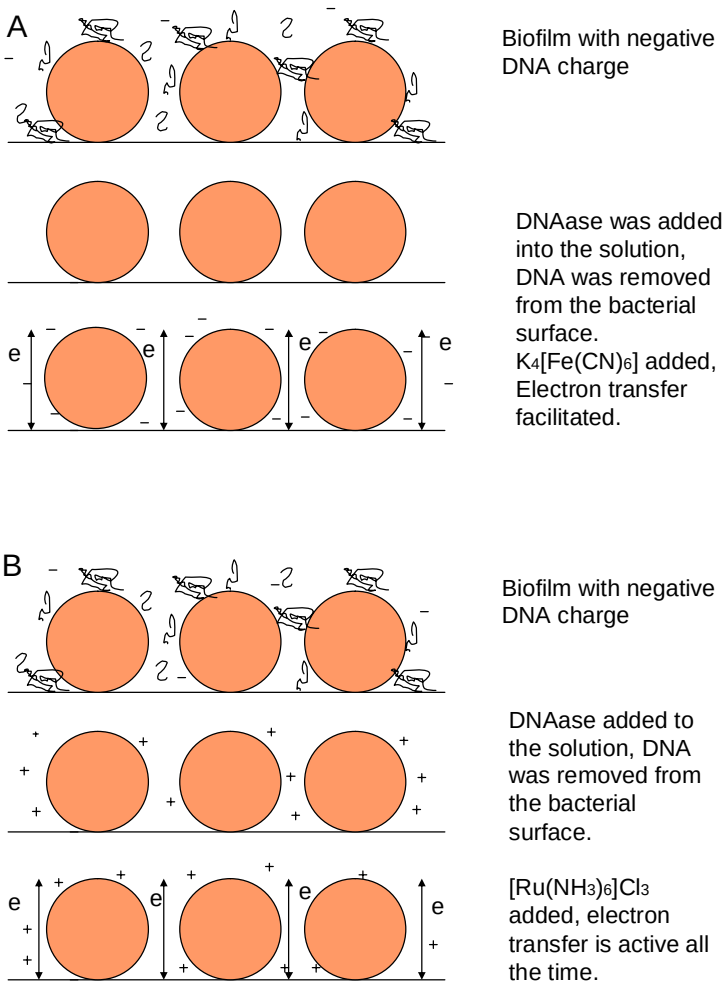

Fig 7.14. A: Molecular model for biofilm with negatively charged DNA and DNAase added. Negatively charged probe molecule present. B: Molecular model for biofilm with positively charged DNA and DNAase added. Positively charged probe molecule present.

We assume the negative charge of biofilms comes from e-DNA. DNAase can remove e-DNA, (Fig 7.14). When e-DNA is removed from the bacterial surface, electron transfer of the negatively charged probe molecules is facilitated (Fig.7.14 A). Efficient electron transfer of the positively charged probe molecules continues and the voltammetric signal

is even strengthened (Fig 7.14B). The model of Fig 7.14 summarizes the observations of DNAase action. DNAase action shows little effect on the voltammetry of the positively charged probe molecules. This is as expected if facile diffusion channels are already available in the fully matured and e-DNA supported biofilm. The DNAase effect is much stronger and towards more efficient access to the Au(111)-electrode surface for the negatively charged probe molecules. This is expected if negative charge, initially blocking e-DNA fragments has left the surface by DNAase action. These studies show new sides of bacterial biofilm growth and structure, as well as probing simple electrochemical processes in biological environment.

7.7 Conclusion

In this chapter, we have studied *Streptococcus mutans* (*S. mutans*) biofilm growth and growth inhibition on Au(111)-surfaces using atomic force microscopy (AFM) and interfacial electrochemistry of redox probe molecules. We have compared the biofilm growth on mica and Au(111)-surfaces, which was followed by sampling at given times, drying the samples naturally and imaging. These two kinds of surfaces have different growth pattern at the initial stage and similar biofilm pattern at the final stage. The redox probes were chosen for their positive ($[Ru(NH_3)_6]^{3+/2+}$, $[Co(terpy)_2]^{3+/2+}$, terpy = 2,2',2"-terpyridine) $[Co(NH_3)_6]^{3+/2+}$ and $[Co(phen)_3]^{3+/2+}$ (phen = 1,10-phenanthroline) or negative ($[Fe(CN)_6]^{3-/4-}$, $[IrCl_6]^{3-/4-}$) electrostatic charge. Inhibition factors of these six probe were also investigated by AFM. $[Ru(NH_3)_6]^{3+/2+}$, and the homologous compound $[Co(NH_3)_6]^{3+/2+}$ were the only probe compounds to inhibit growth.

Voltammetric approaches have been used in bacterial biofilms of whole biological cells adsorbed on electrochemical electrode surfaces, either directly or on surface layers of redox polymers [19-22]. These studies focus on the interfacial electron transfer between binding of the cells and the voltammetric response of redox proteins in the bacterial membrane surface close enough to the electrode surface. In the present study, an electrochemical approach has been used to probe the electrode/biofilm interface in a different way. Both simple interfacial electrochemical electron transfer processes in the inhomogeneous bacterial biofilm environments and properties of the biofilms themselves

were probed, the latter by AFM. In this way electrochemical electron transfer processes based on coordination chemical compounds extend related work at Au-electrodes covered by alkanethiol-based molecular monolayers[38,39]. Single-crystal Au(111)-electrodes were used to distinguish the biofilm structure from surface inhomogeneity in the metal surface structure. In the next chapter, other voltammetric approaches and reductive desorption were applied to study the biofilm on bare and modified Au(111)-surfaces.

The positively and negatively charged redox probe couples displayed different inhibition and voltammetric patterns. Cyclic voltammetry (CV) of both $[Ru(NH_3)_6]^{3+/2+}$ (positively charged, biofilm growth inhibitor) and $[Co(terpy)_2]^{3+/2+}$ (positively charged, no biofilm growth inhibition) displayed fully reversible CVs on biofilm covered electrodes, almost indistinguishable from CV at bare Au(111)-electrode surfaces. In comparison, the CVs of $[Fe(CN)_6]^{3-/4-}$ and $[IrCl_6]^{3-/4-}$ (both negatively charged and no growth inhibition) were distorted from planar diffusion behaviour on bare Au(111)-electrode surfaces towards spherical diffusion behaviour on *S. mutans* biofilm covered Au(111)-electrode surfaces. This supported that the biofilm surface has negative charge. We assume the negative charge of the biofilm surfaces comes from e-DNA of biofilm EPS. DNAase treatment was imposed on the biofilm covered Au(111)-electrode surface in PBS buffer, and it seems that DNAase partly restores planar diffusion CV of $[Fe(CN)_6]^{3-/2-}$ and $[IrCl_6]^{3-/4-}$. A decrease of the growth rate and the appearance of molecular scale structures near the bacterial edges were observed by AFM. The different voltammetric behaviour of positively and negatively charged redox probe molecules can so far be described to electrostatic properties of the local surface environment.

References

1. Costerton, J.W.; Stewart, P.S. and Greenberg, E.P. Bacterial biofilms: a common cause of persistent infections. *Science*, **1999**, 284: 1318–1322.
2. Islam, B. ;Khan, S. N. ; Khan, A. U. Dental caries: from infection to prevention. *Medical Science Monitor*, **2007**, 13 ,196-203.

3. Zhu, L. ; Kreth, J.; Cross, S.E.; Gimzewski, J. K. ; Shi, W. and Qi, F. Functional characterization of cell-wall-associated protein WapA in *Streptococcus mutans*. *Microbiology*, **2006**, 152, 2395-2404.
4. Kuramitsu, H. K. *Streptococcus mutans*: molecular genetic analysis. In Gram-Positive Pathogens, Fischetti, V. A.; Novick, R. P. ; Ferretti, J. J.; Portnoy, D. A.; Rood, J. I. Eds. **2000**, Washington, DC: *American Society for Microbiology*, pp. 280-286.
5. Van Hoogmoed, C.G. ; Dijkstra, R. J. B. ; Van der Mei, H. C. and Busscher, H. J. Influence of Biosurfactant on Interactive Forces between *Mutans Streptococci* and Enamel Measured by Atomic Force Microscopy. *Journal of Dental Research*, **2006**, 85, 54-58.
6. Binnig, G.; Quate , C.F. and Gerber C. Atomic force microscopy. *Physical Review Letters*, **1986**, 56: 930-933.
7. Dufrene, Y. F. Atomic force microscopy, a powerful tool in microbiology. *Journal of Bacteriology*, **2002**, 184, 5205-5213.
8. Dufrene, Y. F. and Hinterdorfer, P. Recent progress in AFM molecular recognition studies. *Pflugers Archic-European Journal of Physiology*, **2008**, 256, 237-245.
9. Qin, Z.; Zhang, J.; Hu, Y.; Chi, Q.; Mortensen, N. P.; Qu, D.; Molin, S. and Ulstrup, J. Organic compounds inhibiting *S. epidermidis* adhesion and biofilm formation. *Ultramicroscopy*. **2009**, 109, 881-888.
10. Duarte, S.; Klein, M.I.; Aires, C.P.; Cury, J.A.; Bowen, W.H. and Koo, H. Influences of starch and sucrose on *Streptococcus mutans* biofilms. *Oral Microbiology Immunology*, **2008**, 23(3): 206-12.
11. Cross, S. E. ; Kreth, J. ; Zhu, L. ; Sullivan, R.; Shi, W. ; Qi, F.; Gimzewski, J. K. Nanomechanical properties of glucans and associated cell-surface adhesion of *Streptococcus mutans* probed by atomic force microscopy under in situ conditions. *Microbiology*, **2007**, 153: 3124-3132.
12. Busscher, H. J. ; Van De Belt-Gritter, B. ; Dijkstra, R. J. B. ; Norde, W. and Van der Mei, H. C. *Streptococcus mutans* and *Streptococcus intermedius* adhesion to

fibronectin films are oppositely influenced by ionic strength. *Langmuir,* **2008**, 24: 10968-10973.

13. Cross, S. E. ; Kreth, J. ; Zhu, L. ; Qi, F. ; Pelling, A. E. ; Shi, W. and Gimzewski, J. K. Atomic force microscopy study of the structure-function relationships of the biofilm-forming bacterium *Streptococcus mutans*. *Nanotechnology*, **2006**, 17: 1-7.
14. Xu,C.; Van De Belt-Gritter, B.; Dijkstra, R.J.B. ; Norde, W. ; Van der Mei, H.C. and Busscher.H.J. Interaction forces between salivary proteins and *Streptococcus mutans* with and without Antigen I/II. *Langmuir,* **2007**, 23: 9423-9428.
15. Velegol, S. B. and Logan, B. E. Contributions of bacterial surface polymers, electrostatics, and cell elasticity to the shape of AFM force curves. *Langmuir,* **2002**, 18: 5256-5262.
16. Velegol, S. B.; Pardi, S. ; Li, X. ; Velegol, D.; Logan, B. E. AFM imaging artifacts due to bacterial cell height and AFM tip geometry. *Langmuir,* **2003**, 19: 851-857.
17. Giao, M.S.; Montenegro, M.I. and Vieira, M.J. Monitoring Biofilm formation by using cyclic Voltammetry-effect of the experimental conditions on biofilm removal and activity. *Water Science and Technology*, **2003**, 47: 51-56.
18. Wang, Y.; Tsujimura, S. ; Cheng, S.; and Kano, K. Self-excreted mediator from Escherichia coli K-12 for electron transfer to carbon electrodes. *Applied Microbiology and Biotechnology*, **2007**, 76: 1439-1446.
19. Busalmen, J. P.; Berna, A. and Feliu, J. M. Spectroelectrochemical examination of the interaction between bacterial cells and gold electrodes. *Langmuir*, **2007**, 23: 6459-6466.
20. Hu, Z.; Jin, J.; Abruna, H. D.; Houston, P. L.; Hey, A.G.; Ghiorse, W.C.; Shuler, M. L.; Hidalgo, G. and Lion, L. W. Spatial distributions of copper in microbial biofilms by scanning electrochemical microscopy. *Environmental Science and Technology*, **2007**, 41: 936-941.
21. Vostiar, I. ; Ferapontova, E. E. and Gorton, L. Electrical "wiring" of viable Gluconobacter oxydans cells with a flexible osmium-redox polyelectrolyte. *Electrochemistry Communications,* **2004**, 6: 621-626.

22. Timur, S. ; Haghigghi, B. Tkac, J. ; Pazarhoĝlu, N. ; Telefoncu, A. and Gorton, L. Electrical wring of *Pseudomonas putida* and *Pseudomonas flluorescens* with osmium redox polymers. *Bioelectrochemistry,* **2007**, 71: 38-45.
23. Marsili, E.; Rollefson, J.B.; Baron, D.B.; Hozalski, R.M. and Bond, D. R. Microbial biofilm voltamemetry: direct electrochemical characterization of catalytic electrode-attached biofilms. *Applied and Environmental Microbiology*, **2008**, 74 (23): 7329-7337.
24. Kasemo, B. Biological surface science. *Surface Science*, **2002**, 500: 656-67**7.**
25. Hamelin, A. Cyclic voltammetry at gold single –crystal surface. Part 1. Behaviors at low index faces. *Journal of Electroanalytical Chemistry*. **1996**, 401: 1-11.
26. Chi, Q. ; Zhang, J. ; Friis, E. P. ; Andersen, J. E. T. and Ulstrup, J. Electrochemistry of self-assembled monolayers of the blue copper protein Pseudomonas aeruginosa azurin on Au(111). *Electrochemistry Communications*, **1999**, 1: 91-96.
27. Kjær, A.M. and Ulstrup, J. Effects of reactant ionic charges and nonlocal dielectric screening on electron transfer between bis(terpyridine)cobalt(II) and tris(phenanthroline) tris(bipyridine) and analogous, electrically neutral sulfonated cobalt(III) complexes. *Inorganic Chemistry*, **1986**, 25: 644-651.
28. Bjerrum, J. ; McReynolds, J. P. In: Inorganic Synthesis; Fernelius, W. C. , Ed.; McGraw-hill, New York, 1946, **1946**, Vol.II, pp. 217-218.
29. a. Baker, B. R. ; Basolo, F. ; Neumann, H. J. Chem. Soc. 1959, 371-375. b. Hogg, R. ; Wilkins, R. G. Exchange studies of certain chelate compounds of the transitional metals. Part VIII. 2,2′,2″-terpyridine complexes *Journal of Chemical Society*. 1962, 341-350. c. Conrad, L. S. ; Christensen, H. E. C. and Ulstrup, J. Electron transfer and spectral a-band properties of the di-heme protein cytochrome c4 from *Pseudomonas stutzeri*. *European Journal of Biochemistry*, **1995**, 231: 133-141.
30. Solomonson, L. P. in Cyanide in Biology, Vennesland, B. ; Conn, E. E. ; Knowles, C. J. , Westley, J. and Wissing, F. , Eds., 1981, pp. 11–28.

31. Matsubara, T. and Ford, P. C. Some applications of cyclic voltammetry to the reactions and properties of ruthenium ammine complexes. Reduction potentials and rate studies. *Inorganic Chemistry*, **1976**, 15: 1107-1110.
32. Cummins, D. and Gray, H. B. Electron-transfer protein reactivities. Kinetic studies of the oxidation of horse heart cytochrome *c*, Chromatium vinosum high potential iron-sulfur protein, *Pseudomonas aeruginosa* azurin, bean plastocyanin, and Rhus vernicifera stellacyanin by pentaammminepyridineruthenium(III). *Journal of American Chemical Society,* **1977,** 99: 5158-5167.
33. a. Farina, R. and Wilkins, R. G. Electron-transfer rate studies of a number of cobalt-(II)-cobalt(III) systems. *Inorganic Chemistry*. 1968, 7: 514-518. b. Kjær, A. M.and Ulstrup, J. Electron transfer from cytochrome *c* to tris(1,10-phenanthroline)cobalt(III) and its electrically neutral sulfonated analog as a probe for direct, image, and nonlocal electrostatic interactions at the protein surface. *Inorganic Chemistry,* **1987**, 26: 2052-2058.
34. Hanania, G. I.; Irvine, D. H. and George, P. Thermodynamic Aspects of Potassium Hexacyanoferrate(III)-(II)-Reduction Potentials. *Journal of Physical Chemistry,* **1967**, 71: 2022-2030.
35. Bossu, F. P.; Chellappa, K .L. and Margerum, D. W. Ligand effects on the thermodynamic stabilization of copper(III)-peptide complexes. *Journal of American Chemistry Society*, **1977**, 99: 2195-2203.
36. Flemming, H. ; Neu, T. R. and Wozniak, D. J. The EPS matrix: The “house of biofilm cells”. *Journal of Bacteriology*, **2007**, 189, 7945-7947.
37. Kjær, A. M.; Kristiánsson, I. and Ulstrup, J. Electronic and solvent electron-transfer rate parameters from charge-transfer spectroscopy of betaine-1 and the $[Fe(CN)_6]^{4-}$ · dimethyl viologen ion pair. *Journal of Electroanalytical Chemistry and interfacial electrochemistry,* **1986**, 204: 45-58.
38. Love, J. C. ; Estroff, F. A. ; Kriebel, J. K. ; Nuzzo, R. G. and Whitesides, G. M. Self-assembled monolayers of thiolates on metals as a form of nanotechnology. *Chemical Reviews,* **2005**, 105: 1103-1169.

39. Chi, Q.; Zhang, J. and Ulstrup, J. Surface Microscopic Structure and Electrochemical Rectification of a Branched Alkanethiol Self-Assembled Monolayer. *Journal of Physical Chemistry. Part B,* **2006**, 110: 1102-1106.

Chapter 8 Investigation of *Streptococcus mutans* biofilm growth on modified Au (111) surfaces using AFM and electrochemistry

8.1. Introduction

In the previous chapter, adhesion properties of *Staphylococcus epidermidis* at the initial stage (Chapter 6), and of *Streptococcus mutans* (*S.mutans*) biofilm growth and its surface charges on Au(111) surfaces (Chapter 7) were studied by AFM and electrochemistry. In this chapter, we describe another study of *S.mutans* biofilm growth on modified Au (111) surfaces based on AFM and electrochemistry.

In the present study we explore a different combination of AFM and electrochemical approaches to *S. mutans* biofilm behavior compared with the approach described in chapter 7. Au(111)-surfaces were modified by self-assembled molecular monolayers (SAMs) of thiol-based molecules. The thiol group links the molecules to the Au-surface while the other end of the molecule faces the solvent. Au(111)-surfaces can be modified into hydrophobic and hydrophilic, or electrostatically charged and neutral surfaces. The modified surface layers can also be "rigid" or soft" by using variable-length pure and functionalized alkanethiols.

Au(111)-surfaces modified by molecular self–assembled monolayers (SAMs) have been used for protein voltammetry even to mapping single-molecule *in situ* protein structure and electrochemical function [1-3]. In the present study, we have used this approach to bacterial adhesion. Fig 8.1 shows schematically the bacterial biofilm formation on the Au (111)-supported SAMs. *S. mutans* growth was first studied by AFM on different SAM-modified Au(111)-surfaces in order to understand the interaction between bacterial surface-adhesion and electrochemically active growth surfaces. Four different thiol-based molecules were chosen. Two are long straight-chain thiols with a hydrophobic and a hydrophilic terminal group, i.e. hexadecanethiol, $HS(CH_2)_{15}CH_3$ and mercapto-hexadecanoic acid, $HS(CH_2)_{15}COOH$, respectively. Two others are the short rigid linker

molecules, L-cysteine and cysteamine. The former exposes both a negatively (-COO^-) and a positively charged terminal group, (-NH_3^+), the latter only a positively charged group (-NH_3^+), Fig.8.2.

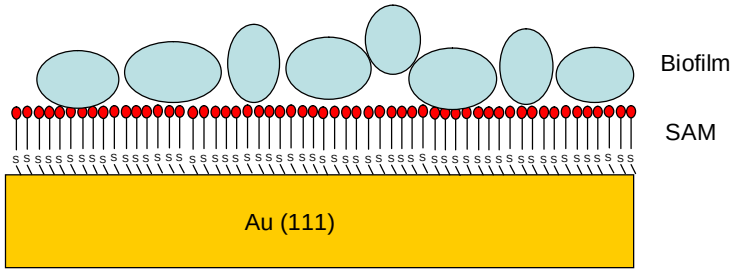

Fig 8.1 A model of *S.mutans* biofilm interaction with thiol-based SAMs on Au (111). From the present work.[4]

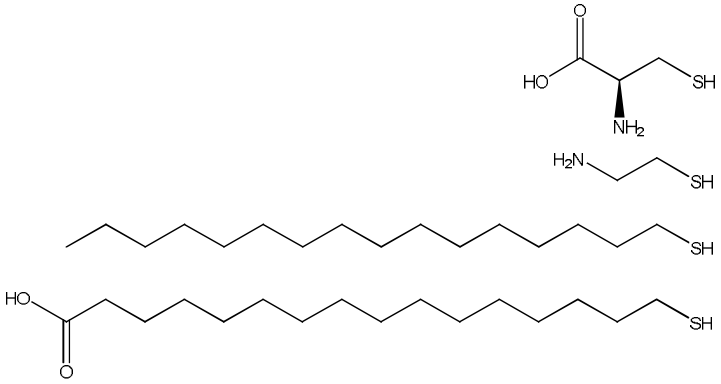

Fig. 8.2 Schematic molecular structures of the four alkanethiols used: $HSCH_2CHNH_2CO_2H$, $HS(CH_2)_2NH_2$, $HS(CH_2)_{15}CH_3$ and $HS(CH_2)_{15}CO_2H$. From the present work.[4]

The electrochemical part is focused on electrochemical reductive desorption (RD) of the thiol-based SAMs in the presence and absence of *S. mutans* bacterial sub-monolayers using cyclic (CV) and linear sweep voltammetry (LSV). The RD process gives strong voltammetric peaks at significantly negative potentials represented by the scheme:

$$Au\text{-}SR + e \rightarrow Au + {}^{-}SR$$

RD is a sensitive fingerprint of the local electrochemical interfacial environment. The Au-S bond strength is indicated by peak position and peak shape of this single-electron electrochemical signal. In addition, RD represent details of the local interfacial environment including effects caused by the adsorption of bacteria on the Au-S modified surface.

We have studied the reductive desorption of SAM-modified Au (111)-surfaces on which *S mutans* biofilms have grown. The electrochemical data were paralleled by AFM of the same surfaces. The growth and RD peak potentials displayed systematic variation along the series of the four SAMs. Hydrophilic and hydrophobic SAM-modified surfaces help us to understand the properties of the bacterial surface based on voltammetric reductive desorption.

8.2. Experimental section

8.2.1 Bacterial strains and growth medium

A *S. mutans* strain (ATCC 25175) was a gift from Laboratory of Microbiology, Department of Odontology, Faculty of Health Sciences, University of Copenhagen (Associate Professor Tove Larsen and Laboratory Technician Natalia Christiansen). *S. mutans* was stored in Brain Heart Infusion broth (BHI) medium at -80 ^{o}C and incubated in BHI broth shaken at 37 ^{o}C overnight [5].

8.2.2 Cultivation of biofilms on solid surfaces

S. mutans was cultivated on bare and SAM-modified Au (111) in BHI media for 24 hours and sampled by AFM after suitable time periods (4 h and 24 h). Overnight cultures of *S.mutans* strains grown in BHI medium were diluted to OD_{600} = 0.05 into fresh BHI medium. The clean gold sample was added, sealed by Parafilm, and incubated for given lengths of time at 37 ºC. The Au(111) sample was then washed three times with Millipore water. The sample was placed in a new Petri dish to dehydrate naturally for one day

before imaged by AFM, but used directly without drying for cyclic voltammetry and linear sweep voltammetry. Bare Au(111)- or SAM-modified Au(111)-surfaces without *S. mutans* were used as reference experiments.

8.2.3 Reagents

$HS(CH_2)_{15}CH_3$ (1-hexadecanethiol, MHD, >90%), NaOH ultrapure solution (30%) and ethanol (99.99%) were from Merck. $HS(CH_2)_{15}CO_2H$ (ω-mercaptohexadecanoic acid, MHDA, 98%) and L-Cysteine (> 98%) were from Sigma-Aldrich. Cysteamine (98%) was from Fluka. The PBS buffer (0.010 M phosphate, 0.14 M NaCl and 0.027 M KCl, pH = 7.4) was prepared from PBS tablets (Medicago, Sweden). Millipore water (18.2 MΩ cm) was used throughout.

8.2.4 SAM-modified Au(111)-surfaces

Au(111)-electrode surfaces were used either in the form of bead electrodes prepared by the method of Hamelin [6,7], or as 12 mm diameter Au(111) discs (Surface Preparation Lab, The Netherlands). The Au(111)-surface quality was checked by voltammetry and *in situ* STM[7]. Before use, Au (111) was annealed in a hydrogen flame, quenched in Millipore water saturated with hydrogen gas and transferred to freshly prepared BHI medium or freshly prepared thiol solutions. The SAM-modified Au(111)- surfaces were prepared by immersing the Au(111) electrodes overnight in 1 mM solutions of $HS(CH_2)_{15}CH_3$ or $HS(CH_2)_{15}CO_2H$ in ethanol or 1 mM L-Cys or Cysteamine in Millipore water followed by rinsing with ethanol and Millipore water.

8.2.5 Atomic force microscopy (AFM), sample preparation and image recording

The Atomic force microscope was a PicoScan 5500 from Agilent instrument (Agilent Technologies, Chandler, AZ, USA) with a 100 μm scanner and cantilevers (NP-S) from Veeco (Camarillo, CA, USA). The contact mode was used. All AFM images shown are

representative of a large number of images. The 12 mm diameter Au(111)-discs were used for AFM observation.

8.2.6 Electrochemistry

Cyclic voltammetry was carried out using an Autolab-system (Eco Chemie, The Netherlands). The electrochemical cell was kept in a Faraday cage, and the hanging meniscus method used. A freshly prepared reversible hydrogen electrode (RHE) was used as a reference electrode and checked against a saturated calomel electrode (SCE) after each measurement. A bright coiled Pt wire served as counter electrode. All potentials are reported vs. SCE. Purified Ar (5 N, Chrompack) was used to deoxygenate all solutions and an argon stream kept over the solution. The PBS buffer (0.010 M phosphate, 0.14 M NaCl, 0.0027 M KCl, pH = 7.4) and 0.1 M NaOH solution (for RD) were supporting electrolytes. Pure and SAM-modified Au (111) with bacterial biofilms or BHI media were washed by Millipore water and transferred directly to the electrochemical cell.

8.3. AFM of S.mutans

8.3.1 *S. mutans* growth on modified Au(111) surface

In my project, we investigated *S.mutants* biofilm growth conditions on modified Au(111) surfaces, and compared with electrochemical results on the same modified Au(111) surface. We explored first *S mutans* biofilm growth on bare single-crystal Au(111)-surfaces or SAM modified Au(111)-surfaces by AFM. Both the short functionalized strongly hydrophilic L-Cys and cysteamine, and the long hexadecane thiol (strongly hydrophobic) and mercaptohexadecanoic acid (hydrophic with a hydrophilic end group) were used. Figs.8.3 and 8.4 present AFM images of *S. mutans* biofilms grown for 4 and 24 hours on a bare Au(111)-surface and on Au(111)-surfaces modified by the 16-carbon thiol SAMs with hydrophilic (MHDA) or hydrophobic end groups (MHD). Bacterial biofilms can grow with time on all the bare Au (111) and SAM-modified Au(111)-surfaces from 4 hours to 24 hours. The biofilms on the bare Au(111)-surface has similar growth pattern as biofilms on the hydrophilic (MHDA), while the biofilms grow faster on

the hydrophobic (MHD) SAM-modified Au(111)-surface. Similar results were observed for 18-carbon octadecanethiol SAMs (Fig 8.5B), for which the biofilm coverage is even higher than on 16-carbon MHD SAMs (Fig 8.3F). The AFM images also show that *S. mutans* grow in almost the same patterns on either bare Au(111), and on L-Cysteine and cysteamine modified Au(111)-surfaces (Fig 8.5A shows only L-Cysteine). From the detailed comparison of the biofilm growth after the 4 hours (Fig 8.4), they seem all similar. In chapter 7, we observed that biofilm formation has different growth patterns on Mica and Au(111) surface at the initial time, perhaps because of the different surface structures of the two substates.

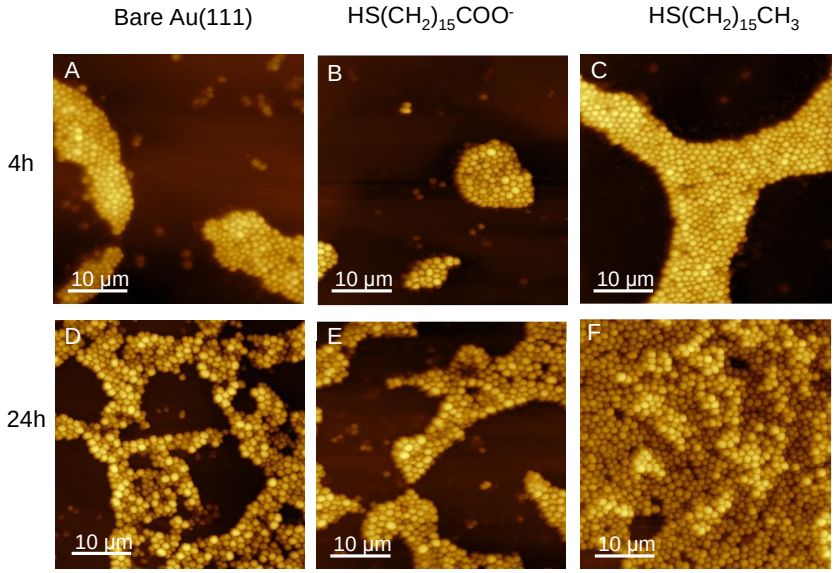

Fig 8.3 AFM images of *S. mutans* biofilms grown for 4 and 24 hours on bare and modified Au (111) surface. A and D: Au (111); B and E : $HS(CH_2)_{15}CO_2H$; C and F; $HS(CH_2)_{15}CH_3$. A, B, C: 4 hour; D, E, F: 24 hour. 40 × 40 μm^2. Contact mode.

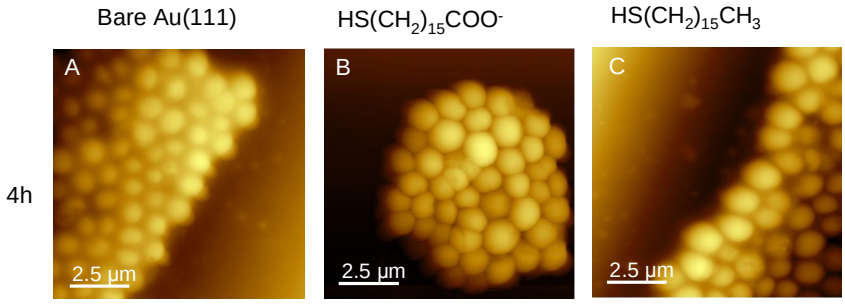

Fig 8.4 AFM images of *S. mutans* biofilms grown for 4 hours on bare and modified Au (111)-surface. A: Au (111); B: $HS(CH_2)_{15}CO_2H$; C; $HS(CH_2)_{15}CH_3$. 10 × 10 μm^2. Contact mode.

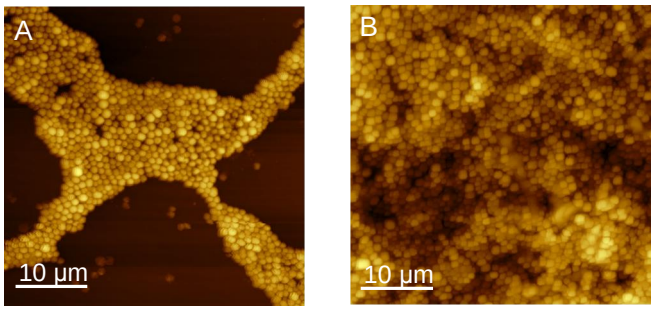

Fig 8.5 AFM images of *S. mutans* biofilms grown for 24 hours on modified Au (111)-surface. A: L-Cys; B: 18-carbon octadecanethiol SAMs $HS(CH_2)_{17}CH_3$. 40 × 40 μm^2. Contact mode.

8.3.2 *S. mutans* degradation on modified Au(111) surface

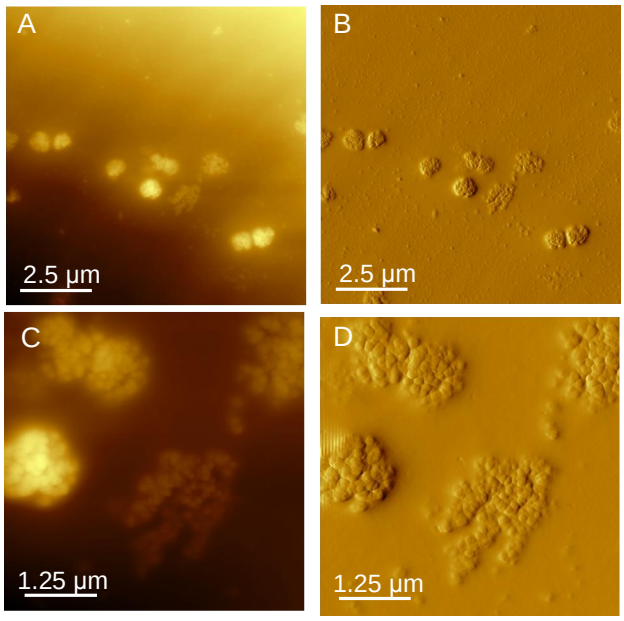

Fig 8.6 AFM images of degraded cells scattered over the $HS(CH_2)_{15}CH_3$ modified Au(111)-surface.

During the experiments, we found *S.mutans* cells that appeared to have degraded on the thiol modified Au (111)-surfaces. This was not observed on bare Au (111)-surfaces, Chapter 7[5]. Fig. 8.6 shows that some *S. mutans* cells have degraded on the MHDA and MHD SAM-modified Au (111)-surfaces during the initial stage, 4 hour growth. These

cells do not form biofilms but are distributed individually over the alkanthiol SAM surface. This pattern is in contrast to bare Au(111)- or mica surfaces[5]. Individually scattered degraded cells are seldomly found on the fully developed biofilms on modified Au(111)-surface, say after 24 hour growth. It is also possible that the modified surface has left some active thiol molecules, which are not bound on the Au (111) and form Au-S bond. On the other hand, it shows the potential of MHDA and MHD molecular to inhibit or degrade the bioiflm formation.

8.3.3 Summary

Au-electrodes differently modified by thiol-based SAMs provide a perspective for bacterial growth on a wide variety of hydrophobic and hydrophilic surfaces. We studied *S mutans* biofilm growth on bare single-crystal Au(111)-surfaces or Au(111)-surfaces modified by SAMs of both the short functionalized strongly hydrophilic L-Cys and cysteamine, and by SAMs of the long hexadecane thiol (strongly hydrophobic) and mercaptohexadecanoic acid (hydrophobic with a hydrophilic end group). The combination of the electrochemical approach with AFM atomically was used for this planar Au (111)-surface.

S. mutans biofilms grow in BHI medium both on bare Au (111)-surfaces and on Au (111)-surfaces modified by any of the four SAMs. The growth was tracked by AFM. AFM images showed that *S. mutans* had grown to multilayers on all the four modified Au(111)-electrode surfaces after 24 hours. The growth rates were slightly different and fastest for MHD-modified surfaces but the biofilms after 24 hours were indistinguishable.

The membrane proteins and other active compounds on the bacterial surfaces can determine the overall cell hydrophilicity or hydrophobicity. *P. aeruginosa* and *E. coli* tend to adhere most strongly to the hydrophilic surfaces, whereas others adhere preferentially to hydrophobic surfaces[8]. AFM tips modified by whole bacterial cells have been used to detect specific (strong) hydrophobic adhesion forces between the tip-modifying bacteria and the underlying substrate surfaces[9]. In a previous study, different *S.*

mutans strains display both hydrophobic and hydrophilic properties depending on growth conditions and substrates, in other words *S. mutans* is neither "absolutely" hydrophobic nor "absolutely" hydrophilic [10]. In the present study, *S. mutans* could grow well on all the four modified Au (111)- surfaces. It is clearly to be the strongest on hydrophobic surfaces and especially on the long-chain 16-carbon hydrophobic MHD (and 18-carbon octadecanethiol) SAM-modified Au(111)-surfaces. The bacterial cell degradation at the initial time was noticed in Fig 8.6. The thiol moleculaes may therefore, have some other function that can be considered for future medical treatment.

8.4 CV of Au (111)/SAMs

8.4.1 CV of Au (111)/SAMs in PBS buffer

In this part of the experiments, we studied control experiments CV of modified Au (111)-surfaces onto which bacteria had been immobilized. PBS buffer pH was 7.4, which is easy for bacterial biofilm growth. The reductive Au-S desorption process was the fingerprint, Fig 8.7 shows reductive desorption (RD) of the four different alkanethiols SAMs on the Au(111)-surface, i.e. the two short-chain L-cys (A) and cysteamine (B), and two long straight-chain alkanethiols $HS(CH_2)_{15}CH_3$ (C) and $HS(CH_2)_{15}CO_2^-$ (D) in 10 mM PBS buffer, pH 7.4 in the absence of bacteria. The voltammograms of L-cys and cysteamine voltammograms have a sharp peak with satellite peaks, while the voltammograms MHDA and MHD have only a single strong peak. The dominating peak potentials are significantly more negative for the long alkanethiols, like -1.11 V for both MHD and MHDA, than for the short functionalized thiols, -0.61 and -0.52 V for L-Cys and cysteamine, respectively. These observations follow reported trends [11,12] due to the less favourable desorption and solvation of the longer hydrophobic alkanethiols than of the shorter strongly hydrophilic thiol-based molecules. There is a limitation to the sensitivity of the peaks because the reductive desorption signals often overlap with signals from dihydrogen evolution in this pH-range. Completion of the RD process requires four to five successive scans. The satellite peaks seem to disappear first for L-cys but remains for cysteamine (at -0.80 V) until complete molecular desorption. This is

consistent with other voltammetric behaviour of cysteamine and with the dual orientation of this molecule as disclosed clearly by *in situ* STM [3].

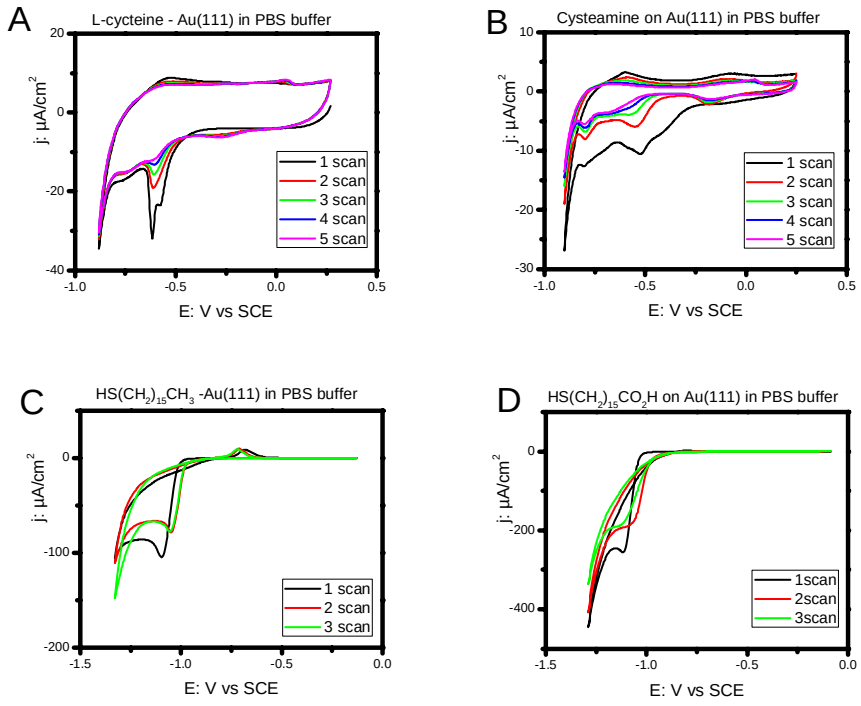

Fig 8.7 CVs of the four alkanethiol SAMs on Au(111)-surfaces, in 10 mM PBS buffer, pH 7.4. Scan rate 20 mV s^{-1}, A: $HSCH_2CHNH_3^+CO_2^-$; B: $HS(CH_2)_2NH_3^+$; C: $HS(CH_2)_{15}CH_3$; D: $HS(CH_2)_{15}CO_2^-$.
Black line: 1st scan; Red line: 2nd scan; Green line: 3rd scan; Blue line: 4th scan; Pink line: 5th scan. The surface coverage and RD potential of the dominating peak for 1st scan: A: 2.69×10^{-10} mol cm^{-2}, -0.614V ; B: 1.21×10^{-10} mol cm^{-2}, -0.521V; C: 9.80×10^{-10} mol cm^{-2}, -1.110V ; D: 1.36×10^{-9} mol cm^{-2}, -1.108V;

8.4.2 CVs of Au (111)/SAMs in 0.1M NaOH solution

PBS, pH around 7 represents biological buffer solutions. But sharper RD signals can be obtained in strongly alkaline media due to stronger suppression of interfereing electrochemical dihydrogen solution and better solvation of the liberated thiolate anion [3,11-14]. Fig 8.8 shows linear sweep voltammograms for the RD process of the sixteen carbon -CH_3 terminated and –COO^- terminated alkanethiol SAMs on the Au(111) surface in 0.1M NaOH solution. The RD peak potential, E_p for the –COO^- terminated alkanethiol is about 60 mV more positive than for the -CH_3 terminated alkanethiol surface (Fig 8.8A).

The surface coverage of the latter is decreased from 7.13×10^{-10} mol cm^{-2} to 5.45×10^{-10} mol cm^{-2} after the first scan and then remains stable in following scans, while E_p is shifted from -1.19 to -1.17 V. The surface coverage of the $-COO^-$ terminated alkanethiol (Fig 8.8B), is decreased from 8.88×10^{-10} to 6.01×10^{-11} mol cm^{-2} followed by complete disappearance after several more scans, while E_p is shifted from -1.13 V to -0.99 V, which is more positive than for the $-CH_3$ terminated thiol. This is due to the much higher solubility of MHDA than of MHD in aqueous solution. All the SAM peak potentials in the absence of bacterial biofilms are summarized in Table 8.1.

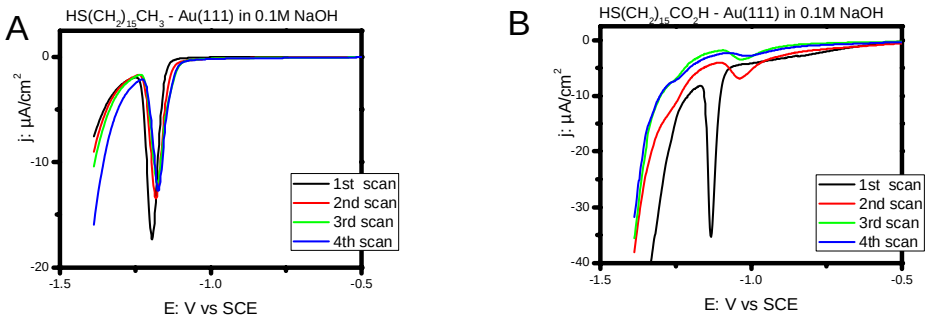

Fig 8.8 LSV for reductive desorption of $HS(CH_2)_{15}CH_3$ and $HS(CH_2)_{15}CO_2^-$ SAMs on Au(111)-surfaces. 0.1 M NaOH solution, pH 13. Scan rate 10 mV s^{-1}. A: $HS(CH_2)_{15}CH_3$; B: $HS(CH_2)_{15}CO_2^-$. The surface coverage and RD peak potentials are: Black line: 1st scan (A: 7.13×10^{-10} mol cm^{-2}, -1.19 V and B: 8.88×10^{-10} mol cm^{-2}, -1.13 V); Red line: 2nd scan (A: 5.93×10^{-10} mol cm^{-2}, -1.18V and B: 2.62×10^{-10} mol cm^{-2}, -1.04V); Green line: 3rd scan (A: 5.71×10^{-10} mol cm^{-2}, -1.18 V and B: 1.93×10^{-10} mol cm^{-2}, -1.03V); Blue line: 4th scan (A: 5.45×10^{-10} mol cm^{-2}, -1.17 V and B: 6.01×10^{-11} mol cm^{-2}, -0.99 V).

8.5 CV of S.mutans on SAM-modified Au(111)

8.5.1 CV of *S.mutans* on SAM-modified Au(111) in PBS buffer

Bacterial biofilms were grown on the modified Au (111) surface. Fig 8.9 shows CVs of bare and of L-Cys and cysteamine modified Au (111)-surfaces in PBS buffer in the absence (upper voltammetric traces) and presence of *S. mutans* grown on the surface (lower voltammetric traces). *S. mutans* had grown in the BHI medium for 24 hours and the voltammograms then been recorded. Fig 8.10 shows a similar representation of the

CVs of bare, and $HS(CH_2)_{15}CH_3$ and $HS(CH_2)_{15}CO_2^-$ modified Au(111)-surfaces in PBS buffer. The upper voltammetric traces refers only to the bare and SAM-modified Au(111) in PBS buffer. The middle traces show the voltammograms in the presence of the BHI growth medium but in the absence of the biofilm on the bare and SAM-modified Au(111) as a control. The lower voltammetric traces refer to the bare and SAM-modified Au(111) in the presence of a *S. mutans* biofilm in BHI medium.

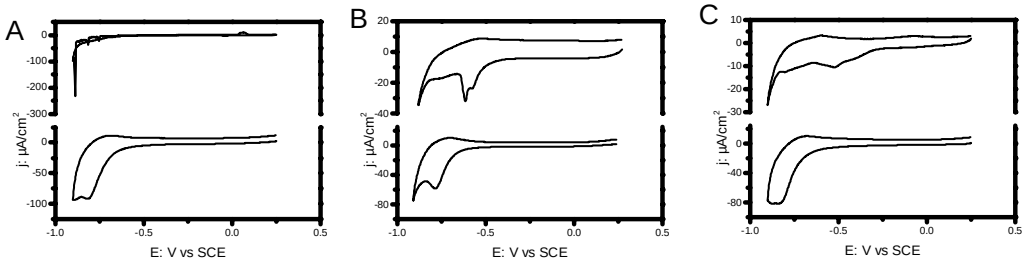

Fig 8.9 CVs of L-Cys, $HSCH_2CHNH_3^+CO_2^-$ and cysteamine, $HS(CH_2)_2NH_3^+$; Au(111) surfaces in the absence (upper voltammetric traces) and presence of 24 h *S. mutans* biofilms in BHI medium (lower voltammetric traces). 10 mM PBS buffer, pH 7.4. Scan rate 20 mV s^{-1}. A: bare Au(111) surfaces; B: L-Cys Au(111) surfaces; C: cysteamine Au(111)-surfaces. In the ABC, the first line is bare or modified Au(111) in PBS buffer, the second line is *S. mutans* biofilms for 24h growth in BHI media on bare or modified Au (111).

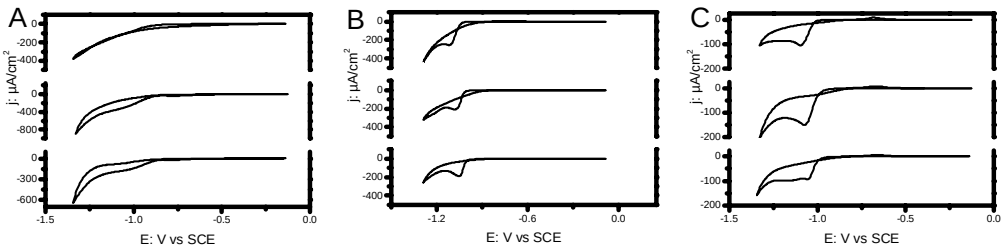

Fig 8.10 CVs of MHD, $HS(CH_2)_{15}CH_3$ and MHDA, $HS(CH_2)_{15}CO_2^-$ Au(111) surfaces. 10 mM PBS buffer, pH 7.4. Scan rate 20 mV s^{-1}. A: bare Au(111) surfaces; B: $HS(CH_2)_{15}CO_2^-$ Au(111) surface; C: $HS(CH_2)_{15}CH_3$ Au(111) surfaces. In A, B, and C, the upper voltammetric traces are for bare or modified Au (111) in PBS buffer, and the lower voltammetric traces for *S. mutans* biofilms after 24h growth in BHI media on bare or modified Au (111). The middle voltammetric traces are a control with only BHI media after 24 h adsorption on bare or modified Au (111).

It is first noted that the adsorption of *S. mutans* biofilms on bare Au(111) and on L-Cys and cysteamine modified Au(111), Fig.8.9 gives a strong and rather broad voltammetric signal in the RD region peaked at -0.75 to -0.79 V. The peak is shifted negatively compared to the RD signals of L-Cys and cysteamine in the absence of biofilm and shows only slight differences among the three Au(111)-electrode surfaces.

The voltammetric reflection of the biofilm and the growth medium adsorption on bare and modified Au(111)-surfaces based on the long-chain alkanethiols is more subtle, Fig 8.10. A broad peak again appears at bare Au(111) in the middle and lower voltammetric traces, Fig 8.10.A. The RD peak of the MHDA-modified Au(111)-surface also show only small differences when BHI growth medium and the biofilms are present, with E_p slightly positively shifted, from -1.11V to -1.08V and -1.05V, respectively in Fig 8.10.B. A similar RD pattern of biofilm/BHI adsorption on the MHD-modified Au(111)-surface is shown with at least two peaks both shifted positively relative to the pure MHD RD peak (the strongest peak from -1.11V to -1.08 V and -1.04 V) in Fig 8.10.C. The MHD and MHDA peaks are closely similar, but the MHDA peak decays with time and disappears, while the MHD peak only decays slightly and then stays stable.

BHI medium is the medium for the bacterial biofilm formation, and is close to the natural growth conditions. Here we used BHI medium as a control experiments to find out the voltammetric changes from *S.mutans* biofilms Fig.8.10, middle shows voltammetric traces of the BHI medium alone without *S. mutans* biofilm. The BHI voltammograms on bare and MHDA- and MHD- modified Au(111)-surfaces are only slightly different. This follows the observations for the other hydrophilic L-Cys- and cysteamine-modified Au(111)-surfaces.

Conclusions from the data in Figs.8.9 and 8.10 are then, first that the SAMs initially present on the Au(111)-surface remains after live *S mutans* and growth medium addition and are not displaced by other thiols from BHI or bacterial surfaces. The RD signals of both the three hydrophilic SAMs (L-Cys, cysteamine and MHDA) and of the

hydrophobic MHD SAM only have slight differences. All the coverages and peak potentials are summarized in Table 8.1.

Table 8.1 Summary of linear sweep voltammograms for the reductive desorption of pure, $HS(CH_2)_{15}CH_3$, $HS(CH_2)_{15}CO_2^-$, L-Cys, $HSCH_2CHNH_3^+CO_2^-$ and cysteamine, $HS(CH_2)_2NH_3^+$ on bare Au(111)-surfaces in PBS buffer, pH 7.4. Scan rate 20 mV s^{-1}.

SAMs	The first scan	Charge (*10^{-5} C cm^{-2})	Surface coverage (*10^{-10} mol cm^{-2})	Peak potential VS SCE (V)
$HS(CH2)_{15}CO_2^-$	Blank	13.13	13.61	-1.108
/ Au (111)	Medium 24h	6.87	7.12	-1.078
	S.mutans 24h	10.12	10.49	-1.045
$HS(CH_2)_{15}CH_3$	Blank	9.45	9.80	-1.110
/ Au (111)	Medium 24h	8.41	8.72	-1.075
	S.mutans 24h	1.06	1.10	-1.042
Bare Au (111)	Blank		No peak	
	Medium 24h		No peak	
	S.mutans 24h		No peak	
L-cys / Au (111)	Blank	2.60	2.69	-0.614
	Medium 24h		No peak	
	S.mutans 24h		No peak	
Cysteamine	Blank (peak 1)	1.16	1.21	-0.521
/ Au (111)	Blank (peak 2)	0.04	0.05	-0.803
	Medium 24h		No peak	
	S.mutans 24h		No peak	

8.5.2 CV of *S. mutans* on modified Au(111) in 0.1M NaOH solution

As a comparison LSVs of the RD process of MHDA- and MHD-modified Au(111)-surfaces in 0.1 M NaOH were also recorded in the absence and presence of *S. mutans* biofilms and BHI growth medium. Fig 8.11 shows LSV for the RD of $HS(CH_2)_{15}CH_3$ and $HS(CH_2)_{15}CO_2^-$ SAMs on Au(111)-surfaces in 0.1 M NaOH solution, in only PBS buffer (Black), in the presence of *S. mutans* biofilms and BHI growth medium (green lines) or in the absence of *S. mutans* biofilms and in the presence of the BHI growth medium alone

(red lines). Both the BHI growth medium and the *S. mutans* biofilm in BHI medium give small but sharp and clear RD signals on bare Au(111)-surfaces, Fig.8.11A, with E_p-values of -0.92 V and -0.94 V, respectively. These peaks cannot be detected in PBS buffer on bare Au(111)-surfaces. It can be unknown small thiols molecules in the BHI medium and *S.mutans* with BHI medium according to the peak height and peak charges, and the size of the large charge. Table 8.2 summarizes the surface coverage and E_p value of the RD peak from the first scan. The sharp RD peaks of the pure and functionalized alkanethiols are maintained on adsorption of either *S. mutans* with BHI medium or the BHI medium alone. The MHDA and MHD surface coverage in PBS buffer is bigger than that in the presence of either BHI medium alone or *S. mutans* biofilms with BHI medium. E_p in the presence of *S. mutans* is slightly more negative than in the presence of the BHI medium alone or for the pure alkanethiol SAMs in PBS buffer, while E_p of the BHI medium alone is slightly positive compared with the values for both the *S. mutans* biofilms and pure alkanethiol SAMs, Table 8.1. The data support that the *S. mutans* biofilms are preferentially attached to the hydrophobic surface whereas the BHI medium itself behaves as hydrophilic character in this case. Fig 8.11B and Fig 8.11C show the same feature as in Fig 8.7, i.e. RD peak for -CH_3 terminated MHD first decays and then stays stable over successive scans, while the RD peak of -COO^- terminated MHDA decays and moves in positive direction on successive scanning, ultimately disappearing. That is because -COO^- terminated MHDA molecules can dissolve in the PBS buffer with time, while -CH_3 terminated MHD molecules can only dissolve to a small extent in PBS buffer and is then reabsorbed on the Au(111) surface again.

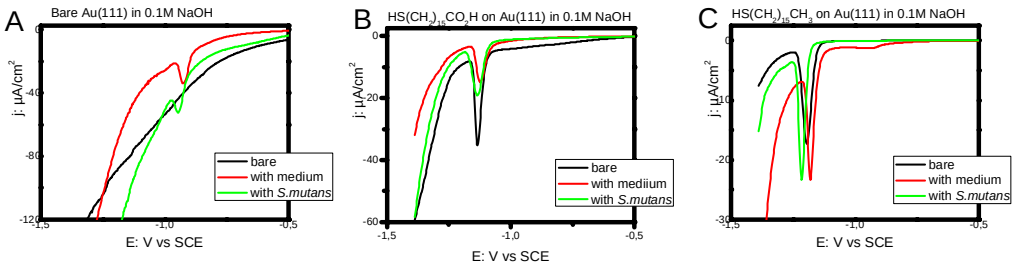

Fig 8.11 LSV for the RD at bare, and at MHD, $HS(CH_2)_{15}CH_3$ and MHDA, $HS(CH_2)_{15}CO_2^-$ Au(111) surfaces in 0.1 M NaOH solution, pH 13 in the absence and presence of *S. mutans* biofilm with BHI growth medium and with the BHI growth medium alone. Scan rate 10 mV s^{-1}. A: bare Au(111) surface; B:

$HS(CH_2)_{15}CO_2^-$; C: $HS(CH_2)_{15}CH_3$ on Au(111) surfaces. In A, B, and C, the black line is pure or modified Au(111) in 0.1M NaOH solution, the red line is with only BHI media after 24 h adsorption on Au(111) or modified Au(111), and the green line *S. mutans* biofilms with BHI medium after 24 h growth in BHI medium on Au(111) or modified Au(111).

Table 8.2 Summary of linear sweep voltammograms for the reductive desorption of pure, $HS(CH_2)_{15}CH_3$ and $HS(CH_2)_{15}CO_2^-$ on Au(111) surfaces in 0.1 M NaOH solution, pH 13. Scan rate 10 mV s^{-1}.

SAMs	The first scan	Surface coverage ($*10^{-10}$ mol cm^{-2})	Peak potential VS SCE (V)
$HS(CH2)_{15}CO_2H$ / Au (111)	Blank	8.50	-1.134
	Medium 24h	5.16	-1.123
	S.mutans 24h	7.33	-1.132
$HS(CH_2)_{15}CH_3$ / Au (111)	Blank	7.13	-1.204
	Media24h	5.85	-1.183
	S.mutans 24h	6.54	-1.212
Bare Au (111)	Blank	No peak	
	Medium 24h	6.53	-0.924
	S.mutans 24h	4.54	-0.943

8.5.3 Summary

Use of variably modified metallic surfaces as substrates for bacterial biofilm growth provide a potential idea for the use of electrochemistry to characterize and control bacterial growth [5,15-17]. *S mutans* biofilm formation on bare single-crystal Au(111)-surfaces or Au(111)-surfaces modified by SAMs of L-Cys and cysteamine, and by SAMs of hexadecane thiol (strongly hydrophobic) and mercaptohexadecanoic acid (hydrophic with a hydrophilic end group) has been explored. The combination of the electrochemical approach with AFM was based on the use of atomically planar Au(111)-surfaces.

The electrochemistry (CV and LSV) was used to characterize the resulting biofilms by using the thiol reductive desorption process as a probe reaction. The peak potential and shape of the peaks of this process are sensitive detectors of the SAM modified surfaces and their local environment. The sensitivity of the RD peak is noted to detect the protein

adsorption on top of thiol-based SAMs in the previous study[18]. Here we have found that it is also sensitive to adsorption of both *S. mutans* biofilms and of the BHI growth medium itself.

The RD CVs and LSVs of the *S.mutans* biofilm with BHI medium and only BHI medium covered bare and SAM-modified Au(111)-surfaces at pH 7.4 were similar, Fig.8.9. Similar voltammetric patterns of the two straight-chain long thiols MHD and MHDA were also shown by only the BHI medium (before growth) and *S.mutans* biofilm with BHI medium (after bacterial growth) on bare and SAM-modified Au(111)- surfaces in Fig 8.10. It seems that the RD signal is hard to distinguish between the bacterial biofilm and the biological PBS buffer.

The RD data in 0.1 M NaOH show differences. First, the RD feature remains very sharp on adsorption of BHI medium and *S. mutans* biofilms on both MHD- and MHDA-modified Au(111)-surfaces. Secondly, a clear and relatively sharp peak also appears when either BHI medium or bacteria with BHI medium are adsorbed on a bare Au(111)-surface. Third, the RD peak on the hydrophobic MHD surface is distinctly shifted compared to the RD peak of the MHD SAM alone, and notably in different directions for the *S. mutans* biofilm with BHI medium (negative shift) and for the BHI medium alone (positive shift). A similar difference is also observed between *S. mutans* biofilm plus BHI growth medium and BHI growth medium alone on bare Au(111).

These observations can be compared with the AFM/electrochemical study of *S. mutans* biofilms described in chapter 7[5]. Bare Au(111)-surfaces (and mica surfaces) and six small reversible redox probes were used there. In Chapter 7, we disclosed electrostatic field effects as reflected in the different voltammetric behaviour of positively and negatively charged transition metal probe molecules at the biofilm-covered Au (111) surfaces. Here it is pointed that *S.nutans* biofilms are preferentially adsorbed on hydrophobic surfaces. The overall interfacial Au(111)/SAM/biofilm/solution interface is therefore complex with covalent, hydrophobic and electrostatic interactions but subject to mapping in some detail by the combined electrochemical and AFM approach.

8.6 Conclusion

Streptococcus mutans Biofilms are the most important direct cause of human dental caries formation. In this chapter, we have studied *S. mutans* biofilm formation and properties on Au(111)-electrode surfaces modified by self-assembled molecular monolayers (SAMs) of different thiol-based molecules based on a combination of atomic force microscopy (AFM) and electrochemistry. The thiols were chosen to include both small, strongly hydrophilic molecules (cysteamine and the amino acid L-cystein) and long straight-chain alkanethiol-based molecules with either hydrophobic (hexadecanethiol, MHD) or hydrophilic (mercapto-hexadecanoic acid, MHDA) end groups. The voltammetric reductive desorption (RD) peak is a sensitive probe of the SAM local environment. The RD peaks of the thiol-based SAMs in the absence and presence of *S.mutans* biofilms in BHI medium and BHI medium were therefore studied .

AFM showed that *S. mutans* grows to dense monlayers on all the four modified Au(111)-electrode surfaces after 24 hours. The growth rates were slightly different and fastest for MHD-modified surfaces but the biofilms after 24 hours showed no differences. Reductive desorption signals of the four compounds in PBS buffer, pH 7.4 were very similar in the absence and presence of *S.mutans* biofilms in BHI medium and BHI medium alone. RD in strongly alkaline solution where RD peak resolution is higher was also addressed. The strong RD peaks of the long pure and functionalized MHD and MHDA in 0.1 M NaOH remained in the presence of either *S.mutans* biofilms in BHI medium or BHI medium alone. The RD peak potential of the hydrophilic MHDA surface had small changes but the RD peak of the hydrophobic MHD SAM is distinctly shifted compared to the pure MHD SAM. The shifts were further in different directions for the *S. mutans* biofilm with BHI medium (negative shift) and for the BHI medium alone (positive shift). Both the AFM images and the electrochemical data support that the biofilms form more efficiently and interact more strongly with the hydrophobic surface than with the hydrophilic surfaces.

In conclusion, the combined AFM and electrochemical approaches has provided mapping of the biofilm formation at the single bacterial level of resolution and some

disentanglement of surface forces in the metal/SAM/biofilm/solution interfacial region. Proteins have been structurally mapped to single-molecule resolution and the voltammetric behaviour of the fully functional proteins immobilized on the same SAM-modified Au(111)-surfaces characterized, which can be compared with the present work[18]. In the future, we may observe directly the live bacterial biofilms with high resolution and control the biofilm formation on SAM-modified Au(111)-surfaces by the combination of AFM mapping and electrochemical characterization.

References

1. Imabayashi, S.; Iida, M.; Hobara, D.; Feng, Z.; Niki, K. and Kakiuchi, T. Reductive desorption of carboxylic acid terminated alkanethiol mnolayers from Au (111) surface. *Journal of Elelctroanalytical Chemistry*, **1997**, 428: 33-38.
2. Vericat, C.; Vela, M.E.; Benitez, G.; Carro, P. and Salvarezza, R.C. Self-assembled monolayers of thiols and dithiols on gold: new challenges for a well-known system. *Chemical Society Review*, **2010**, 39: 1805-1834.
3. Zhang, J.; Bilič, A,; Reimers, J.R. ; Hush, N.S. and Ulstrup, J. Coexistence of multiple conformations in cysteamine monolayers on Au(111). *Journal of Physical Chemistry B*, **2005**, 109: 15353-15367.
4. Hu, Y.; Zhang, J. and Ulstrup, J. Investigation of *Streptococcus mutans* biofilm growth on modified Au (111)-surfaces using AFM and electrochemistry. *Journal of Electroanalytical Chemistry*, **2011**, 656 (1-2): 41-49.
5. Hu, Y.; Zhang, J and Ulstrup. J. Interfacial Electrochemical Electron Transfer Processes in Bacterial Biofilm Environments on Au(111). *Langmuir*, **2010,** 26 (11): 9094-9103.
6. Hamelin, A. Cyclic voltammetry at gold single –crystal surface. Part 1. Behaviors at low index faces. *Journal of Electroanalytical Chemistry*. **1996**, 401: 1-11.
7. Chi, Q. ; Zhang, J. ; Friis, E. P. ; Andersen, J. E. T. and Ulstrup, J. Electrochemistry of self-assembled monolayers of the blue copper protein Pseudomonas aeruginosa azurin on Au(111). *Electrochemistry Communications*, **1999**, 1: 91-96.

8. Neu, T.R. Significance of baterial surface-active compounds in interaction of bacteria with interfaces. *Microbiological Reviews*, **1996**, 60 (1): 151-166.
9. Liu, Y.; Strauss, J., and T.A. Camesano. Adhesion forces between Staphylococcus epidermidis and surfaces bearing self-assembled monolayers in the presence of model proteins. *Biomaterials*, **2008**, 29: 4374-4382.
10. Grivet, M, Morrier, J.J., Benay, G. and Barsotti, O. Effect of hydrophobicity on in vitro streptococcal adhesion to dental alloys. *Journal of Material Science: Materials in Medicine*, **2006**, 11: 637-642.
11. Widrig, C. A.; Chung, C. and Porter, M. D. The electrochemical desorption of n-alkanethiol monolayers from polycrystalline Au and Ag electrodes. *Journal of Electroanalytical Chemistry*, **1991**, 310: 335.
12. (a.) Ralph, T. R.; Hitchman, M. L.; Millington, J. P. and Walsh, F.C. The electrochemistry of L-cystine and L-cysteine part 1 : Electrosynthesis of L-cysteine at solid electrodes. *Journal of Electroanalytical Chemistry*, **1994**, 375: 1-17. (b.) The electrochemistry of L-cystine and L-cysteine part 2: Electrosynthesis of L-cysteine at solid electrodes. *Journal of Electroanalytical Chemistry*, **1994**, 375: 17-27.
13. Fawcett, W. R.; Fedurco, M. ; Kovacoca, Z. and Borkowska, Z. Oxidation of cysteine, cysteinesulfinic acid and cysteic acid on a polycrystalline gold electrode. *Journal of Electroanalytical Chemistry*, **1994**, 368: 265- 275. (b.) *Journal of Electroanalytical Chemistry*, **1994**, 375: 912.
14. Zhang, J.; Chi, Q.; Andersen, J. E. T.; Friis, E. P. Nielsen, J.U. and Ulstrup, J. Two-Dimensional Cysteine and Cystine Cluster Networks on Au(111) Disclosed by Voltammetry and in Situ Scanning Tunneling Microscopy. *Langmuir*, **2000**, 16 : 7229-7237.
15. Giao, M.S. ; Montenegro, M.I. and Vieira, M.J. Monitoring Biofilm formation by using cyclic Voltammetry-effect of the experimental conditions on biofilm removal and activity. *Water Science and Technology*, **2003**, 47: 51-56.
16. Busalmen, J. P.; Berna, A. and Feliu, J. M. Spectroelectrochemical examination of the interaction between bacterial cells and gold electrodes, *Langmuir*, **2007**, 23: 6459-6466.

17. Timur, S. ; Haghigghi, B.; Tkac, J. ; Pazarhoĝlu, N. ; Telefoncu, A. and Gorton, L. Electrical wring of *Pseudomonas putida* and *Pseudomonas flluorescens* with osmium redox polymers. *Bioelectrochemistry*, **2007**, 71: 38-45.
18. Chi, Q. ; Zhang, J. ; Friis, E. P. ; Andersen, J. E. T. and Ulstrup, J. Electrochemistry of self-assembled monolayers of the blue copper protein *Pseudomonas aeruginosa* azurin on Au(111). *Electrochemistry Communications*, **1999**, 1: 91-96.

Chapter 9 AFM of *Pseudomonas aeruginosa* and *Pseudomonas putida*

9.1 Introduction

In this chapter, we will focus on biofilms of *Pseudomonas aeruginosa* and *Pseudomonas putida*. All species and strains of *Pseudomonas* have some defining characteristics including: rod shape, Gram-negative, one or more polar flagellae providing motility, and aerobic and non-spore forming.

Pseudomonas aeruginosa is a versatile Gram-negative environmental bacterium which can cause a wide range of opportunistic infections. *P. aeruginosa* is notorious for its biofilm formation, which can protect bacterial cells from antibiotic treatments, host immune attack and other stress factors such as UV radiation[1,2]. *P. aeruginosa* biofilm formation is a dynamic process which commonly involves attachment, formation of microcolonies and macrocolonies, and dispersal[3], see Chapter 2. Bacterial surface structures such as type IV pili and flagellum and their mediated motilities are essential for *P. aeruginosa* biofilm structure development[4-6]. The roles of several EPS materials on *P. aeruginosa* biofilm formation are reported by different research groups. There are two kinds of polysaccharides, the glucose-rich Pel polysaccharide encoded by the *pel* gene cluster and the mannose-rich Psl polysaccharide encoded by the *psl* gene cluster. They were thus reported to be required for formation of *P. aeruginosa* liquid-air interface and biofilms[7,8]. Extracellular DNA (eDNA) was reported to be involved in bacterial cell attachment, cell-to-cell interconnection and macrocolony formation during *P. aeruginosa* biofilm development[9,10]. However, there are very few studies showing the interactions between bacterial cells and EPS materials during bacterial biofilm formation.

Pseudomonas putida is a Gram-negative rod-shaped saprotrophic soil bacterium with a diverse metabolism, including the ability to degrade organic solvents such as toluene[11]. This ability has been put to use in bioremediation, or to biodegrade oil. *P. putida* is a safe strain of bacteria, unlike *P. aeruginosa.* which is an opportunistic human pathogen. Large externalized, repeat-rich proteins have emerged as important factors in the attachment of

the bacteria to biotic and abiotic surfaces. The Large adhesion protein (LapF), a huge protein (6310 amino acids, aa) associated with the cell surface, is required for microcolony assembly from single attached cells into formation of biofilms. Mutants defective in IapF exhibiting competitive deficiencies, was found in plant roots[12]. These mutants exhibit normal irreversible attachment on both biotic and abiotic surfaces. The lapF phenotype appears at the mature biofilm under nutritionally rich conditions. LapF gene expression is controlled by the stress-responsive sigma factor RpoS and is elevated within growing microcolonies on abiotic surfaces and plant tissues. The large adhesion protein LapA protein, another enormous cell surface protein (8682 aa), is a key requirement for the reversible to irreversible transition during attachment[13]. There is a model, in which LapA and LapF act in a relay to drive the stable colonization of surfaces and subsequent assembly of the multicellular structures, Fig 9.1.

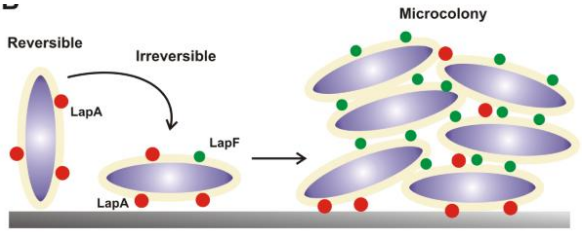

Fig 9.1 Model for *P. putida* transition from reversible to irreversible attachment, and subsequent microcolony formation. LapA is depicted as the larger red dot; LapF is the smaller green dot. The general structures for these proteins are not yet known and the globular shape implied in the figure is not meant to represent their structure, but roughly described by their amino acid number. Reprint from [13].

In this chapter we shall use AFM to study the biofilms both of *P. aeruginosa* and *P. putida* as well as their EPS. Particularly, AFM provides some detailed information about the EPS, protein and e-DNA at the single-cell level and of bacterial biofilm formation. The function of e-DNA was addressed electrochemically on Au(111) surfaces in Chapter 7, but will here be addressed directly by AFM.

The roles of *Pel* and *Psl* polysaccharides and type IV pili during *P. aeruginosa* biofilm development were specifically investigated. Compared with previously reported studies of e-DNA in *P. aeruginosa* biofilm development, this study suggested that polysaccharides and e-DNA might compensate each other during the *P. aeruginosa*

biofilm development. The function of surface protein Lap A and Lap F during *P.pudita* biofilm formation was also studied.

9.2 Materials and Methods

9.2.1 Strains and cultivation conditions

These parts of the work were done by Dr. Liang Yang in Prefessor Søren Molin's group at DTU Biosys. *P. aeruginosa* PAO1 was used as the wild-type strain[14]. The *pilA* mutant was constructed by allelic displacement in the PAO1 wild-type as described[14]. (An allele is one of two or more forms of a gene or a genetic locus (a group of genes), allelic the similar gene locus). The *pelApslBCD* mutants were constructed by allelic displacement in the PAO1 wild-type as described[14]. The *pilApelApslBCD* mutants were constructed by allelic displacement in the *pilA* mutant as described[14]. *P. putida* KT2440 was used as the wild-type strain. Mutant LapF was protein LapF gene defective.

9.2.2 Atomic Force Microscopy (AFM)

Mica pretreatment followed the description Section 7.2.2. *P. aeruginosa* overnight cultures were diluted 100 times in ABTG medium with or without 10 μg/ml DNaseI (Sigma Aldrich). *P. putida* overnight cultures were diluted 100 times in LB medium. They were then incubated in Eppendorf tubes with mica slips at 37 ^{o}C for 24 hours without shaking. After incubation the biofilms formed at the air-liquid interface on the mica slips were dipped 3 times into doubly distilled water, and air-dried at room temperature for AFM analysis.

As in previous chapters, AFM images in air were obtained by a PicoScan 5500 from Agilent instrument (Agilent Technologies, Chandler, AZ, USA) with a 100 μm scanner and cantilevers (NP-S) from Veeco (Camarillo, CA, USA). This instrument was used in the contact mode. The spring constant of the tip was 0.12 N/m. Deflection images and topography images were simultaneously acquired at a scan rate of 1.44 lines /s. All the cellular measurements were collected from contact mode topography images.

9.2.3 Roughness analysis

Surface roughness values of the extracellular ultra structure of cells were taken from high-resolution AFM topography images and calculated using Gwyddion (free download software). In general, roughness analysis is relative height analysis. The arithmetic roughness average R_a values and the root mean square roughness R_q were determined in the roughness analysis. For *P. aeruginosa*, R_a and R_q were collected for one hundred 250×250 nm^2 areas on approximately 10-20 cells for each strain from 10*10 μm^2 scale size, with an average of five to ten measurements per cell, to obtain the average and standard deviation. For *P. putida*, R_a and R_q were collected for one 400×400 nm^2 area on one cell or protein cluster. (Due to the sample limitation, the roughness analysis is different) .

The following equations in chapter 6 [15] were used:

$$R_a = \frac{1}{n}\sum_{i=1}^{n}\left|h_i - \langle h \rangle\right| \tag{9.1}$$

$$R_q = \sqrt{\frac{1}{n}\sum_{i=1}^{n}\left(h_i - \langle h \rangle\right)^2} \tag{9.2}$$

n is the number of data points, R_a the average distance between the *i* th height (h_i) and the mean height (h) of the all n data points, and R_q the root mean square distance between the i th height (h_i) to the mean height (h) of all n data points.

9.3 Effects of polysaccharides on surface morphology and roughness of P. aeruginosa biofilms

It is reported that e-DNA is required for the subpopulation interactions between the motile and non-motile subpopulation during the formation of mature mushroom-shaped macrocolony structures of *P. aeruginosa* biofilms[16,17]. Here we address the question whether e-DNA and the polysaccharides might be associated together and form complex 'concrete-like' structures as biofilm EPS materials. To test this, *P. aeruginosa* wild-type PAO1 strain and its isogenic *pilA*, *pelApslBCD* and *pilApelApslBCD* mutants in static biofilm cultures in the presence and absence of DNaseI were grown. Then we used high-resolution Atomic Force Microscopy (AFM) to investigate the role of polysaccharides

and e-DNA on the surface morphology and roughness of *P. aeruginosa* biofilms. It was found that type IV pili, e-DNA and polysaccharides could affect the surface morphology and roughness of *P. aeruginosa* biofilms significantly. From Table 9.1 the cell surface of PA01 is rougher than the cell surface of *pelApslBCD, pilA* and *pilApelApslBCD* mutant biofilms. DNaseI treatment changed the morphology and reduce the roughness of biofilms formed by PAO1 and *pelApslBCD* mutant more significantly than the *pilA* and *pilApelApslBCD* mutant biofilms (Fig.9.2 and Fig.9.3). The bacterial cells are smoother after DNAase I treatment, Fig 9.3. These results suggest that type IV pili was required for e-DNA binding, in accordance with previous reports[17,18]. Type IV pili is the main components of EPS to form biofilm. More interesting, DNaseI treatment could change the morphology and reduce the roughness of biofilms formed by *pelApslBCD* mutant to a larger extent than PAO1 strain biofilms (Table 9.1, Fig 9.3). The details of the biofilm formation were compared between PA01 and *pelApslBCD* mutant in Fig.9.3 (A and C, B and D). These results show that Pel and Psl polysaccharides can stabilize the interactions between type IV pili and e-DNA. In *pelApslBCD* biofilms, the lack of polysaccharides might lead to weak binding between type IV pili and eDNA under the influence of shear force of the media flow, which will in turn reduce the associations between the motile and non-motile subpopulations. In *pilApelApslBCD* biofilms, the lack of polysaccharides and type IV pili biofilm only leaves protein and e-DNA to form EPS. The roughness of the cell surfaces has here decreased a lot.

This study has thus examined the detailed roles of Pel and Psl polysaccharides on *P. aeruginosa* biofilm formation. It was found that both Pel and Psl polysaccharides were required for the formation of microcolony and macrocolony structures during *P. aeruginosa* biofilm formation. The results also suggest that Pel and Psl polysaccharides might associate with e-DNA and form complex ‘concrete-like’ structures as biofilm EPS materials.

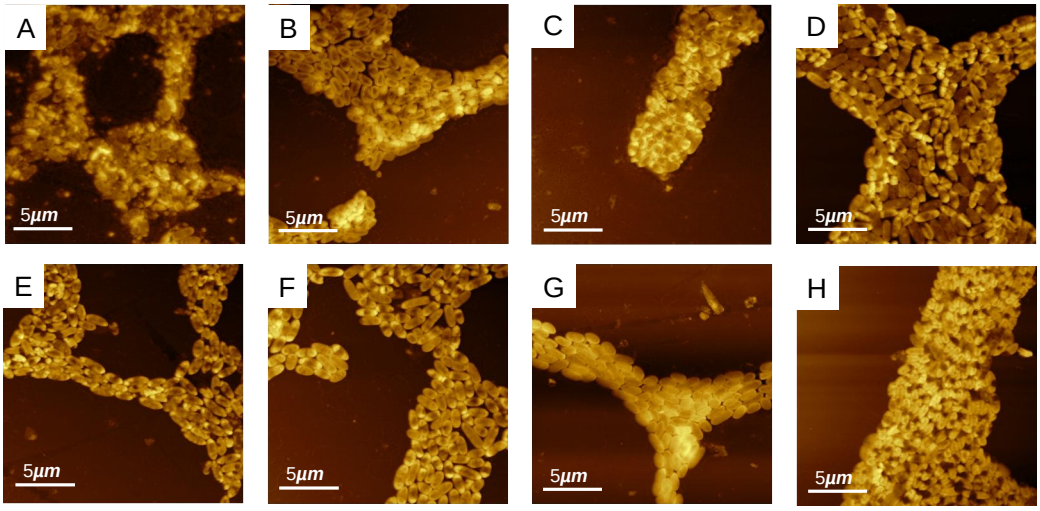

Fig 9.2 AFM images of 24-hour-old *P. aeruginosa* PAO1 biofilm (A&E), pilA biofilm (B&F), pelApslBCD biofilm (C&G) and pilApelApslBCD biofilms (D&H) in LB medium. A, B, C, D : biofilms grown without DNaseI E, F, G, H: biofilms grown in the presence of 10 μg/ml DNaseI. Scale bar: 20μm. A: Lots of EPS such as protein, polysaccharides, pili and dead cell fragments surround the biofilm cells. B,C,D, E, F, G, and H had clear mica surface background.

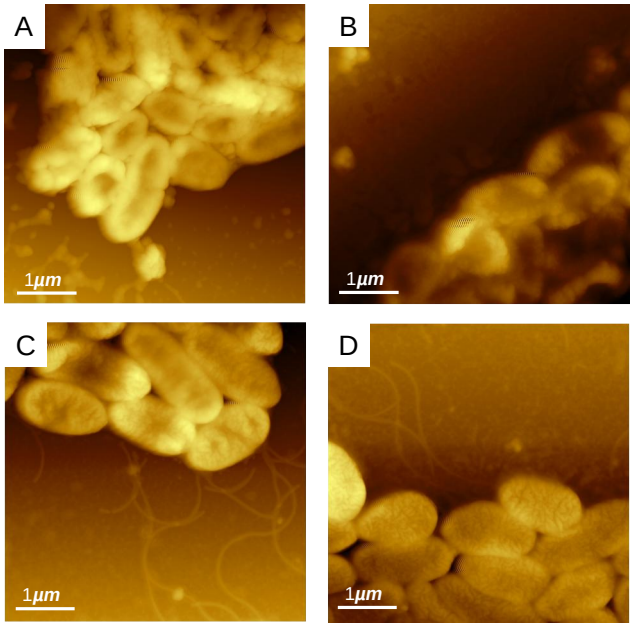

Fig 9.3 High resolution AFM images of 24-hour-old P. aeruginosa PA01 biofilm (A&C) and pelA/pslBCD biofilm (B&D). A, B: biofilms grown without DNaseI; some cell fragment surround the biofilm; C,D: biofilms grown in the presence of 10 μg/ml DNaseI. Only the pili can easily be identified. Scale bar: 5μm.

Table 9. 1. Roughness analysis.

P.aeruginosa	DNaseI treatment	R_a (nm)	R_q (nm)
PAO1	-	10.7±2.0	12.8.±2.2
PAO1	+	9.0±1.7	10.8±2.1
pilA	-	9.4±1.5	11.1±1.8
pilA	+	8.8±1.6	10.5±1.9
pelApslBCD	-	10.2±1.7	12.1±2.1
pelApslBCD	+	4.6±1.0	5.6±1.2
pilApelApslBCD	-	6.4±1.3	7.8±1.7
pilApelApslBCD	+	5.4±1.4	6.5±1.4

9.4 Effects of polysaccharides on surface morphology and roughness of P. putida biofilms

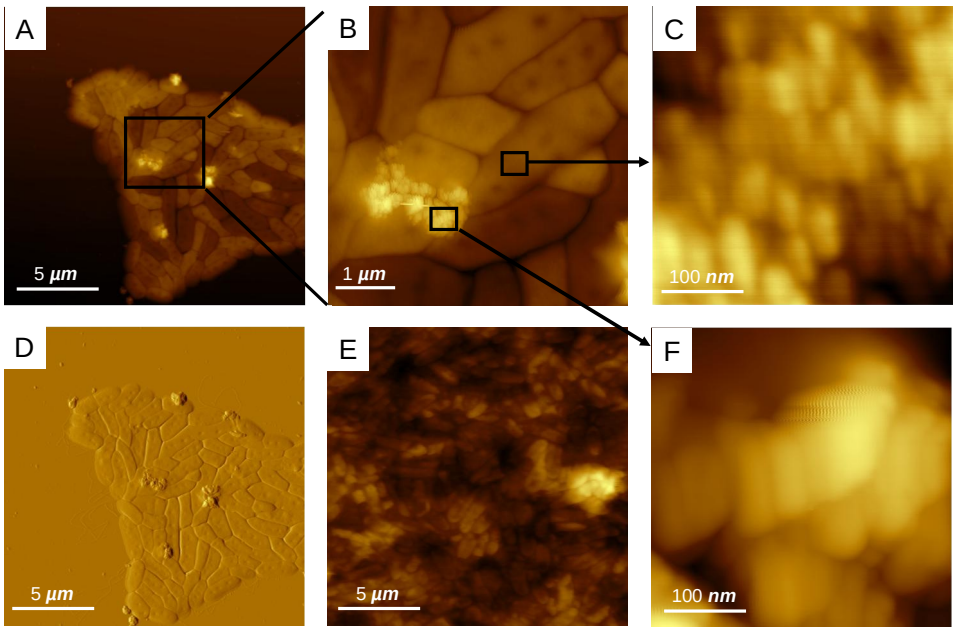

Fig 9.4 High-resolution AFM images of 24-hour-old of *P.Putida* wt (A, B, C, D and F) and *P.Putida* LapF (E). C: *P.Putida* bacterial surface, F: protein cluster. B is the small scale of A; C and F are directly from different part of B. A, B, C, E and F : topography; D: deflection. Scale bar: A,D,E :20 µm, B: 5 µm, and C, F: 400 nm.

The major extracellular protein component in *P. putida* biofilms was also characterized. Protein as EPS material is not commonly studied. *P. putida* wt produces a large size protein as EPS material in the first 8 hours, and then digest the protein after a further 8

hour growth due to starvation and secretion of proteinase (Fig 9.4 and 9.5). *P. putida lapF* mutant, also produces a large size protein as EPS material in the first 8 hours, but cannot digest the protein after 8 hour growth since the proteinase gene (*lapF*) is inactivated[13]. This mutant thus forms better and thicker biofilms (Fig 9.4E). Fig 9.4 B is a small scale image of Fig 9.4 A. Fig 9.4 C is the surface of one *P. putida* cell and Fig 9.4 F is a protein cluster. From the size of the structure, it might be protein. Protein as parts of EPS plays an important role in biofilm formation. At 24 hour, *P. putida* wt has not finished digesting the proteins, and the undigested proteins are easier to assemble to protein clusters. The result of the roughness analysis showed that the protein cluster (R_a = 31.3, R_q = 25.7) is rougher than the *P. putida* surface (R_a = 6.59, R_q = 7.78). Protein clusters are distributed on the biofilm cell boundary (Fig 9.4 A) or outside the biofilms (Fig 9.5 A). Pili of bacterial cells can also be identified (Fig 9.5 B and E bottom arrow). Pili are long and thin tubes and can only be observed outside the bioiflm . However, it is hard to say whether the protein clusters are LapF or LapA. It could be either of them or both. Further experiments are needed to identify the protein.

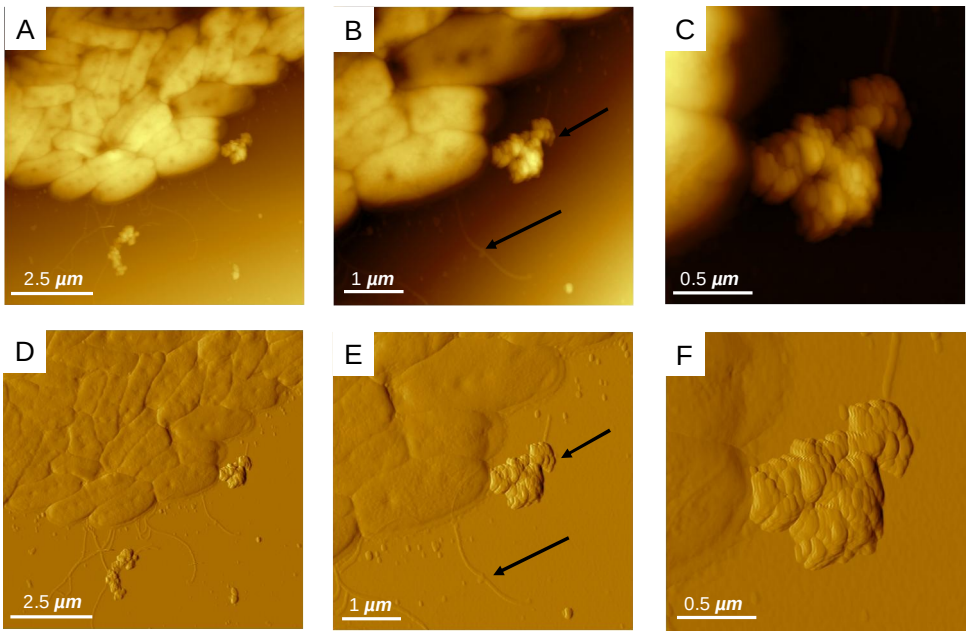

Fig 9.5 AFM of biofilm *P.Putida* wt for 24h in LB medium. From left to right: (A, D) 10 µm, (B, E) 5 µm, and (C, F) 2 µm, A,B,C: topography; D, E, F: deflection. B and E upper arrows: Protein cluster. Bottom arrows: pili. C and E: clear proteins cluster

In conclusion, the major extracellular protein component in *P. putida* biofilms was also characterized by AFM, but the protein cluster LapF or LapA are not confirmed. The protein confirmation can use other biological methods, such as protein purification and protein sequencing, or by imaging protein as control by AFM.

Reference

1. Costerton, J.W.; Lewandowski, Z.; Caldwell, D.E.; Korber, D.R. and Lappin-Scott, H.M. Microbial biofilms. *Annual Review Microbiology*, **1995**, 49: 711-745.
2. Hoiby, N.; Krogh Johansen, H.; Moser, C.; Song, Z.; Ciofu, O., and Kharazmi, A. *Pseudomonas aeruginosa* and the in vitro and in vivo biofilm mode of growth. *Microbes and Infection*, **2001**, 3: 23-35.
3. Monds, R.D. and O'Toole, G.A. The developmental model of microbial biofilms: ten years of a paradigm up for review. *Trends Microbiology*, **2009**, 17: 73-87.
4. O'Toole, G.A., and Kolter, R. Flagellar and twitching motility are necessary for *Pseudomonas aeruginosa* biofilm development. *Molecular Microbiology*, **1998**, 30: 295-304.
5. Klausen, M.; Aaes-Jorgensen, A.; Molin, S. and Tolker-Nielsen, T. Involvement of bacterial migration in the development of complex multicellular structures in *Pseudomonas aeruginosa* biofilms. *Molecular Microbiology*, **2003**, 50: 61-68.
6. Klausen, M.; Heydorn, A.; Ragas, P.; Lambertsen, L.; Aaes-Jorgensen, A.; Molin, S. and Tolker-Nielsen, T. Biofilm formation by *Pseudomonas aeruginosa* wild type, flagella and type IV pili mutants. *Molecular Microbiology*, **2003**, 48: 1511-1524.
7. Friedman, L. and Kolter, R. Two genetic loci produce distinct carbohydrate-rich structural components of the *Pseudomonas aeruginosa* biofilm matrix. *Journal of Bacteriology*, **2004**, 186: 4457-4465.
8. Friedman, L. and Kolter, R. Genes involved in matrix formation in *Pseudomonas aeruginosa* PA14 biofilms. *Journal of Bacteriology*, **2004**, 51: 675-690.

9. Allesen-Holm, M.; Barken, K.B.; Yang, L.; Klausen, M.; Webb, J.S.; Kjelleberg, S. A characterization of DNA release in *Pseudomonas aeruginosa* cultures and biofilms. *Molecular Microbiology*, **2006**, 59: 1114-1128.
10. Whitchurch, C.B.; Tolker-Nielsen, T.; Ragas, P.C. and Mattick, J.S. Extracellular DNA required for bacterial biofilm formation. *Science*, **2002**, 295: 1487.
11. Marques, S. and Ramos, J.L. Transcriptional control of the *Pseudomonas putida* TOL plasmid catabolic pathways. *Molecular Microbiology*, **1993**, 9(5):923-9.
12. Martinez-Gil, M.; Yousef-Coronado, F. and Espinosa-Urgel, M. LapF, the second largest *Pseudomonas putida* protein, contributes to plant root colonization and determines biofilm architecture. *Molecular Microbiology*, **2010**, 77(3): 549-561.
13. Fuqua, C. Passing the baton between Laps: adhesion and cohesion in *Pseudomonas putida* Biofilms. *Molecular Microbiology*, **2010**, 77(3): 533–536.
14. Yang, L.; Hu, Y.; Liu, Y.; Zhang, J.; Ulstrup, J. and Molin, S. Distinct roles of extracellular polymeric substances in *Pseudomonas aeruginosa* biofilm development. *Environmental Microbiology*, **2011**, 13, (7): 1705-1717.
15. Cross, S. E. ; Kreth, J. ; Zhu, L. ; Qi, F. ; Pelling, A. E. ; Shi, W. and Gimzewski, J. K. Atomic force microscopy study of the structure-function relationships of the biofilm-forming bacterium *Streptococcus mutans*. *Nanotechnology*, **2006**, 17: 1-7.
16. Barken, K.B.; Pamp, S.J.; Yang, L.; Gjermansen, M.; Bertrand, J.J.; Klausen, M. Roles of type IV pili, flagellum-mediated motility and extracellular DNA in the formation of mature multicellular structures in *Pseudomonas aeruginosa* biofilms. *Environmental Microbiology*, **2008**, 10: 2331-2343.
17. Yang, L.; Nilsson, M.; Gjermansen, M.; Givskov, M. and Tolker-Nielsen, T. Pyoverdine and PQS mediated subpopulation interactions involved in *Pseudomonas aeruginosa* biofilm formation. *Molecular Microbiology*, **2009**, 74: 1380-1392.
18. van Schaik, E.J.; Giltner, C.L.; Audette, G.F.; Keizer, D.W.; Bautista, D.L. and Slupsky, C.M. DNA binding: a novel function of *Pseudomonas aeruginosa* type IV pili. *Journal of Bacteriology*, **2005**, 187: 1455-1464.

Chapter 10 Conclusion

Bacterial biofilms is an increasingly important issue in a broad variety of contents where biological liquids are in contract with solid surfaces. In this thesis, the advanced technology AFM combined with elelectrochemistry has brought insight about different structural aspects of bacterial biofilm growth and surface adhesion. The focus of the study is on the initial steps of the biofilm formation, and the adhesion of the bacterial surfaces between the bare or functionalized AFM tips, the interaction between the bacteria and different surfaces, e.g. Mica or bare and modified Au(111)-electrode surfaces, and the biofilm surface charges. AFM has been used to obtain the high resolution images of the bacteria at the nanoscale, and to the study of adhesion properties of the live cell surface in liquid, the growth pattern of different bacterial strains, growth inhibition by drugs, and the function of the EPS. Electrochemical methods have been based on cyclic voltammetry (CV), reductive desorption (RD) and use of electrochemical probe molecules. Particularly atomically planar, single-crystal Au(111)-electrode surfaces modified by self-assembled molecular monolayers (SAMs) have been used throughout in order to study the relationship between bacterial cells and the surface.

Adhesion forces on single live cell surfaces were applied to four different strains of *Staphylococcus epidermidis* in liquid aqueous environment. These strains were selected for their special surface proteins related with the initial attachment on the surface, and include two biofilm positive strains and two biofilm negative strains. The force measurement and imaging of strain RP62a was recorded in real time. Comparison of the adhesion maps by hydrophobically modified tips with bare hydrophilic silicon nitride tips showed that hydrophobic effects are not the primary driving forces towards adhesion. High-resolution AFM imaging showed no detectable differences among the four strains. Two chemical inhibition compounds have strong effects on the adhesion between the bare tips and the bacteria.

In addition, biofilm formation of three other bacteria were studied, *Pseudomonas aeruginosa*, *Pseudomonas putida* and *Streptococcus mutans*. Mutant strains of the first

two were compared to study the function of EPS (such as protein, e-DNA and polysaccharides). The inhibition effects of six electrochemical probes and the function of e-DNA were also studied using *S. mutans*. These studies based on two different approaches via AFM and electrochemistry confirmed that e-DNA is an important component in bacterial biofilms.

AFM and electrochemistry were combined in a new appeoach to study the bacterial biofilm formation. Cyclic voltammetry was first used to study *S. mutans* on the Au(111)-surface, using six redox probes, i.e. positively ($[Ru(NH_3)_6]^{3+/2+}$, $[Co(phen)_3]^{3+/2+}$ and $[Co(terpy)_2]^{3+/2+}$ (phen = 1,10-phenanthroline; terpy = 2,2',2"-terpyridine) and negatively charged ($[Fe(CN)_6]^{3-/4-}$. $[IrCl_6]^{3-/4-}$) transition metal complexes. The positively and negatively charged redox probe showed different inhibition and voltammetric patterns. $[Ru(NH_3)_6]^{3+/2+}$, and the homologous compound $[Co(NH_3)_6]^{3+/2+}$ were the only probe compounds to cause growth inhibition. On the other hand, cyclic voltammetry (CV) of both $[Ru(NH_3)_6]^{3+/2+}$ (positively charged, biofilm growth inhibitor) and $[Co(terpy)_2]^{3+/2+}$ (positively charged, no biofilm growth inhibition) displayed fully reversible CV on biofilm covered electrodes, almost indistinguishable from CV at bare Au(111)-electrode surfaces. In comparison, the CV of $[Fe(CN)_6]^{3-/4-}$ and $[IrCl_6]^{3-/4-}$ (both negatively charged and no growth inhibition) was distorted from planar diffusion behaviour on bare Au(111)-electrode surfaces towards spherical diffusion behaviour on *S. mutans* biofilm covered Au(111)-electrode surfaces. DNAase teatment of the biofilm covered Au (111)-electrode surface partly restores planar diffusion CV of $[Fe(CN)_6]^{3-/2-}$ and $[IrCl_6]^{3-/4-}$. This points out that *S. mutans* biofilm is negatively charged and that negatively charged e- DNA, removed by DNAase is an important constituent of the EPS.

Reductive desorption (RD) was used to study the differences and the relationship between the surface of *Streptococcus mutans* biofilms, and bare and SAM modified Au (111) surfaces. Four molecules were chosen to modify the Au(111) surfaces: $HS(CH_2)_{15}CH_3$ (hexadecanethiol, MHD) and $HS(CH_2)_{15}COOH$ (mercapto-hexadecanoic acid, MHDA), L-cysteine and cysteamine. AFM showed that the growth rates of *S. mutans* were slightly different and fastest for MHD-modified surfaces but the biofilms

after 24 hours were indistinguishable. Reductive desorption signals of the four compounds in PBS buffer, pH 7.4 were very similar in the absence and presence of *S.mutans* biofilms in BHI medium and BHI medium alone. The RD data of the long pure and functionalized MHD and MHDA in 0.1 M NaOH in the absence and presence of *S.mutans* biofilms in BHI medium and BHI medium alone shows, however, differences. First, the RD features are very sharp on adsorption of BHI medium and *S. mutans* biofilms with BHI medium on both MHD- and MHDA-modified Au(111)-surfaces. Secondly, a clear peak also appears when either BHI medium alone or bacteria with BHI medium are adsorbed on a bare Au(111)-surface, but the peaks are more positive potentials than on both MHD- and MHDA-modified Au(111)-surfaces. Third, the RD peak on the hydrophobic MHD surface is distinctly shifted compared to the RD peak of the MHD SAM alone, and notably in different directions for the *S. mutans* biofilm with BHI medium (negative shift) and for the BHI medium alone (positive shift). A similar difference is observed between *S. mutans* biofilm plus BHI growth medium and BHI growth medium alone on bare Au(111). Both the AFM images and the electrochemical data show that the biofilms are more strongly attached to the hydrophobic surface than to the hydrophilic surfaces.

In the future, AFM could be used to observe living cells in situ in aqueous media in order to understand the drug effects on cell surfaces, the interaction between bacteria and the surfaces, and the bacterial biofilm growth. Based on my study, the *S.mutans* biofilms tend to attach to negatively charged and hydrophobic surfaces. We could use electrochemical control to change the adhesion between the biofilm and modified surfaces e.g either remove the biofilm or enhance the biofilm adhesion. In addition, AFM combined with electrochemistry can be used for electrochemical control of bacterial growth. We can design the electrochemistry monitor to detect the bacterial biofilm growth at different conditions (pH, temperature, nutrition, modified surfaces) and finally find out the useful ways to prevent the bacterial biofilm formation.

In conclusion, we have used a different and partly novel approach of AFM and electrochemistry combination, which brings us into a new area to understand bacterial biofilm/Au (111) –surfaces /solution, and bacterial biofilm/SAM /solution interfacial region. Based on this new approach, we have investigated the nature of the adhesion forces between the bacteria and the surfaces or the bacteria and functionalized AFM tips, the nature of EPS and their relationship of biofilm formation (e-DNA, protein and pili) and some chemical inhibition effects on bacterial biofilms.

Appendices

My project is also part of a strategic research project that involved extensive instrument testing of a DME A/S AFM, specifically instrument testing (Appendix A) and cantilever testing (Appendix B), In addition, some other technical methods applied in the project are described: Preparation of gold coated tips (Appendix C), polycarbonate based sample preparation (Appendix D) and preparation of Au(111) electrodes (Appendix E).

Appendix A

DME AFM instrument development. The Contact mode (DC) and Tapping Mode (AC) with four specific cantilevers manufactured by DME were tested. The results are summarized in the table.

	Contact mode (DC)		**Tapping mode (AC)**	
Type of tip	**in air**	**in liquid**	**in air**	**in liquid**
2611 AC In air	Works (2922) Good resolution ***	Does not work. Imaging can be achieved, but bacteria cannot be seen. (2923)	Works(2938) Good resolution *** Almost same as DC in air	Does not work (no frequency curve)
2521 In liquid DC tips	Works. Tip can approach, but bacteria cannot be seen.	Works. Resolution is not high enough. *** Instrument parameters had to be adjusted all the time	Works. Imaging but not clear, Worse than DC mode in air.	Works. Approach can be achieved. The tips can damage the sample.
2567 DC In air	Work. Better resolution. **** No imaging first time. The second time, the imaging is perfect after trying the AC mode.	Does not work. The tip can approach, but there is no imaging	Works. Good resolution. ** Work frequency curve is sharp. Imaging is clear.	Does not work. No work frequency curve, Approach can be achieved.
2663 AC In liquid	Does not work. Much noise. No imaging, for second tip there is some unclear imaging.	Does not work. The imaging is not good. For the second tip, there is no imaging.	Does not work, no images. For the second tip, no frequency curve.	Does not work. The imaging is not clear, No imaging for the second tip.

4 Tips and tip modes

Name of Tips	DME 2611	DME 2663	DME 2521	DME 2567
Title	DS 95-xxx Sense Mode™ AC probe	DS 95-xxx Sense Mode™ AC probe	DS 95-xxx Sense DC Bio probe	DS 95-xxx Sense DC Bio probe
Cantilever length	App. 160 Micron	App. 160 Micron	445-455 Micron	445-455 Micron
Cantilever width	App. 45 Micron	App. 45 Micron	45-55 Micron	45-55 Micron
Cantilever thickness	App 4,6 Micron	App 4,6 Micron	1.5-2.5 Micron	1.5-2.5 Micron
Spring / Force. Const	App. 42N/m	App. 42 N/m	0.07-0.40 N/m	0.07-0.40 N/m
Resonance freq	App. 285 kHz	App. 285 kHz	9-17 kHz	9-17 kHz
Tip height	10-15 micron	10-15 micron	10-15 micron	10-15 micron
Tip curvature radius	Typically < 10 nm	Typically < 10 nm	Typically < 10 nm	Typically < 10 nm
Cantilever coating	Nano World Arrow™ NCR	Nano World Arrow™ NCR	Aluminum Nano World Point probe# CONTR	Aluminum Nano World Point probe# CONTR
Probe holder	Dual Scope™ plug- and plag#2	Dual Scope™ plug- and plag#2	Dual Scope™ plug- and plag#2	Dual Scope™ plug- and plag#2

Appendix B

Cantilevers and Tips:

AFM cantilevers applied in the thesis (Force curve and functional tips) MLCT, MLST and OTR4 were used in Chapter 6, in Université Catholique de Louvain, Belgium. NP-S were used in Chapter 7, 8 and 9 in DTU.

Name of Tips	MLCT	MLST	NP-S	OTR4
Tip specification	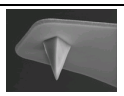	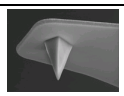	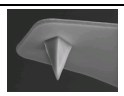	
Geometry	Anisotropic	Anisotropic	Anisotropic	Cast
Tip Height (h)	2.5 - 8.0 µm	2.5 - 8.0 µm	2.5 - 8.0 µm	2.5 – 3.5 µm
Front Angle (FA)	15 ± 2.5º	15 ± 2.5º	15 ± 2.5º	36 ± 2 º
Side Angle (SA)	25 ± 2.5º	25 ± 2.5º	25 ± 2.5º	36 ± 2 º
Back Angle (SA)	17.5 ± 2.5º	17.5 ± 2.5º	17.5 ± 2.5º	36 ± 2 º
Tip Radius (Nom)	20 nm	10 nm	10 nm	15 nm
Tip Radius (Max)	60 nm	40 nm	40 nm	20 nm
Tip Setback (TSB) (Nom)	5 µm	5 µm	5 µm	4 µm
Tip Set Back (TSB)(RNG)	3 - 7 µm	3 - 7 µm	3 - 7 µm	3 – 5.5 µm
Cantilever Specification	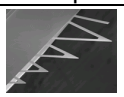	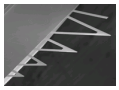	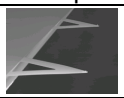	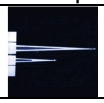
Probe material	Silicon Nitride	Silicon Nitride	Silicon Nitride	Silicon Nitride
Thickness (t) (Nom)	0.55 µm	0.55 µm	0.6 µm	0.4 µm
Thickness (t) (RNG)	0.5-0.6 µm	0.5-0.6 µm	0.55-0.65 µm	0.3 - 0.5 µm
Reverse Side Coating	40 ± 10nm of Ti/Au	40 ± 10nm of Ti/Au	40 ± 10nm of Ti/Au	30nm Au
Chosen tip*	C Triangular	C Triangular	D Triangular	B Triangular
Length (L) (Nom)	310 µm	310 µm	205 µm	200 µm
Width (L) (Nom)	20 µm	20 µm	25 µm	30 µm
Frequency	7 KHz	7 KHz	18 KHz	11 KHz
k (force constant)	0.01 N/m	0.01 N/m	0.06 N/m	0.02 N/m
Company	Veeco	Veeco	Veeco	Veeco

* One cantilever may have 2, 4 or 5 different tips, the chosen tips are applied in this thesis.

Three cantilever types were applied to CFM using the Veeco instrument.

	OTR4	**MSCT or MLCT**
Deflection sensitivity (nm/V)	45	75 (60-75)
Spring constant(N/m)	0.02	0.01
Trig threshold (nm)	10	20-30

Appendix C

Preparation of gold coated tips and surfaces

The following steps show how to prepare the hydrophobic tips and surfaces. Two days are needed. Oxide-sharpened microfabricated Si_3N_4 cantilevers with spring constants of 0.01 N/m (Microlevers, Veeco Metrology Group, Santa Barbara, CA) and silicon wafers (Siltronix, France) were used. This part was done in Yves Dufrene's group. The procedure is illustrated in the figure.

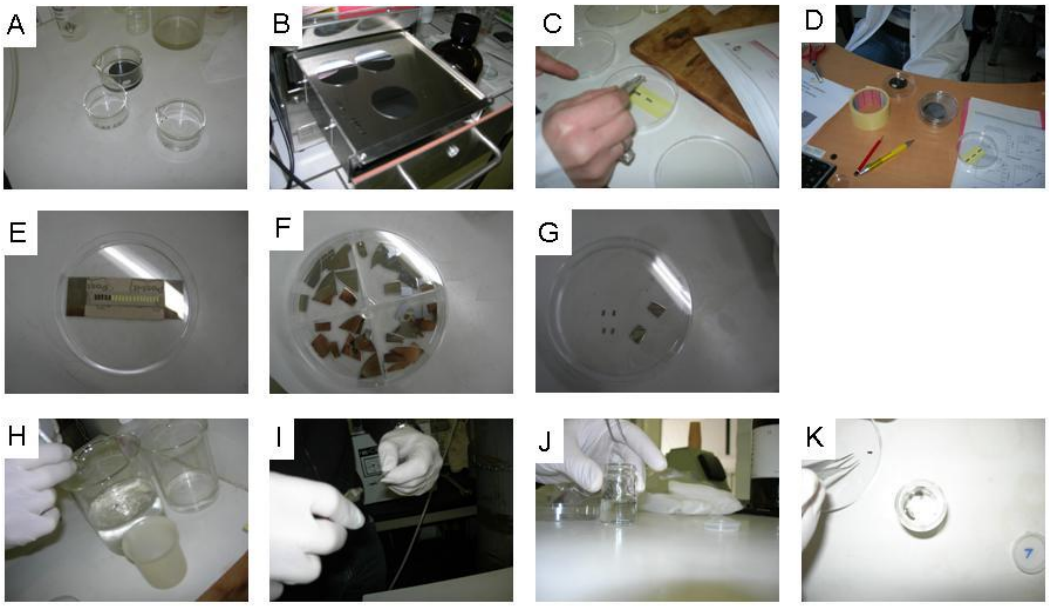

Day 1:

A. Silicon wafers and the tips (MLCT or MLST) were put separately into glass ware (in the middle, glass ware with black color and transparent color, respectively) and with ethanol for 20 minutes and dried with a gentle nitrogen flow.
B. The cleaned tips and silicon wafers were cleaned further for 15 min by UV and ozone treatment (Jelight Co.) rinsed with ethanol, and dried with a gentle nitrogen flow.
C. A glass slide was covered by double-sided adhesive tape. The top of the double-sided adhesive tape was covered by 3M Post-It notes on the left and right lines while the middle line around 1 cm wide was left uncovered. The cantilevers were

plated properly as a line in the middle and stuck on the double-sided adhesive tape of glass slides (also seen in Fig E).

D. The reverse side of the glass slides and silicon wafers two small pieces of double-sided adhesive tape were stuck separately. These were stuck to the round plates (the supporter) of the electron beam thermal evaporator. The machine will then automatically coat Silicon wafers and the tips with a 5 nm thick Cr layer followed by a 30 nm thick Au layer. This took one or two hours.

Day 2:

E. The glass slide with gold-coated AFM tips, can be stored in a Petri Dish with cover for several months.

F. The gold coated silicon wafers were cut into small pieces.

G. The gold coated silicon wafers surfaces and tips were cleaned for 15 min by UV and ozone treatment (Jelight Co.)

H. The gold coated silicon wafers surface and AFM cantilever were rinsed with ethanol.

I. The gold coated silicon wafers surface and AFM cantilever were dried with a gentle nitrogen flow.

J. The gold coated silicon wafers surface and AFM cantilever were immersed overnight in 1 mM solutions of $HS(CH_2)_{17}CH_3$ in ethanol and then rinsed with ethanol.

Appendix D

Polycarbonate-base sample preparation

Polycarbonate membrane tracked-cells were done in Yves Durene's group. Most procedures followed reference[1].

Cell culture preparation (3 days):

1. Day 1: Strain from -80ºC freezer were plated on TSB (Trypic Soy Broth) agar (30 g TSB broth and 12 g agar with 1 Liter Millipore water, which is autoclaved at 121 ºC and 15 psi for at least 30 minutes). The strain on TSB agar was cultured overnight at 37ºC.
2. Day 2: Bacterial clones from TSB agar were put into10 ml TSB medium with 10µg / ml erm (erythromycin) or tet (tetracyklin) or blank (without antibiotics) for strains (RP62a. 1457atlE) or (12228) or (1457) separately. Culture overnight at 37ºC.
3. Day 3: OD of the overnight culture was measured. New fresh 25ml TSB medium at OD 0.1 was obtained and left for around 2 hours at exponential stage of bacterial growth to reach OD 0.3.
4. Day 3: Transfer the bacterial suspension into the desirable tubes and centrifuge at 7500g rev / min for 10 min at 0 ºC.(Centrifugation is at low temperature and high speed)
5. Day 3: Remove the upper layer of the suspension, wash with PBS buffer or MQ to suspension, and then repeat the washing and centrifugation from 4 and 5 three times.
6. Day 3: Finally recover the suspension with PBS buffer or MQ round 20 or 25 ml and then filtrate through membrane.

Preparation and mounting of the sample (2 h):

1. Clean the AFM liquid cell with detergent (RBS-25) and rinse abundantly with MQ water and further with ethanol. Then dry with a gentle nitrogen flow.

2. Resuspend freshly harvested bacterial cells in imaging solution (MQ water, buffer or culture medium) to obtain a suspension containing10^6 cells per ml. (Notice: Using hydrophobic tips to identify the different strains of *S .epidermidis* , the imaging solution can only be MQ water, but not PBS buffer, because PBS buffer will influence cell surface adhesion and make the force curves indistinguishable)
3. 1–2 ml of the cell suspension is added into 10 ml MQ water and shaked for one minute, filter through a porous polycarbonate membrane with 0.8 μm pore size (notice: in order to keep the membrane hydrophobic, put it in the 100 ºC oven for at least one night, otherwise the new membranes are hydrophilic which cannot track the cell on the membrane).
4. Using tweezers, grab the membrane edge, transfer it into a Petri dish containing the imaging solution and gently agitate to remove non-immobilized cells. Wash by buffer or MQ water three times. (Notice: polycarbonate membranes have a smooth and a rough side. Better results will be obtained by imaging the smooth side, which can easily be identified by the eye because it is better reflecting than the rough side. To minimize the presence of cell debris on the membrane surface (a problem that may dramatically alter the imaging resolution, it is strongly recommended to filter the suspension on the rough side, then turn it upside down to expose the smooth side finally toward the scanning tip. In my case, smooth side up, the bacteria slip through from the smooth to the rough side, scanning also smooth side.)
5. Carefully cut a 1×1 cm^2 square of the membrane, quickly dry the bottom side using precision wipes and then attach it to a steel sample supporter using a small piece of double-sided adhesive tape. Mount the supporter onto the scanner. (While mounting the wet sample, it is important to minimize as much as possible contact with air which may denature the cell surface.)
6. Quickly cover the sample with a few drops of imaging solution and then mount the AFM liquid cell.
7. Place the AFM setup onto a mechanically isolated platform. (High-resolution imaging requires external vibration isolation, which can be achieved with an actively damped table.)

8. Wait for at least 10 min to minimize thermal drift. Focus the laser beam onto the cantilever end and adjust the photodiode signal.
9. Perform either real-time topographic imaging or CFM by following the steps in options A and B, respectively see below. Chemical Force Microscopy (CFM) involves functionalization of the AFM tips with well-defined chemical groups and recording force curves between the modified tips and the cells.

A. Real-time topographic imaging (4 h):

1. After selecting an imaging size of 0 mm, engage the AFM tip. AFM tips approached in the middle point of sample, then AFM will directly record single force curves between tip and sample. AFM will not record any images at this stage, therefore to select an imageing size of 0 mm. Check whether consecutive curves are stable and show sharp transitions. Set the imaging force at 250 pN and switch to imaging mode. (Notice: The force acting between the tip and the sample is a key control parameter in order to obtain reliable, high-resolution images. Large imaging forces may dramatically reduce the image resolution, and cause molecular damage or detachment of the immobilized cells.)
2. Record low-resolution images (e.g., 50 × 50 mm^2 areas) while adjusting the feedback parameters and minimizing the applied force between each recording. (Notice: In the constant-force mode, the sample height is adjusted to keep the deflection of the cantilever constant using a feedback loop. Most AFM systems use at least two gain controls to vary the feedback loop, that is, proportional and integral gains. In general, use a proportional gain higher than the integral gain and be sure that both gains are high enough so that the tip can track accurately every surface feature. However, too high gains will result in oscillations and instabilities.)
3. Try imaging a single cell trapped into a pore while increasing the image resolution. (Notice: Display both height and deflection images because they usually yield complementary information.)
4. Although height images provide quantitative height measurements, deflection images are more sensitive to fine surface details, making them valuable to reveal

the ultrastructure of corrugated cell surfaces. Lateral dimensions are accurately measured in deflection images, but these do not provide quantitative height measurements. If no cells are found, disengage the tip, move several hundred micrometers away and restart from Step A by engaging the tip again. (Notice: Finding trapped cells may be difficult depending on the species investigated. Immobilization in porous membranes is generally straightforward for spherical cells such as yeast and fungal spores, but the method may not be suited for other shapes such as rod-shaped bacteria.)

5. Zoom in on top of a single cell to record high-resolution images of the surface while optimizing the imaging rate and maintaining a low imaging force. (Notice: An AFM image is obtained by raster-scanning the tip over the sample, that is, the sample or the tip is moved along a line in the so-called 'fast scanning' direction and then moves up to another scan line in the 'slow scanning' direction. The scanning rate is defined as the rate in the fast scanning direction, and thus depends on the scanning frequency and on the image size. The scan rate should not be too fast when nanometer resolution is desired because at fast scan rates the tip may not respond faithfully to nanoscale features. On the other hand, slow scan rates may cause sample damage when imaging soft surfaces. Scan rates should therefore, typically be in the range of 0.5–2 mm s^{-1}.)
6. For dynamic studies, record a series of images on the same location of the cell. The use of a temperature controlled stage (e.g., 30 or 37. 1ºC) makes it possible to track structural changes associated with growth and division. (Notice: Withdraw the tip from the cell surface between each recording to minimize tip contamination and/or sample damage because both effects dramatically alter the image resolution. If this happens during the course of an experiment, change the tip before proceeding further. In general, stop real-time experiments after 4 h to avoid cell lysis.)

B. Chemical Force Microscopy (CFM)

1. Follow Appendix C.

2. For the CFM measurements, first localize a cell of interest with an unmodified tip disengage the tip and change it with a hydrophobic, functionalized tip. Normally, we need to redo A if we want to change the unmodified tip to a modified tip. Then restart until the cell is found again. (Notice: Engaging the functionalized tip directly on the cell of interest is generally difficult. In this respect, optical microscopy may be helpful to localize specific regions of the porous membrane while changing the tips.)
3. Record either force curves at single locations or spatially resolved curves over areas of given size. (Notice: Minimize the contact time between hydrophobic tip and sample because the lifetime of a functionalized tip may be very short due to tip contamination.
4. Problem: A. To get reliable force data on a given cellular system, users should record several hundreds of force curves using many independent tips and samples. B. Data treatment: estimates the adhesion force for each curve using the microscope software and displays the values either in the form of an adhesion force histogram or of an adhesion force map). Gray levels represent the adhesion values (brighter pixels meaning larger adhesion force).

Reference

1. Dufrene,Y. F. Atomic force microscopy and chemical force microscopy of microbial cells. *Nature Protocols*, **2008**, 3 (7): 1132-1138.

Appendix E

Preparation of Au (111)- electrodes

E.1 preparing the bead

Au(111) – electrodes were prepared by the method of Hamelin[1]. First a gold wire with the diameter of 1 mm was fixed over a H_2/ O_2–flame. The wire was melted until a drop appeared. Even though the gold wire used is 99.99999% gold, there are still some impurities that appear at the top of the bead after melting. The bead is allowed to crystallize and then melted again. This process is repeated several times. When the bead is heated the impurities appear lighter than the gold. The interface between melted and solid gold – the melt line – is continuously moved up and down in the bead by lowering and raising the temperature of the flame, which is controlled by changing the flow of hydrogen. If this operation is performed slowly the impurities will be collected at and transported by the melt line. It is thereby possible to move the impurities up to the base of the bead. The bead is melted 10-15 times. The impurities are further collected on the surface of the bead and can be removed by scraping them off with a clean scalpel after cooling of the bead. They can also be removed by electropolishing. The melting and scraping procedure is repeated 5 to 8 times, until the amount of impurities is low. The bead should now be a single crystal of gold. The eight (111) facets are the clearest and largest. It is usually only possible to observe up to seven (111) facets due to the connection between the bead and the wire. The usual maximum diameter of beads is 3 mm.

E.2 Adjusting the facet

The facets created on the bead are quite small and not practical to use. One of them is therefore chosen to be sanded so that the area is increased. The next step in the process is to fix the electrode via the gold-wire to a steel cylinder using epoxy glue. The glue is left to dry overnight and the bead is then adjusted by fixing a laser pointer so that it points into a mirror, which is adjusted at an angle allowing the beam to hit the facet, Fig. E.1. The reflection from the laser beam in the facet is then reflected in the mirror and

produces a spot on the wall a couple of meters away. The electrode is now turned and adjusted so that the laser beam is always on the facet. This provides an aligned horizontal facet. The electrode is now cast in a polymer (See below) and left in the oven at 800ºC overnight to solidify.

Table E.1 a polymer for one Au (111) bead prescription

Nonenylsuccinic anhydride	5.2 g
4-vinylcyclohexenedioxide	2.0 g
Epoxyresin, diglycidylether of polypropyleneglycol	1.2 g
2-dimethylaminoethanol	0.08 g

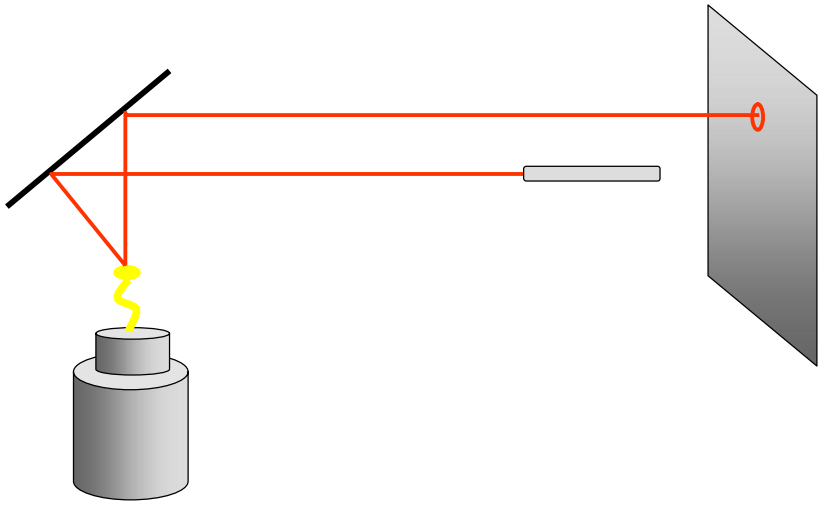

Fig E.1 setup for adjustment of the Au (111) –facet. Using a laser to find the right facet on the gold surface.

E.3 Polishing the electrode

The electrode in the polymer matrix is first polished with diamond-paper with grit number 320. Grit number describes the number of holes in the filter per square inch through which the particles on the sanding paper passes. This means that the larger the number, the smaller the particles. Polishing was stopped a while before the broadest place of the bead was reached. The polymer with the electrode was then washed in demineralized water. The polishing steps were repeated with grit numbers 500, 800, 1200, 2400 and 4000 for two minutes on each paper. The polishing was continued on a cloth with a suspension of Al_2O_3 grain size of 1.0, 0.1 and 0.05 µm step-wise for about 25

minutes or until no scratches were visible neither to the naked eye, nor in a magnifying glass. Care should be taken in the first polishing steps, so that the final polishing steps are performed when the bead has been polished down to maximum area, i.e. halfway through the bead.

E.4 Finishing touches

The polymer around the electrode is dissolved in a chloroform bath over a few days and then transferred to an ethanol bath for one day. The electrode is then washed thoroughly with Millipore water and annealed in the oven at 860 ºC, by flame annealing in a hydrogen flame and quenched in Millipore water. The voltammogram can be compared with voltammograms in the literature and the quality of the electrode assessed.

E.5 Electropolishing and annealing of Au (111) electrodes

The single crystal Au(111) electrodes are difficult to use and expensive to buy. Great care was therefore taken to ensure that they work flawlessly.

The electropolishing is carried out to remove any molecules adsorbed on the surface and the process itself also removes a few layers of surface atoms. The electrode is first placed in a beaker containing 0.5 M H_2SO_4 together with a platinum wire. The Au(111)-electrode is connected to the (+)-pole of the power supply and the platinum wire to the (-)-pole. The voltage is set to constant current and approximately 10 V and turned on. All of the electrode in contact with the acid then turns red from gold oxide formation. The reaction is left to continue for about 30 seconds and the electrode then lifted out of the solution. The voltage is turned off and the electrode washed with water. The electrode is then placed in a beaker with 1 M HCl. Chloride dissolves the gold oxide by forming a complex and after 10-20 seconds the electrode has a yellow color again, Equation E1. After electropolishing which roughens the surface, the electrode is annealed in an oven at 860 ºC for at least six hours to re-create high structural order on the surface. The electrode is then annealed in a hydrogen flame which enlarges the size of the surface terraces. After the flame-annealing, the electrodes are ready for use.

$$2Au + 3H_2O \rightarrow Au_2O_3 + 6H^+ + 6e^-$$
$$Au_2O_3 + 8Cl^+ + 6H^+ \rightarrow 2\left[AuCl_4\right]^- + 3H_2O \quad \text{(E.1)}$$

E.6 Preparation of Reversible Hydrogen Electrodes (RHE)

Reversible Hydrogen Electrodes (RHE) were made according to the principle shown in Fig. 4.2. A 1.0 mm diameter flame annealed platinum wire is inserted in a clean 10 cm pyrex glass tube and the tube melted onto the Pt wire by heating it in a hydrogen flame for 5-10 seconds. The heating is performed from several directions to make the tube fit the wire closely. Electrolyte is added to the tube from a cleaned glass pipette, once the tube has cooled down. A stream of a few hydrogen bubbled through a solution of electrolyte. The tube is immersed in the solution and hydrogen bubbles are allowed to enter the tube. The hydrogen gas should cover approximately half the Pt wire inside the tube. The potential follows the equation: E = -59.3 mV × pH at 25°C.

Reference

1. Hamelin A. cyclic voltammetry at gold single –crystal surface. Part 1. Behaviors at low index faces. *Journal of Electroanalytical Chemistry*, **1996**, 407: 1-11.

Publication

- Hu, Y.; Ulstrup, J.; Zhang, J.; Molin, S. and Dupres, V. Drug effect on *S. epidermidis* adhesion investigated by AFM. *Physical Chemistry Chemical Physics*, **2011**, 13 (21): 9995-10003.

- Hu, Y.; Zhang, J. and Ulstrup, J. Investigation of *Streptococcus mutans* biofilm growth on modified Au (111)-surfaces using AFM and electrochemistry. *Journal of Electroanalytical Chemistry*, **2011**, 656 (1-2): 41-49.

- Yang, L.; Hu, Y.; Liu, Y. Zhang, J.; Ulstrup, J. and Molin. S. Distinct roles of extracellular polymeric substances during *Pseudomonas aeruginosa* biofilm development**.** *Environmental Microbiology*, **2011**,13 (7):1705-1717.

- Hu, Y.; Zhang, J. and Ulstrup. J. Interfacial Electrochemical Electron Transfer Processes in Bacterial Biofilm Environments on Au(111). *Langmuir*, **2010,** 26 (11): 9094-9103.

- Qin, Z.; Zhang, J.; Hu, Y.; Chi, Q.; Mortensen, N. P.; Qu, D.; Molin, S. and Ulstrup, J.. Organic compounds inhibiting *S. epidermidis* adhesion and biofilm formation. *Ultramicroscopy*, **2009**, 109: 881-888.